

Oliver Zaudtke

Measurement of  
Direct-Photon Production and  
Neutral Pion Double Helicity Asymmetry  
in Ultra-Relativistic  $p + p$  Collisions

— 2007 —



Experimentelle Physik

Measurement of  
Direct-Photon Production and  
Neutral Pion Double Helicity Asymmetry  
in Ultra-Relativistic  $p + p$  Collisions

Inauguraldissertation  
zur Erlangung des Doktorgrades  
der Naturwissenschaften im Fachbereich Physik  
der Mathematisch-Naturwissenschaftlichen Fakultät  
der Westfälischen Wilhelms-Universität Münster

vorgelegt von  
**Oliver Zaudtke**  
aus Haselünne

— 2007 —

Dekan: Prof. Dr. J. P. Wessels  
Erster Gutachter: Prof. Dr. J. P. Wessels  
Zweiter Gutachter: Prof. Dr. C. Weinheimer

Tag der mündlichen Prüfung:

Tag der Promotion:

# Contents

1	Introduction	5
2	Theoretical Basics	9
2.1	The Strong Interaction . . . . .	9
2.1.1	The Running Coupling Constant . . . . .	9
2.1.2	Quark-Antiquark Potential . . . . .	10
2.2	Nucleon-Nucleon Reactions . . . . .	11
2.2.1	Particle Spectra in Nucleon-Nucleon Collisions . . . . .	12
3	The Relativistic Heavy Ion Collider	17
3.1	RHIC as a Polarized Proton Collider . . . . .	19
3.1.1	Spin Dynamics and Resonances . . . . .	21
3.1.2	Siberian Snakes and Spin Rotators . . . . .	25
3.1.3	Spin Flippers . . . . .	28
3.1.4	Polarization Measurement . . . . .	28
3.2	Experimental Program at RHIC . . . . .	29
3.2.1	BRAHMS . . . . .	30
3.2.2	PHOBOS . . . . .	31
3.2.3	STAR . . . . .	31
4	The PHENIX Experiment	33
4.1	Physics Goals of PHENIX . . . . .	33
4.2	PHENIX Detector Setup . . . . .	34
4.2.1	PHENIX Magnets . . . . .	35
4.2.2	Global Detectors . . . . .	35
4.2.3	Central Arm Spectrometers . . . . .	36
4.2.4	Muon Spectrometers . . . . .	39

5	The Electromagnetic Calorimeter	41
5.1	Electromagnetic Showers . . . . .	42
5.2	Types of Electromagnetic Calorimeters . . . . .	45
5.3	The Lead-Glass Calorimeter . . . . .	46
5.4	The Lead-Scintillator Calorimeter . . . . .	48
5.5	EMCal Online System . . . . .	49
5.5.1	PHENIX Timing System . . . . .	50
5.5.2	Front End Modules . . . . .	51
5.5.3	Level-1 Trigger System . . . . .	54
5.5.4	Data Collection Modules . . . . .	54
5.5.5	Event Builder . . . . .	55
5.5.6	Level-2 Trigger . . . . .	55
<b>I</b>	<b>Direct-Photon Production</b>	<b>57</b>
6	Direct-Photon Production in p + p Collisions	59
6.1	Mechanisms of Direct-Photon Production in Hard Parton Scatterings . . . . .	59
6.1.1	Prompt-Photon Production . . . . .	60
6.1.2	Fragmentation Photons . . . . .	63
6.2	Direct-Photon Production in A + A . . . . .	64
6.3	Earlier Results of Direct-Photon Production in N + N Collisions . . . . .	67
7	Measurement of Direct Photons in p + p Collisions	71
7.1	Analysis Method . . . . .	71
7.2	Data Selection and Correction . . . . .	72
7.2.1	Data Summary Table . . . . .	73
7.2.2	Analyzed Data Sets . . . . .	75
7.2.3	Run Selection . . . . .	76
7.2.4	Event Selection . . . . .	76
7.2.5	Energy Scale Correction . . . . .	78
7.2.6	Identification of Bad Towers . . . . .	82
7.3	Measurement of Inclusive Photons . . . . .	83
7.3.1	Photon-Like Clusters . . . . .	85
7.3.2	Corrections of the Photon-Like Cluster Spectrum . . . . .	87
7.3.3	Fully Corrected Inclusive Photon Spectrum . . . . .	105

7.3.4	Systematic Uncertainties of the Inclusive Photon Spectrum . . . . .	112
7.4	The Measured $\gamma/\pi^0$ Ratio . . . . .	116
7.4.1	Systematic Uncertainties of the Measured $\gamma/\pi^0$ Ratio . . . . .	117
7.5	The Simulated $\gamma/\pi^0$ Ratio . . . . .	124
7.5.1	Background Cocktail . . . . .	125
7.5.2	Effect of Shower Merging . . . . .	126
7.5.3	Systematic Uncertainties of the Simulated $\gamma/\pi^0$ Ratio . . . . .	129
7.6	Derivation of the Direct-Photon Signal . . . . .	131
7.6.1	Calculation of the Photon Excess . . . . .	131
7.6.2	Signal-To-Background Ratio . . . . .	132
7.6.3	Direct-Photon Error Propagation . . . . .	133
7.6.4	Direct-Photon Cross Section . . . . .	136
7.7	Combination of PbGl and PbSc Direct-Photon Spectra . . . . .	139
7.7.1	Combination Method . . . . .	140
7.7.2	Combined Results . . . . .	142
7.8	Comparisons with the Final Direct-Photon Spectrum . . . . .	144
<b>II Double Helicity Asymmetry</b>		<b>147</b>
8	The Proton Structure . . . . .	149
8.1	Elastic and Inelastic Scattering . . . . .	149
8.1.1	Form Factors . . . . .	150
8.1.2	Structure Functions . . . . .	150
8.1.3	Parton Distribution Functions . . . . .	153
8.2	Spin Structure of the Proton . . . . .	156
8.2.1	The Proton Spin Puzzle . . . . .	156
8.2.2	Polarized Parton Distribution Functions . . . . .	157
8.3	Measurement of $\Delta G$ at RHIC . . . . .	159
9	Double Helicity Asymmetry in $\pi^0$ Production . . . . .	165
9.1	Analysis Method . . . . .	165
9.2	Data Selection . . . . .	167
9.3	Relative Luminosity . . . . .	168
9.4	Polarization Measurement . . . . .	169
9.5	Energy Scale Correction . . . . .	169

9.6 Geometric Acceptance . . . . .	171
9.7 Photon-Like Cluster Sample . . . . .	171
9.8 Reconstruction of Neutral Pions . . . . .	172
9.8.1 Yield Corrections . . . . .	175
9.8.2 Bunch Crossing Numbering . . . . .	176
9.9 $A_{LL}$ Calculation . . . . .	176
9.9.1 Background Estimation . . . . .	179
9.9.2 $A_{LL}$ Error Calculation . . . . .	181
9.9.3 Signal and Background $A_{LL}$ . . . . .	182
9.9.4 Final Corrected $A_{LL}$ . . . . .	183
9.9.5 Average Transverse Momentum . . . . .	187
9.10 Cross Checks . . . . .	189
9.11 Comparison to Model Calculations . . . . .	192
Summary	197
Zusammenfassung	201
A Variables of Ultra-Relativistic Kinematics	205
B List of Analyzed Runs	207
B.1 Direct-Photon Analysis . . . . .	207
B.1.1 List of Analyzed Minimum Bias Runs . . . . .	207
B.1.2 List of Analyzed Gamma3 Filtered Runs . . . . .	208
B.2 Double Helicity Asymmetry Analysis . . . . .	209
C Bad Tower Maps	211
D Photon-Like Cluster Spectra	213
E Data Tables - Direct Photons	215
E.1 Cross Section of Inclusive Photon Production in p + p Collisions . . . . .	215
E.2 Invariant Yield of Neutral Pion Production in p + p Collisions . . . . .	218
E.3 Direct-Photon Production Cross Section in p + p Collisions . . . . .	221
F Data Tables - $A_{LL}$	225
F.1 Signal and Background $A_{LL}$ . . . . .	225
Danksagung	239

# 1. Introduction

One major objective of nuclear physics is to understand the elementary structure of matter and the fundamental forces which are responsible for the observed phenomena. Since the first half of the 20th century the proton and the neutron, both referred to as nucleons, together with the electron are considered as the building blocks of everyday atomic matter. While so far there has been no experimental indication for a substructure of the electron, deep-inelastic lepton-nucleon scattering (DIS) experiments in the late 1960's revealed that the proton is composed of even smaller subcomponents. These particles were first called *partons* and later identified as *quarks* which were predicted independently by Gell-Mann [GM64] and Zweig [Zwe64] based on data from hadron spectroscopy. The experimental as well as theoretical achievements led to the introduction of the *constituent quark model*, in which the proton and neutron are just two representatives of the so-called *hadrons* which are all composed of quarks.

Two types of hadrons are known today: *baryons* and *mesons*. Baryons (like proton and neutron) consist of three quarks ( $qqq$ ) while mesons contain a quark-antiquark pair ( $q\bar{q}$ ). To present knowledge there are six different kinds of quarks, also called *flavors* and the corresponding antiquarks: **up**, **down**, charm, strange, **top** and **bottom**. They are fermions with spin 1/2 and carry electric charge of either  $+2/3e$  or  $-1/3e$ , where  $e$  is the electric charge of the proton. In experiments up to date no substructure of the quarks was found. Hence, quarks are considered as elementary particles.

As part of the quark model a new quantum number was introduced: the *color charge*. Each quark carries one of three colors: *blue*, *red* or *green* (antiquarks carry anticolors). This ensures that baryons which consist of three identical quarks, e.g.  $\Delta^{++} = (\text{u}, \text{u}, \text{u})$ , do not violate the Pauli exclusion principle. No experiment so far was able to observe single free quarks, which supports the assumption that only color neutral objects<sup>1</sup> exist as free particles in nature.

Hadrons are strongly interacting particles, i.e. the force that holds hadronic matter together and governs the evolution of hadronic reactions is the fundamental strong interaction. The quantum field theory describing the behavior of the strong force is quantum chromodynamics (QCD). The theoretical framework was developed in the 1970's adopting basic concepts of quantum electrodynamics (QED), the quantum field theory which successfully describes electromagnetism. For a general review of QCD please refer to [Wil82]. The exchange particles of QCD (also called gauge bosons) which mediate

---

<sup>1</sup>The quarks of a baryon each carry a different color, while the quark-antiquark pair of a meson carries a color and the corresponding anticolor. In both cases the colors add up to white (color neutral).

the strong force between color charged objects are the so-called *gluons* ( $g$ ). They are massless bosons and carry spin 1. A specific characteristic of QCD is that the gluon also carries color charge. Hence, in QCD the gauge bosons themselves couple to each other which has far-reaching consequences for the properties of the strong interaction (see Section 2.1).<sup>2</sup>

In the constituent quark model the nucleon (like all baryons) consists of three quarks, also called *valence quarks*, which were thought to account for all properties of the nucleon (quantum numbers, mass). Although the valence quarks are sufficient to explain the observed spectroscopic properties (excitation states, decays), DIS experiments at very high energies have revealed a far more complex structure. Today the composition of the nucleon is described by valence quarks and a large number of gluons and virtual quark-antiquark pairs. The virtual quark-antiquark pairs are referred to as *sea quarks*. According to the energy uncertainty principle quark-antiquark pairs can exist for a short period of time without violating energy conservation. All these components (partons) contribute to some extent to the observed properties of the nucleon depending on the energy scale at which the nucleon is probed. Even after decades of experimental and theoretical work the structure of the nucleon is not completely understood. Especially the momentum distribution of the gluons inside the proton is largely unknown. This is due to the fact that DIS experiments depend on the electromagnetic coupling of a lepton to the probed parton. Therefore such experiments are not directly sensitive to the electrically neutral gluons.

A tool to study the gluon density in the nucleon is provided by particle production in ultra-relativistic proton-proton ( $p + p$ ) collisions which involves the gluon in the initial state. Especially the production of direct photons has been recognized already in the early 1980's as a tool to access the gluon distribution inside the proton [Pap82]. In high energy  $p + p$  collisions, direct-photon production at large transverse momenta  $p_T$ <sup>3</sup> is described by perturbative QCD (pQCD). At leading order the gluon contributes to the production of direct photons via quark-gluon Compton scattering:  $q + g \rightarrow q + \gamma$ . A more general review of direct-photon production mechanisms in elementary  $p + p$  collisions is given in Chapter 6. By constraining the measurement of direct photons to those photons produced in quark-gluon Compton scattering the only free parameter in the calculation is the gluon distribution.

The measurement of the cross section of inclusive direct-photon production in elementary  $p + p$  collisions is of paramount interest not only because of its sensitivity to the gluon density but also for other reasons. It provides an excellent test of pQCD predictions and can help to study parton-to-photon fragmentation functions. Moreover, it serves as

---

<sup>2</sup>In QED the corresponding exchange particle, the photon, is electrically neutral and therefore photons do not couple to each other.

<sup>3</sup>A definition of kinematic variables used in ultra-relativistic reactions is given in Appendix A.

the baseline for the interpretation of direct-photon data obtained in heavy-ion collisions (see Chapter 6).

By studying particle production in polarized p + p collisions (i.e. the spins of the two protons are oriented with respect to their direction of motion prior to the collision) it is possible to measure the polarized distribution of the gluon inside the proton and consequently explore what is generally referred to as the *proton spin puzzle*. In the naive parton model the proton spin of 1/2 is expected to be the straightforward sum of two parallel valence quark spins and one antiparallel. However, in the late 1980's it was discovered in DIS experiments of polarized leptons on polarized protons that all quarks (valence and sea) carry only a small fraction of the proton spin [Ash88, Ash89]. Since then this unexpected result is known as the proton spin puzzle. In the complex parton model including sea quarks and gluons it is reasonable to assume that the intrinsic spin of the gluon makes a non-vanishing contribution to the proton spin. While not directly accessible in DIS experiments, the polarized gluon distribution is directly related to the spin dependent cross section of particle production in polarized p + p collisions which involves the gluon in the partonic production mechanism. More precisely the polarized gluon distribution can be explored by measuring the double helicity asymmetry of the production cross section, also called  $A_{LL}$  (this is described in more detail in Chapter 8).

The analysis of direct photons in polarized p + p collisions provides the cleanest tool to access the polarized gluon distribution. Another channel which is sensitive to the gluon distribution is the production of hadron jets, in particular the production of neutral pions ( $\pi^0$ ). In pQCD gluon-gluon ( $g + g \rightarrow g + g$ ) and gluon-quark ( $g + q \rightarrow g + q$ ) scattering contributes at leading order to jet production. However, the calculation of the  $\pi^0$  production cross section requires the knowledge of fragmentation functions which describe the fragmentation of the scattered partons into neutral pions. This introduces an additional theoretical uncertainty in the interpretation of the data. Yet the virtue of utilizing the  $\pi^0$  channel to explore the polarized gluon distribution is the rather simple measurement of neutral pions compared to direct photons in p + p collisions.

In this thesis two independent analyses are presented: the measurement of the inclusive direct-photon production cross section and the measurement of the double helicity asymmetry in inclusive  $\pi^0$  production both at mid-rapidity in ultra-relativistic p + p collisions at  $\sqrt{s} = 200$  GeV. The analyzed data set was collected with the PHENIX detector in collisions of longitudinally polarized protons at RHIC. For the direct-photon measurement the data were analyzed regardless of the polarization resulting in the spin-averaged or unpolarized direct-photon cross section. The measurement of  $A_{LL}$ , however, explicitly takes into account the polarization of the colliding protons. While the direct-photon  $p_T$ -distribution is measured with a precision unmatched so far at RHIC energies and therefore allows for the first time a comparison to pQCD predictions over many orders of magni-

tude, the double helicity asymmetry of  $\pi^0$  production demonstrates the first measurement of this kind in ultra-relativistic polarized p + p collisions at all and allows a first direct constraint on the polarized gluon distribution.

## 2. Theoretical Basics

The evolution of p + p collisions is governed by the strong interaction. The strength of the interaction is described by the coupling "constant" of QCD. The structure of this "constant" has some important consequences for the potential of the strong interaction and can be observed in particle spectra measured in ultra-relativistic p + p collisions. The factorization theorem of pQCD allows the calculation of cross sections for reactions with large momentum transfer and hence enables high precision tests of QCD.

### 2.1 The Strong Interaction

#### 2.1.1 The Running Coupling Constant

The force between strongly interacting particles is described by quantum chromodynamics. In each quantum field theory the strength of the force is described by the coupling constant of the interaction. In QED the strength of the electromagnetic coupling is given by the fine structure constant  $\alpha \approx 1/137$ . While  $\alpha$  shows only a weak energy dependence the strength of the coupling in QCD heavily depends on the energy scale at which the strongly interacting matter is probed, often chosen to be the momentum transfer  $Q^2$  of the reaction. To first order the coupling constant of QCD,  $\alpha_s$ , can be written as follows [Yag05]:

$$\alpha_s(Q^2) \approx \frac{12\pi}{(33 - 2N_f) \cdot \ln(Q^2/\Lambda_{\text{QCD}}^2)}, \quad (2.1)$$

where  $N_f$  denotes the number of contributing quark flavors.  $\Lambda_{\text{QCD}}$  is the QCD scale parameter and is the one fundamental parameter of QCD. It has to be determined by comparison of QCD predictions to experimental data and depends on the number of quark flavors  $N_f$  with quark masses  $\ll Q^2$ .  $\alpha_s$  measured in different experiments at different energy scales is shown in Figure 2.1. It clearly shows the variation of  $\alpha_s$  with  $Q^2$ . Therefore  $\alpha_s$  is often referred to as *running coupling constant*. For more details refer to e.g. [Yao06].

For calculations in QCD perturbation theory is applicable if  $\alpha_s$  is small ( $\alpha_s \ll 1$ ), i.e. if the strong coupling becomes weak. Equation 2.1 shows that this is the case for large momentum transfer ( $Q^2 \gg \Lambda_{\text{QCD}}^2$ ). It is an important feature of the strong interaction that for  $Q^2 \rightarrow \infty$  the coupling between quarks vanishes. Since large values of  $Q^2$  are equivalent to small distances between the interacting particles, quarks behave as if they were free when they are very close together. This phenomenon is known as *asymptotic freedom*. On the other hand for small momentum transfer ( $Q^2 \lesssim \Lambda_{\text{QCD}}^2$ ), equivalent to

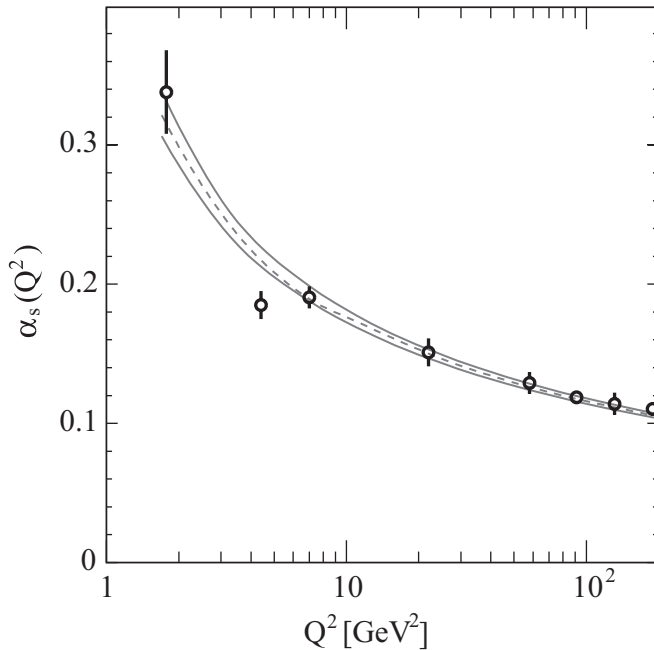


**Figure 2.1:** The running coupling constant of QCD as a function of the momentum transfer  $Q^2$ . The data points represent measurements of  $\alpha_s$  at certain energy scales. The lines show central values and the corresponding uncertainty. For further details refer to [Yao06].

large distances, the coupling becomes very large. The *confinement* of quarks in hadrons (single free quarks have not been observed yet) is attributed to this characteristic of the strong interaction and is probably related to the interaction among the colored gluons. A theoretical description in this strongly coupled domain is difficult because a treatment in perturbation theory is not applicable (non-perturbative regime).

### 2.1.2 Quark-Antiquark Potential

The similarity of charmonium states (a bound system composed of a  $c\bar{c}$ -quark pair<sup>1</sup>) to the energetic states of positronium (a well-known electromagnetically bound  $e^+e^-$  system) and the experimental observation that only color neutral objects exist as free particles in nature suggests the following phenomenological potential of the strong force between quarks as a function of the distance  $r$  [Pov99]:

$$V_s(r) = -\frac{4}{3} \frac{\alpha_s(r) \hbar c}{r} + k \cdot r, \quad (2.2)$$

<sup>1</sup>E.g. the heavy mesons  $J/\Psi$  and  $\Upsilon$  are charmonium states.

where the first term is similar to the Coulomb potential and dominates at small distances. For asymptotically small  $r$  the coupling constant  $\alpha_s(r) \rightarrow 0$  and therefore leads to the asymptotic freedom. The second term is dominant at large distances. The potential energy increases linearly with increasing distance between the quark-antiquark pair and hence describes the confinement. While the field lines of a Coulomb potential reach far into space (like the field of an electric dipole) the field lines of a potential given by  $k \cdot r$  (the color field between a  $q\bar{q}$  pair) are restricted to a narrow tube (also called a *string*) because of the gluon-gluon interaction. Because the field energy within the tube increases linearly with increasing  $r$  removal of a quark from a hadron would require an infinite amount of energy. Instead, if the field energy reaches a certain threshold it is more favorable to form two separate  $q\bar{q}$  pairs, i.e. two strings. This process of creating new color neutral hadrons is referred to as *hadronization*.

## 2.2 Nucleon-Nucleon Reactions

Particle production in high energy nucleon-nucleon ( $N + N$ ) reactions provides a tool to study the strong interaction. The total  $p + p$  cross section  $\sigma_{\text{total}}^{\text{p+p}}$  as a function of the center-of-mass energy  $\sqrt{s}$  is shown in Figure 2.2 [Yao06]. At  $\sqrt{s} \approx 10$  GeV the total cross section is roughly  $\sigma_{\text{total}}^{\text{p+p}} \approx 40$  mb and increases only slowly as  $\sqrt{s}$  increases. The reaction processes contributing to the total cross section can be subdivided into elastic processes, in which the total kinetic energy of the colliding nucleons remains unchanged and inelastic processes, in which the colliding nucleons lose energy. As one can see from Figure 2.2 above a  $\sqrt{s}$  of a few GeV the  $p + p$  reaction is dominated by inelastic processes. In  $p + p$  collisions at high energies the probability for a nucleon to lose a considerable fraction of its initial energy is large. The deposited energy results in the production of new particles. Therefore inelastic  $p + p$  reactions are characterized by particle production.

About 80-90% of the produced particles are pions ( $\pi^\pm, \pi^0$ ), since they are the hadrons with the smallest mass. The total number of produced particles is called *multiplicity*. It has been shown by various experiments that the charged multiplicity<sup>2</sup> increases logarithmically with  $\sqrt{s}$  and can be parameterized by [Won94]:

$$\langle N_{\text{ch}} \rangle = 0.88 + 0.44 \cdot \ln s + 0.118 \cdot (\ln s)^2, \quad (2.3)$$

where  $s$  is the squared center-of-mass energy in GeV<sup>2</sup>. For  $p + p$  collisions at  $\sqrt{s} = 200$  GeV this means  $\langle N_{\text{ch}} \rangle \approx 20$ . Neutral particles produced in the collision are mainly neutral pions. By assuming that equal numbers of  $\pi^+$ ,  $\pi^-$  and  $\pi^0$  are produced the total multiplicity in  $p + p$  collisions at  $\sqrt{s} = 200$  GeV can be approximated by  $\frac{3}{2} \cdot \langle N_{\text{ch}} \rangle \approx 30$ .

---

<sup>2</sup>The number of charged particles produced in the collision.

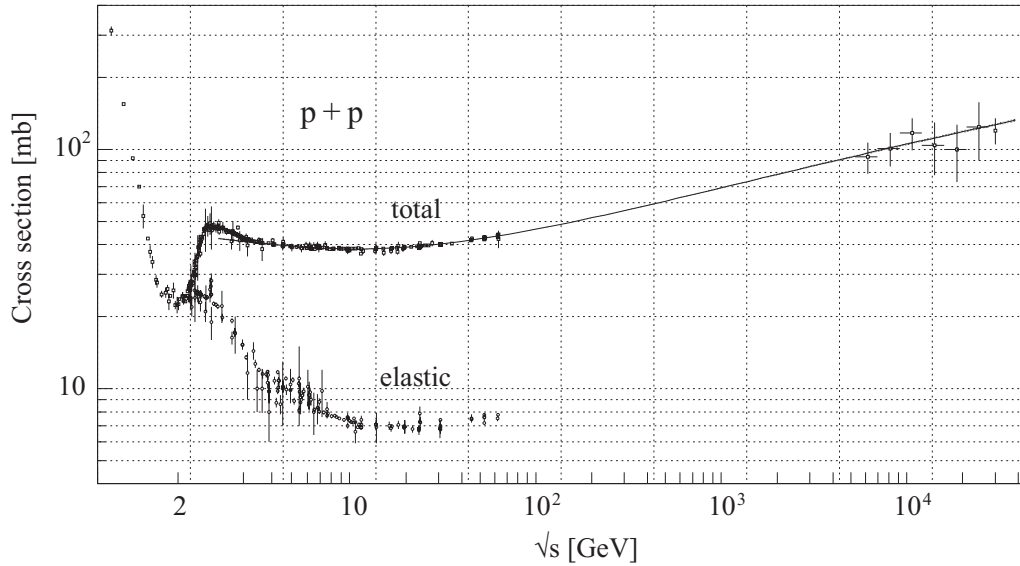


**Figure 2.2:** Total cross section for  $p + p$  reactions as a function of  $\sqrt{s}$  [Yao06]. Above  $\sqrt{s} \approx 10$  GeV the cross section is dominated by the inelastic cross section which is roughly constant in this energy regime.

### 2.2.1 Particle Spectra in Nucleon-Nucleon Collisions

Typical  $p_T$  distributions of charged particles produced in  $p + p$  and  $p + \bar{p}$  collisions at different  $\sqrt{s}$  measured by various experiments are shown in Figure 2.3. Such particle spectra can be divided into two domains in terms of underlying production mechanisms: the *soft region* for particles with transverse momenta far below  $1 \text{ GeV}/c$  and the *hard region* for particles with transverse momenta far above  $1 \text{ GeV}/c$ . The shape of the  $p_T$  distribution is different in both kinematic regions.

#### Soft Region

The bulk of particles produced in  $N + N$  collisions has small transverse momenta with a mean given by  $\langle p_T \rangle \approx 0.3 \text{ GeV}/c$ . The shape of the spectrum below  $p_T = 1 \text{ GeV}/c$  is well described by an exponential of the form  $e^{-\alpha p_T}$ , with  $\alpha \approx 6 \text{ (GeV}/c)^{-1}$  (see Figure 2.3). The underlying production mechanisms in this region are characterized by small momentum transfers  $Q^2$  (i.e.  $Q^2 \lesssim \Lambda_{QCD}^2$ ) and are referred to as soft processes. A quantitative analysis of soft processes in QCD is difficult because perturbation theory cannot be applied. Instead a number of phenomenological techniques have been developed to study processes in the non-perturbative regime qualitatively (e.g. string models). Refer to e.g. [Won94] for further details.

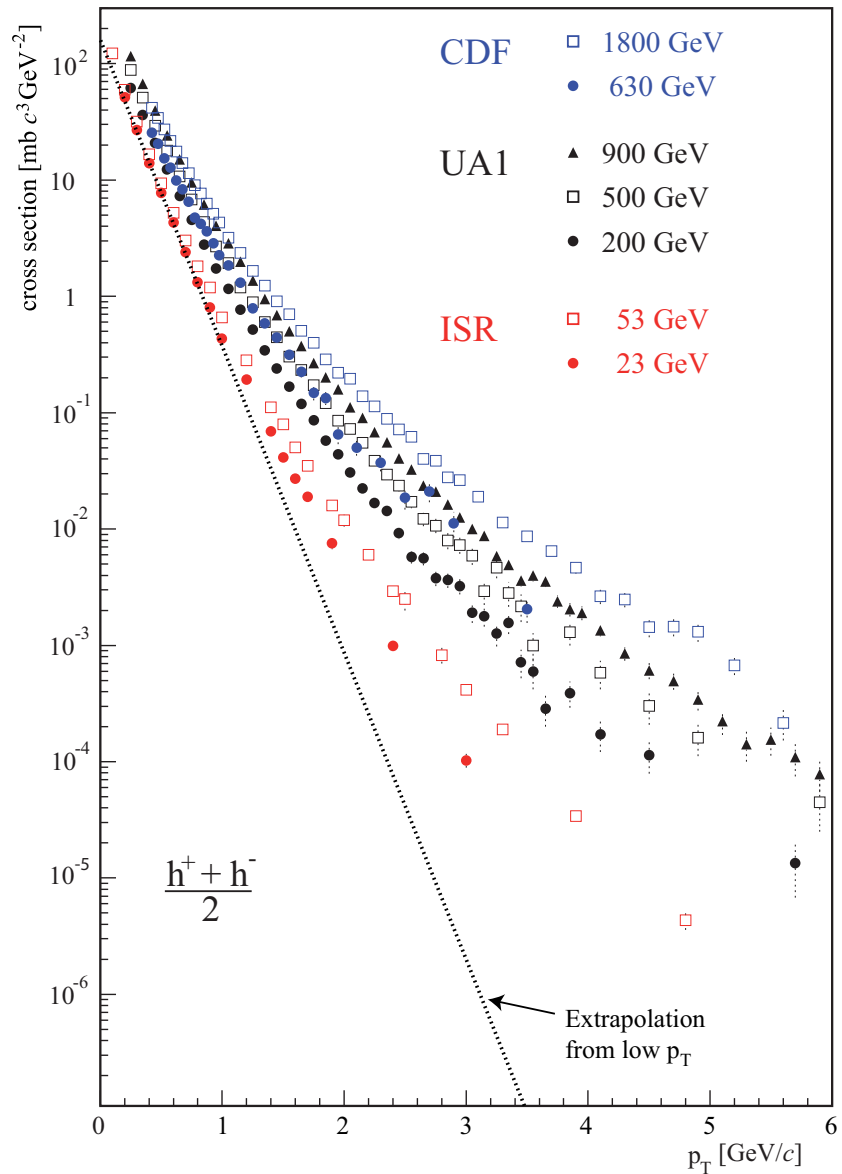


**Figure 2.3:** Inclusive charged particle production measured in  $p + p$  and  $p + \bar{p}$  collisions at different energies as a function of the transverse momentum [Dre02].

### Hard Region

As one can see in Figure 2.3 the shape of the particle spectrum at high  $p_T$  cannot be extrapolated from the exponential at low  $p_T$ . The mechanisms of particle production in this regime are characterized by large momentum transfers  $Q^2$ . The collision can be interpreted as the elastic scattering of "hard" partons off each other. Hence such processes

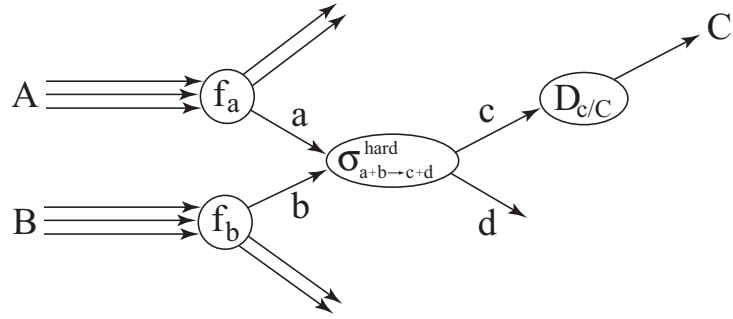


**Figure 2.4:** Illustration of a hard scattering process with the subsequent hadron fragmentation.

are referred to as hard processes. Since for large  $Q^2$  the strongly interacting matter is only weakly coupled, the techniques of perturbative QCD can be applied to make quantitative predictions. Hence, although the probability for particle production at high  $p_T$  is small, the measurement of particle spectra in this kinematic regime is an important tool for precision tests of pQCD.

In Figure 2.4 the inclusive hard scattering reaction:

$$A + B \rightarrow C + X \quad (2.4)$$

is depicted where the focus is on the production of the hadron  $C$ . The term *inclusive* means that, although all particles which are produced along the reaction are implicitly included in  $X$ , only particle  $C$  is explicitly identified. The underlying process of the reaction is the hard scattering of parton  $a$  in  $A$  with parton  $b$  in  $B$  in which a large momentum is transferred. The scattered partons  $c$  and  $d$  lead to the subsequent observation of particle jets along the direction of the scattered partons.

According to the *factorization theorem* in pQCD the inelastic cross section of hard reactions can be separated into long-distance (large  $Q^2$ ) and short-distance (small  $Q^2$ ) processes. Since pQCD gives only meaningful results for reactions involving large momentum transfers the long-distance terms are referred to as non-perturbative while the short-distance terms are referred to as perturbative. According to [Col85] the inelastic cross section for a reaction given in Equation 2.4 can be factorized in the following way:

$$\begin{aligned} d\sigma_{AB \rightarrow C}^{\text{hard}} &= \sum_{a,b,c} f_a(x_a, Q^2) \otimes f_b(x_b, Q^2) \\ &\otimes d\sigma_{ab \rightarrow c}^{\text{hard}}(x_a, x_b, z_c, Q^2) \otimes D_{c/C}(z_c, Q^2), \end{aligned} \quad (2.5)$$

where  $f_a$  ( $f_b$ ) is the non-perturbative parton distribution function (PDF) of parton  $a$  ( $b$ ) in hadron  $A$  ( $B$ ) and  $x$  is the momentum fraction which is carried by the parton, i.e. parton

a (b) carries a fraction  $x_a$  ( $x_b$ ) of the momentum of hadron  $A$  ( $B$ ).  $d\sigma_{ab \rightarrow c}^{\text{hard}}$  is the perturbatively computable parton scattering cross section for the reaction  $a + b \rightarrow c + X$ . And  $D_{c/C}$  is the non-perturbative fragmentation function (FF) which describes the fragmentation process of the scattered parton  $c$  into the hadron  $C$ , which carries a momentum fraction  $z_c$  of the parton momentum. The  $a, b, c$  sum is over all partonic channels  $a + b \rightarrow c + X$ .

The non-perturbative parts, i.e. the distribution of the partons in the initial state (before the hard scattering) and the fragmentation process of the scattered partons in the final state (after the hard scattering) have to be determined experimentally (see Section 8.1.3 for more information on the extraction of PDF's from experimental data). However, both parton distribution functions as well as fragmentation functions are assumed to be universal, i.e. they are the same regardless of the scattering process involved. This means, that PDF's and FF's can be measured in reactions which allow the most precise determination and are then utilized as input for a given pQCD calculation.

If a photon is produced in the hard scattering (i.e. parton  $c$  in Figure 2.4 is substituted by a photon  $\gamma$ ) the calculation of the cross-section does not require a fragmentation function. Thus the measurement of such *prompt* photons allows a more precise test of pQCD since the calculation is not subject to uncertainties arising from the fragmentation process (see Chapter 6 for more details).

The separation of long- and short-distance processes in factorized pQCD introduces unphysical scales in the computation of cross sections according to Equation 2.5 which have to be chosen arbitrarily: two *factorization scales*,  $\mu_F$  and  $\mu'_F$  which are chosen each to distinguish between the hard and soft components of the cross section and the *renormalization scale*  $\mu_R$  which is associated with the running of the strong coupling constant  $\alpha_s$ . A typical choice is to set all three scales to the same value  $\mu$  which is of the order of the hard scale given by the momentum transfer  $Q^2$  or the transverse momentum  $p_T$  of the observed hadron<sup>3</sup>, i.e.  $\mu_F = \mu'_F = \mu_R = \mu = p_T$ . The scale dependence is often estimated by additional calculation of the cross section at the scales  $\mu = 2p_T$  and  $\mu = p_T/2$ . For more information on factorization in pQCD please refer to e.g. [Col85, Lib78].

---

<sup>3</sup>In hard inelastic scatterings the momentum transfer is of the order of the square of the transverse momentum of the observed leading particle ( $Q^2 \sim O(p_T^2)$ ).



### 3. The Relativistic Heavy Ion Collider

The idea to build the Relativistic Heavy Ion Collider (RHIC) was first formulated in 1983. Construction began in 1991 and was completed eight years later in 1999. The scientific objectives of RHIC comprise the study of the highly excited matter created in ultra-relativistic heavy ion collisions as well as the proton spin structure by colliding polarized protons. The collider was built at Brookhaven National Laboratory (BNL)<sup>1</sup>. It consists of two separate concentric storage rings with superconducting magnets. The magnets are cooled down to below 4.6 K using supercritical helium. The two rings are denoted arbitrarily as the “Blue Ring” (where the beam travels in the clockwise direction) and the “Yellow Ring” (where the beam travels in the counter clockwise direction). Head-on collisions of the two beams can be achieved at six intersection regions (IR). At RHIC particles with an atomic mass number up to  $A \sim 200$  can be accelerated. The availability of two ion sources and a proton source together with two completely independent storage rings provides the possibility to accelerate and study collisions of equal (e.g. Au + Au) and unequal ion species (e.g. d + Au) as well as collisions of protons. The Alternating Gradient Synchrotron (AGS) as well as other smaller hadron accelerators (Tandem Van de Graaff, Booster), which already existed at BNL before the construction of RHIC, are used as the injector to the collider rings. Some of the important elements of the RHIC collider complex are shown in Figure 3.1.

RHIC is designed to accelerate heavy-ion beams up to an energy of 100 GeV per nucleon and polarized proton beams up to an energy of 250 GeV. Therefore RHIC is able to achieve center-of-mass energies of  $\sqrt{s_{NN}} = 200$  GeV and  $\sqrt{s} = 500$  GeV per nucleon-nucleon pair in Au + Au and p + p collisions, respectively. These energies reach well into the regime of perturbative QCD and the highly excited matter created in central Au + Au collisions is expected to be in a deconfined state. After the initial engineering tests first collisions of heavy ions were achieved on June 12, 2000 at a center-of-mass energy of  $\sqrt{s_{NN}} = 56$  GeV per nucleon-nucleon pair. Collisions of Au ions at the design energy were achieved in the following year on July 18, 2001. In the same year first physics data of colliding proton-proton beams were accumulated. The design luminosity  $L$  for Au + Au collisions and for p + p collisions is  $L = 2 \times 10^{26} \text{ cm}^{-2}\text{s}^{-1}$  and  $L = 2 \times 10^{32} \text{ cm}^{-2}\text{s}^{-1}$ , respectively [Har03].

The collider is operated in a bunched beam mode. The beam in either rings consists of 120 bunches. A maximum of 112 bunches is filled with heavy ions or protons. Eight

---

<sup>1</sup>located on Long Island, New York

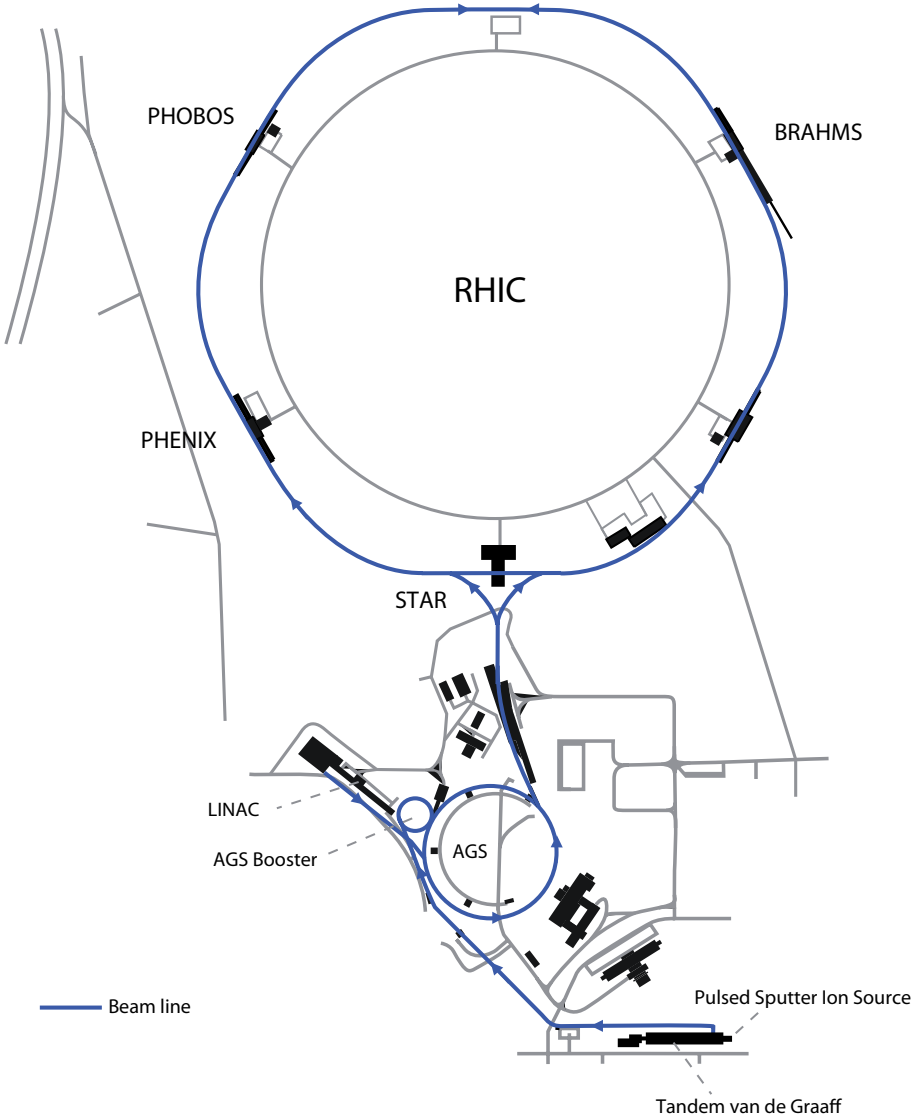


**Figure 3.1:** Schematic view of the RHIC facility. The illustration is taken from [Büs02].

bunches remain empty for the abort gap in order to ensure safe dumping of the beam. Each bunch contains  $\sim 1 \times 10^9$  Au ions and  $\sim 2 \times 10^{11}$  protons, respectively.

The basic steps in the acceleration of heavy ions is as follows. A large variety of ion species can be extracted from a pulsed sputter ion source. The negatively charged ions are accelerated in the Tandem Van de Graaff. A stripping foil removes electrons leaving partially stripped ions with positive charge. Ions exit the Tandem with a kinetic energy of  $\sim 1$  MeV per nucleon. After further stripping the highly positively charged ions are injected into the Booster synchrotron where the beams are captured into six bunches and accelerated to 95 MeV per nucleon. All but two electrons are stripped at the exit of the Booster before they are injected into the AGS, where the beams are debunched and

rebunched into four final bunches. The AGS accelerates the ions to 8.86 GeV per nucleon. The bunches are then transferred to one of the RHIC rings where they are accelerated to their colliding energy. On their way to the collider the ions pass the last stripping foil where they are fully ionized. A more detailed description of the acceleration cycle for heavy ions is given in [Har03].

The acceleration of polarized protons requires a different source and involves additional devices to maintain polarization throughout acceleration. This is discussed in more detail in Section 3.1.

Four major experiments were designed for RHIC which on the one hand are similar in some aspects and on the other hand are complementary to each other. This has the advantage that, while all experiments have some specific objectives, many scientific discoveries can be cross checked by the different experimental groups. The experiments can be divided in terms of size, cost and complexity in two large (PHENIX<sup>2</sup> and STAR<sup>3</sup>) and two smaller (BRAHMS<sup>4</sup> and PHOBOS<sup>5</sup>) projects. The purpose of each experiment is described in Section 3.2.

Up to the time of writing of this thesis there have been six completed physics running periods in which different species at different center-of-mass energies have been accelerated and collided. Table 3.1 shows a summary of the finished physics program at RHIC up to now. The p + p data presented in this thesis were accumulated during the third RHIC physics running period.

### 3.1 RHIC as a Polarized Proton Collider

RHIC is the first and to date only high-energy polarized proton collider. With center-of-mass energies up to  $\sqrt{s} = 500$  GeV the collision of transversely or longitudinally polarized protons can be considered as collisions of polarized quarks and gluons. This provides the opportunity to study the spin structure of the proton and might help to shed light on answers to the *spin puzzle* (see Chapter 8). The acceleration of polarized protons up to energies of 250 GeV requires several additional devices that help to maintain, manipulate and monitor polarization. RHIC employs *Siberian Snakes*, *Spin Rotators*, *Spin Flippers* and *Polarimeters* to meet these additional requirements [Ale03]. Figure 3.2 shows a schematic view of the RHIC facility and the pre-acceleration chain from the point of view of the polarized proton collider.

---

<sup>2</sup>Pioneering High Energy Nuclear Interaction EXperiment

<sup>3</sup>Solenoidal Tracker At RHIC

<sup>4</sup>Broad RAnge Hadron Magnetic Spectrometer

<sup>5</sup>PHOBOS is not an acronym.

	year	species	$\sqrt{s_{NN}}$ [GeV]
Run I	July - September 2000	Au + Au	130
Run II	July 2001 - January 2002	Au + Au	200
		p + p	200
Run III	December 2002 - May 2003	d + Au	200
		p + p	200
Run IV	December 2003 - May 2004	Au + Au	200
		Au + Au	62.4
		p + p	200
Run V	2004/2005	Cu + Cu	200
		Cu + Cu	62.4
		Cu + Cu	22.5
		p + p	200
Run VI	2006	p + p	200
		p + p	62.4

**Table 3.1:** Summary of completed RHIC physics running periods since the beginning in 2000 until the day of writing of this thesis.

The polarized proton source installed at RHIC was custom-designed to meet the required intensity of each bunch. It provides protons that are transversely polarized with respect to the beam direction. The optically pumped polarized ion source (OPPIS [And79]) produces a pulse that corresponds to  $\sim 9 \times 10^{11}$  polarized H $^-$ . Taking into account beam losses from the source to the storage rings the intensity provided by the source is sufficient to meet the design luminosity goal. The RHIC source was constructed at TRI-UMF<sup>6</sup> [Mor00]. It is an upgrade of the OPPIS source previously used at KEK<sup>7</sup>. The source consists of an electron cyclotron resonance (ECR) ion source in which the unpolarized protons are produced. The protons pass through an optically pumped rubidium vapor (i.e. an electron spin polarized target) in a weak magnetic field. The spin is transferred via the hyperfine interaction from the electron to the proton. The polarized hydrogen atoms then pick up electrons in a sodium vapor yielding H $^-$ , which are then transferred to the LINAC<sup>8</sup>, where the H $^-$  are accelerated to 200 MeV. Before injection into the AGS Booster the electrons of the H $^-$  beam are stripped and the polarized protons are captured

<sup>6</sup>Tri University Meson Facility in Vancouver, Canada

<sup>7</sup>High Energy Accelerator Research Facility in Tsukuba, Japan

<sup>8</sup>Linear Accelerator

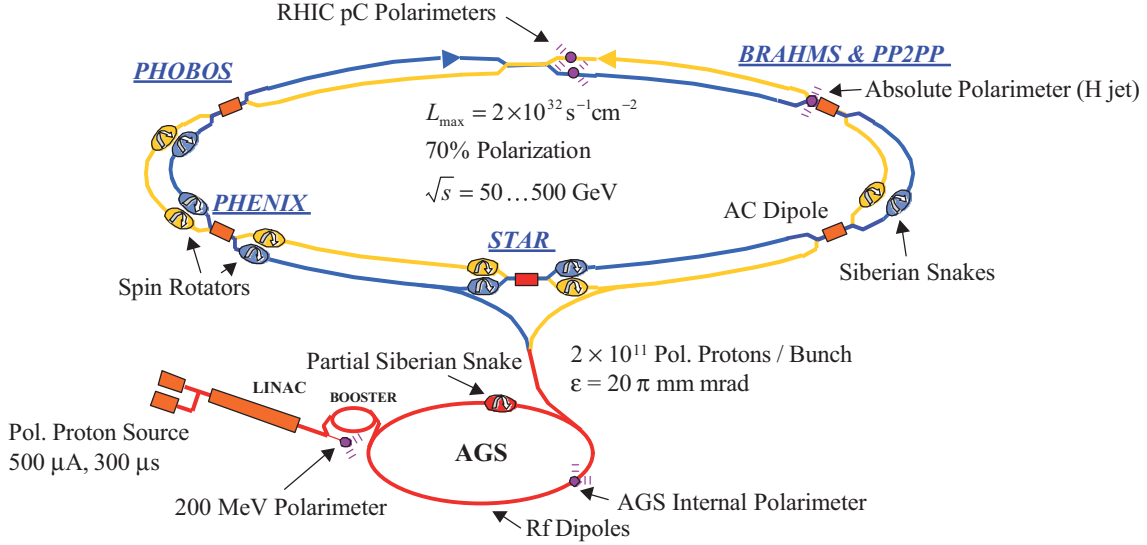


**Figure 3.2:** A schematic view of the RHIC facility showing all devices necessary for the acceleration of polarized protons.

in the Booster in a single bunch. The single bunch is accelerated to 2.35 GeV and then transferred to the AGS, where it is accelerated to 24.3 GeV. The single bunch is then transferred to one of the RHIC storage rings. The acceleration process has to be repeated for all bunches that are to be filled into RHIC. This has the advantage that the polarization of each bunch is prepared independently in the source. The polarization pattern in both rings is chosen in a way that collisions with all four combinations of polarization directions ( $\uparrow\uparrow$ ,  $\uparrow\downarrow$ ,  $\downarrow\uparrow$  and  $\downarrow\downarrow$ ) are established in the same fill. This reduces systematic uncertainties that would arise from fill-by-fill uncertainties. RHIC is designed to achieve and maintain beam polarizations up to 70%.

### 3.1.1 Spin Dynamics and Resonances

In a storage ring like RHIC charged particles are bent on a closed orbit by dipole magnets. The motion of a proton with charge  $e$  and mass  $m_p$  in a vertical magnetic guide field  $\vec{B}$  is governed by the Lorentz force equation:

$$\frac{d\vec{v}}{dt} = -\left(\frac{e}{\gamma m_p}\right) \vec{B}_\perp \times \vec{v}, \quad (3.1)$$

where  $\vec{v}$  is the velocity vector of the particle and  $\gamma = E/m_p$  is the relativistic boost.

In a perfect circular accelerator charged particles would follow a perfect closed loop, the *design orbit*. In reality, the guiding magnets suffer from misalignment and imperfect manufacture. Because of this the actual particle orbit differs from the *design orbit*;

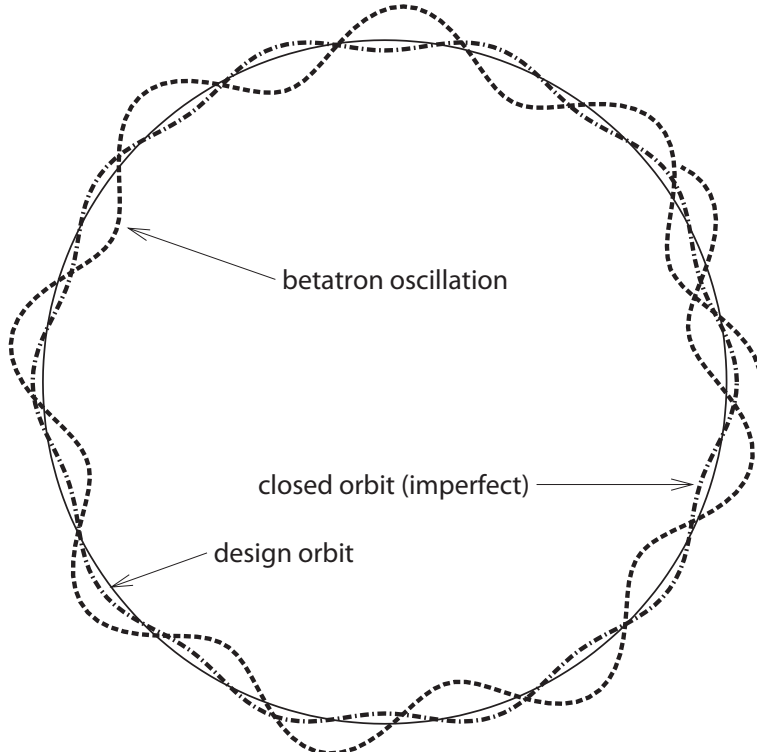


**Figure 3.3:** Sketch of the *design orbit* and the *imperfect closed orbit* in a storage ring of a circular accelerator like RHIC. In addition, a horizontal *betatron oscillation* is shown. See text for explanations.

charged particles move on a so-called *imperfect closed orbit* (see Figure 3.3). However, not all particles in a beam move exactly on the imperfect closed orbit but are spread around it. This results in transverse oscillations, so-called *betatron oscillations* around the closed orbit. There are horizontal and vertical betatron oscillations. Quadrupole magnets are used to focus the particle beam and keep these oscillations under control. Particles in the beam not only have a spread of coordinates but also a spread of energy around the reference value. This leads to longitudinal oscillations, referred to as *synchrotron oscillations*. The longitudinal focusing is done with electric fields in radio-frequency (RF) cavities, which push particles depending on their time of arrival at the cavities. The RF cavities are also used to accelerate the particles to top energy. A key parameter in the description of the oscillations (betatron and synchrotron) is the *tune*  $Q_i$ . It describes the number of oscillations a particle completes in one revolution of the orbital motion:

$$Q_i = \omega_i / \omega_0, \quad (3.2)$$

in which  $\omega_i$  is the frequency of the oscillation ( $i = x, y$  or  $s$  for horizontal, vertical or synchrotron oscillations) and  $\omega_0$  is the revolution frequency of the particle.

When accelerating polarized protons, it is not only necessary to control the orbital motion but also the spin motion of the particle. While the orbital motion is negligibly affected by the particle spin<sup>9</sup> the motion of the spin depends crucially on the orbital motion, because the particle experiences different magnetic fields depending on the actual trajectory. The motion of a spin vector  $\vec{P}$  of a proton in an external magnetic field is described in the rest frame of the particle by the Thomas-Bargmann-Michel-Telegdi (Thomas-BMT) equation [Tho27, Bar59]:

$$\frac{d\vec{P}}{dt} = - \left( \frac{e}{\gamma m_p} \right) [G\gamma\vec{B}_\perp + (1+G)\vec{B}_\parallel] \times \vec{P}, \quad (3.3)$$

where  $G = 1.7928$  is the anomalous magnetic moment of the proton and  $\vec{B}_\perp$  and  $\vec{B}_\parallel$  are the perpendicular and parallel component of the external magnetic field with respect to the particle's direction of motion. Note that in Equation 3.3 the contribution from electric fields is not considered. In a perfect circular accelerator with a uniform vertical magnetic field the particle spins precess around the vertical axis, i.e. the direction of the guiding magnetic field. It becomes evident from Equation 3.3 that at high energies ( $\gamma \gg 1$ ) or in a purely vertical field the parallel component of the magnetic field vanishes. A comparison to the Lorentz force equation (Equation 3.1) then reveals that the spin precesses  $G\gamma$  times around the guiding magnetic field vector, i.e. the vertical component  $\vec{B}_\perp$  of the external magnetic field which is referred to as the stable spin direction in the accelerator, in one full revolution of the particle orbit. This number is referred to as the *spin tune*  $v_{sp} = G\gamma$  and is the most important parameter in the description of spin evolution in accelerators.

The main issue when accelerating polarized protons to high energies (e.g. 250 GeV at RHIC) is that the beam encounters many depolarizing resonances as the energy is increased. When such a resonance is crossed, the spin vector of the particle is perturbed away from its vertical direction, which results in partial or complete polarization loss. Such depolarizing resonances are driven by horizontal magnetic fields. They occur because of magnetic field errors and misalignments and because of betatron and synchrotron oscillations. Resonances that are driven by magnetic field errors and misalignments are referred to as *imperfection resonances* (the spin precession is perturbed because of the horizontal magnetic fields seen on the imperfect closed orbit). *Intrinsic resonances* are driven by horizontal magnetic fields seen in the focusing quadrupoles due to the vertical betatron oscillations (which are “intrinsic” to the collider)<sup>10</sup>. In the acceleration of polarized protons a resonance is encountered if the spin precession frequency equals

---

<sup>9</sup>The spin of a particle affects the orbital motion by the Stern-Gerlach force. However, at relativistic energies the magnitude of the Stern-Gerlach force drops off very rapidly so that the orbital motion is determined solely by the Lorentz force.

<sup>10</sup>Resonances due to horizontal betatron and synchrotron oscillations are negligible compared to the vertical betatron oscillations and therefore are not considered here.

the frequency (or an integer multiple of it) with which a depolarizing magnetic field is crossed. In such a case the perturbing spin precessions can sum up coherently resulting in polarization loss. Usually the resonance conditions are expressed in terms of the spin tune  $v_{sp}$ . The conditions are different for imperfection and intrinsic resonances, respectively. Imperfection resonances arise whenever the following condition is satisfied:

$$v_{sp} = G\gamma = n, \quad (3.4)$$

where  $n$  is an integer. Equation 3.5 shows the resonance condition for intrinsic resonances,

$$v_{sp} = G\gamma = kP \pm Q_y, \quad (3.5)$$

in which  $k$  is an integer,  $P$  is the super-periodicity (i.e. the number of identical sections of the accelerator) and  $Q_y$  is the vertical betatron tune as stated before.

The loss of polarization when a depolarizing resonance is crossed depends on the resonance strength  $\epsilon$  and the crossing rate  $\alpha$  and can be calculated analytically using the Froissart-Stora formula [Fro60]:

$$P_f/P_i = 2e^{-\frac{\pi|\epsilon|^2}{2\alpha}} - 1, \quad (3.6)$$

in which  $P_i$  and  $P_f$  are the initial and final polarization. Two border-line cases of Equation 3.6 are very interesting: if the resonance strength  $\epsilon$  is very small, there will be no depolarization, i.e.  $P_f = P_i$ . If, however, the resonance is very strong, there will be complete spin flip but no polarization loss, i.e.  $P_f = -P_i$ . If the resonance strength is anywhere in between those two scenarios there will be loss of polarization. Equation 3.6 suggests two methods to preserve polarization and which are applied in accelerators of polarized protons: one can either reduce the resonance strength ( $\epsilon$  very small) or cross the resonance very quickly (make  $\alpha$  very large). The strength of imperfection resonances is proportional to the distortion of the imperfect closed orbit. The distortion can be reduced by dipole corrector magnets (*harmonic orbit correction*), hence minimizing the strength of the imperfection resonance. The strength of intrinsic resonances is proportional to the size of the vertical betatron oscillations. By a fast jump of the vertical betatron tune (using pulsed quadrupoles to rapidly shift the tune and hence making  $\alpha$  very large) the intrinsic resonances can be overcome. Both techniques were applied in the acceleration of polarized protons in the AGS [Khi89]. However, because of the large number of (and in part) strong resonances (the AGS is a strong-focusing accelerator), these methods are very tedious, especially when going to even higher energies like at RHIC. A different approach to overcome depolarizing resonances is utilized in so-called *Siberian Snakes*, which are employed in the acceleration process of polarized protons at RHIC. The basic idea of Siberian Snakes is reviewed in the following section. A comprehensive overview on spin dynamics in accelerators can be found in [Man05a, Man05b].

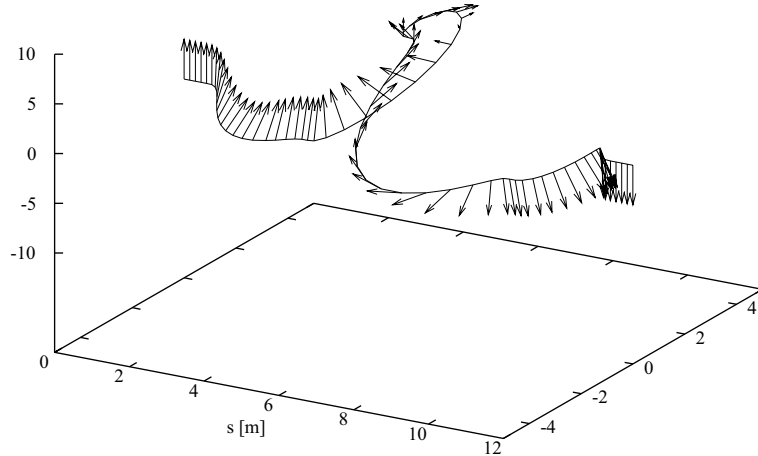


**Figure 3.4:** Spin track in Siberian Snakes installed at RHIC [Ale03].

### 3.1.2 Siberian Snakes and Spin Rotators

Siberian Snakes offer a very elegant solution to overcome all intrinsic and imperfection resonances at once, at least in principle. The basic idea of Siberian Snakes dates back to the late 1970's when Derbenev and Kondratenko proposed to use magnetic fields to avoid all resonances [Der78]. Theoretically a Siberian Snake is a device that rotates the spin of a particle by  $180^\circ$  around an axis in the horizontal plane<sup>11</sup>. This idea is technically feasible because the spin and orbit rotate through different angles when traversing a magnetic field. The origin of the name lies in the geographical region where Derbenev and Kondratenko were working at the time they came up with the idea (Novosibirsk) and the fact that the particle orbit wiggles like a snake in the magnetic fields. Figure 3.4 shows a simulated spin track in the RHIC Siberian Snakes. The axis of the Snake is along the  $s$  direction. Illustrated is the orbit as well as the spin evolution as the particle traverses the Snake.

A practical implementation of a Siberian Snake is a solenoidal magnet. The traversing particle moves along the solenoid axis, hence the Lorentz force vanishes, which means that there is no orbit distortion. The spin of the particle is rotated around the solenoid axis. However, for a fixed rotation angle the required magnitude of the magnetic field scales with the momentum of the particle. This means that Siberian Snakes made of solenoids are basically only practical at low energies because of the required field strength. A solenoidal Siberian Snake is, for instance, implemented at AmPS<sup>12</sup> [Lui97], which is an electron storage ring that reaches a maximum energy of 900 MeV.

Equation 3.3 implies that at high energies ( $\gamma \gg 1$ ) transverse magnetic fields are more suitable to manipulate the spin of a particle. It can be shown using Equation 3.3 that for a fixed spin rotation angle the magnitude of a transverse magnetic field needs only to scale

<sup>11</sup>The horizontal plane is defined by the design orbit.

<sup>12</sup>Amsterdam Pulse Stretcher in Amsterdam, Netherlands

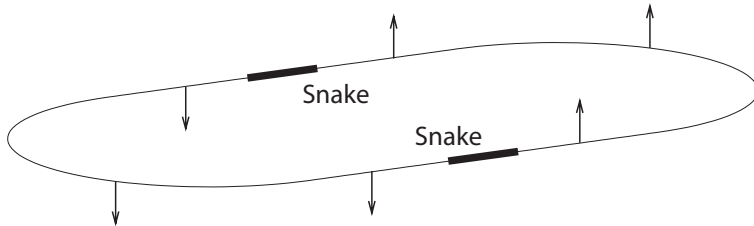


**Figure 3.5:** Stable spin direction in a planar ring with two Siberian Snakes (like RHIC) that are located at diametrically opposite positions [Man05a].

like  $\beta = v/c$ . Therefore Siberian Snakes utilizing transverse magnetic fields can be operated to arbitrarily high energies without requiring unreasonably strong magnetic fields. Due to the transverse magnetic fields the particle is subject to the Lorentz force which bends the particle out of the horizontal plane. However, the orbital excursion scales like  $1/\gamma$ . Hence at high energies the orbital distortion in the Snake can be neglected. However, at low energies this distortion places a serious limitation on the design of transverse Siberian Snakes. At RHIC a very sophisticated design implementing helical magnetic fields is employed [Ale03]. The scheme of four helical magnets that eliminates orbital excursions is used to construct Siberian Snakes as well as spin rotators [Pti95]. In a full-twist helical magnet the field vector is transverse to the axis and rotates  $360^\circ$  around the axis. A system of four such full-twist helical magnets is required to control both spin rotation angle and rotation axis. The rotation axis always lies in the horizontal plane. If the parameters of the magnets are properly chosen then the spin is rotated by  $180^\circ$  and the excursions of the orbit vanish automatically (see Fig. 3.4).

At RHIC two Siberian Snakes are installed in each ring at diametrically opposite positions (see Fig. 3.2). Two Snakes cause the stable spin direction to be vertically up or down (see Figure 3.5). The rotation axes of the two Snakes in each ring are orthogonal to each other and in the horizontal plane. Calculations of the spin rotation matrix in an accelerator with two Snakes show that the spin tune becomes independent of energy:  $v_{sp} = \frac{1}{2}$ . This is the key property of Siberian Snakes in accelerators. In principle, the resonance conditions of imperfection resonances (Equation 3.4) and intrinsic resonances (Equation 3.5) can never be met, as long as the vertical betatron tune is not an half-integer. The fact that with two Siberian Snakes with properly chosen parameters no depolarizing resonances are encountered is not entirely true. For strong resonances the resonance condition can be extended over more than one orbital revolution. This leads to additional depolarizing resonances called Snake resonances [Lee86]. The name is somewhat misleading since Snake resonances are caused by the same spin-orbit coupling mechanisms as any other resonance. They are simply higher order resonances. For strong intrinsic resonances, Snake resonances can cause significant depolarization. However, by careful choice of

the betatron tunes polarized protons can be accelerated up to 250 GeV without serious polarization loss in RHIC [Bai05].

In the AGS the beam is accelerated up to 24.3 GeV ( $G\gamma = 46.5$ ). Thus, the polarized proton bunches encounter 42 imperfection resonances from injection energy to the maximum energy in the AGS. With a super-periodicity of  $P = 12$  there are also 7 intrinsic resonances in the AGS of which four are strong. As was stated above these resonances used to be corrected using a harmonic orbit correction method (imperfection resonances) and a spin tune jump method (intrinsic resonances). However, in recent years a partial Siberian Snake has been used to avoid imperfection resonances. A partial Snake rotates the spin by less than  $180^\circ$  around an axis in the horizontal plane. In the first three years of operation at RHIC a warm 5% partial solenoid Snake was used in the AGS, which means that the spin was rotated by  $9^\circ$  around the solenoid axis. This rotation angle<sup>13</sup> is sufficient to induce complete spin flip at every imperfection resonance (the partial Snake effectively makes the imperfection resonance stronger [Ros89]). A partial Snake does not eliminate intrinsic resonances. Therefore, in addition to the the partial Snake a RF dipole is installed in the AGS which drives the intrinsic resonances, increasing their strength, which then induces complete spin flip at all intrinsic resonances. The longitudinal magnetic field in a solenoid introduces coupling of the vertical and horizontal betatron oscillations because of the Lorentz force, which in turn reduces the polarization due to coupling resonances. Therefore, in 2004, a warm helical partial Snake ( $\sim 7\%$  partial Snake) was installed in the AGS, which removes the transverse coupling resonances. In 2005, a superconducting 20% partial Snake was installed in the AGS, which will help to eliminate the intrinsic resonances in the future making the RF dipole obsolete.

As seen in Figure 3.5 the stable spin direction in RHIC is transverse to the beam direction (vertically up or down). In order to study collisions of longitudinally polarized proton collisions the spin must be rotated to the longitudinal direction. This is achieved by *Spin Rotators* which are constructed out of four helical magnets similarly to the Siberian Snakes, only the chirality and the strength of the magnetic fields have to be adjusted differently. The two large experiments STAR and PHENIX have such spin rotators installed before and after the interaction region in order to have the ability to rotate the spin from the transverse to the longitudinal direction and back (see Figure 3.2). In order to monitor the polarization direction both experiments have the capacity to measure the direction of the beam polarization independently.

---

<sup>13</sup>The strength of the imperfection resonances basically determines by how much the spin must be rotated in the partial Snake in order to avoid depolarization.

### 3.1.3 Spin Flippers

In RHIC the chosen polarization pattern ( $\uparrow\uparrow\downarrow\downarrow$  and  $\uparrow\downarrow\uparrow\downarrow$ ) in both rings ensures that collisions with all four possible combinations of polarization direction occur in the same beam store, which drastically reduces systematic errors which would arise from different beam stores. However, a pair of bunches would still cross always with the same polarization combination during the whole lifetime of a beam store. If there are any correlations between a bunch and its polarization direction this could introduce additional systematic errors. In order to minimize such systematic errors a so-called *Spin Flipper* is installed in each ring at RHIC. A Spin Flipper involves an alternating current (AC) dipole magnet. One of the Siberian Snakes is used to detune the spin tune (move  $v_{sp}$  away from 0.5) and the AC dipole is then used to induce complete spin flip at the resonance. The spin direction of each bunch must be flipped frequently during the lifetime of a beam store in order to reduce potential systematic uncertainties. The Spin Flipper can also be used to measure the spin tune of the accelerator.

### 3.1.4 Polarization Measurement

Polarization of the proton beams is monitored throughout all stages of acceleration and storage in RHIC and its injection chain. This is necessary to locate the origin of possible polarization loss during acceleration. Only the polarimeters installed to measure the polarization in the two RHIC storage rings will be discussed here.

Fast ( $< 10$  sec) measurement of the vertical polarization of the two beams is obtained using a proton-carbon (pC) polarimeter in each ring. The technique is based on the known analyzing power  $A_p^{pC}$  ( $A_p^{pC} \approx 0.04$  [Ale03]) in the elastic scattering of polarized protons in a carbon target in the *Coulomb-nuclear interference* (CNI) region [Jin04b]. This kinematic region is characterized by the interference of the electromagnetic (Coulomb) and hadronic (nuclear) transfer amplitudes in the elastic scattering. A theoretical description of the CNI in hadronic reactions at high energies can be found in [Bou77].

The analyzing power is related to a left-right asymmetry of the elastic pC scattering in the scattering plane perpendicular to the beam polarization. The beam polarization  $P$  is calculated from the measured number of left and right scatters  $N_L$  and  $N_R$  (normalized by luminosity):

$$P = \frac{1}{A_p^{pC}} \frac{N_L - N_R}{N_L + N_R}. \quad (3.7)$$

For pC elastic scattering in the CNI region at very high beam energies (above a few GeV) the proton is scattered in the forward direction at very small angles. Since the measurement of the forward scattered proton would drastically influence the proton beam it is necessary to measure the recoiled carbon nuclei in order to identify elastic scattering.

A very thin ribbon carbon target is used at RHIC, so that the low energy (only hundreds of keV kinetic energy) recoil carbon can leave the target and be detected in silicon strip detectors.

Before the 2004 run the pC CNI polarimeters were calibrated at a beam energy of 22 GeV. The AGS E950 experiment [Toj02] measured the analyzing power of pC elastic scattering in the CNI region (based on the analyzing power of elastic p + p scattering) to within  $\pm 30\%$  accuracy<sup>14</sup>. The energy dependence of  $A_p^{\text{pC}}$  is expected to be small [Tru02]. Hence at 100 GeV beam energy the same analyzing power was applied ( $A_p^{\text{pC}}(100) \sim A_p^{\text{pC}}(22)$ ). However, since the uncertainty of the analyzing power directly translates into the uncertainty of the beam polarization the measured polarization could not be better known than  $\pm 30\%$ . Therefore in 2004 a polarized proton-jet target polarimeter was installed and commissioned at RHIC. This device can measure the absolute polarization with an uncertainty of  $\pm 5\%$ . The underlying method is based on elastic p + p scattering in the CNI region. Since beam and target particles are identical the beam polarization can be directly expressed in terms of the target polarization allowing absolute measurement of the polarization of the proton beam. However, since the interaction rate in the hydrogen-jet target is very low, the hydrogen-jet polarimeter is not suitable as a fast polarization monitor. Therefore it is used to calibrate the pC CNI polarimeter which are used to monitor beam polarization. The measurement of the beam polarization utilized in the analysis of the double helicity asymmetry in  $\pi^0$  production presented in this work (see Chapter 9) depends on the polarized proton-jet target calibration at 100 GeV beam energy [Jin04a].

In addition to the polarimeters that measure the absolute polarization there are local polarimeters installed at the two large experiments, PHENIX and STAR, that allow the experimentalists to set up the spin rotators and to monitor the relative polarization at the point of collision. The measurement is based on the left-right asymmetry (in the plane normal to the beam direction) of the production of neutrons at very forward angles in collisions of transversely polarized protons, which was discovered in the 2003 run [Baz03b]. The large analyzing power ( $\sim -0.11$ ) for transversely polarized protons disappears when the polarization is rotated from the vertical to the longitudinal direction, hence allowing the experimentalists to monitor the effect of the spin rotators.

## 3.2 Experimental Program at RHIC

Four major experiments are installed at four of the six intersection regions (IR) at RHIC: BRAHMS, PHOBOS, STAR and PHENIX. Their locations in RHIC are depicted in Fig-

---

<sup>14</sup>The error combines statistical and systematic uncertainties [Toj02].

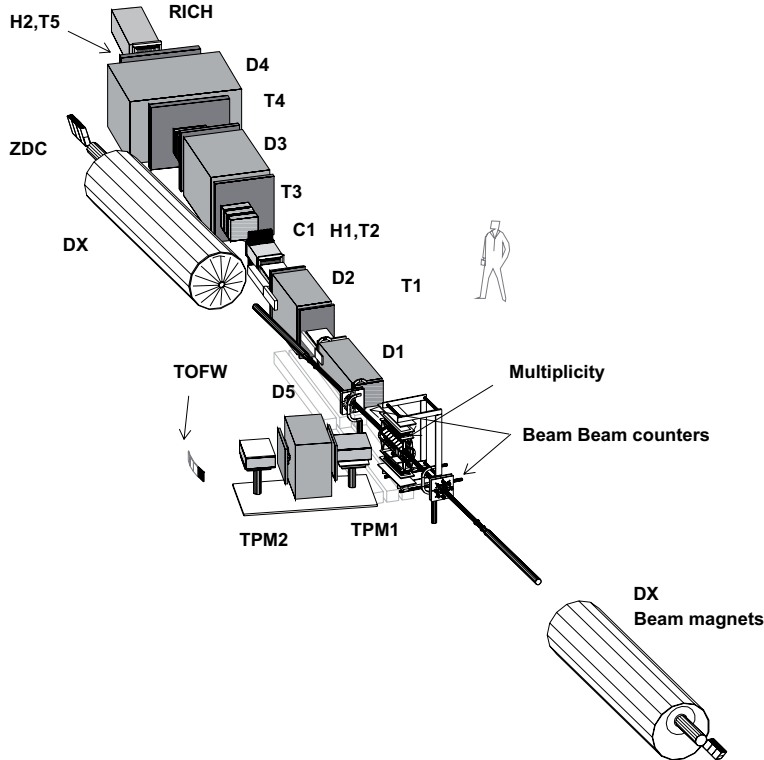


**Figure 3.6:** Sketch of the BRAHMS detector [Ada03].

ure 3.1 and 3.2. While PHOBOS only conducts heavy-ion physics, all three other experiments also have a dedicated program to study spin physics. A smaller experiment, PP2PP, was installed in 2002 at the same IR as BRAHMS. Its purpose is to study elastic scattering of polarized protons. In the following a brief description of the layout and design of BRAHMS, PHOBOS and STAR is given. The PHENIX experiment is described in more detail in Chapter 4. A summary of the results obtained by the four collaborations in the first three years of RHIC operation is given in the so-called *White Papers* [Ars05, Bac05, Ada05, Adc05].

### 3.2.1 BRAHMS

The majority of particles produced in heavy-ion and proton-proton collisions have transverse momenta in the soft physics regime, where techniques of pQCD are not applicable for the description of the interaction. The BRAHMS detector is designed to study the bulk particle production in this kinematic regime to better understand the underlying physics [Ada03]. A schematic layout of the BRAHMS detector is shown in Figure 3.6. It consists of two separate spectrometers which are independently movable. Even though both spectrometers have small solid angles a broad coverage in rapidity ( $y \approx 0 - 4$ )

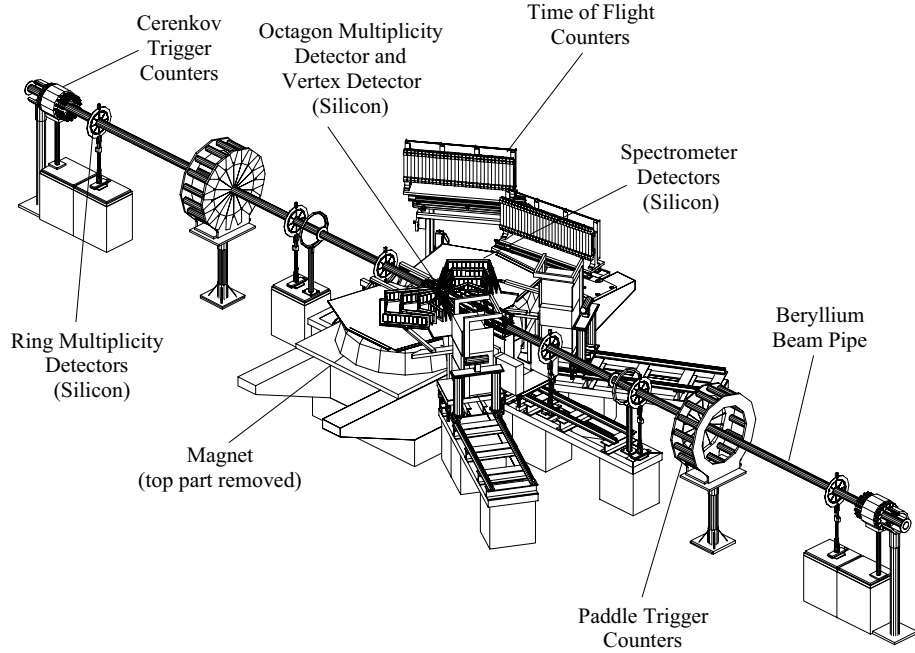


**Figure 3.7:** Sketch of the PHOBOS detector [Bac03].

is obtained by systematic repositioning of the two arms. The spectrometers are equipped with detectors that provide good particle identification and high momentum resolution.

### 3.2.2 PHOBOS

The PHOBOS detector is the only experiment that is located inside the RHIC tunnel. It is designed to study the global event characteristics of ultra-relativistic heavy-ion collision [Bac03]. In order to achieve this, the detector is equipped with a multiplicity detector that provides almost complete coverage of the solid angle (pseudorapidity  $|\eta| < 5.4$  and almost  $2\pi$  in azimuth) and two spectrometer arms for the detailed analysis of charged particles at low  $p_T$  with good momentum resolution. A schematic layout of the PHOBOS detector is shown in Figure 3.7. PHOBOS finished taking data in 2005.

### 3.2.3 STAR

The STAR detector was primarily designed to study high-density QCD in ultra-relativistic nucleus-nucleus collisions and to search for signatures of the Quark-Gluon Plasma (QGP) [Ack03]. While this is also true for the PHENIX detector, the design of the STAR experiment is rather different compared to PHENIX (see Chapter 4). The STAR detector features subsystems for high precision tracking, momentum analysis and particle identification at mid-rapidity especially suitable for the measurement of hadron production over

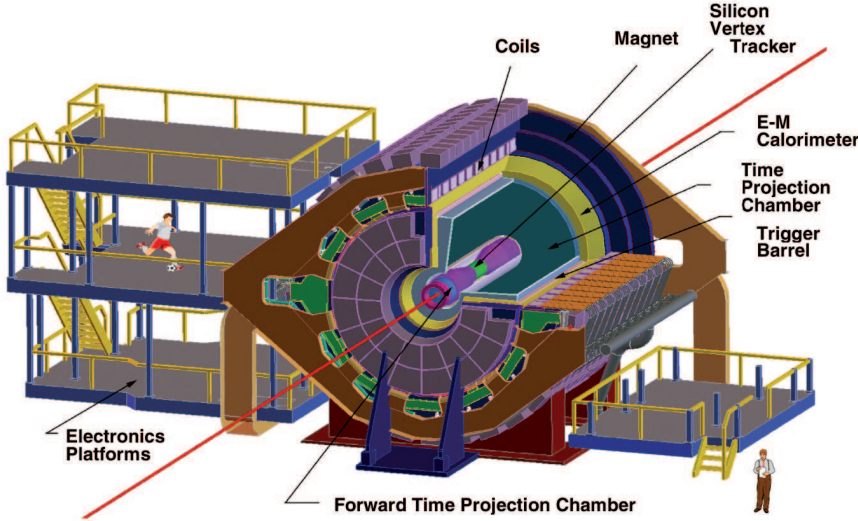


**Figure 3.8:** Sketch of the STAR detector [Ack03].

a large solid angle. More specifically the STAR physics program focuses on the measurement of global observables on an event-by-event basis and the measurement of high- $p_T$  particles that emerge from hard-scatterings. An event-by-event analysis is possible since the charged particle multiplicity is very large at mid-rapidity in heavy-ion collisions at RHIC ( $dN/dy \sim 1000$ ). In order to accomplish the physics objectives, the key subsystem of the STAR detector is a large volume Time Projection Chamber (TPC) with a diameter of 4 m and a length of 4.2 m. The TPC covers almost four units in rapidity ( $|\eta| \leq 1.8$ ) and full azimuth ( $\Delta\phi = 2\pi$ ). A schematic layout of the STAR detector is shown in Figure 3.8. In addition to the heavy-ion physics program STAR has a dedicated spin physics program. Its focus is on the detailed measurement of the spin structure of the proton. Especially the contribution of the gluon spin to the total spin of the proton is investigated. Finally STAR studies ultra-peripheral nucleus-nucleus collisions, in which the nuclei do not collide but interact via longer ranged forces that couple coherently to the nucleons.

# 4. The PHENIX Experiment

The data analyzed in this thesis was accumulated with the PHENIX detector. PHENIX is the second large scale experiment at RHIC in terms of size and cost besides STAR. The detector is about  $\sim 11$  m high with a length of  $\sim 18$  m and a diameter of the central arms of  $\sim 12$  m. In the following, basic information on the PHENIX setup and the major physics goals as formulated at the beginning of the PHENIX project are outlined. A more comprehensive overview of the physics motivation and the detector layout can be found in [Adc03b] and references therein.

## 4.1 Physics Goals of PHENIX

The PHENIX detector was designed to study several fundamental aspects of the strong interaction in ultra-relativistic heavy-ion collisions and especially search for signatures of the QGP. Unlike STAR the focus of PHENIX measurements is not primarily limited to hadron production. Instead a key feature of the PHENIX detector is the measurement of leptons and photons with high precision.

From the initial parton-parton collisions, over the onset of deconfinement to the formation of the hadronic phase there are a number of interesting phases in the evolution of heavy-ion collisions at RHIC. PHENIX is sensitive to hadron jets that are created in hard-scatterings and which are subject to strong interactions with the surrounding medium and therefore are sensitive to medium effects. Deconfinement and chiral symmetry restoration is probed via the measurement of vector mesons, which decay into lepton pairs. The expansion of the fireball after hadronization is measured by Hanbury-Brown-Twiss (HBT) correlations.  $p + p$  as well as  $d + Au$  collisions are also studied by PHENIX in order to investigate the contribution of hard scattering and effects of cold nuclear matter. This information is crucial for the interpretation of the data obtained in heavy-ion collisions.

Direct photons are produced throughout all stages of ultra-relativistic heavy ion-collisions (refer to [Sta05] for a recent review of direct-photon production in heavy-ion collisions). Since photons interact only electromagnetically they leave the medium almost unaltered. Hence they provide unmodified information on all stages of the evolution of the collisions. Moreover, direct-photon production in  $p + p$  provides an excellent tool to test perturbative QCD and to study the gluon density in the proton (see Chapter 6).

Another major physics goal of the PHENIX experiment is the investigation of the spin structure of the nucleus. Ultimately, the contribution of the gluon polarization to

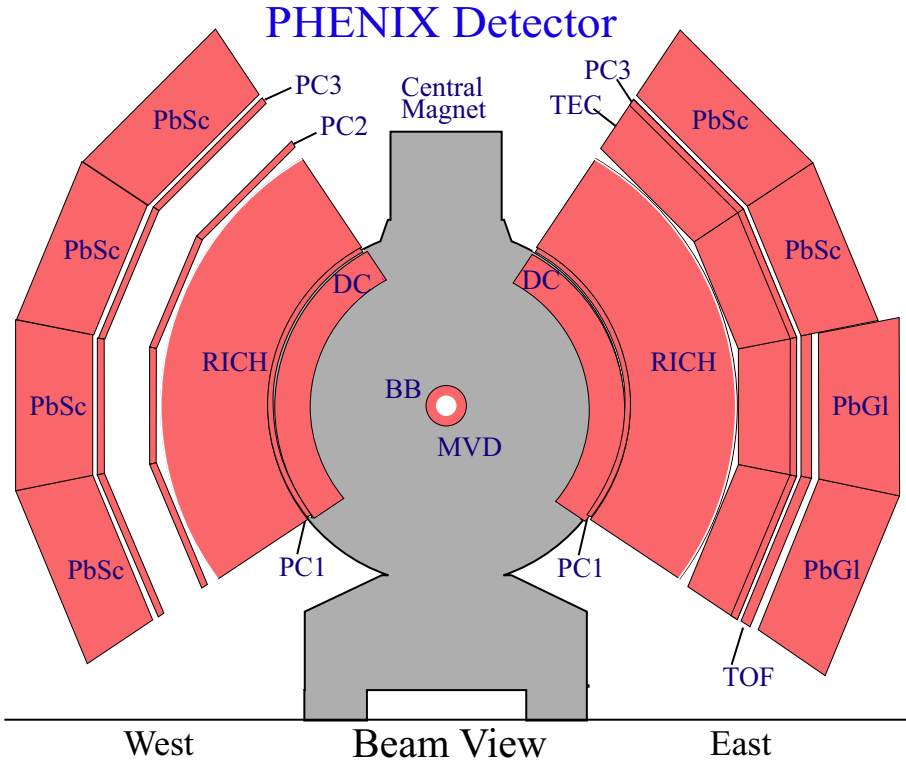


**Figure 4.1:** Beam view of the PHENIX detector layout in Run III.

the proton spin will be measured via the direct-photon channel. The polarization of antiquarks will be measured via the parity-violating asymmetry of W production beyond  $p_T = 20 \text{ GeV}/c$ .

## 4.2 PHENIX Detector Setup

In order to tackle the ambitious physics program PHENIX was designed as a diverse hybrid detector which incorporates several types of detection techniques in order to measure both charged and neutral particles in a large multiplicity environment.

The layout of PHENIX as employed in Run III is shown in Figure 4.1 and 4.2. The detector consists of four spectrometers and a set of global subsystems. Two central spectrometers are arranged like a barrel around the beam axis at mid-rapidity ( $|\eta| < 0.35$ ) and cover an azimuthal angle of  $\Delta\phi = 2 \times 90^\circ$ . The subsystems of the central spectrometers are designed to measure electrons, charged hadrons and photons. Two spectrometers for the detection of muons are positioned up- and downstream (north and south of the interaction point). They cover a pseudo-rapidity range of  $-2.25 < \eta < -1.15$  (South) and  $1.15 < \eta < 2.44$  (North) and full azimuth ( $\Delta\phi = 360^\circ$ ).

In the following basic information on the configuration of the PHENIX detector in the third year of physics running is given.

### 4.2.1 PHENIX Magnets

Momentum analysis of charged particles in PHENIX requires large magnetic field volumes to cover the pseudo-rapidity and azimuthal range of the detectors. Three spectrometer magnets were developed for PHENIX: a central magnet (CM) and two muon magnets (MM) for the north and south muon spectrometers, respectively [Aro03].

The central magnet consists of two sets of circular coils (inner and outer coil - see black squares in Figure 4.2) in the north and south pole faces that create an axial field along the beam axis. Although the resulting magnetic field is not as uniform as a solenoidal field this configuration is preferable since it places no mass in the apertures of the central spectrometer arms. The currents and polarity in the inner and outer coils can be set independently, so that the magnetic field integral can be adjusted at  $0.43 \text{ Tm} < \int BdR < 1.15 \text{ Tm}$  in the radial direction ( $R$  is the distance from the beam axis). The design also allows to minimize the magnetic field integral near the beam axis ( $R \approx 0 \text{ m}$ ) which is desirable for detectors in this radial region to measure low momentum electrons. The residual magnetic field integral outside the magnet and the Drift Chamber (DC) ( $R > 2.4 \text{ m}$ ) is less than  $0.01 \text{ Tm}$  which is important for the performance of the photomultiplier tubes of the *Ring Imaging Cherenkov Counter* (RICH) and the *Electromagnetic Calorimeter* (EMCal).

The muon magnets create a radial magnetic field that forces charged particles on a helix-like trajectory. The magnetic field integral is roughly proportional to the polar angle  $\Theta$  ( $\int Bdl = 0.72 \text{ Tm}$  at  $\Theta = 15^\circ$ ) which is a desirable feature since the momentum of muons in the acceptance of the muon spectrometers is also roughly proportional to  $\Theta$ . The design of the muon magnets is shown in Figure 4.2. The south magnet is  $\sim 1.5 \text{ m}$  shorter than the north magnet and movable in order to allow access to other detector components. The influence on the beam particles is minimal. The muon tracker (MuTr) is mounted on and inside the muon magnets as shown in Figure 4.2. The back plates of the two magnets are made of low-carbon steel and are  $20 \text{ cm}$  and  $30 \text{ cm}$  thick for the south and north magnet, respectively. The plates form the first of several absorber layers of the muon identifier (MuID).

### 4.2.2 Global Detectors

In the analysis of heavy-ion collisions as well as elementary  $p + p$  collisions it is important to measure the global event characteristics. For instance the point of interaction (vertex)

and the timing information have to be known. Moreover, the evolution of heavy-ion collisions crucially depends on the geometry of the collision. Thus the impact parameter or centrality of the collision must be determined. In PHENIX the global event characteristics are measured by a number of subsystems [All03].

A detector which is common to all four major experiments at RHIC is the *Zero-Degree Calorimeter* (ZDC) [Adl03a]. It is located along the beam line on both sides of the nominal interaction point (at  $\pm 18.25$  m). These hadron detectors measure spectator neutrons at very forward angles and provide centrality, vertex and luminosity information.

The *Beam-Beam Counter* (BBC) in PHENIX measures the time of the interaction which is crucial for the time-of-flight measurement, provides vertex information and serves as a minimum bias trigger, which defines an inelastic collision in PHENIX. Combined with signals from the ZDC the BBC also provides information on the centrality of the collision. The BBC consists of two identical sets of quartz Cherenkov Counters which are placed on both sides of the interaction point. The counters are positioned at  $\pm 1.44$  m away from the nominal collision vertex and surround the beam pipe. The BBC measures charged particles in a pseudo-rapidity range of  $3.0 < |\eta| < 3.9$ .

The *Multiplicity/Vertex Detector* (MVD) was designed to measure fluctuations in charged particle distributions and provides global information on charged particle multiplicity and vertex position. The subsystem consists of silicon strip and silicon pad detectors which together cover a pseudo-rapidity region of  $|\eta| < 2.64$ . However, for the data set analyzed in this thesis the MVD did not provide any valuable vertex information.

In the measurement of  $p + p$  collisions the average multiplicity is considerably smaller than in  $Au + Au$  collisions. Because of this and due to its small acceptance the BBC can measure only a fraction of the total inelastic cross section in  $p + p$ . The *Normalization Trigger Counter* (NTC) was designed and installed between the end caps of the MVD and the central magnet pole tips to increase the coverage of the BBC. The subsystem consists of two identical fiber-readout scintillation counters located on either side of the interaction point. The NTC can reduce the error in the total inelastic  $p + p$  cross section significantly but was not used during Run III.

### 4.2.3 Central Arm Spectrometers

The central detector consists of two independent spectrometer arms (East and West), which are slightly different in design. The arms comprise subsystems for charged particle tracking and particle identification (PID). The setup of the two central arms as employed during the third year of RHIC physics running is shown in Figure 4.1.

## Particle Tracking

The PHENIX central arm tracking system utilizes the information provided by three detector subsystems [Adc03a]. It is optimized to track charged particles at low momentum, where the bulk of charged hadrons is produced.

The *Drift Chamber* (DC) is located closest to the point of interaction. It is mounted at a radial distance of 2.0-2.4 m where the magnetic field of the CM has a maximum strength of 0.06 T, which is too small to significantly deflect high-energetic charged particles in the DC. Two identical cylindrically shaped DC systems are located in the west and the east arm of the detector. They cover a pseudo-rapidity range of  $|\eta| < 0.35$  and  $90^\circ$  in azimuthal direction. Each system comprises 20 identical sectors covering  $\Delta\phi = 4.5^\circ$  in azimuth. Each sector consists of a gas volume and different types of wire modules that provide information for track reconstruction in the  $r - \phi$  direction. The momentum of a charged particle is determined by comparing tracks in the DC to the vertex of the collision. Furthermore, the DC information allows the reconstruction of the invariant mass of particle pairs and provides position information for pattern recognition.

The *Pad Chamber* (PC) system consists of three layers (PC1, PC2, PC3) in the west arm and two layers (PC1, PC3) in the east arm. The layers are mounted outside the magnetic field, where the tracks of charged particles are straight lines. PC1 is located just behind the DC. PC2 is mounted behind the RICH in the west arm and PC3 is located in front of the EMCAL. The PC system consists of multiwire proportional chambers which are composed of anode wires inside a gas volume bounded by cathode planes. One of the cathode planes is finely segmented into readout pixels that provide good position resolution. Therefore the PC system provides three-dimensional space points throughout the PHENIX detector which correlate signals in RICH, TEC and EMCAL to momentum measurements in the DC. Since the PC3 is located in front of the EMCAL hits in the PC3 can be correlated to hits in the EMCAL which allows the removal of the charged particle background from the photon sample measured with the EMCAL (see Section 7.3.2).

A *Time Expansion Chamber* (TEC) is installed in the east arm between the RICH and PC3. It measures all tracks of charged particles that pass through the RICH and EMCAL in the  $r - \phi$  direction. The PHENIX TEC consists of four sectors each covering  $\Delta\phi = \pi/8$  in azimuth. Each sector consists of six multiwire tracking chambers in succession. The gas volume of a multiwire chamber comprises a drift region and an amplification region. Beside its tracking capabilities the TEC also measures the energy loss of charged particles in the gas. The  $dE/dx$  signal helps to separate electrons from pions in the momentum region  $0.2 < p_T < 2.5$  GeV/c. Before Run III the TEC was upgraded by adding radiators just in front of the drift region. The transition radiation created in the radiators by fast electrons can help to discriminate electrons from pions up to tens of GeV/c in transverse

momentum with good efficiency. However, the transition radiation has not been utilized in PHENIX data analyses yet.

### **Particle Identification**

Besides the TEC two other subsystems contribute to the particle identification in the central arms of PHENIX [Aiz03].

The RICH is the primary system for the detection of electrons in PHENIX. Charged particles emit Cherenkov light in a medium if they have a velocity larger than the speed of light in that medium. Two RICH systems are installed in the PHENIX detector behind PC1, one in the east and one in the west arm, respectively. Each system has a gas volume of  $40 \text{ m}^3$  and covers the complete acceptance of the PHENIX central spectrometers. The gas ( $\text{CO}_2$ ) in the RICH is chosen in such a way that the threshold for Cherenkov light emitted by pions is above  $p_T = 4 \text{ GeV}/c$ . The Cherenkov light is focused by spherical mirrors on photomultiplier tubes in the  $\phi - z$  direction. The phototubes have magnetic shielding that allows operation in magnetic fields with a maximum of 0.01 T. The central magnet is designed to keep the strength of the magnetic field below this limit outside the DC. By combining the information from RHIC, TEC and EMCal the probability of false identification of pions as electrons is kept below 0.01% for transverse momenta below the pion Cherenkov threshold.

A *Time-of-Flight* (ToF) counter is used to identify charged hadrons, which carry basic information of the matter produced in the collision. The ToF system consists of ten panels each divided into 96 segments. Each segment is composed of a plastic scintillator oriented in the  $r - \phi$  direction and photomultiplier tubes at both ends. The ToF counter is mounted in the east arm in front of the PbGl calorimeter and covers a pseudo-rapidity range of  $|\eta| < 0.35$  and  $45^\circ$  in azimuth. The track of a charged particle is reconstructed using DC and PC1 information. The start time is provided by the BBC and the stop time is measured by the ToF. The achieved timing resolution is  $\sim 100 \text{ ps}$ . This allows good separation of pions and kaons up to  $2.4 \text{ GeV}/c$  and kaon/proton separation up to  $4.0 \text{ GeV}/c$ . The particle identification of charged hadrons is supported by the time-of-flight measurement of the lead-scintillator calorimeter which covers the remaining acceptance of the central arms (see Section 5).

### **Electromagnetic Calorimeter**

For the detection of photons the EMCal is installed at a radial distance of about 5 m in the central arms of PHENIX. The EMCal is crucial for the measurement of direct photons and neutral pions ( $\pi^0$ 's) and is the major detector subsystem which provided the data analyzed for this thesis. The PHENIX EMCal is described in more detail in Section 5.

#### 4.2.4 Muon Spectrometers

The production of vector mesons ( $J/\Psi$ ,  $\Upsilon$ ,  $\phi$ , ...) in ultra-relativistic heavy-ion collisions is expected to be influenced by the created hot and dense hadronic matter if deconfinement and/or chiral symmetry restoration are established. Vector mesons can be measured via their decay into lepton pairs, i.e.  $e^+e^-$  and  $\mu^+\mu^-$ . Leptons such as electrons and muons do not interact strongly with the matter and hence provide information without being subject to strong final state interactions<sup>1</sup>. While  $e^+e^-$  pairs are measured by the central arm spectrometers of PHENIX the detection of muons is accomplished by two muon spectrometers mounted in the forward rapidity region in the north and south arm of PHENIX as shown in Figure 4.2 [Aki03]. The muon spectrometers are designed to measure muons

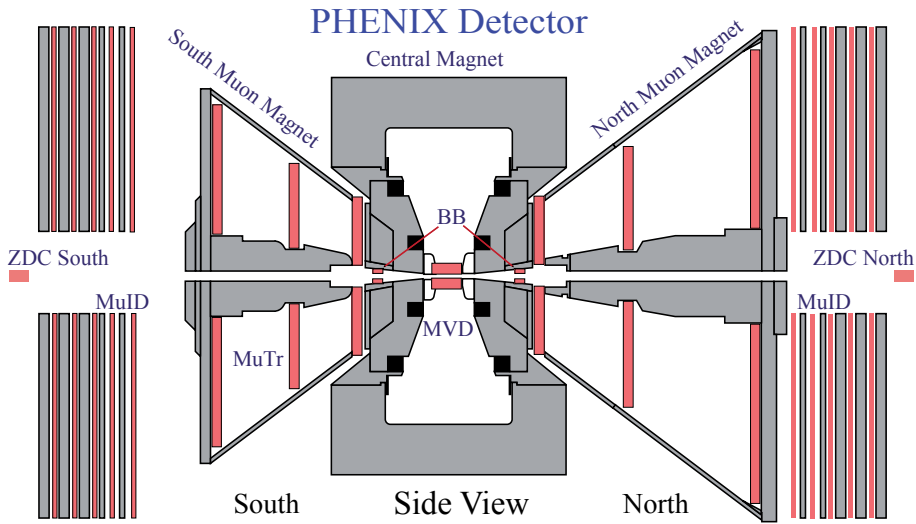


**Figure 4.2:** Side view of the PHENIX detector layout in Run III.

in the rapidity range  $|\eta| \approx (1.2 - 2.4)$ . They provide full azimuthal coverage resulting in a geometric acceptance of approximately 1 sr. Each spectrometer tracks and identifies muons while rejecting other hadrons such as pions and kaons with good efficiency. The spectrometers consist of a Muon Tracker followed by a Muon Identifier.

The MuTr is mounted inside the radial magnetic field of the conical-shaped muon magnets (see Section 4.2.1). It consists of three so-called *stations* which all have the shape of octants. Each station is equipped with multiplane drift chambers. The cathode planes are designed to provide a spatial resolution of  $\sim 100 \mu\text{m}$  which facilitates a mass resolution of muon pairs of  $6\%/\sqrt{M}$  where  $M$  is the invariant mass of the muon pair in  $\text{GeV}/c^2$ . This is in principle sufficient to separate  $\rho/\omega$ ,  $\phi$ ,  $J/\Psi$ ,  $\Psi'$ ,  $\Upsilon$  and  $\Upsilon'$ .

<sup>1</sup>Muons are not only interesting because of the decay of vector mesons into muon pairs. Also the Drell-Yan process as well as the production of the weak  $Z$  and  $W^\pm$  bosons can be studied via the detection of muon pairs and single high- $p_T$  muons, respectively.

Charged pions have a relatively long life time and therefore may be misidentified as muons in the muon arms. Because of the copious production of pions in heavy-ion collisions  $\pi^\pm$  constitute the major contribution to the background. The design criterion of the PHENIX detector for the misidentification of pions as muons is set to  $2.5 \times 10^{-4}$ . In order to achieve this, the MuID consists of several alternating layers of steel absorbers and detector planes. The backplate of the MuTr, which is made of 30 cm (north) and 20 cm (south) steel, respectively, serves as the first absorber layer of the MuID system. Because of the backplates and the material budget in the central arms and MuTr only muons with energies  $> 1.9 \text{ GeV}/c$  reach the MuID in the first place. For the muon to penetrate the MuID completely a minimum energy of 2.7 GeV is required. There are five gaps between the absorber layers which are equipped with streamer tubes (Iarocci tubes [Iar83]) which are operated in proportional mode. The tubes are oriented horizontally and vertically in panels to provide spatial resolution in the  $x$ - and  $y$ -direction. Each gap is equipped with six panels (four large and two small ones) which cover the stated geometric acceptance.

The south muon arm was ready for data taking in 2001 for the second period of physics running, while the north arm was commissioned prior to Run III.

## 5. The Electromagnetic Calorimeter

A key feature of the PHENIX detector is its capacity to measure photons and electrons with high spatial and energy resolution up to large transverse momenta ( $p_T > 10 \text{ GeV}/c$ ). This is accomplished by a finely segmented Electromagnetic Calorimeter (EMCal) [Aph03] which covers the complete geometric acceptance of the central arms of the PHENIX detector (see Figure 4.1). Originally calorimeters were developed to measure the total heat of e.g. chemical reactions<sup>1</sup>. In high-energy physics calorimeters measure the deposited energy by total absorption of the particle. Electromagnetic particles such as electrons and photons deposit their energy via electromagnetic showers. Depending on the type of calorimeter the shower energy is transformed into a measurable quantity (charge or light) in the active part of the calorimeter. The basic principles of calorimeters as particle detectors in high-energy physics are described in Section 5.1 and 5.2.

The EMCal system in PHENIX is divided into eight sectors, each covering an azimuthal range of  $\Delta\phi = 22.5^\circ$  and  $\Delta\eta = 0.7$  in pseudo-rapidity. The good spatial resolution is achieved by the high segmentation in rapidity and azimuthal direction ( $\delta\eta \times \delta\phi \approx 0.01 \times 0.01$ ). Two different detector types are utilized in the PHENIX EMCal, six sectors of a lead-scintillator sampling calorimeter (PbSc) and two sectors of a lead-glass Cherenkov calorimeter (PbGl). The PbSc is installed at a radial distance of  $\sim 5.1 \text{ m}$  behind the PC3 (two sectors in the east and four sectors in the west arm), while the PbGl is located behind the TOF at a radial distance of  $\sim 5.4 \text{ m}$  (both sectors in the east arm). The EMCal subsystems are based on different detection principles (see Section 5.2). This results in differing linearity, response to hadrons and shower shape and hence in different systematic characteristics. The advantage of having two calorimeters with different systematics within the same experiment allows internal cross checks and increases the confidence in the physics results and corresponding uncertainties.

Besides the measurement of single photons or electrons the characteristics of the PHENIX EMCal allow the measurement of neutral mesons (such as the neutral pion ( $\pi^0$ )) via reconstruction of their invariant mass from photon or  $e^+e^-$  pairs, respectively, since single showers of the decay products can be identified up to very high  $p_T$ . This is crucial for the background determination in the analysis of direct photons. Moreover, since charged as well as neutral particles deposit at least a fraction of their energy in the EMCal the calorimeter can be used to measure the transverse energy  $E_T$  of the reaction. The excellent timing resolution of the EMCal, in particular of the PbSc, allows time-of-flight measurements to distinguish photons and electrons from hadrons. Finally, like

---

<sup>1</sup>calor (Latin) = heat

all calorimeters, the EMCal provides fast information on particle energy, shower profiles etc. and therefore is highly suitable for the trigger system. Data recorded by the EM-Cal provides the major information for the analysis of direct photons and neutral pions at mid-rapidity presented in this work.

## 5.1 Electromagnetic Showers

In order to understand the detection mechanism of photons and electrons in electromagnetic calorimeters it is important to understand the evolution of electromagnetic showers in materials with high atomic number  $Z$ . In matter high-energy photons primarily undergo pair production ( $\gamma \rightarrow e^+e^-$ , Compton scattering and photo-electric absorption are negligible in this energy regime). The created high-energy electrons and positrons predominantly lose energy in matter via the emission of bremsstrahlung [Fab03]. The cross sections of bremsstrahlung and pair production depend on the radiation length  $X_0$  of the material which depends on the characteristics of the atomic species [Yao06]:

$$X_0(\text{g/cm}^2) \simeq \frac{716.4 \text{ g cm}^{-2}A}{Z(Z+1)\ln(287/\sqrt{Z})}, \quad (5.1)$$

where  $A$  is the atomic weight of the material.  $X_0$  denotes the mean distance over which a high-energy electron loses all but  $1/e$  of its energy by bremsstrahlung and  $7/9$  of the mean free path for pair production by a high-energy photon, i.e.  $1 - e^{-7/9} \approx 54\%$  of high-energy photons undergo pair production along a track of length  $X_0$ .

An electromagnetic shower is either initiated by an high-energy photon or electron. The primary particle entering the medium either undergoes pair production or bremsstrahlung emission. If the energy of the secondary particles is sufficiently large they continue to undergo bremsstrahlung emission and pair production, respectively, producing even more secondary particles with degraded energy. Depending on the energy of the primary particle, these processes recur many times resulting in an electromagnetic cascade. The secondary particles in the cascade are referred to as shower particles. Figure 5.1 illustrates how a typical electromagnetic shower could evolve in a high- $Z$  medium. At a certain shower depth the number of secondary particles produced per unit path length reaches a maximum. After this point the number of secondaries decreases quickly. This change marks the termination of the electromagnetic shower and is characterized by the critical energy  $E_C$  in the absorber at which the electrons start losing energy by ionization and atomic excitation rather than generation of secondaries by bremsstrahlung emission.  $E_C$  can be approximated in solids by  $E_C \simeq \frac{610 \text{ MeV}}{Z+1.24}$  [Fab03]. For lead  $E_C \sim 7 \text{ MeV}$ . The depth of the shower maximum in units of the radiation length can be approximated

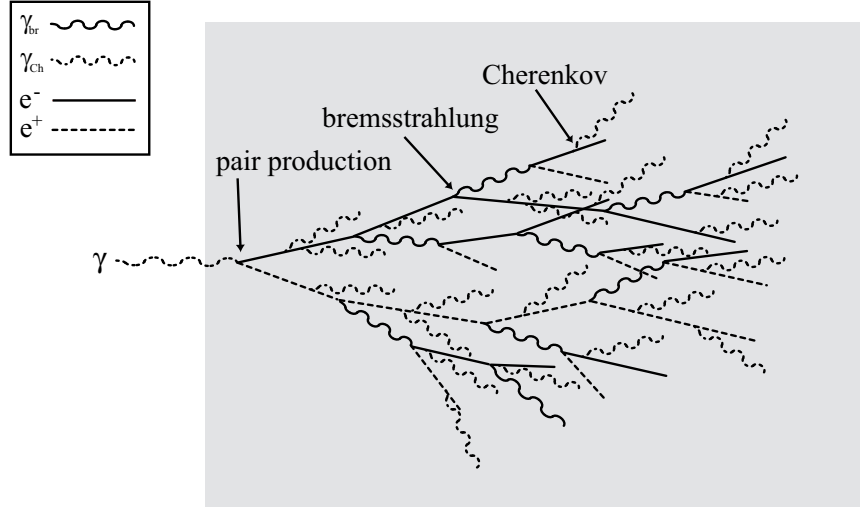


**Figure 5.1:** Schematic illustration of an electromagnetic shower cascade in a high- $Z$  medium. The primary high-energy photon decays into  $e^+e^-$  which subsequently emit bremsstrahlung  $\gamma_{\text{br}}$ , etc. Also the emission of Cherenkov photons  $\gamma_{\text{Ch}}$  by the charged particles in matter is indicated.

by [Yao06]:

$$\frac{X_{\max}}{X_0} \simeq \ln \left( \frac{E_0}{E_C} \right) + C \quad (5.2)$$

where  $E_0$  is the energy of the primary particle and  $C = \pm 0.5$ , + for photons and - for electrons/positrons. Eq. 5.2 reflects the logarithmic relation of the primary energy and the required thickness of the calorimeter to absorb the electromagnetic shower.

The shape of electromagnetic showers, described by the longitudinal and lateral spread, have characteristic properties that can be exploited to distinguish photons and electrons from hadrons. Since the spread of the shower depends on the material properties the length units are usually given in terms of  $X_0$  in order to have a material independent description. While the longitudinal spread (Equation 5.2) is governed by the high-energy part of the shower the lateral spread is determined by multiple scatterings of low-energy electrons away from the shower axis<sup>2</sup>. The lateral extension of the shower can be described fairly accurately in terms of the *Molière radius*  $R_M$  [Yao06]:

$$R_M \simeq X_0 \left( \frac{E_s}{E_C} \right), \quad (5.3)$$

where  $E_s = 21$  MeV is the so-called scattering energy.  $R_M$  describes the average lateral deflection of electrons at the critical energy along a path length of  $X_0$ . On average 95% of

<sup>2</sup>The opening angle of  $e^+e^-$  and photons from bremsstrahlung are negligibly small.

the shower energy is contained in a cylinder with radius  $2R_M$  (in homogeneous calorimeters). For reasonable position measurements of the shower the size of the segmentation of the calorimeter must be comparable to  $R_M$ .

The number of secondary particles created in an electromagnetic shower is directly proportional to the energy of the primary particle. By measuring the signal produced by the shower particles the energy of the incident particle can be determined. Depending on the type of calorimeter the signal is, for instance, the light produced in a scintillator, the charge produced in a gas or the number of Cherenkov photons produced in the medium<sup>3</sup>.

Though strongly interacting particles virtually do not lose energy by bremsstrahlung they also induce showers as they traverse a medium. However, the shower evolution is primarily determined by hadronic interactions. Hadronic showers are characterized by a number of inelastic hadronic interactions of the primary and secondary hadrons with nuclei of the absorber material from which new particles emerge<sup>4</sup>. In analogy to the radiation length the nuclear absorption length  $\lambda_a$  defines the distance after which  $1 - e^{-1} \approx 63\%$  have suffered an inelastic nuclear interaction. Similar to the Molière radius the lateral expansion of hadronic showers can be described in terms of  $\lambda_a$ : 95% of the total energy is deposited in a cylinder of radius  $\lambda_a$ . The evolution of hadronic showers is much more complex than that of electromagnetic showers. On the one hand inelastic hadronic interactions implies a variety of processes such as particle production, spallation, fission etc. On the other hand charged particles that do not suffer hadronic interactions lose a small fraction of their energy by ionization, which is described by the Bethe-Bloch formula. Such charged hadrons are referred to as *minimum ionizing particles* (MIP). Their energy loss is constant over a wide range of energy. In addition, the situation is further complicated by leptonic decays of neutral mesons such as neutral pions and etas which introduce an electromagnetic part to the hadronic shower. In electromagnetic calorimeters the nuclear absorption length is usually large compared to the radiation length. Therefore hadrons deposit only a small fraction of their energy in the calorimeter. Because of the different scales for electromagnetic and hadronic showers in a specific material ( $X_0$  and  $\lambda_a$ ) electromagnetic showers show significantly smaller spread in longitudinal and lateral direction than hadronic showers for comparable primary particle energies.

---

<sup>3</sup>Cherenkov photons (also indicated in Figure 5.1) are emitted when charged particles such as electrons and positrons traverse a medium at a velocity larger than the speed of light in that medium. While the energy loss by Cherenkov radiation is negligible, the number of Cherenkov photons produced in the shower is linearly connected to the total track length of electrons and positrons in the cascade, which in turn is linearly connected to the energy of the primary particle. Hence the number of Cherenkov photons provides a direct measure of the energy of the primary electron or photon.

<sup>4</sup>Elastic interactions do not contribute to the shower since they do not produce any secondary particles.

## 5.2 Types of Electromagnetic Calorimeters

There are basically two types of calorimeters: homogeneous and sampling calorimeters. In homogeneous calorimeters the entire volume of the detector consists of active medium, i.e. the electromagnetic shower evolves in the same medium which accounts for the signal generation. Such calorimeters are built from heavy (high-Z) materials which enhance the development of the electromagnetic shower. The chosen medium is either a scintillator, a gas or a Cherenkov radiator which converts the deposited energy into a signal that is related to the energy of the primary particle. Homogeneous calorimeters provide the best possible energy resolution, which is due to the fact that the whole energy of an incident particle is deposited in the active medium. The intrinsic energy resolution is determined by the statistical fluctuations of the number of shower particles. The resolution is worsened by effects like *leakage* and *attenuation*. Because of the limited size of the calorimeter a high-energy photon or electron might not deposit all its energy in the active medium (*leakage*). Scintillation and Cherenkov photons have to travel some distance in the calorimeter before detection and might be absorbed along the way (*attenuation*). Both effects depend on the actual position of the shower in the calorimeter and therefore affect the energy scale in a non-linear way. Such non-linearity effects have to be considered in the energy calibration of the data (see Section 7.2.1). Homogeneous calorimeters are solely employed as electromagnetic calorimeters. The PbGl calorimeter installed in PHENIX and described in Section 5.3 is a homogeneous Cherenkov calorimeter.

In sampling calorimeters passive and active medium are separated from each other, i.e. the evolution of the shower cascade mainly takes place in a high-Z absorber (passive material) and the signal is created in a scintillator, semiconductor, etc. (active medium). This has the advantage that both materials can be independently optimized for the requirements in the experiment. Hadronic calorimeters are usually sampling calorimeters because they allow to combine heavy absorbers and very compact design. For the same reason sampling calorimeters are less expensive than comparable homogeneous calorimeters. However, the intrinsic energy resolution of sampling calorimeters is worse. Since only a small part of the shower energy is deposited in the active medium, the energy resolution suffers from so-called sampling fluctuations. They arise because the distribution of the energy deposit among absorber and active medium differs from event to event. This introduces a significant contribution to the uncertainty of the energy measurement. Of course, sampling calorimeters are subject to non-linearity effects just like homogeneous calorimeters. A conventional design of a sampling calorimeter is implemented in the PHENIX PbSc where layers of active and passive materials alternate in a sandwich-like structure (see Section 5.4).

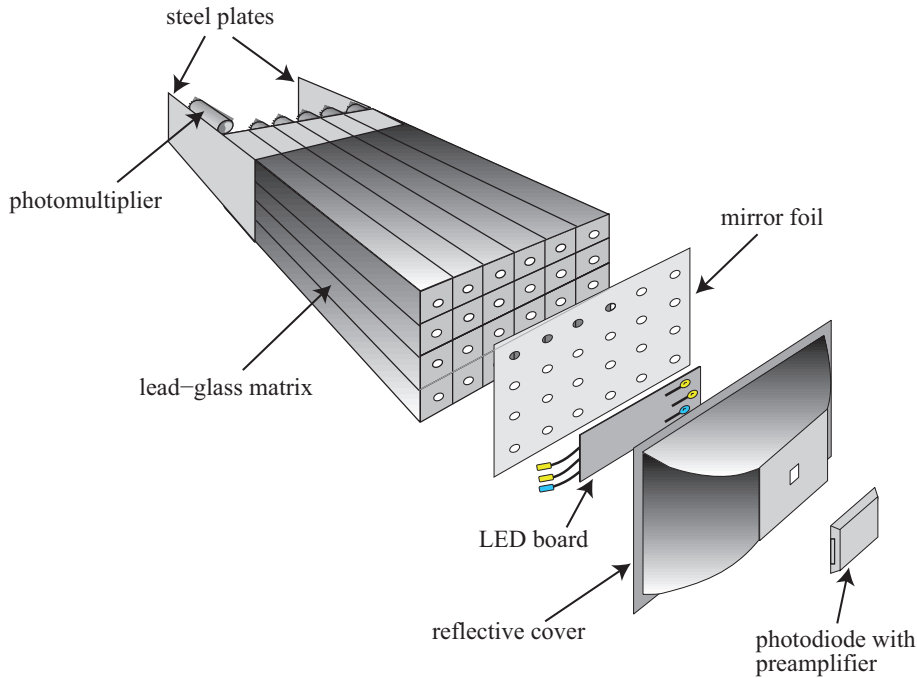


**Figure 5.2:** Exploded view of a PbGl supermodule showing all relevant components [Aph03].

A recent overview of calorimetry in high-energy particle physics giving more details on different designs and energy resolution can be found in [Fab03].

### 5.3 The Lead-Glass Calorimeter

The PbGl calorimeter was used successfully in the CERN experiment WA98 before it was disassembled and shipped to BNL where it was installed in the PHENIX experiment. Many design features were chosen to meet the requirements of both experiments. The PbGl calorimeter is a homogeneous Cherenkov calorimeter perfectly suited for the detection of electromagnetic particles such as electrons and photons. The smallest detector unit which is readout by its own FEU-84 photomultiplier tube (PMT) is a *module*. It is made of 51% PbO and 49% SiO<sub>2</sub>. Each module is wrapped with an aluminized mylar foil and encased in a shrink tube for optical isolation and covers a surface of 4.0 cm × 4.0 cm with a length of 40 cm. 4 × 6 PbGl modules are packaged together to form a self-supporting supermodule which is illustrated in Figure 5.2. Thin steel plates on either side at the end of the supermodule were incorporated during the gluing process. In WA98 this structure was used to shield the PMT's. In PHENIX shielding is accomplished by the space frame so that the steel plates are only required for mounting inside the space frame. In fact some of the steel plates were shortened to gain space for the readout electronics [Awe97]. Each supermodule has its own readout electronics and reference system and thus can

Parameter	Value	
	PbGl	PbSc
number of sectors	2	6
total number of modules/towers	9216	15552
spatial coverage	$\sim 15 \text{ m}^2$	$\sim 48 \text{ m}^2$
material	TF1 (51% PbO + 49% SiO <sub>2</sub> )	0.4 cm Polystyrene 0.15 cm Pb
lateral segmentation	$4.0 \times 4.0 \text{ cm}^2$	$5.535 \times 5.535 \text{ cm}^2$
number of sampling cells	—	66
radiation length $X_0$	2.78 cm	2.02 cm
nuclear absorption length $\lambda_a$	38.1 cm	44.1 cm
active depth	$14.4 \times X_0$ $1.05 \times \lambda_a$	$18 \times X_0$ $0.85 \times \lambda_a$
Molière radius $R_M$	3.68 cm	—
critical energy $E_C$	16 MeV	—
nominal energy resolution	$6.0\%/\sqrt{E}(\text{GeV})$	$8.1\%/\sqrt{E}(\text{GeV}) \oplus 2.1\%$

**Table 5.1:** Relevant parameters and characteristics of the lead-glass and lead-scintillator calorimeter in PHENIX.

be regarded as a single independent detector system. This flexible detector structure was chosen to meet the very different requirements of the WA98 and PHENIX experiment and made the installation in PHENIX significantly easier. 192 of such supermodules compose a PbGl sector. The PHENIX EMCAL contains two PbGl sectors in the lower part of the central east arm. This makes a total of 9216 PbGl modules, 4608 modules in each sector. With a surface of  $16 \text{ cm}^2$  per module the PHENIX PbGl calorimeter covers a geometric acceptance of  $\sim 15 \text{ m}^2$ . A list of relevant parameters and properties is given in Table 5.1.

An independent reference system using light emitting diodes (LED) is mounted at the front of each supermodule to monitor and correct the gain factors of each of the 24 modules [Pei96] (see Figure 5.2). The combination of three LED's (one blue and two yellow LED's) with three different pulse generators is required to reproduce the characteristics of signals generated by Cherenkov photons. The light from the LED's is distributed to the modules by reflection at the inside of the plastic cover. A mirror foil with holes on the front of the supermodule reduces light absorption and adjusts the amount of light seen by each module (the LED light intensity seen by each module depends on the location of the module). The reference system allows to check for gain variations, spectral sensitivity and linearity of the calorimeter system. In order to monitor the LED intensity a PIN photodi-

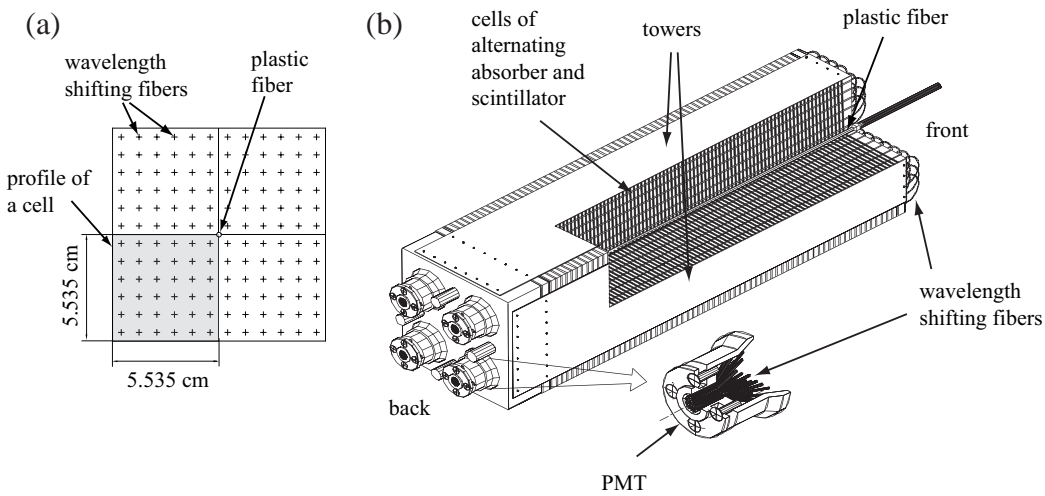


**Figure 5.3:** Schematic view of a PbSc module: (a) profile of a module revealing the fibers penetrating the towers and (b) cutaway view of a module and all its relevant components [Aph03].

ode is incorporated in the reference system. The original WA98 calibration of the PbGl calorimeter system is preserved within 10% using the LED reference system [Aph03].

## 5.4 The Lead-Scintillator Calorimeter

The PbSc is an electromagnetic sampling calorimeter with a sandwich-like structure. It is subdivided into individual *towers* with an active depth of 37.5 cm. Each tower comprises 66 cells which each consists of a layer of lead absorber and a scintillator (like a sandwich). The scintillating medium is an organic scintillator (p-bis[2-(5-Phenylloxazolyl)]-benzene (POPOP) with p-Terphenyl (PT)). Light from the scintillators is collected by 36 wavelength shifting fibers that penetrate all 66 cells and is transferred to a FEU115M PMT at the back of the tower. This structure allows to determine the energy deposit of a particle at various depth of the detector. Four towers are grouped mechanically together to form a module<sup>5</sup>. A cross section and the interior of a PbSc module showing all basic elements is shown in Figure 5.3.  $6 \times 6$  modules are combined in a supermodule which is held together by welded steel skins giving a rigid structure. Each of the six PbSc sectors comprises  $3 \times 6$  supermodules. Each sector is composed of 2592 individual towers

<sup>5</sup>Note that the term module is used differently for the PbGl, where it denotes the smallest detector unit. To avoid confusion the term *tower* is always used in the following as synonym for the smallest detector unit in either PbSc and PbGl.

adding up to a total of 15552 PbSc towers in the PHENIX EMCal. Since each tower has a cross-section area of  $5.535 \times 5.535 \text{ cm}^2$  all six sectors cover an area of  $\sim 48 \text{ m}^2$ . A summary of all relevant parameters of the PbSc is given in Table 5.1. The comparison of the two calorimeter subsystems in PHENIX reveals that hadrons deposit more energy in the PbGl. However, since low energy charged hadrons do not emit Cherenkov light but create scintillation light the PbSc is more susceptible to low energy hadrons.

The reference and monitoring system of the PbSc is based on a ultraviolet (UV) YAG laser whose light is distributed to each module utilizing a system of optical splitters and quartz fibers [Aph03]. Thereby the light is transmitted over a distance of approximately 50 m. At each module the light is injected into a plastic fiber that runs along the center of the module (see Figure 5.3). Light from this “leaky” fiber excites the scintillator stack in each surrounding tower in such a way that the longitudinal profile of a  $\sim 1 \text{ GeV}$  electromagnetic shower is simulated. The intensity of the laser light at each supermodule is monitored by PIN photodiodes. Since there are many steps involved in the light distribution from the laser to each tower the total efficiency for the conversion of UV light into photoelectrons in the PMT is very small. Hence a high-power laser is required. The initial calibration of the PbSc calorimeter was carried out using cosmic muons and test-beams of electrons and charged hadrons [Dav98]. The reference system ensured an uncertainty on the energy scale below 5% on day one of RHIC operation.

## 5.5 EMCal Online System

The PHENIX detector comprises roughly 375,000 read-out channels. The signals of the various detector subsystems have to be processed in a number of ways involving i.a. digitization, filtering and storage of data. This complex task is handled by the PHENIX Online System which comprises several subsystems. All detector-specific electronics end with the Front End Modules (FEM’s) which are located on the detector subsystem. The Front End Electronics (FEE) integrated on the FEM’s is responsible for the conversion of analog detector signals into digital data packets. The Level-1 (LVL1) trigger system collects detector signals (via the FEM) and decides if a certain event is interesting based on programmable thresholds. Upon the receipt of a LVL1 accept instruction the digitized data packets are passed to the Data Collection Modules (DCM’s). The DCM’s receive large amounts of unformatted data and perform i.a. compression and formatting. The rest of the PHENIX Data Acquisition (DAQ) communicates only with a single set of DCM’s. The compressed data is send to the Event Builder (EvB) where the final stage of event assembly takes place, i.e. data fragments from each data stream are assembled to form complete events. The EvB also provides the environment for the Level-2 (LVL2) trigger system which reduces the data rate in Au + Au collisions to a rate that can be handled by

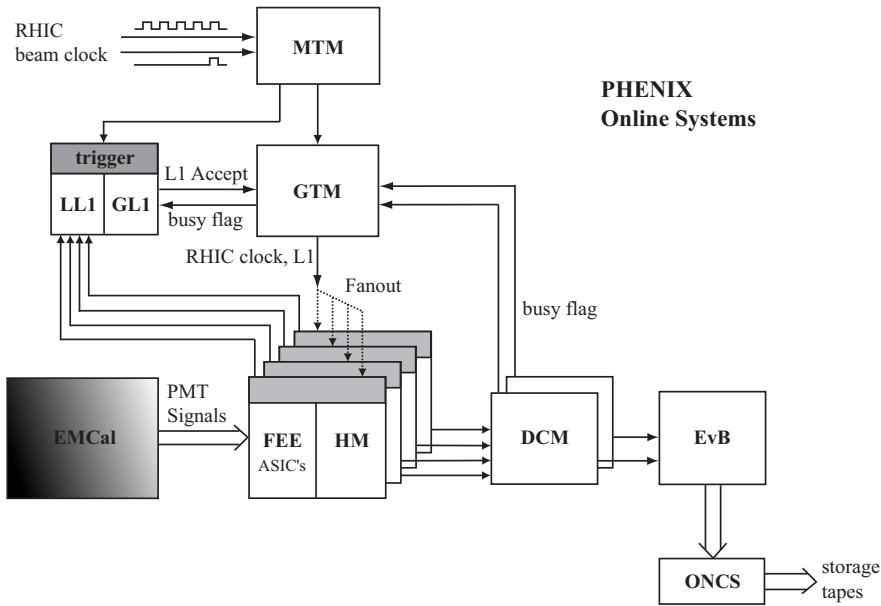


**Figure 5.4:** Block diagram illustrating the EMCal data acquisition in the PHENIX Online System. The layout for other PHENIX subsystems differ only in detail.

the PHENIX storage system. The LVL2 trigger is a software-based trigger as opposed to the hardware-based LVL1 trigger system. The compressed event data is passed to the PHENIX Online Control System (ONCS) for monitoring and is stored on buffer boxes before they are archived on storage tapes. This rather simplified outline of the PHENIX Online System is illustrated in Figure 5.4. The FEE of the various subsystems differs only in detail, i.e. the basic elements are identical for all subsystems. In the following the PHENIX data acquisition system and its specifics for the EMCAL subsystem are described in more detail. A comprehensive description of the PHENIX Online System is given in [Adl03c] and references therein.

### 5.5.1 PHENIX Timing System

The processing and conversion of the analog signals from the various subsystems are carried out synchronously with the RHIC beam clock. At RHIC bunch crossings occur at a frequency of 9.43 MHz. This means events have a minimum timing distance of  $\sim 106$  ns. In PHENIX the timing signal is distributed by the Master Timing System (MTS) to all FEM's which participate in the data collection process. The correct allocation of event data packets to the bunch crossing number is of major importance for the spin physics program at PHENIX.

The RHIC clock is provided by the Accelerator Control (AC) group. Two key signals are sent via optical serial links to the first stage of the PHENIX timing system, the Master Timing Module (MTM): One is a harmonic of the accelerator clock and the other one is a reference signal that marks the first bunch crossing and allows absolute numbering. The MTM sends a copy of the RHIC clock to the Granule Timing Modules (GTM's) and the LVL1 trigger system. The GTM's are the second stage in the timing system. The PHENIX detector system is divided into two sets of elements: *granules* and *partitions*. A granule denotes the smallest detector unit and can be a subsystem or part of a subsystem. Granules that share the same busy signals and LVL1 triggers are combined in so-called partitions. The GTM's are synchronized by the MTM. They manage busy signals from the DCM's, relay them to the LVL1 trigger system and provide the RHIC clock and LVL1 trigger accepts to the granules, i.e. FEM's. The basic concept of the PHENIX Timing system is illustrated in Figure 5.4.

### 5.5.2 Front End Modules

The EMCAL readout electronics comprises almost 25.000 readout channels. For both EMCAL subsystems 144 individual towers are read out by one single FEM (this corresponds to  $2 \times 3$  SM's in case of PbGl and 1 SM in case of PbSc). The FEM's are identical for PbGl and PbSc. The RHIC beam clock denotes a bunch crossing and hence a possible collision. For each bunch crossing the analog signals (negative current pulses) from the PMT's are sampled by the FEE. The PMT signals fulfill two functions: first the energy measurement of the incident particle and second the arrival time of the electromagnetic shower in the detector (e.g. arrival of Cherenkov photons at the rear end of the module). The energy and timing signals are processed by custom designed 4-channel ASIC<sup>6</sup> chips which serve 4 PMT's simultaneously. The EMCAL timing signal is discriminated and a TAC signal linearly related to the arrival time is stored in a ring buffer of 64 Analog Memory Units (AMU's). The energy signal is amplified in a Variable Gain Amplifier (VGA) by a factor of 4 - 12 which can be set remotely and independently for each PMT channel. This allows to compensate for gain variations among PMT's that share the same high voltage supply. The amplified energy signal is then split into a *low gain* and a *high gain* signal. The *low gain* signal is directly stored in one of 64 AMU's of a ring buffer, while the *high gain* signal is amplified by a factor of 16 before storage in a similar ring buffer of 64 AMU's. The separation into a *low gain* and *high gain* signal provides better energy resolution over the expected range of energies measured with the EMCAL (20 MeV - 20 GeV) using a single 12-bit ADC.

---

<sup>6</sup>Application Specific Integrated Circuit

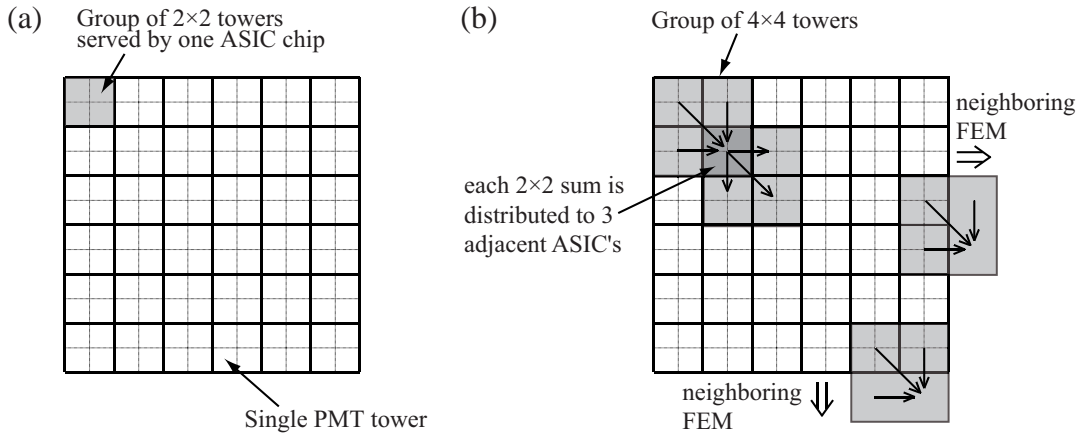


**Figure 5.5:** (a) Matrix of PMT towers read out by a single FEM. A  $2 \times 2$  array of PMT towers is served by a single ASIC chip. Hence 36 ASIC chips are required for the read-out giving a  $6 \times 6$  array of disjoint  $2 \times 2$  sums. (b) 36 overlapping  $4 \times 4$  sums per FEM are formed by combining four neighboring  $2 \times 2$  sums. At the boundaries of the FEM the  $2 \times 2$  sums are relayed to neighboring FEM's making the trigger effectively seamless.

In PHENIX there are two methods of digitization. In the first method analog signals from subsystems such as the EMCAL are stored in AMU's and are digitized upon the receipt of a LVL1 accept. In the second method the data is digitized in real time and stored on Digital Memory Units (DMUs) prior to receiving a LVL1 accept. The latter method is employed in subsystems such as BBC and ZDC. The storage of data in the AMU's happens synchronously with the RHIC beam crossings. Since two beam crossings are 106 ns apart, the 64 AMU's can buffer the data for approximately  $7 \mu\text{s}$  which is well above the latency of the LVL1 trigger system which is  $\sim 4.2 \mu\text{s}$  or 40 beam clock ticks. The AMU cells and the ADC units are contained on another custom designed ASIC chip, where the ADC signals are collected and reformatted before they are sent to the DCM's. All functions associated with FEE control such as LVL1 trigger receipt, collection and formatting of data, communication of LVL1 accepted data to the DCM's, etc. are controlled by a Heap Manager (HM) which is also implemented on the FEM's.

The EMCAL is part of the EMCAL-RICH Level-1 trigger (ERT) which is designed to select events that contain high-energy electrons or photons. The ERT is fired by a photon if the energy deposit of the electromagnetic shower in the EMCAL within some finite area is above a predefined threshold. The ERT is often referred to as a *high- $p_T$  photon trigger*. In the third year of RHIC physics running the luminosity in  $p + p$  was too high for the PHENIX DAQ to record all events. The use of the ERT ensures that all events containing a high-energy photon or electron are recorded. Four PMT signals from an

array of  $2 \times 2$  towers are processed by each ASIC chip in the FEE. This is shown in Figure 5.5(a) for one FEM. Each ASIC chip builds the analog sum of all four PMT signals. Individual suspicious towers can be masked out remotely. The sum of the  $2 \times 2$  trigger tiles is then compared to a programmable threshold by the LVL1 system. A trigger on disjoint  $2 \times 2$  sums has the drawback that the effective threshold is position dependent since not all showers are confined to one single  $2 \times 2$  tile. Hence some showers require a much larger energy to satisfy the trigger. To overcome this problem the EMCAL trigger is designed to trigger on the sum of overlapping tiles of  $4 \times 4$  PMT towers. A copy of the  $2 \times 2$  sum of each ASIC chip is distributed to three adjacent ASIC chips as illustrated in Figure 5.5(b). Hence each  $2 \times 2$  sum is combined with three other neighboring  $2 \times 2$  sums to form a  $4 \times 4$  sum. At FEM boundaries the  $2 \times 2$  sums are relayed to neighboring FEM's to ensure seamless trigger coverage. The LVL1 system compares the  $4 \times 4$  sums to three different thresholds, which are remotely programmable. Settings of the EMCAL ERT thresholds during the  $p + p$  run in year three are summarized in Table 5.2. Thresholds are set in terms of Digital-To-Analog Converter (DAC) tics. The values given in Table 5.2 are the corresponding nominal energies. The trigger information is only available at the FEM level, i.e. it is only known which FEM created the trigger. Hence if a trigger tile becomes noisy the complete FEM needs to be masked off to ensure correct trigger information. However, with the help of a pedestal scan noisy tiles could be identified and set to the highest possible DAC value effectively masking the tile for the trigger. During the  $p + p$  run in year three eight different EMCAL-RICH triggers were used [Bau03]. However, for the analyses presented in this thesis only data recorded with the ERT\_4 $\times$ 4c in coincidence with the minimum bias trigger (BBCLL1) was used to extent the analyses to higher  $p_T$  (this data set is referred to in the following as the *Gamma3* data sample). The minimum bias condition is satisfied if at least one PMT in each BBC fired in a collision (see Section 7.2.2). A custom designed trigger board summarizes the trigger information provided by one FEM and relays the information to the LVL1 system. The stored trigger

trigger	PbGl [GeV]	PbSc [GeV]
ERT_2 $\times$ 2	0.8 (0.4)	0.8 (0.4)
ERT_4 $\times$ 4a	1.4	2.1
ERT_4 $\times$ 4b	2.1	2.8
ERT_4 $\times$ 4c	0.7	1.4

**Table 5.2:** Nominal EMCAL energy thresholds of the different ERT settings for the  $p + p$  run in year three. The  $2 \times 2$  trigger thresholds were changed during the run.

information contains only the FEM on which the ERT fired but not the particular trigger tile.

### 5.5.3 Level-1 Trigger System

The PHENIX LVL1 trigger system has two purposes: First it defines events in PHENIX which potentially contain interesting physics and second it reduces the amount of data to a rate that can be handled by the PHENIX DAQ<sup>7</sup>. Since in RHIC minimum bias p + p collisions occur at a rate of  $\sim 500$  kHz the data rate from the detector subsystems must be scaled down. The LVL1 triggered data is then used as seed for the higher level triggers (LVL2).

The LVL1 trigger system is divided into two subsystems: the Global Level-1 (GL1) and the Local Level-1 (LL1) system. The LL1 system communicates directly with the FEE of the detector subsystems. Input data (PMT sums in case of the EMCAL) is processed by the LL1 algorithms and sent to the GL1 system for every bunch crossing. The GL1 combines the LL1 data and provides the trigger decision to the GTM's which initiate the readout of the FEM's. The GL1 manages busy signals relayed by the DCM's as well as from the trigger and compares the trigger bit pattern to a programmable scaledown counter in order to reduce the event data rate below the limit of the DAQ.

### 5.5.4 Data Collection Modules

Approximately 375,000 channels of electronics in PHENIX are simultaneously sampled and stored in digital or analog memory and upon the receipt of a LVL1 accept (after a trigger latency of  $4\ \mu s$ ) are transferred to the data collection system. At maximum trigger rate over 100 GB per second are send to the DCM's which are designed to handle this large amount of uncompressed event data fragments and perform several tasks such as zero suppression, data formatting, buffering and output of the compressed data to the PHENIX Event Builder (EvB). Each DCM board has four parallel data input streams and is hence connected to four FEM's. Since the FEM's are not designed to perform zero suppression, compressors within the DCM's remove ADC values from the data streams that correspond to zero signals in order to achieve better suppression. Each DCM is capable of buffering the information of up to five complete events before transfer to the EvB and is able to control FEM readout via busy flags which can be issued to the GTMs.

---

<sup>7</sup>The required time for processing the LVL1 trigger and complete transfer of the data packet to the DCM's limits the rate of possible data acquisition to  $\sim 12.5$  kHz.

### 5.5.5 Event Builder

The EvB marks the final stage of event assembly. It receives parallel data streams of event data fragments from the DCM boards, which are assembled into complete events. It also performs LVL2 trigger processing on the events and communicates accepted events to the PHENIX Online Control System (ONCS). The EvB is able to handle event rates of about 12.5 kHz achieved in p + p running. Because of the large event size in Au + Au collisions data rates well above 100 MB/s were already expected in the first few years of PHENIX operation. Therefore the EvB is designed for data rates up to 500 MB/s. Since the maximum data storage rate is much smaller, LVL2 rejection is necessary in heavy ion collisions.

As noted before the PHENIX detector is divided into granules which can be combined in partitions. To follow this partitioning scheme the EvB is designed to read out a configurable collection of input data streams (granules) using so-called Sub-Event Buffers (SEB's). The SEB's receive and buffer the data from the DCM's. They are controlled by the EvB Controller (EBC) which initiates the data transfer of a particular event from a programmable set of SEB's to the Assembly/Trigger Processors (ATP's). The ATP's perform the final event assembly and transmit the event data to ONCS for monitoring and data storage. Processing LVL2 algorithms on the event data takes place in the ATP's to reduce the data rate to a rate which can be archived to disk.

### 5.5.6 Level-2 Trigger

The event size in central heavy ion collisions such as Au + Au can exceed 150 kB. Together with the event rate expected at RHIC design luminosity the LVL1 triggered data rate can easily exceed rates of 100 MB/s. The rate at which event data can be archived to disk is well below this rate and hence the LVL1 triggered data set must be further scaled down. This is achieved by the software driven LVL2 trigger system. C++ coded LVL2 algorithms, which operate in the ATP's, are designed to select events that appear to contain interesting physics. Unlike the LVL1 trigger the LVL2 algorithms perform more sophisticated operations such as cluster finding, track matching and invariant mass reconstruction. The LVL2 triggered data together with a minimum bias sample is then archived to disk.

The p + p data sample analyzed for this thesis was recorded without any LVL2 triggers during the third year of RHIC physics running. Therefore any corrections or scalers required for LVL2 triggered data did not have to be taken into account for the analyses presented in this work.



# **Part I**

## **Direct-Photon Production**



# 6. Direct-Photon Production in $p + p$ Collisions

Photons created in particle collisions are referred to as *direct* photons if they emerge directly from the collision. This definition excludes all photons coming from hadronic decays such as  $\pi^0 \rightarrow \gamma\gamma$  or  $\eta \rightarrow \gamma\gamma$ . In elementary nucleon-nucleon collisions at large transverse momenta direct photons are produced in hard inelastic scatterings of the point-like partons. The total emission rate can be calculated using the factorization theorem in perturbative QCD (see Equation 2.5).

There are a number of incentives for the investigation of direct photons in  $p + p$  collisions. The gluon distribution inside the proton is directly involved in the production mechanisms of direct photons and hence can be probed by the measurement of the direct-photon cross section. In addition, unlike theoretical calculations of hadron production, predictions for direct-photon production are less affected by the choice of fragmentation functions and therefore the measurement of direct photons provides a more direct tool to test pQCD. Moreover, the distribution of direct photons in  $p + p$  serves as a crucial baseline for the measurement in heavy-ion collisions ( $A + A$ ) at the same  $\sqrt{s_{NN}}$  per nucleon-nucleon pair. In ultra-relativistic heavy-ion collisions direct photons are also emitted by the created QCD medium (thermal radiation). Therefore, the contribution from hard-scatterings must be identified in order to be able to quantify the thermal contribution.

## 6.1 Mechanisms of Direct-Photon Production in Hard Parton Scatterings

The inclusive spectrum of direct photons in  $p + p$  at large transverse momenta can be divided into two components according to the underlying partonic mechanisms: (1) prompt photons, which are created directly in the partonic scattering and (2) fragmentation photons, which are emitted by a scattered parton as part of the fragmentation process. In the following a basic theoretical survey of the most fundamental processes of direct-photon production in hard partonic scatterings is given. More detailed descriptions can be found for instance in [Won94, Gor93, Bae90, Aur88].

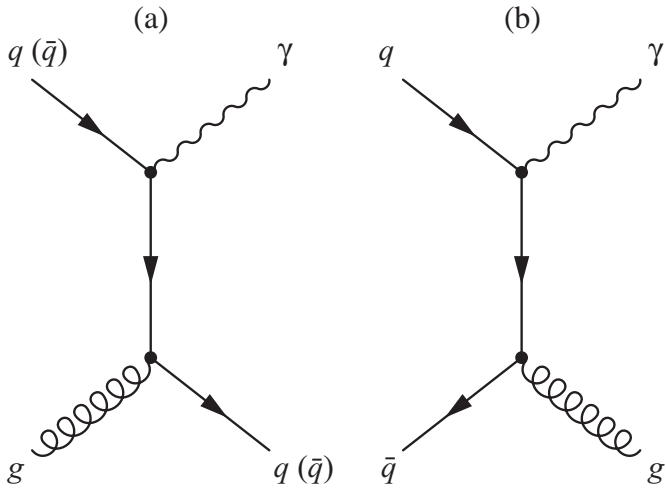


**Figure 6.1:** Feynman diagrams of prompt-photon production at leading order in pQCD: (a) quark-gluon Compton scattering and (b) quark-antiquark annihilation.

### 6.1.1 Prompt-Photon Production

At leading order (LO) in pQCD<sup>1</sup> two processes contribute to the spectrum of prompt photons: (1) quark-gluon Compton scattering, in which a gluon scatters off of a quark (or antiquark) resulting in a quark (or antiquark) and a photon in the final state ( $g + q(\bar{q}) \rightarrow \gamma + q(\bar{q})$ ). The process is analogous to the electromagnetic Compton scattering in which a photon scatters off of a charged particle. And (2) quark-antiquark annihilation, in which a quark and an antiquark annihilate resulting in a gluon and a photon ( $q + \bar{q} \rightarrow \gamma + g$ ). The analogous process in QED is the  $e^+e^-$  annihilation. The corresponding Feynman diagrams of these two QCD processes are shown in Figure 6.1. Since the photon couples electromagnetically to the quark (antiquark) the fine structure constant enters the transition amplitude for the corresponding vertex.

Due to quark-gluon Compton scattering the distribution of the gluon contributes to the prompt-photon cross section at leading order. Moreover, in  $p + p$  collisions the annihilation of quark-antiquark pairs is suppressed due to the small  $\bar{q}$  density compared to the

<sup>1</sup>In quantum field theory the order of the calculation is given by the number of vertices that contribute to the process. Each vertex contributes a factor of  $\sqrt{\alpha}$  to the transition amplitude,  $\alpha$  being the coupling constant of the interaction at play. At lowest order (referred to as leading order) the process comprises only two vertices and hence the transition amplitude is proportional to  $\alpha$ . Higher order processes contain more than two vertices and therefore are less probable. In QED  $\alpha$  is given by the fine structure constant so that higher-order contributions soon become negligible. However, in QCD higher-order processes often make a significant contribution to the total cross section because of the strong coupling and therefore need to be considered in precise calculations.

density of  $g$  in the initial state. Hence the production of prompt photons in  $p + p$  is dominated by quark-gluon Compton scattering and thus the measurement of prompt photons is highly suitable to probe the gluon distribution inside the proton.

Since prompt photons are directly produced in the hard scattering the fragmentation function required in pQCD reduces to a  $\delta$ -function. Therefore, the theoretical predictions of prompt-photon production do not depend on the non-perturbative fragmentation functions which have to be determined experimentally, e.g. for calculations of the  $\pi^0$  cross section. The measurement of prompt photons therefore provides an excellent test of pQCD without the uncertainty generally introduced by the fragmentation process.

The differential cross section of quark-gluon Compton scattering is related to the differential cross section of the well known QED equivalent, the electromagnetic Compton scattering ( $\gamma + q \rightarrow \gamma + q$ ) [Won94]<sup>2</sup>:

$$\begin{aligned} \frac{d\sigma}{dt}(g + q \rightarrow \gamma + q) &= \frac{\alpha_s}{\alpha} \left( \frac{e}{e_q} \right)^2 \cdot \frac{d\sigma}{dt}(\gamma + q \rightarrow \gamma + q) \\ &= \left( \frac{e_q}{e} \right)^2 \frac{8\pi\alpha_s\alpha}{(s - m_q^2)^2} \left[ \left( \frac{m_q^2}{s - m_q^2} + \frac{m_q^2}{u - m_q^2} \right) \right. \\ &\quad \left. + \left( \frac{m_q^2}{s - m_q^2} + \frac{m_q^2}{u - m_q^2} \right) - \frac{1}{4} \left( \frac{s - m_q^2}{u - m_q^2} + \frac{u - m_q^2}{s - m_q^2} \right) \right]. \end{aligned} \quad (6.1)$$

where  $m_q$  is the quark mass and  $e$  and  $e_q$  are the electromagnetic charge of the electron and the quark, respectively.  $s$ ,  $t$  and  $u$  are the Mandelstam variables, which are defined in Appendix A. It can be shown (see e.g. [Won94]) that in ultra-relativistic reactions, when the rest mass of the quark  $m_q$  is negligible, the four-momentum of the photon in the final state is approximately the same as the four-momentum of the quark in the initial state. Therefore the quark-gluon Compton scattering at ultra-relativistic energies can be regarded as a process in which the initial quark is converted into a photon with approximately the same energy and momentum.

The differential cross section of quark-antiquark annihilation at leading order can be derived in a similar way utilizing the differential cross section of the QED process  $e^+ + e^- \rightarrow \gamma + \gamma$ . Quark-antiquark annihilation is related to the process  $q + \bar{q} \rightarrow \gamma + \gamma$  via [Won94]:

$$\frac{d\sigma}{dt}(q + \bar{q} \rightarrow \gamma + g) = \frac{\alpha_s}{\alpha} \left( \frac{e}{e_q} \right)^2 \frac{d\sigma}{dt}(q + \bar{q} \rightarrow \gamma + \gamma). \quad (6.2)$$

---

<sup>2</sup>The differential cross sections for  $g + q \rightarrow \gamma + q$  and  $g + \bar{q} \rightarrow \gamma + \bar{q}$  are identical and are not distinguished in the following discussion.

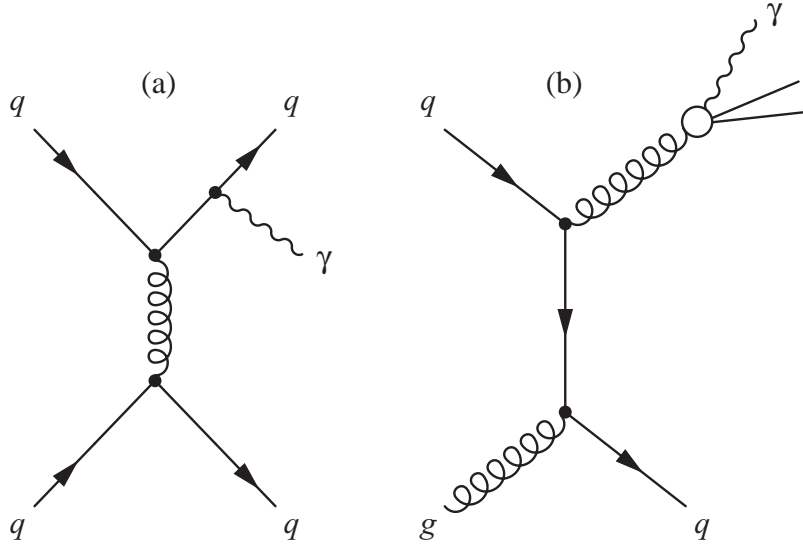


**Figure 6.2:** (a) NLO Feynman diagram of bremsstrahlung emission in which a photon is radiated by a scattered quark and (b) emission of a photon as part of the parton-jet fragmentation after LO quark-gluon scattering.

Using the relation of the differential cross section of  $q + \bar{q} \rightarrow \gamma + \gamma$  to the corresponding QED annihilation process, the differential cross section of quark-antiquark annihilation can be written in terms of the Mandelstam variables [Won94]:

$$\frac{d\sigma}{dt}(q + \bar{q} \rightarrow \gamma + \gamma) = \left(\frac{e_q}{e}\right)^2 \frac{8\pi\alpha_s\alpha}{s(s - 4m_q^2)} \left[ \left( \frac{m_q^2}{t - m_q^2} + \frac{m_q^2}{u - m_q^2} \right) + \left( \frac{m_q^2}{t - m_q^2} + \frac{m_q^2}{u - m_q^2} \right) - \frac{1}{4} \left( \frac{t - m_q^2}{u - m_q^2} + \frac{u - m_q^2}{t - m_q^2} \right) \right]. \quad (6.3)$$

Similar to quark-gluon Compton scattering quark-antiquark annihilation can be depicted in ultra-relativistic reactions as a process in which a quark or antiquark in the initial state is converted into a photon in the final state with similar energy and momentum.

Equation 6.1 and 6.3 describe the pQCD cross sections of the two leading order mechanisms of prompt-photon production. In order to calculate the total emission rates of prompt photons in hard p + p collisions the momentum distributions of quarks, antiquarks and gluons inside the colliding protons have to be known and convoluted in the calculation according to Equation 2.5 (see Section 8.1.3 for a discussion on parton distribution functions).

At next-to-leading order (NLO) in pQCD processes as the one depicted in Figure 6.2(a) in which a photon is emitted by a scattered quark contribute to the spectrum

of direct photons. These photons are referred to as bremsstrahlung and arise as a higher-order correction to any pure QCD  $2 \rightarrow 2$  process which involves a quark in the final state (such as  $q + q \rightarrow q + q$ ).

## 6.1.2 Fragmentation Photons

In hard parton-parton scatterings the scattered quark or gluon can fragment into a photon. These photons are referred to as fragmentation photons and also contribute to the spectrum of direct photons. Such a process is depicted in Figure 6.2(b). The cross section of the partonic hard scattering (here:  $q + g \rightarrow q + g$ ) can be calculated at leading order in pQCD. However, the emission of a photon as part of the parton-jet fragmentation is described by a non-perturbative parton-to-photon fragmentation function (FF). Hence, unlike the theoretical description of prompt-photon production the prediction of the fragmentation component suffers from the additional uncertainty introduced by the only experimentally accessible FF's.

The parton-to-photon fragmentation makes a significant contribution to the inclusive direct-photon spectrum (i.e. prompt + fragmentation photons) as indicated in Figure 6.3. The NLO pQCD calculation at  $\sqrt{s} = 200$  GeV, provided by W. Vogelsang, uses the CTEQ6M parton distribution functions [Pum02] and the BFGII parton-to-photon fragmentation functions [Bou98]. As one can see from the figure the contribution from fragmentation is significant over the entire  $p_T$  range covered by the calculation. At low transverse momentum ( $p_T \lesssim 2$  GeV/c) the direct-photon spectrum is dominated by fragmentation. However, in this kinematic regime the applicability of perturbative QCD already becomes restricted.

Fragmentation photons are usually accompanied by hadrons also produced in the fragmentation process. The same applies for bremsstrahlung, where the scattered quark which radiated the photon eventually fragments into hadrons. By contrast, prompt photons at leading order are usually characterized by the absence of any accompanying hadronic energy since the parton in the final state of quark-gluon Compton scattering or quark-antiquark annihilation is emitted in the opposite direction of the photon. Prompt photons are therefore often referred to as *isolated* photons. This feature can in principle be utilized experimentally to extract the spectrum of prompt photons. Moreover, by disentangling the prompt and the fragmentation component it is possible to explicitly study the fragmentation process in direct-photon production.

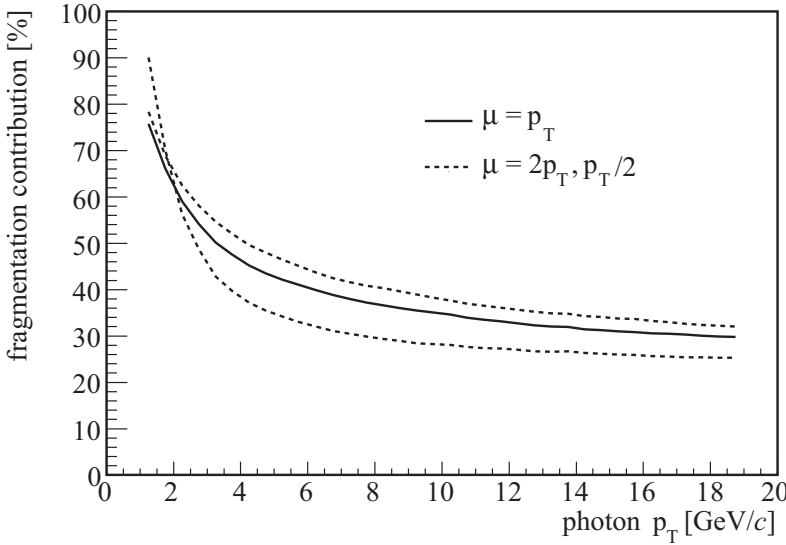


**Figure 6.3:** The fragmentation component as a fraction of the inclusive direct-photon spectrum in  $p + p$  at  $\sqrt{s} = 200$  GeV for three different theory scales ( $\mu = p_T/2$ ,  $\mu = p_T$  and  $\mu = 2p_T$ ). The pQCD predictions at NLO use the CTEQ6M parton distribution functions and BFGII parton-to-photon fragmentation functions (calculations performed by W. Vogelsang).

## 6.2 Direct-Photon Production in $A + A$

As was noted earlier the direct-photon cross section measured in elementary  $p + p$  collisions is required as a baseline for the interpretation of direct-photon data obtained in heavy-ion collisions at the same center-of-mass energy per nucleon-nucleon pair  $\sqrt{s_{NN}}$ . In order to emphasize the importance of the  $p + p$  reference for the interpretation of the measurement in heavy-ion collisions a short introduction on direct-photon production in heavy-ion collisions is given in the following. For a recent and more detailed discussion on this topic please refer to e.g. [Sta05].

In high energy heavy-ion collisions the density in the reaction zone is so large that quarks and gluons are no longer bound in color-singlet states. Instead the partons can be considered as free moving particles over an extended region of space and time. This highly excited state of nuclear matter is generally referred to as *quark-gluon plasma* (QGP). Direct photons provide a unique probe to study the characteristics of a QGP. Since photons interact only electromagnetically they can leave the strongly interacting reaction zone almost unaltered and hence carry unbiased information on the created medium.

In high energy  $A + A$  collision direct photons are not only created in the early hard parton scatterings. If a strongly interacting medium such as the QGP is developed in

the collision its constituents are thermalized, i.e. the quarks and gluons are in thermal equilibrium. Such a medium creates thermal radiation. At lowest order the underlying processes that lead to the emission of thermal photons are the same as for prompt-photon production, i.e. quark-antiquark annihilation and quark-gluon Compton scattering. For the calculation of the thermal emission rates the parton distributions in the medium are required. They are given by the Fermi-Dirac (quarks and antiquarks) and the Bose-Einstein (gluons) statistics, respectively. As thermal photons are predominantly produced in the early hot phase of the fireball evolution, their measurement can help to constrain the initial temperature of the reaction zone (a concise description of thermal radiation in heavy-ion collisions can be found in [KB04a]). Calculations indicate that in central Au + Au collisions at  $\sqrt{s_{NN}} = 200$  GeV thermal radiation from a QGP could be the dominant source of direct-photon production for  $1 \text{ GeV}/c < p_T < 3 \text{ GeV}/c$  [Tur04]. However, the direct-photon signal in this  $p_T$  range is very small. Therefore, a precise measurement of the contribution from hard scatterings in this  $p_T$  range is crucial in order to be able to extract a significant thermal signal.

In order to constrain the contribution from initial hard scattering to the total spectrum of direct photons (or to any other particle spectrum) measured in  $A + A$  the yield obtained in  $p + p$  can be extrapolated using the so-called *binary collision scaling*. In a simple approach a collision of two nuclei at relativistic energies can be pictured as a superposition of individual hard nucleon-nucleon ( $N + N$ ) scatterings. By assuming that each  $N + N$  collision in a heavy-ion reaction can be taken as an elementary  $p + p$  collision the expected yield of particle production in  $A + A$  collisions is simply given by the measured yield in  $p + p$  scaled by the number of binary  $N + N$  collisions in  $A + A$ . The assumptions made for binary scaling are justified because at large momentum transfer the partons can be considered as asymptotically free and each hard scattering occurs on a very short time scale so that multiple scatterings of the same nucleon do not affect each other. At large transverse momenta ( $p_T > 5 \text{ GeV}/c$ ) direct-photon production in  $A + A$  collisions is dominated by hard scattering. Binary collision scaling can be tested by calculating the so-called *nuclear modification factor*:

$$R_{AB} = \frac{dN/dp_T|_{AB}}{\langle N_{\text{coll}} \rangle_{AB} \cdot dN/dp_T|_{NN}}, \quad (6.4)$$

where the numerator is the yield measured in collisions of nuclei  $A$  and  $B$  and the denominator is the scaled yield measured in  $p + p$ .  $\langle N_{\text{coll}} \rangle_{AB}$  is the average number of inelastic, binary  $N + N$  collisions in the  $A + B$  reaction. It was shown by PHENIX that direct-photon production in Au + Au at  $\sqrt{s_{NN}} = 200$  GeV is consistent with binary scaling in the range  $p_T = 4 - 13 \text{ GeV}/c$  [Adl05b]. This is illustrated in Figure 6.4. It shows the nuclear modification factor for direct photons in central Au + Au collisions at  $\sqrt{s_{NN}} = 200$  GeV. However, the calculation utilizes a NLO pQCD prediction as reference, which introduces

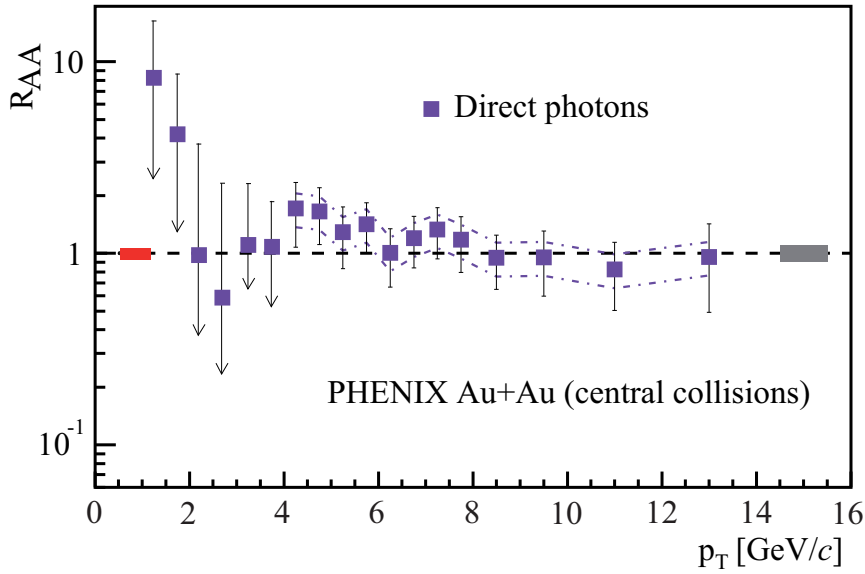


**Figure 6.4:** Nuclear modification factor for direct photons in central Au + Au collisions at  $\sqrt{s_{NN}} = 200$  GeV. The figure is taken from [Adl06a].

an additional theoretical uncertainty (indicated by the dash-dotted lines).

The nuclear modification factor for particle production is also studied to quantify possible effects introduced by the nuclear environment or the medium created in the collision. According to Equation 2.5 cross sections in pQCD depend on the parton distributions and fragmentation functions. If the initial parton distribution is modified in the nucleus prior to the collision (initial state effect) or the scattered parton is affected by the medium prior to fragmentation (final state effect) the nuclear modification can depart from unity. In fact, one of the most striking observations at RHIC is the strong suppression of hadrons in central Au + Au collisions at  $\sqrt{s_{NN}} = 200$  GeV as compared to the binary scaled yield in p + p [Adc02, Adl02, Adl03d]. This suppression, which is usually referred to as jet quenching, can be explained by the energy loss of hard scattered quarks and gluons via gluon bremsstrahlung induced by the surrounding medium of high color charge density [Gyu03]. As photons are not subject to the strong interaction they are not sensitive to final state effects. Therefore, the absence of suppression in direct-photon production in Au + Au (Figure 6.4) supports the theoretical explanation that the observed suppression is caused by the medium created in the collision.

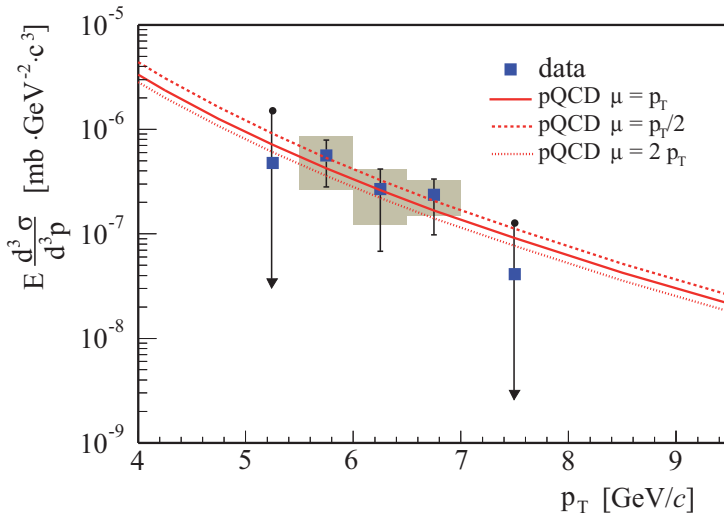


**Figure 6.5:** Inclusive direct-photon spectrum in  $p + p$  at  $\sqrt{s} = 200$  GeV measured by PHENIX [Adl05c].

### 6.3 Earlier Results of Direct-Photon Production in $N + N$ Collisions

The inclusive direct-photon spectrum in  $p + p$  collisions at  $\sqrt{s} = 200$  GeV has been measured by PHENIX in the second physics running period (Run II  $p + p$ ) [Adl05c]. The cross section is shown in Figure 6.5. The integrated luminosity accumulated in PHENIX Run II  $p + p$  allowed the extraction of only three significant data points in the range  $5.5 < p_T < 7$   $\text{GeV}/c$ . Therefore the spectrum is not suitable to serve as reference for the calculation of the nuclear modification factor (see Figure 6.4). However, the good agreement between the data points and NLO pQCD calculations supports the usage of the theoretical prediction in the calculation of  $R_{AA}$  (at least in the  $p_T$  region covered by the  $p + p$  data).

Besides PHENIX at RHIC, which started its physics program in 2000, a number of other experiments have extensively studied the production of direct photons in nucleon-nucleon collisions at various center-of-mass energies since the 1980's. While fixed-target experiments measured direct photons in  $p + p$  as well as  $p + \bar{p}$  collisions up to  $\sqrt{s} = 63$  GeV [Ana82, Bal98, Apa04], collider experiments studied direct-photon production only in  $p + \bar{p}$  collisions in the energy range  $546 \text{ GeV} < \sqrt{s} < 1.96 \text{ TeV}$  [Alb88, Ali91, Abe94, Aba06]. A selection of this world data is shown in Figure 6.6 together with a comparison to a recent NLO pQCD analysis [Aur06]. It should be noted that the

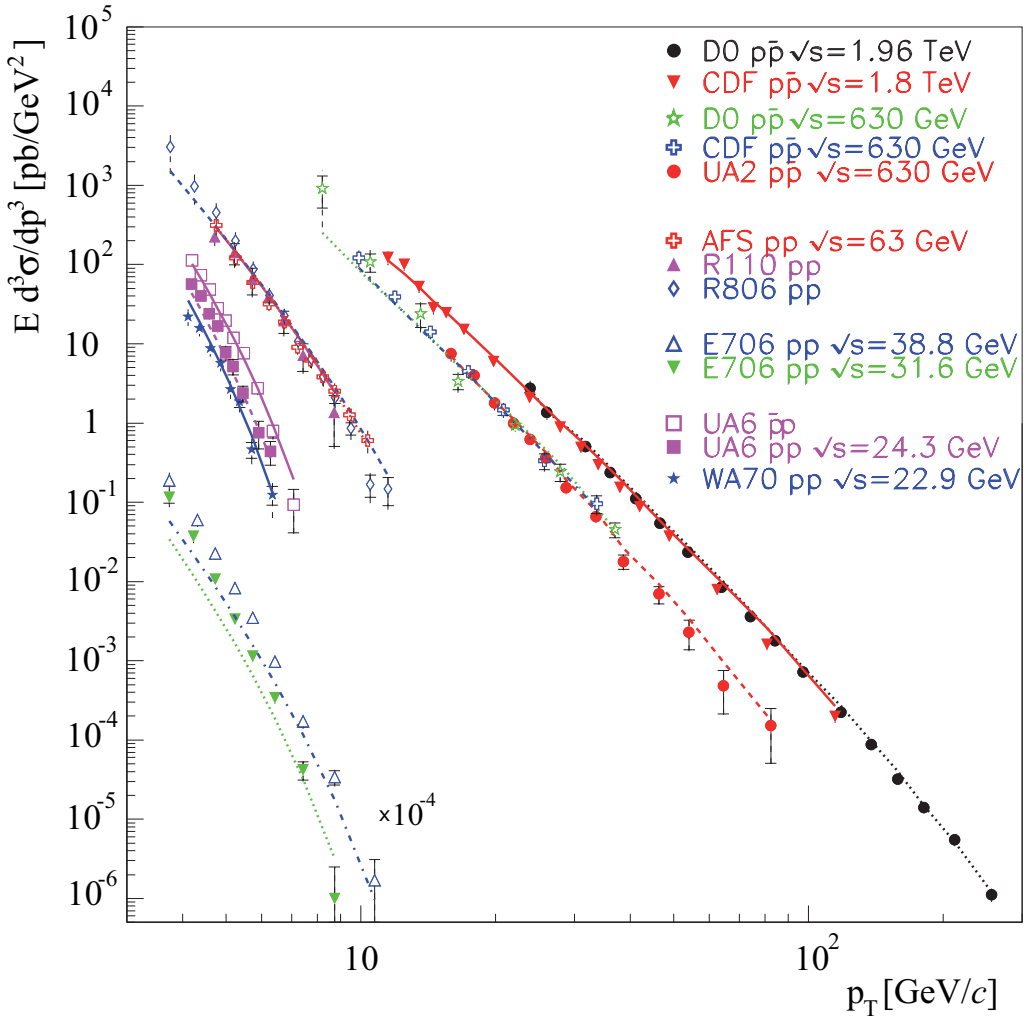


**Figure 6.6:** World data of direct-photon production in  $p + p$  and  $p + \bar{p}$  collisions at various  $\sqrt{s}$ . The solid lines represent pQCD predictions at next-to-leading order. Please note that the E706 data points are scaled by a factor of  $10^{-4}$ . The figure is taken from [Aur06].

figure comprises isolated (prompt) photon as well as inclusive direct-photon spectra. The data spans two orders of magnitude in collision energy and agrees with theoretical predictions over nine orders of magnitude, except for the direct-photon result obtained by the E706 collaboration in  $p + p$  at Tevatron fixed target energies ( $\sqrt{s} = 38.8$  GeV and  $\sqrt{s} = 31.6$  GeV). As one can see in the figure the NLO pQCD prediction underestimates the data for  $p_T < 7$  GeV/ $c$ . The E706 collaboration has put forward the so-called  $k_T$  *enhancement*, which is a phenomenological approach to explain the discrepancy between the E706 data and pQCD predictions [Apa04]. In this model the partons in the initial

state lose energy via soft gluon radiation. This non-perturbative process is parameterized in terms of an effective transverse momentum ( $k_T$ ) which is added to the incoming partons. A  $k_T$  enhanced NLO pQCD calculation provides a much more improved description of the E706 data. Although it has been claimed recently that most of the existing world data from fixed-target as well as collider experiments are well described by pure pQCD predictions [Aur06] there have been global analyses (see e.g. [Hus95]) which indicate that the theoretical description of direct-photon production, especially at fixed-target energies, requires  $k_T$  enhancement. The question whether  $k_T$  enhancement is necessary is still an open question and more data is required to settle it.



# 7. Measurement of Direct Photons in p + p Collisions

As discussed in Chapter 6, the analysis of direct-photon production in elementary p + p collisions at RHIC energies is interesting for a number of reasons, e.g. it gives access to the gluon distribution in the proton (the extraction of the polarized gluon distribution via the measurement of direct photons is addressed in Chapter 8), provides the baseline for the interpretation of direct-photon data from heavy-ion ( $A + A$ ) collisions, and above all tests the predictions of perturbative QCD.

The major part of the analysis work presented in this thesis is the systematic study of inclusive direct-photon production in p + p collisions. The data were acquired with the PHENIX detector (especially with the EMCAL) in the third RHIC beam time at a center-of-mass energy of  $\sqrt{s} = 200$  GeV. The spin-averaged (and hence unpolarized) direct-photon cross section is presented, i.e. the analysis does not take into account the different bunch spin patterns (see Section 3.1). Thus this analysis does not allow any conclusion on the polarized gluon distribution. In this chapter the analysis of direct-photon production in p + p collisions using the so-called *cocktail method* is described in detail.

## 7.1 Analysis Method

The measurement of direct photons is very challenging and tedious, because of the small direct-photon production cross section and the large background of decay photons. Various analysis techniques have been developed to extract the small direct-photon signal. The method utilized for this thesis is the cocktail method. The basic idea of this technique is rather simple: starting point is the measured inclusive photon spectrum  $\gamma^{\text{incl}}$  which is composed of direct photons and decay photons (the cocktail). The background of decay photons is mainly due to two-photon decays of  $\pi^0$ 's and  $\eta$ 's. The background is estimated in a fast Monte-Carlo simulation utilizing the measured neutral pion spectrum. The measured ratio of inclusive photons and neutral pions,  $(\gamma^{\text{incl}}/\pi^0)_{\text{meas}}$ , is compared to the ratio of simulated decay photons and neutral pions,  $(\gamma^{\text{decay}}/\pi^0)_{\text{sim}}$ . This *double ratio*,

$$R_\gamma = \frac{(\gamma^{\text{incl}}/\pi^0)_{\text{meas}}}{(\gamma^{\text{decay}}/\pi^0)_{\text{sim}}}, \quad (7.1)$$

quantifies the excess of photons, and a ratio above unity indicates a direct-photon signal which can be extracted as a fraction of the measured inclusive photon yield:

$$\gamma^{\text{direct}} = \gamma^{\text{incl}} - \gamma^{\text{decay}} = \left(1 - \frac{1}{R_\gamma}\right) \cdot \gamma^{\text{incl}}. \quad (7.2)$$

Equation 7.2 is easily verified using  $R_\gamma = \gamma^{\text{incl}}/\gamma^{\text{decay}}$ . There are two reasons for using the  $\gamma/\pi^0$  ratio: First, the ratio of  $\gamma^{\text{decay}}/\pi^0$  is easily simulated in a fast Monte-Carlo simulation using the measured neutral pion spectrum; and second, since the inclusive photon and the neutral pion spectrum are determined from the same data sample many systematic uncertainties cancel in the ratio  $\gamma/\pi^0$ , notably the uncertainty on the global energy scale (see Section 7.4.1).

The simulation of decay photons is based on the neutral pion spectrum measured in the same running period with the PHENIX detector [Bat05b, Bat05a]. The  $\pi^0$  analysis is not discussed in detail for the direct-photon analysis. However, more information on the invariant mass analysis to reconstruct neutral pions from the EMCAL data is given in Section 9.8 as part of the double helicity asymmetry analysis.

Both analyses of direct photons and neutral pions are completely consistent: they are based on the same data set with identical energy calibration, the same suspicious or deficient EMCAL modules were excluded and identical photon identification cuts and the same Monte-Carlo code for the simulation of geometric acceptance and reconstruction efficiency were applied. This ensures that systematic uncertainties which arise in the analyses are identical for the  $\pi^0$  and inclusive photon measurement to a large extent and thus lead to the cancellation in the  $\gamma/\pi^0$  ratio mentioned above.

## 7.2 Data Selection and Correction

Before the direct-photon spectrum can be extracted from the measured data set a number of preparatory steps are required. The raw data recorded during the data taking period is formatted offline and condensed to save disk space and analysis time. The data set is filtered to meet certain quality criteria, suspicious events are excluded and the remaining data is allocated to particular analysis classes. Also suspicious or malfunctioning parts of the EMCAL are removed from the analysis. Details on the various analysis steps are given in the following.

## 7.2.1 Data Summary Table

The EvB (see Section 5.5.5) assembles data in the PHENIX *Raw Data Format* (PRDF). Data collected during a physics Run<sup>1</sup> is not stored in a single output file but split up into individual *runs*<sup>2</sup>. A single run is subdivided into several run segments. Each segment contains events usually collected over a time period of 30 minutes up to 2 hours. The EMCal raw data is saved in terms of ADC values and tower coordinates<sup>3</sup>. However, in PHENIX analyses are not conducted on the raw data but on so-called Data Summary Tables (DST's). DST's contain actual physical quantities which in case of the EMCal are hit position, cluster energy, time-of-flight etc. This information is reconstructed from the raw data during the offline DST production and stored for each run in individual DST files. Not all EMCal information stored in the DST is relevant to the presented analysis. Only the reconstruction and correction of the required information is briefly described in the following.

### Tower Energy Calibration

A crucial part in the reconstruction of EMCal data is the conversion of the raw tower information into calibrated energy and timing information. The energy calibration requires the application of calibration factors which reflect the energy equivalent of one ADC channel. These calibration factors emerge from the initial calibration of the system and are corrected for time dependent changes of the reference system and changes in the readout electronics. Moreover, additional corrections for which the reference system could not account for are applied. A more detailed description of the tower energy calibration can be found in [KB04a, Büs02]. Eventually, a list of calibrated towers is stored in the DST's.

### Energy Corrections

The calibration process described in the previous section does not take into account the non-linearity effects mentioned in Section 5.2. Light attenuation and leakage in the calorimeter lead to a non-linear reduction of the signal output of the detector. This is corrected to some extent during the offline production. A fine tuning of the energy scale, however, is done during the analysis of neutral pions. Since the measured mass of the neutral pion is directly connected to the energy scale, it can be used to tune the energy calibration. The procedure to correct the energy scale using the  $\pi^0$  peak is described in Section 7.2.5.

---

<sup>1</sup>The p + p Run in year 3 of PHENIX operation accumulated data over a time period of  $\sim 5$  weeks.

<sup>2</sup>The term *run* used in this context must not be confused with, e.g. p + p Run, which denotes the complete running period.

<sup>3</sup>Data from other subsystems are saved in a similar way.

## Cluster Information

A typical electromagnetic shower in the EMCal is spread over more than one tower. A group of adjacent towers that belong to the same shower is called a *cluster*. The efficient identification of clusters is also a vital part in the reconstruction process. The cluster algorithm is designed to find individual clusters and identify the local maximum, which is a tower with an energy above a threshold of 80 MeV and with the maximum amplitude in a  $3 \times 3$  region. If a cluster consists of more than one local maximum then the single cluster is split into separate clusters taking into account position and amplitude of the maxima. However, the cluster splitting routine is limited as it efficiently separates overlapping showers from  $\pi^0$  two-photon decays only up to  $p_T = 10 \text{ GeV}/c$  ( $15 \text{ GeV}/c$ ) in the PbSc (PbGl). The separation of two photons from  $\pi^0$  decays can be extended to higher  $p_T$  by a shower profile analysis. This is described in Section 7.3.3. For each identified cluster the first and second moment of the tower position distribution within the cluster is calculated. The first moment of the cluster which is identical to the center-of-gravity of the cluster is calculated as follows:

$$(\bar{x}, \bar{y}) = \left( \frac{\sum_i E_i x_i}{\sum_i E_i}, \frac{\sum_i E_i y_i}{\sum_i E_i} \right), \quad (7.3)$$

where the tower coordinates are given by  $(x_i, y_i)$  and the weight is the corresponding tower energy  $E_i$ . What is needed in the analysis is the impact position of the electromagnetic particle on the EMCal (also referred to as hit position). If the angle of incidence is not zero (i.e. the incidence is not perpendicular to the surface) the center-of gravity does not correspond to the impact position. Moreover, the center-of-gravity and the impact position is influenced by the finite size of the towers. Both dependencies<sup>4</sup> are taken into account during production and the impact position is calculated from the center-of-gravity. For each cluster the impact position and the tower with the highest energy is stored in the DST. The latter one is needed for the identification of dead or suspicious towers (see Section 7.2.6). The second moment of the cluster which is referred to as the dispersion  $D$  describes the lateral extension of the shower in the EMCal. In one dimension the dispersion is calculated by:

$$D = \frac{\sum_i E_i x_i^2}{\sum_i E_i} - \left( \frac{\sum_i E_i x_i}{\sum_i E_i} \right)^2. \quad (7.4)$$

Due to the finite size of the towers the calculated dispersion depends on the impact position within the tower [Sch94]. To account for this the dispersion is corrected with the first moment of the cluster (Equation 7.3):

$$D_{\text{corr}} = D - (|\bar{x}| - \bar{x}^2). \quad (7.5)$$

---

<sup>4</sup>The angular dependence and the influence of the finite tower size is determined using test beams and simulations.

The corrected dispersion (in  $x$ - and  $y$ -direction) of each cluster is stored in the DST only for the PbGl.

For the PbSc a different quantity is calculated during production and is used for photon identification. The distribution of the energy deposit in electromagnetic showers was studied using test beams and simulations yielding a parameterization of the average shape of electromagnetic clusters in the PbSc [Baz99]. The measured shower shape is compared to this parameterization and the deviation is expressed in terms of  $\chi^2$ , which is stored in the DST. More details are given in [KB04a]. How the dispersion and  $\chi^2$  are utilized for photon identification is described in Section 7.3.1.

### Micro- and NanoDST's

The complete set of DST's that represents the  $p + p$  data sample of Run III requires a large amount of disk space. However, not all quantities stored in the DST's are needed for physics analyses. This led to the introduction of *microDST*'s. This data format represents a reduced set of quantities to save disk space, e.g. in case of the PbSc all information on the calibrated towers has been removed. The microDST framework is designed to allow the implementation of so-called *afterburners*. The idea is that required corrections which were not known during offline production can be applied by the analyst himself prior to the actual analysis. In this process the existing set of information in the microDST is replaced by the corrected quantities. For instance a bug in the cluster splitting algorithm in the production code of the Run III  $p + p$  PbGl data necessitated the use of an afterburner. Fortunately the calibrated tower information had not been dropped in case of the PbGl and so a fixed cluster splitting algorithm and subsequent *reclustering* (cluster identification) could be applied [Büs06].

MicroDST's contain the information of all detectors in one file. In order to achieve further reduction of the file size the *nanoDST* framework was introduced. Since particular analyses do not require the same data sets in terms of detector subsystems and trigger information it is reasonable to divide the data into separate output files. Hence for each PRDF up to 27 individual nanoDST's are produced<sup>5</sup>. To further reduce the data size certain threshold cuts have been applied which were tested during the analysis of the microDST's, e.g. a minimum cluster energy cut. The direct-photon results presented in this thesis are based on the analysis of nanoDST's.

#### 7.2.2 Analyzed Data Sets

For the analysis of direct photons two data sets satisfying different trigger conditions were analyzed: *Minimum Bias* events and *Gamma3* events. In PHENIX, a minimum bias event

---

<sup>5</sup>For each PRDF one DST and one microDST is produced.

in p + p is defined by at least one hit in each of the BBC's. Minimum bias events represent the least biased events in the experiment: only the limited BBC acceptance and efficiency introduces a bias to the measured data sample (see Section 7.3.3). Because of the limited DAQ rate at which data could be processed in Run III a prescale factor was applied to reduce the amount of minimum bias data.

In order to enhance the measurement of highly energetic photons, a data set satisfying the Gamma3 high- $p_T$  trigger was recorded (see Section 5.5.2). Because the Gamma3 trigger requires a coincidence of the BBCLL1 and ERT\_4×4c trigger, the high- $p_T$  photon enriched sample is a subset of the minimum bias data set. However, since no prescale factor is applied for the Gamma3 triggered events (i.e. all events that fired the Gamma3 trigger are recorded) the number of underlying minimum bias events exceeds the number of actually stored minimum bias events (see Section 7.2.4). For the Gamma3 trigger not only the efficiency of the minimum bias trigger but also the efficiency of the ERT must be considered (see Section 7.3.2).

### 7.2.3 Run Selection

Before the actual analysis the data sets are subject to certain quality checks in order to remove runs that for instance exhibit suspicious deviations from the average behavior of the complete data sample. These quality checks involve e.g. the analysis of hit multiplicities and mean hit  $p_T$  in the EMCAL as a function of the run number. Moreover, runs which exhibit abnormal behavior in the BBC and ZDC response are removed from the data sample. In addition, runs in the ERT triggered data set that have too high or too low rejection factors<sup>6</sup> are removed from the sample [Bau03]. Furthermore, the Gamma3 data set contains only runs with the same FEM acceptance, i.e. only runs are considered in which the same set of FEM's was active during data taking. After the removal of all suspicious runs the list of *good* runs comprised runs from 88115-92446. A complete list of analyzed runs for the two data sets is given in Appendix B.1.

### 7.2.4 Event Selection

Only events with a z-vertex of  $\pm 30$  cm around the nominal vertex as measured by the BBC, ZDC and MVD<sup>7</sup> were analyzed. This minimizes the background of scattered particles and excludes regions that are shadowed by the pole tips of the central magnet.

---

<sup>6</sup>The rejection factor indicates how many minimum bias trigger counts are obtained per selected special trigger like the ERT.

<sup>7</sup>In the data production the z-vertex of the event is reconstructed separately using information from the BBC, ZDC and MVD. If for one subsystem the vertex could not be reconstructed the corresponding vertex information is missing in the DST. During the analysis it is always tried first to retrieve the z-vertex as measured by the BBC. If this fails the vertex given by the ZDC and then by the MVD is utilized.

For the analysis all events are subdivided into four analysis classes each referring to a particular set of trigger conditions. For two classes a special analysis requirement was applied in order to keep the ERT efficiency under control (FEM flag). This FEM condition is satisfied if the cluster with the maximal energy of the event lies on the FEM for which the Gamma3 trigger has fired (the FEM requirement is described in more detail in Section 7.3.2). The different analysis classes are summarized in Table 7.1. All minimum

Name	BBCLL1	Gamma3	FEM flag
MB1	yes	no	no
MB2	yes	yes	no
ERT1	yes	yes	yes
ERT2	no	yes	yes

**Table 7.1:** Analysis classes used in the analysis. The BBCLL1 denotes the minimum bias trigger and Gamma3 the ERT\_4×4c trigger in coincidence with the minimum bias trigger. The analysis condition *FEM flag* is described in more detail in Section 7.3.2.

bias events are contained in classes MB1 and MB2 and are extracted from the minimum bias data sample. Classes ERT1 and ERT2 comprise all high- $p_T$  events that are extracted from the Gamma3 triggered data sample. Only Gamma3 events that satisfy the FEM condition are analyzed. Table 7.2 gives the number of events  $N_{\text{evt}}$  in both data sets that were analyzed for the direct-photon analysis. The analysis classes MB1 and MB2 can be

Data Sample	Classes	$N_{\text{evt}}$
MB	MB1 + MB2	25.24 million
Gamma3	ERT1 + ERT2	45.12 million

**Table 7.2:** Number of analyzed events in the two data sets.

used to calculate the total rejection factor  $f_{\text{reject}}^{\text{gamma3}}$  of the Gamma3 trigger for the analyzed data set. As illustrated in Table 7.2 the sum of events in MB1 and MB2 gives all events in the minimum bias data set ( $N_{\text{evt}}^{\text{mb}}$ ). MB2 alone denotes those events in the minimum bias data set which also satisfy the Gamma3 trigger ( $N_{\text{evt}}^{\text{mb} \wedge \text{gamma3}}$ ). Hence  $f_{\text{reject}}^{\text{gamma3}}$  can be calculated as follows:

$$f_{\text{reject}}^{\text{gamma3}} = \frac{N_{\text{evt}}^{\text{mb}}}{N_{\text{evt}}^{\text{mb} \wedge \text{gamma3}}} = \frac{N_{\text{evt}}^{\text{MB1}} + N_{\text{evt}}^{\text{MB2}}}{N_{\text{evt}}^{\text{MB2}}} \quad (7.6)$$

The rejection factor allows the calculation of the number of underlying minimum bias events  $\tilde{N}_{\text{evt}}^{\text{mb}}$  for the Gamma3 data sample from the number of recorded Gamma3 events  $N_{\text{evt}}^{\text{gamma3}}$ :

$$\tilde{N}_{\text{evt}}^{\text{mb}} = f_{\text{reject}}^{\text{gamma3}} \cdot N_{\text{evt}}^{\text{gamma3}} \quad (7.7)$$

The total rejection factor of the Gamma3 trigger for the analyzed data set calculates to  $f_{\text{reject}}^{\text{gamma3}} \approx 109$  and therefore the number of measured Gamma3 events corresponds to  $\tilde{N}_{\text{evt}}^{\text{mb}} \approx 4.93$  billion events.

### 7.2.5 Energy Scale Correction

The energy scale of the calorimeter has a direct impact on the measured invariant mass of neutral pions. Because the energy resolution of the detector is limited the measured mass follows a Gaussian around a mean value. The position of this  $\pi^0$  peak can be used to tune the absolute energy scale of the EMCal. The nominal invariant mass of the  $\pi^0$  is  $m_{\pi^0} = 134.9766 \pm 0.0006 \text{ MeV}/c^2$  [Yao06]. However, due to the finite energy resolution of the EMCal and the fact that the  $\pi^0$   $p_{\text{T}}$ -distribution is a steeply falling spectrum, the measured mass of the  $\pi^0$  is expected to be shifted to higher masses. The position of the  $\pi^0$  mass peak can be predicted using a fast Monte-Carlo simulation that realistically models the energy response of the EMCal. The comparison of the simulated to the measured peak position provides the correction needed to shift the energy scale of the EMCal to the correct position. Since the same fast Monte-Carlo code is used to compute the reconstruction efficiency (see Section 7.3.2), only details that are relevant for the  $\pi^0$  peak calibration are described here. The limited energy resolution of the detector is implemented in the fast Monte-Carlo simulation by an energy smearing of the cluster energy. The energy is smeared randomly according to a Gauss distribution around the original cluster energy. The  $\sigma_E$  of the Gaussian is given by:

$$\frac{\sigma_E}{E} = \frac{C_1}{\sqrt{E/\text{GeV}}} \oplus C_2 , \quad (7.8)$$

where  $\oplus$  denotes a quadratic sum. The EMCal has a nominal energy resolution (see Table 5.1) which was determined in test beam studies [Aph03]. However, since the properties of the detector can alter with time it is desirable to determine the energy resolution specifically for each running period of the experiment. Therefore the energy dependent ( $C_1$ ) and constant ( $C_2$ ) parameters in Equation 7.8 are fixed by comparing the  $\pi^0$  peak width obtained in the simulation to the measured width as a function of  $p_{\text{T}}$  in the current data set. This is done for each EMCal sector individually. The parameters that are applied in the simulation are given in Table 7.3. Each sector is named in the analysis. Sectors of the east arm have the name Ex while sectors of the west arm are named Wx (with

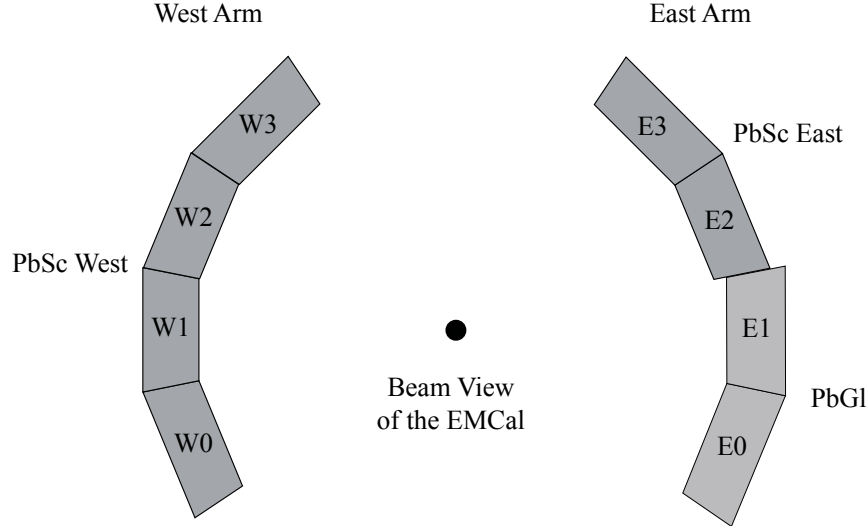


**Figure 7.1:** The figure illustrates the naming of the eight EMCAL sectors used in the analysis.

$x = 0, 1, 2, 3$ ). The naming of the eight EMCAL sectors used in the analysis is illustrated in Figure 7.1. Thereby the two sectors E0 and E1 represent the PbGl and the remaining six sectors the PbSc. The comparison of the measured  $\pi^0$  peak width to the tuned simulation for the combined PbGl and PbSc sectors, respectively, show excellent agreement over the entire  $p_T$  range (see Figure 7.2). As soon as the energy resolution of the EMCAL is correctly reproduced in the fast Monte-Carlo, the simulated  $\pi^0$  peak position gives access to the expected correct energy scale of the EMCAL. For the measurement of direct photons

Sector	$C_1$ [%]	$C_2$ [%]
E0	8.5	6.0
E1	8.5	5.8
E2	8.2	5.0
E3	8.2	6.0
W0	8.2	5.0
W1	8.2	5.0
W2	8.2	5.0
W3	8.2	5.7

**Table 7.3:** Energy smearing parameters used in the fast Monte-Carlo for all eight sectors of the EMCAL in Run III p + p.

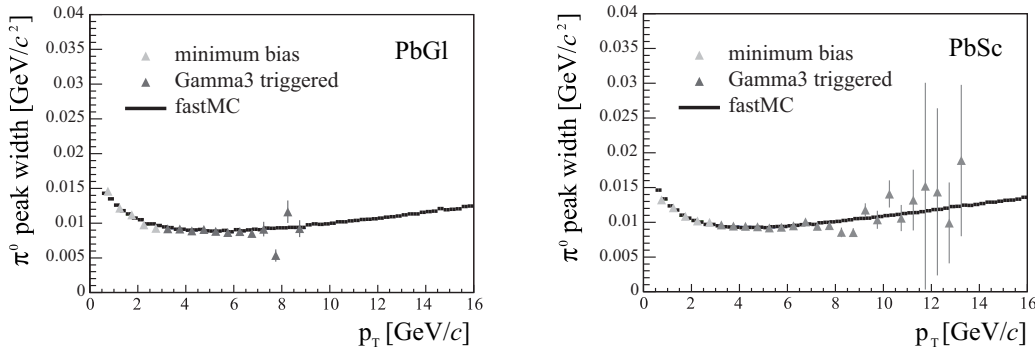


**Figure 7.2:** Comparison of the measured and the simulated  $\pi^0$  peak width using the smearing parameters given in Table 7.3 for the PbGl (left) and the PbSc (right), respectively.

it is desirable to correct the energy scale for single photons. Therefore, for the calibration study the energy asymmetry  $\alpha$  of  $\pi^0$  decays, which is defined as follows:

$$\alpha = \left| \frac{E_1 - E_2}{E_1 + E_2} \right|, \quad (7.9)$$

where  $E_1$  and  $E_2$  are the energy of the two decay photons, is restricted in the analysis as well as in the simulation to small values ( $\alpha < 0.2$ ). This restriction selects decay photons with similar energies  $E_1 \approx E_2$ . With this requirement the  $\pi^0$  peak position can be studied as a function of the mean photon energy  $E = \frac{E_1+E_2}{2}$  and hence allows to draw conclusions for the energy scale of single photons. The ratio of the simulated and the measured  $\pi^0$  peak position directly reflects the energy scale correction to be applied to the data. The empirical form of this linearity correction is given by:

$$\frac{E_{\text{corr}}}{E} = (a_1 + a_2 \cdot e^{a_3 \cdot E}), \quad (7.10)$$

where  $E$  is the cluster energy stored in the DST and  $E_{\text{corr}}$  is the cluster energy after the linearity correction. The correction parameters  $a_i$  ( $i=1, 2, 3$ ) are obtained for each sector of the EMCal individually. They are listed in Table 7.4. After correction of the energy scale the measured  $\pi^0$  peak position agrees well with the expected peak position obtained in the fast Monte-Carlo simulation. This is illustrated in Figure 7.3 for the PbGl and PbSc, respectively. It must be noted that neutral pions which decay in some distance to the collision vertex lead to a shift of the  $\pi^0$  mass peak to lower values because the opening angle of the  $\pi^0$  two-photon decay is not reconstructed correctly. Neutral pions that are produced in the collision decay directly at the vertex because of their very short life time of  $\tau = 8.4 \cdot 10^{-17}$  s [Yao06]. However, the strange meson  $K_s^0$ , which is also produced in ultra-relativistic p + p collision, has a mean life time of  $\tau = 8.953 \cdot 10^{-11}$  s [Yao06]. This life time is long enough for the  $K_s^0$  to decay considerably far away from the collision

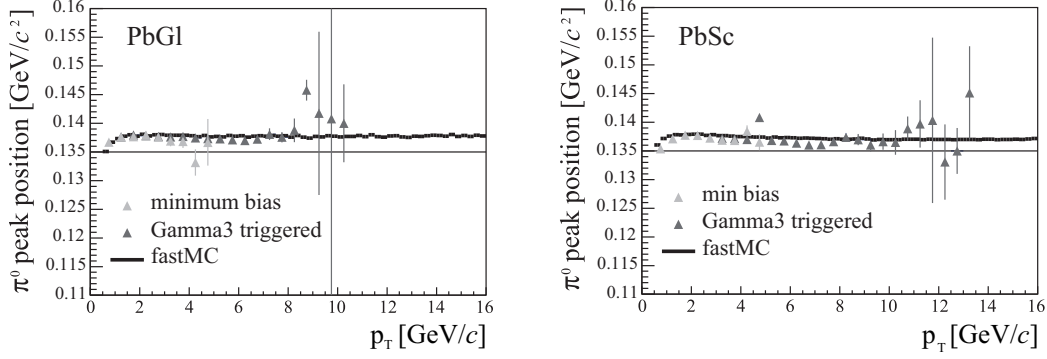


**Figure 7.3:** The comparison of the simulated  $\pi^0$  peak position and the measured  $\pi^0$  peak position after the energy scale correction for the PbGl (left) and the PbSc (right), respectively.

vertex.  $K_s^0$  have a decay channel into two neutral pions ( $K_s^0 \rightarrow \pi^0\pi^0$ ) with a branching ratio of approximately 31%. Hence a small fraction of  $\pi^0$ 's that is measured by the EMCAL do not come exactly from the vertex and shift the measured invariant  $\pi^0$  mass peak. In the fast Monte-Carlo  $K_s^0$  decays are not considered and therefore the energy scale is not reflected correctly by the simulation. In order to account for the impact of these so-called *non-vertex* decays on the energy scale a non-vertex correction is introduced in the fast Monte-Carlo. Because this correction is applied within the efficiency correction it is described in more detail in Section 7.3.2.

Another aspect which considerably influences the energy scale is the alignment of the EMCAL sectors. By analyzing electron tracks it was found that the PbGl and PbSc sectors might be misaligned to some extent compared to the originally surveyed position [Per05]. For instance the PbGl appears to be closer to the beam line while the PbSc appears to be

Sector	$a_1$	$a_2$	$a_3$
E0	1.015	-0.03	-0.727
E1	1.01	-0.037	-1.773
E2	0.996	0.07	-1.772
E3	1.	0.06	-1.217
W0	0.998	0.05	-1.03
W1	1.	0.04	-0.671
W2	0.98	0.05	-0.652
W3	1.	0.03	-0.893

**Table 7.4:** Parameters of the empirical energy scale correction based on the  $\pi^0$  peak position.

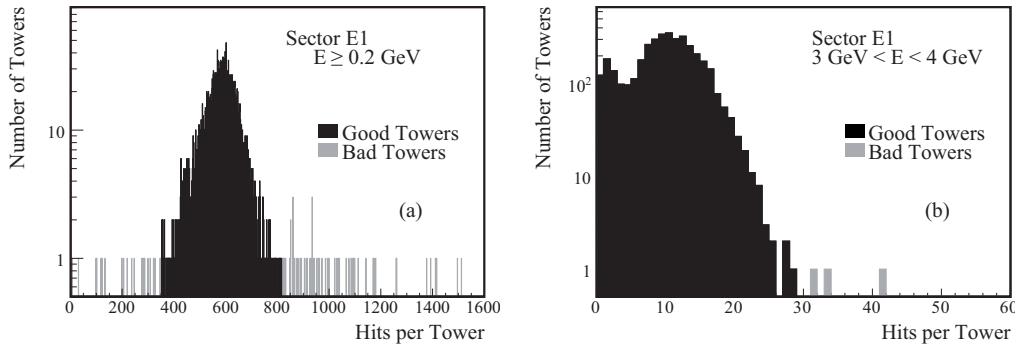


**Figure 7.4:** Hit distributions in sector E1. The distributions show the hit frequency per tower for two different energy ranges: (a)  $E \geq 0.2 \text{ GeV}$  and (b)  $3 \text{ GeV} < E < 4 \text{ GeV}$ . Black entries represent good towers while grey entries are excluded as bad towers.

further away. In addition, the analysis suggests a shift in beam direction and a tilt around some non-negligible angle. All this would lead to an incorrect reconstruction of the  $\pi^0$  mass and hence results in a miscalibration if the  $\pi^0$  peak position is used. However, the suggested corrections for the  $\pi^0$  and photon spectra were not applied, since the alignment analysis was not completely accepted within the PHENIX collaboration.

### 7.2.6 Identification of Bad Towers

In the measurement of direct photons it is crucial that all towers of the EMCAL that do not work properly are excluded from the analysis. Especially at high transverse momenta ( $p_T > 5 \text{ GeV}/c$ ) where only few direct photons are produced in the collision a malfunctioning tower could easily distort the measured spectrum. On the one hand towers that do not contribute to the energy signal at all are denoted as *dead*. A common reason for dead towers are faulty photomultipliers that produce no signal at all. Furthermore, PMT's that are known to behave in an unphysical way are switched off prior to data taking. A dead tower within a cluster reduces the measured cluster energy. Hence, clusters which deposit a significant amount of their energy in a dead tower must be removed from the analysis. On the other hand towers which are not dead but show a strong deviation from the mean behavior (in terms of energy spectra and hit distributions) are denoted as *bad*. A tower that fires unusually more often than others even without any physics input can be identified accidentally as a direct photon, thus affecting the measured spectrum, which would be especially problematic at high  $p_T$  as already mentioned.

During data production known dead/bad towers are marked in the DST's. However, since for the production only a limited number of quality checks are conducted, the list

of bad towers<sup>8</sup> in the DST is not complete. Therefore, prior to the actual analysis of direct photons the EMCAL data must be analyzed with respect to bad towers. This was done as part of the neutral pion analysis described in [Bat05b, Bat05a]. The basic idea of the method is to study the hit-per-tower distribution within each EMCAL sector separately and to look for individual towers which show significant deviations from the averaged parameters of the measured distribution. The hit position thereby is defined by the tower with the highest energy within the cluster. A typical hit distribution obtained with the PbGl sector E1 is shown in Figure 7.4. The mean and the root mean square (RMS) of the distribution are calculated and towers which show a significant deviation from the mean (the threshold depends on the RMS of the distribution) are excluded (grey entries in Figure 7.4). This procedure is done iteratively since towers which are far off from the mean increase the RMS and hence influence which towers are excluded. The analysis of bad towers is carried out for different cluster energy ranges. This improves the probability to find bad towers which only show up at higher energies (note the different scale of the  $x$ -axis in Figures 7.4(a) and (b)).

All identified bad towers together with the towers marked during data production are summarized in a *bad tower map*. The analysis is confined to hit distributions which are acquired during the complete  $p + p$  running period. Therefore a static bad tower map is obtained which excludes towers for the complete data set. Figure 7.5 shows the bad tower map of the PbGl sector E1 obtained with the Run III  $p + p$  data set. Note that some deficient FEM's were excluded completely from the analysis. They are visible as rectangular white areas in Figure 7.5. About 42% of all towers in sector E1 are excluded. Table 7.5 shows the percentages of excluded towers for all sectors of the EMCAL. The bad tower maps for all eight sectors are shown in Appendix C. In the photon analysis a cut on the position of the cluster is applied. If the tower with the largest energy within a cluster coincides with a bad tower in the bad tower map the cluster is removed from the analysis. All first order neighbors of a bad tower are also excluded from the analysis (i.e. the  $3 \times 3$  area surrounding a bad tower) since an electromagnetic cluster usually spreads over more than one tower. In addition all edge towers of a sector as well as the first order neighbors (only for the PbGl sectors to account for the finer granularity) are excluded from the analysis to minimize leakage effects (see Figure 7.5).

## 7.3 Measurement of Inclusive Photons

As described in Section 7.1 the basic idea of the cocktail method is to extract direct photons from the measured inclusive photon spectrum on a statistical basis (cf. Equation 7.2).

---

<sup>8</sup>In the following the term *bad towers* is used for both, dead and bad towers.

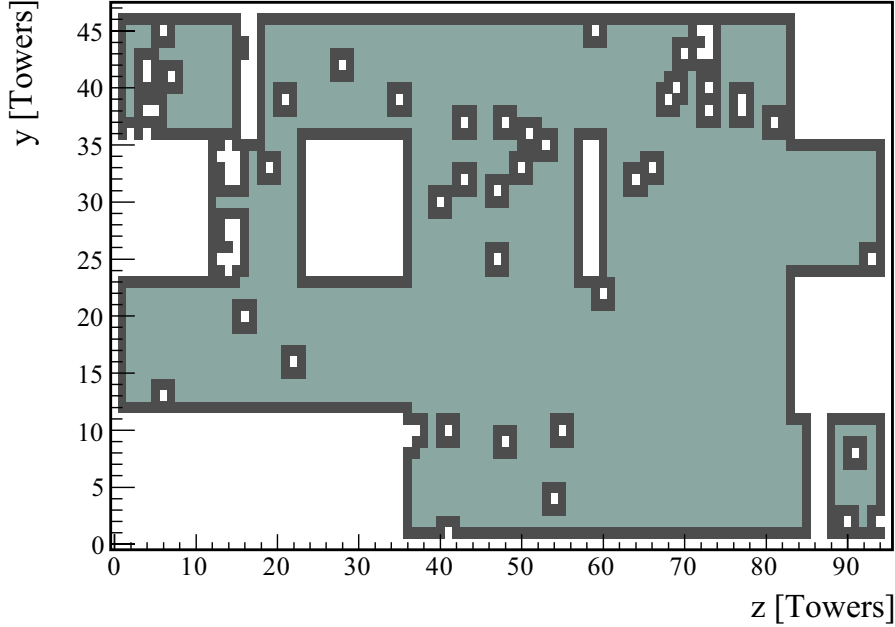


**Figure 7.5:** The map of bad towers for sector E1. White areas are bad towers and are excluded from the analysis as well as the first order neighbors which are marked as dark grey in the map. Large rectangular white areas are due to suspicious FEM's which were excluded from the analysis. The remaining light grey areas are accepted as “good” towers [Bat05b].

Hence the first step in the analysis is the determination of the inclusive photon spectrum utilizing the EMCal data. The inclusive photon spectrum comprises all photons that emerge from the collision region and all photons that are created in subsequent particle decays. All these photons produce clusters in the EMCal if they hit the detector. However, charged particles (e.g.  $\pi^\pm$ ,  $e^\pm$ ) as well as neutral particles (e.g. neutrons) also form clusters in the EMCal which can be misidentified as photons. A fraction of these non-photonic clusters can be removed from the data set by the application of so-called particle identification (PID) cuts (see Section 7.3.1). The remaining spectrum can be regarded as the photon-like cluster spectrum  $\Delta N_{\text{cluster}}$  as measured with the EMCal. In order to determine the inclusive photon yield from  $\Delta N_{\text{cluster}}$  a number of corrections are necessary as illustrated in the following equation:

$$\frac{d^2N_\gamma^{\text{incl}}}{dp_T dy} = \frac{(1 - X_{n\bar{n}}) \cdot (1 - X_{\text{ch}})}{\epsilon_\gamma \cdot a_\gamma \cdot (1 - p_{\text{conv}})} \cdot \frac{\Delta N_{\text{cluster}}}{\Delta p_T \Delta y}, \quad (7.11)$$

where  $X_{n\bar{n}}$  and  $X_{\text{ch}}$  are the fraction of neutral hadrons and charged particles, respectively, remaining in the sample of photon-like clusters even after the PID cuts. Since the EMCal does not have full azimuthal coverage an acceptance correction  $a_\gamma$  has to be applied. Furthermore, the efficiency of the photon reconstruction  $\epsilon_\gamma$  determined mainly by the limited

Sector	Bad Towers in %
E0	39.1
E1	42.1
E2	37.0
E3	45.6
W0	25.8
W1	23.8
W2	33.7
W3	47.3

**Table 7.5:** Fraction of towers which are excluded from the analysis for each EMCAL sector. The numbers include not only bad/dead towers but also edge towers and first order neighbors which are also not considered in the analysis (see text for details).

energy resolution but also by the efficiency of the PID cuts is taken into account. Finally, photons which convert into  $e^+e^-$  pairs are removed by the  $X_{ch}$  correction and hence must be added back to the sample. The probability of photon conversion is given by  $p_{conv}$ . All required corrections are described in more detail in Section 7.3.2. Equation 7.11 shows the differential form of the inclusive photon yield. It is determined per unit rapidity  $\Delta y$  and transverse momentum  $\Delta p_T$ . Multiplying Equation 7.11 by the factor  $\frac{1}{2\pi p_T N_{evt}}$  gives the fully corrected Lorentz invariant yield of inclusive photon production.

### 7.3.1 Photon-Like Clusters

#### Photon Identification

As described in Section 5.1 the lateral extension of the shower in the EMCAL can be used to enhance photon identification and remove hadronic showers from the data sample. Different cuts on the shower shape are applied in the photon analysis for the PbGl and PbSc data, respectively.

For the PbGl the extension in  $x$ - and  $y$ -direction in terms of the dispersion is calculated during data production and stored in the DST for each cluster (see Section 7.2.1). Electromagnetic showers spread over a smaller area than hadronic showers. Hence an upper limit on the dispersion can be utilized to exclude hadronic clusters. An optimized threshold was derived in [KB00] via simulations:

$$D_{cut}(\theta) = 0.27 - 0.145 \cdot \theta + 0.00218 \cdot \theta^2. \quad (7.12)$$

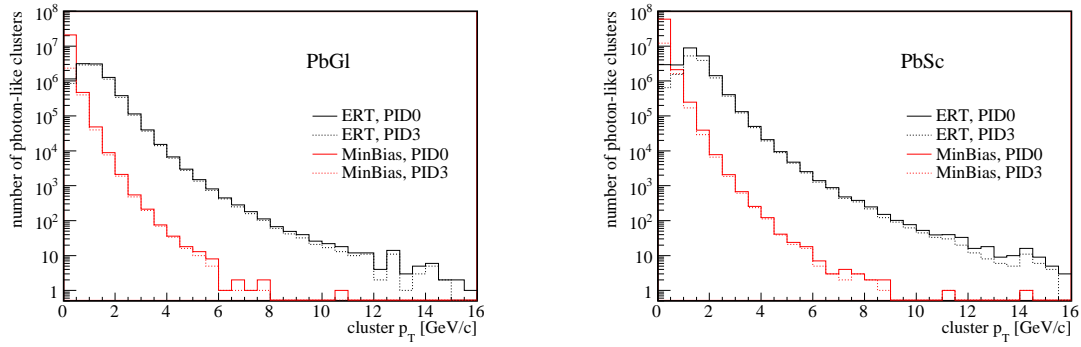


**Figure 7.6:** Spectra of photon-like clusters measured in PbGl and PbSc with and without PID cuts for the two different data samples.

The cut depends on the angle of incidence  $\theta$  (given in degrees in Eq. 7.12) of the incoming particle (with increasing incident angle the shower spreads over an increasing number of towers). In the analysis the maximum of the dispersion in  $x$ - and  $y$ -direction is compared to the threshold.

Clusters in the PbSc are characterized by a  $\chi^2$  which indicates the probability for the cluster to be an electromagnetic shower (see Section 7.2.1). Clusters with  $\chi^2 > 3$  are removed from the data sample in the photon analysis. More information on the  $\chi^2$  cut can be found in [KB04a].

Besides the cut on the shower shape of the cluster which is the main tool for the identification of photon-like clusters a loose cut on the cluster energy is applied ( $E_{\text{cluster}} < 200$  MeV). This threshold mainly removes noisy channels but does not notably improve photon identification.

## Spectra

As mentioned above all hits in the EMCAL that are not removed by the PID cuts form the so-called photon-like cluster spectrum. The  $p_T$  spectra are divided into  $p_T$  bins in which the corresponding number of clusters are counted. Figure 7.6 shows the measured cluster spectra derived from the minimum bias and the high- $p_T$  filtered data sample for the PbGl and PbSc, respectively. The ERT spectrum extends to far higher transverse momenta. Furthermore, the effect of the PID cuts on the spectra is shown: PID0 denotes no cut (solid line) while PID3 represents all applied cuts, namely the cut on the cluster energy and on the shape of the cluster. The logarithmic scale somewhat hides the considerable difference in the corresponding spectra. However, the explicit numbers of photon-like clusters per  $p_T$  bin (see Tables in Appendix D) reveal the effect of the PID cuts. The

photon-like cluster spectra have to be corrected for several effects. These corrections are described in detail in the following section.

### 7.3.2 Corrections of the Photon-Like Cluster Spectrum

The fully corrected inclusive photon spectrum is determined from the photon-like cluster spectrum as described by Equation 7.11. The raw spectrum is still contaminated with clusters produced by charged hadrons and electrons as well as neutral particles such as neutrons and antineutrons. Moreover, highly energetic photons which traverse matter have a certain probability to suffer pair production. All this directly influences the cluster spectrum and must be taken into account and corrected. The invariant yield of inclusive photons is calculated per unit rapidity at mid-rapidity and for full azimuth. However, the geometric acceptance of the EMCAL is limited at mid-rapidity due to the incomplete azimuthal coverage (see Section 5) of the central arms and because of the large number of bad towers that are excluded from the analysis. Therefore, the number of measured clusters must be extrapolated via a geometric acceptance correction. The limited energy resolution of the EMCAL smears the measured energy. The effect is simulated and corrected with the so-called reconstruction efficiency<sup>9</sup>. The finite position resolution, the efficiency of the PID cuts and the non-vertex correction (see Section 7.2.5) are also taken into account in the reconstruction efficiency. Finally, a correction of the limited ERT efficiency must be applied to the high- $p_T$  filtered data sample in order to account for photon losses at the trigger threshold. All these corrections are described thoroughly in the following.

#### Geometric Acceptance

The acceptance correction as well as the reconstruction efficiency described in the next section is determined with a fast Monte-Carlo simulation. The same code was used in the neutral pion analysis of the same data set [Bat05b, Bat05a] and was originally developed by [Rey03a]. It simulates the geometry and the detector properties as accurately as possible.

The simulation of the geometric acceptance of the EMCAL for single photons in a certain phase space is rather simple. It is given by the number of particles that hit the active area of the detector compared to the number of photons emitted in the considered phase space. For the photon analysis the phase space is given by the rapidity interval of  $-0.45 < y < 0.45$  and complete azimuthal coverage  $\Delta\phi = 2\pi$ . In the simulation photons

---

<sup>9</sup>The name *reconstruction efficiency* has its origin in the  $\pi^0$  analysis. The finite energy resolution affects the reconstruction of the neutral pion via the two-photon decay [Bat05b].

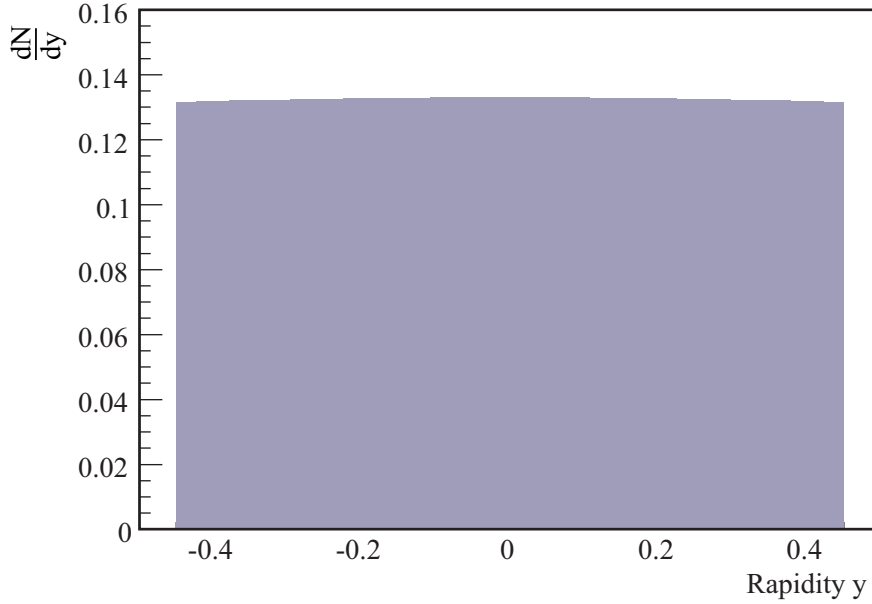


**Figure 7.7:** Rapidity distribution used in the fast Monte-Carlo to simulate single photons in the rapidity range  $-0.45 < y < 0.45$ . The shape follows a Gaussian around zero with  $\sigma = 3.0$  and therefore appears to be almost flat.

are created randomly within this phase space. The transverse momentum  $p_T$  of the simulated photons are chosen to be uniformly distributed ( $0.5 < p_T < 40 \text{ GeV}/c$ ) to have the same statistics over the entire  $p_T$  range. The  $z$ -vertex is assumed to be uniformly distributed and is restricted to  $|z_{\text{vertex}}| < 30 \text{ cm}$  as this cut is applied in the analysis of the real data. While the azimuthal direction is a flat distribution over  $2\pi$  the rapidity distribution is chosen to have a Gaussian shape which is illustrated in Figure 7.7. The Gaussian is chosen to be distributed around zero with a  $\sigma = 3.0$ , which makes the distribution rather flat in the rapidity range  $-0.45 < y < 0.45$ . The geometric acceptance is calculated by dividing the  $p_T$  distribution of photons that hit the EMCal by the  $p_T$  distribution of generated photons. The result is shown in Figure 7.8. Since only the active part of the EMCal contributes to the geometric acceptance the same map of bad towers which is used in the analysis of the real data (see Section 7.2.6) is included in the fast Monte-Carlo. The simulated geometric acceptance reveals a drop with increasing transverse momentum. This is due to the fact that the depth of an electromagnetic shower depends on the energy of the incident particle. Therefore, for a particle that hits the detector surface with a large angle of incidence the impact position and the tower of maximum energy in the cluster differs from each other. This leads to leakage effects at the edges of the EMCal. The probability for a photon to leak out of the detector increases with increasing energy. In the fast Monte-Carlo the relation between the maximum tower position and the angle of

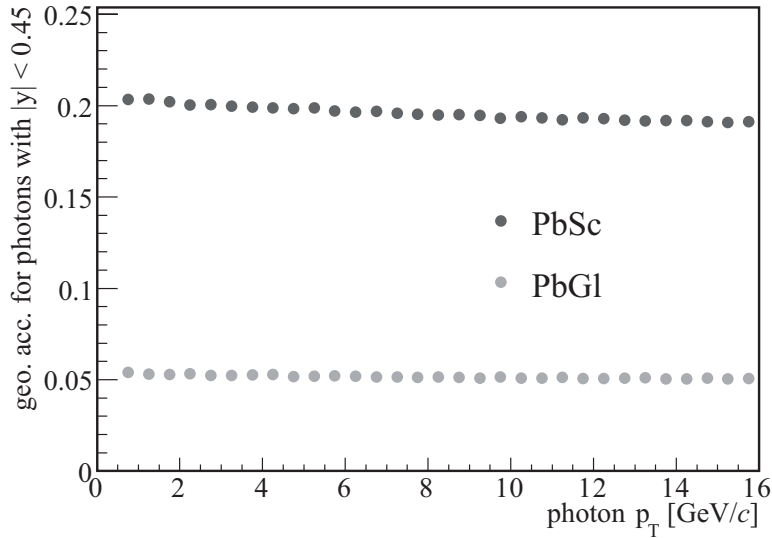


**Figure 7.8:** The geometric acceptance of the PbGl and PbSc in the Run III running period studied with a fast Monte-Carlo simulation. A slight decrease in the acceptance with increasing transverse momentum is observed which is caused by the energy dependence of the shower depth (see text for further details).

incidence is parameterized (for a photon in the Monte-Carlo only impact position and angle of incidence are simulated) and the observed drop in Figure 7.8 indicates the expected leakage effect.

### Reconstruction Efficiency

The measurement of a particle spectrum is modified by detector specific effects and the application of cuts in the analysis. Therefore the measured spectrum of inclusive photons  $f(p_T)_{\text{measured}}$  deviates from the true input spectrum  $f(p_T)_{\text{true}}$ . The reconstruction efficiency  $\varepsilon_{\text{reco}}$  is defined as the ratio of the two:

$$\varepsilon_{\text{reco}}(p_T) = \frac{f(p_T)_{\text{measured}}}{f(p_T)_{\text{true}}} \quad (7.13)$$

The main factor which makes the efficiency  $\varepsilon_{\text{reco}}$  deviate from unity is the limited energy resolution in combination with the steeply falling  $p_T$  distribution. For a flat  $p_T$  distribution the same number of particles are shifted out of a certain bin as are shifted into it. Therefore the effect of the finite energy resolution on the measured number of particles in a certain  $p_T$  bin would cancel by itself. However, in case of a steeply falling spectrum the shift from lower to higher  $p_T$  bins is always considerably larger than vice versa. Hence the spectrum is shifted towards higher transverse momenta which leads to an efficiency

Parameter	PbGl	PbSc
$c_0$ [mm]	28.0	20.0
$c_1$ [mm]	6.73	8.35
$c_2$ [mm]	1.61	0.15

**Table 7.6:** Parameters describing the position resolution in PbGl and PbSc, respectively. The parameter  $c_0$  corresponds to the radiation length in the detector material (see Table 5.1).

$\epsilon_{\text{reco}} > 1$  for most  $p_T$  bins. As was discussed in Section 7.2.5 the limited energy resolution of the detector is incorporated in the simulation by a smearing of the cluster energy. The parameters are fixed with the help of the  $\pi^0$  peak width (see Table 7.3).

Another detector effect that influences the measured spectrum is the finite position resolution of the detector. The hit position is required for the reconstruction of the particle  $p_T$  and therefore any shift of the hit position also shifts the  $p_T$  distribution. Like the cluster energy the impact position of the particle is smeared according to a Gaussian in the fast Monte-Carlo. The sigma of the Gaussian distribution comprises two components:  $\sigma_{xy}^{\theta=0^\circ}$  which describes the resolution for zero incident angle  $\theta$  and  $\sigma_{xy}^\theta$  which describes the angular dependence. The two components are given by:

$$\begin{aligned}\sigma_{xy}^{\theta=0^\circ} &= \frac{c_1}{\sqrt{E/\text{GeV}}} \oplus c_2, \\ \sigma_{xy}^\theta &= c_0 \cdot \sin(\theta).\end{aligned}\quad (7.14)$$

The overall sigma describing the total angular dependent position resolution is given by the quadratic sum of the two components:

$$\sigma_{xy}(\theta) = \sigma_{xy}^{\theta=0^\circ} \oplus \sigma_{xy}^\theta. \quad (7.15)$$

$\sigma_{xy}(\theta)$  is given in mm. The parameters are specified in Table 7.6 and are based on the nominal position resolution given in [Aph03]. The parameters  $c_1$  and  $c_2$  for the PbSc are taken from the PbGl. In order to account for the different granularity in the two EMCAL subsystems the PbSc position resolution is scaled by the ratio of the tower dimensions in PbGl and PbSc. The parameter  $c_0$  corresponds to the radiation length in the two subsystems.

As mentioned above the reconstruction efficiency (also referred to as efficiency correction) corrects not only for detector specific effects but also for cuts applied in the analysis. The shower shape cut (see Section 7.3.1) has a limited efficiency (i.e. also photons are removed by the cut) which must be taken into account in the analysis. In the fast Monte-Carlo only the tower which is hit by the particle is known, i.e. no cluster is simulated. This has the drawback that the shower shape cut cannot be applied in the simulation

in the same way as in the analysis of the real data. Instead the efficiency of the shower shape cut is realized in the fast Monte-Carlo as a survival probability  $p_{\text{survival}}^\gamma$  of single photons. The survival probability  $p_{\text{survival}}^\gamma$  can be determined from the  $\pi^0$  raw yields obtained from the same data set [Bat02]. The procedure is the following: the raw  $\pi^0$  yield is determined with and without shower shape cut for each sector individually. The constant ratio of the two spectra gives the probability  $p_{\text{survival}}^{\pi^0}$  to lose a  $\pi^0$  due to the shower shape cut as a function of  $\pi^0$  energy. By applying a strong asymmetry cut ( $\alpha < 0.2$ ) the ratio of the  $\pi^0$  yields can be plotted as a function of the mean photon energy  $E = \frac{E_1+E_2}{2}$ . The advantage of this method is that the reconstruction of neutral pions via the invariant mass analysis ensures that only photons constitute the spectrum. Thus together with the strong asymmetry cut the survival probability for photons can be simply derived as follows:

$$p_{\text{survival}}^\gamma = \sqrt{p_{\text{survival}}^{\pi^0}}. \quad (7.16)$$

$p_{\text{survival}}^\gamma$  is derived for each sector and the average is calculated for the two EMCAL subsystems. The survival probability for single photons due to the shower shape cut is  $(98 \pm 2)\%$  for the PbGl and  $(98^{+2}_{-4})\%$  for the PbSc, respectively.

The energy PID cut is reproduced in the fast Monte-Carlo by applying a cut on the smeared energy of the simulated particle. However, since the energy threshold is very low the PID cut has only a minor influence on the reconstruction efficiency.

As was mentioned in Section 7.2.5 a non-vertex correction is required in order to take into account measured neutral pions which did not decay at the vertex. These non-vertex decays shift the measured  $\pi^0$  peak and hence influence the energy scale which is determined using the measured  $\pi^0$  peak position. The reconstructed peak position of neutral pions which do not come from the vertex is at a lower invariant mass. Since the linearity correction of the energy scale is determined by the ratio of the simulated (which does not include any non-vertex decays) to the measured  $\pi^0$  peak position the corrected scale is shifted towards higher energies. It was shown in simulation studies that this shift is described by an offset of  $0.7\% \pm 1.0\%$  independent of the energy [Baz03c]. In order to correct for this the same offset is introduced in the calculation of the efficiency correction in the fast Monte-Carlo, i.e. the particle energy is shifted by  $+0.7\%$ . By applying the efficiency correction to the measured spectrum the effect of non-vertex  $\pi^0$ 's is hence corrected.

Equation 7.13 implies the knowledge of the true inclusive photon spectrum  $f(p_T)_{\text{true}}$ . However, since the efficiency correction is needed to determine the true spectrum, the latter is in principle not known at the beginning of the analysis. Therefore, the efficiency correction must be determined in an iterative way. In the first iteration an assumed spectrum, e.g. based on the raw cluster spectrum or some earlier measured spectrum, is used as input to the simulation. This approach results in a first approximation of the efficiency

correction which is applied to the raw cluster spectrum, providing a new input distribution. This process is repeated until convergence of the reconstruction efficiency is achieved. In the simulation a parameterization of the measured inclusive photon yield  $dN/dp_T$  is used. This parameterization is composed of a low and a high- $p_T$  part to account for the different physics mechanisms which are responsible for particle production in the different  $p_T$  regions (see Section 2). The shape of the distribution at low  $p_T$  is well described by a Hagedorn function:

$$\frac{dN^{\text{Hag}}}{dp_T} = \frac{A}{(p_0 + p_T)^m}. \quad (7.17)$$

At high  $p_T$  the distribution follows a power law:

$$\frac{dN^{\text{Power}}}{dp_T} = \frac{B}{p_T^n}. \quad (7.18)$$

$A$ ,  $B$ ,  $p_0$  and  $n$  are free parameters of the parameterizations. In order to ensure a smooth transition between the two regions a Woods-Saxon type function (with free parameters  $a_1$  and  $a_2$ ) is used as a weight for both contributions:

$$\begin{aligned} \frac{dN}{dp_T} &= a_{WS} \cdot \frac{dN^{\text{Hag}}}{dp_T} + (1 - a_{WS}) \cdot \frac{dN^{\text{Power}}}{dp_T}, \\ \text{with } a_{WS} &= \frac{1}{1 + \exp\left(\frac{p_T - a_1}{a_2}\right)}. \end{aligned} \quad (7.19)$$

The fit of the two individual parameterizations to the data is shown in Figure 7.9(a). The data points represent the fully corrected inclusive photon yield measured in the PbGl which was used to extract the direct-photon signal. The Hagedorn and the power law were fitted in the region below and above  $p_T = 6 \text{ GeV}/c$ , respectively but plotted in the entire  $p_T$  range. In order to point out deviations between the fitted parameterization and the data points the relative difference is illustrated in Figure 7.9(b). The open circles show that the Hagedorn fails to describe the data above  $p_T \approx 5.5 \text{ GeV}/c$ , while the power law (closed circles) do not describe the data well below  $p_T \approx 5.5 \text{ GeV}/c$ . The transition between the two functions is smoothed by the Woods-Saxon type function that is shown in Figure 7.9(b) (in arbitrary units). It must be noted here that the measured spectrum of inclusive photons is distorted by the so-called *cluster merging effect*. This must be taken into account in the determination of the fit parameters which are needed to describe  $f(p_T)_{\text{true}}$ . A detailed description of the cluster merging effect and its correction is given in Section 7.3.3.

The input spectrum is simulated employing the same assumptions for single photons as for the acceptance correction, e.g.  $|z_{\text{vertex}}| < 30 \text{ cm}$ , flat  $p_T$  distribution etc. However, because the shape of the  $p_T$ -distribution has a major impact on the efficiency correction

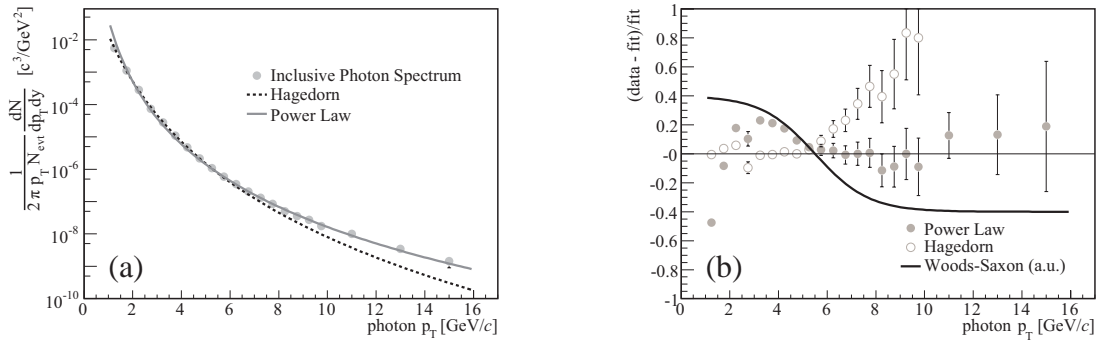


**Figure 7.9:** (a) Fully corrected inclusive photon yield measured in the PbGl (grey circles) and the fit of the two parameterizations to the data. The Hagedorn is fitted in the range  $1 \text{ GeV}/c < p_T < 6 \text{ GeV}/c$  and the power law in the range  $6 \text{ GeV}/c < p_T < 16 \text{ GeV}/c$ . (b) The relative difference of the fits to the data. The open and closed circles show the good agreement of the Hagedorn function and the power law with the data at low respectively high  $p_T$ . The weight function to ensure smooth transition between the two regions is shown as a black line (Woods-Saxon type function) in arbitrary units.

each particle is weighted according to its  $p_T$  at creation. This procedure has the advantage that the same accuracy is achieved over the entire  $p_T$  range. The efficiency correction is then determined simply by using Equation 7.13, i.e. by dividing the  $p_T$  distribution of accepted and smeared photons by the spectrum of input particles that hit the detector. Figure 7.10 shows the reconstruction efficiency after the final iteration for the PbGl and PbSc, respectively. The efficiency is determined with and without particle identification cuts. The application of the energy and shower shape cut (PID3) leads to a reduction of the efficiency since they remove real photons from the data sample. The difference between PID0 and PID3 is primarily caused by the limited efficiency of the shower shape cut (the cut removes about 2% of real photons). It should be noted at this point that the term “reconstruction efficiency” suggests a correction less than unity. However, since for single photons the reconstruction efficiency primarily corrects for the energy smearing of the detector (which shifts particles from low to high  $p_T$ ) the corrections rise above unity and must be considered as a correction rather than an efficiency (hence the term “efficiency correction”).

### Charged Particle Background

As was mentioned above even after the shower shape cut a fraction of charged hadrons (primarily charged pions) remains in the spectrum of photon-like clusters. Also electrons and positrons which emerge from vector meson decays or pair production ( $\gamma \rightarrow e^+e^-$ ) distort the inclusive photon spectrum. In order to identify these charged hits and remove

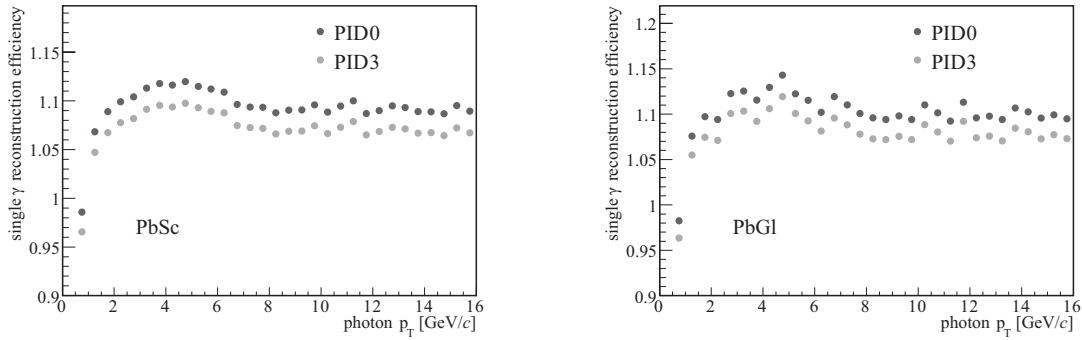


**Figure 7.10:** The reconstruction efficiency of single photons simulated for the PbSc and PbGl with (PID3) and without (PID0) particle identification cuts. The difference between PID3 and PID0 arises mainly from the shower shape cut which has a limited efficiency of 98% and therefore removes real photons from the data sample. The reconstruction efficiency for single photons is above unity and thus must be considered as a correction rather than an efficiency, which primarily corrects the effect of the limited energy resolution together with the steeply falling spectrum.

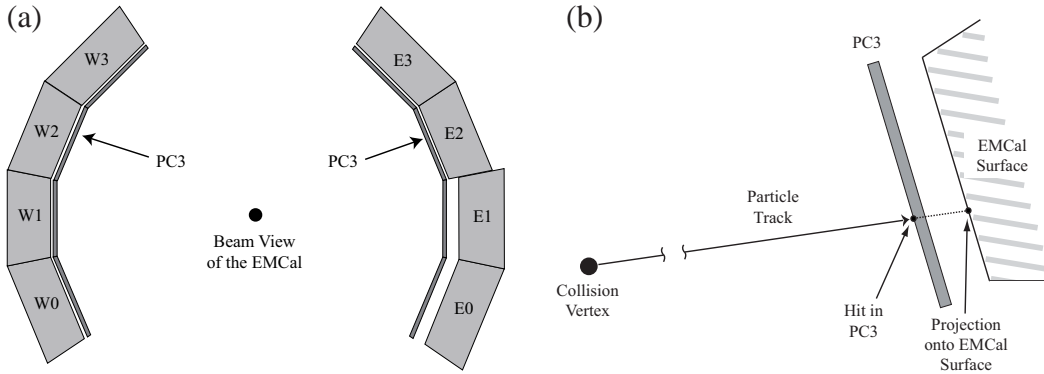


**Figure 7.11:** (a) The PC3 is located directly in front of the EMCAL and therefore is ideally suited as a charged particle veto (CPV) detector for charged hits in the EMCAL. (b) Schematic illustration of the projection of the charged PC3 hit onto the EMCAL surface.

them from the EMCAL data one of the pad chambers is utilized. As described in Section 4.2.3 the pad chambers are part of the charged particle tracking system in PHENIX. The PC3 has the advantage that it is positioned directly in front of the EMCAL (see Figure 7.11(a)). Charged particles create a signal in the PC3 (in the following also referred to as a charged hit) before they create a cluster in the EMCAL. By correlating charged hits with clusters in the EMCAL the fraction of charged particles in the photon-like cluster

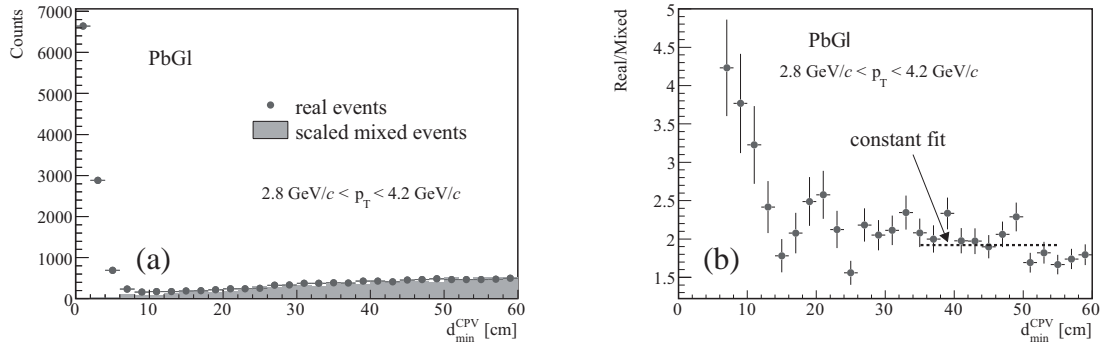


**Figure 7.12:** (a) Distribution of the minimum distance  $d_{\min}^{\text{CPV}}$  between PC3 hit projection and EMCAL cluster for real and mixed events in the PbGl for the range  $2.8 \text{ GeV}/c < p_T < 4.2 \text{ GeV}/c$ . The mixed distribution results from pairing EMCAL clusters from one event to PC3 hits in another event and is scaled to the real distribution. (b) The ratio of the real and mixed distribution. The constant fit at large distances determines the scaling factor for the mixed distribution.

spectrum can be determined. A correlation between EMCAL clusters and charged hits in the PC3 is established by defining a veto radius. All EMCAL clusters that have a charged hit projection within the chosen veto radius are removed from the sample. However, the background subtraction is not done hit-by-hit but on a statistical basis. The method was already applied in previous photon analyses, e.g. in the Au + Au direct-photon analysis using PHENIX Run II data [KB04b]. The approach is the following: Each charged particle hit in the PC3 is projected onto the EMCAL surface by using the straight line from the vertex to the charged hit. This is illustrated in Figure 7.11(b). In a next step for each hit in the EMCAL the distance  $d_{\min}^{\text{CPV}}$  to the nearest charged hit projection in the same event is calculated. This is done for each EMCAL hit in the photon-like cluster spectrum for different  $p_T$  ranges and for the minimum bias and ERT filtered data set separately. A typical distribution of  $d_{\min}^{\text{CPV}}$  is shown in Figure 7.12(a) for  $2.8 \text{ GeV}/c < p_T < 4.2 \text{ GeV}/c$  for hits in the PbGl. EMCAL clusters can be correlated to charged hits if  $d_{\min}^{\text{CPV}}$  is below some threshold (the veto radius). Hence all charged hits lie in the "peak" visible at small values of  $d_{\min}^{\text{CPV}}$  in Figure 7.12(a). The threshold depends on the considered  $p_T$  range and must be adjusted to the data.

Although the multiplicity in  $p + p$  collisions is small, uncorrelated EMCAL clusters and charged hit projections randomly yield minimum distances below the chosen threshold and thus would misleadingly contribute to the charged background. This so-called *combinatorial background* can be determined using the so-called *mixed event* technique (hence the distinction between *real* and *mixed events* in Figure 7.12(a)). In this method the  $d_{\min}^{\text{CPV}}$  distribution for uncorrelated pairs is determined by mixing EMCAL clusters and

charged hits from different events thereby ensuring that all formed pairs are completely uncorrelated. Because the statistics of real and mixed pairs are different, the background of mixed pairs must be scaled to the distribution of real pairs. This is done using the ratio of the  $d_{\min}^{\text{CPV}}$  distribution of real and mixed events. The constant fit to the ratio at large distances as shown in Figure 7.12(b) is used as the scaling factor. The combinatorial background in the distribution of real events is well reproduced by this technique (see Figure 7.12(a)). At large transverse momenta the statistical fluctuations become larger and a reliable constant fit to the ratio is not possible. In this case the integrals of the real and the scaled mixed distribution are calculated in a range at large  $d_{\min}^{\text{CPV}}$  and the scaling factor is determined as the ratio of the two integrals.

After the subtraction of the combinatorial background from the distribution of real events the integral under the peak up to the chosen veto radius (the veto radius decreases with  $p_T$  and ranges from 30 cm at low to 6 cm and high  $p_T$ ) represents the number of EMCAL hits that can be correlated with a charged hit in the PC3 ( $N_{\text{cluster}}^{\text{charged}}$ ). This number is compared to the total number of EMCAL hits in the same  $p_T$  range ( $N_{\text{cluster}}^{\text{total}}$ ) and yields the fraction of charged hits  $X_{\text{ch}}$  in this  $p_T$  bin:

$$X_{\text{ch}} = \frac{1}{\epsilon_{\text{PC3}}} \cdot \frac{N_{\text{cluster}}^{\text{charged}}}{N_{\text{cluster}}^{\text{total}}}. \quad (7.20)$$

Equation 7.20 takes into account the limited efficiency  $\epsilon_{\text{PC3}}$  of the PC3. On the one hand the PC3 does not cover the complete EMCAL acceptance. On the other hand the PC3 has areas which were inactive during the data taking period and therefore did not contribute to the charged signal. Either aspects worsen the efficiency of the PC3 within the EMCAL acceptance. Strictly speaking the PC3 efficiency can be regarded as a geometric acceptance matched to the EMCAL acceptance.<sup>10</sup> Therefore the PC3 efficiency was estimated by projecting the PC3 acceptance onto the EMCAL surface and by identifying areas in the PC3 which show unusual low activity compared to the average. The procedure is the following: so-called *veto maps* for each EMCAL sector were filled with EMCAL hits that have an associated charged hit in the PC3, i.e. the EMCAL hit has a PC3 hit projection within a radius of 4 cm. This very tight condition was chosen because a single pad in the PC3 covers approximately an area that corresponds to a circle with radius of 4 cm. Figure 7.13 shows the veto map (open boxes) together with the EMCAL hit map (colored boxes) for the PbGl sector E0. White areas indicate bad towers in the EMCAL which are not considered in the analysis (see Section 7.2.6). By comparing the EMCAL hit map and the veto map there are already some areas in the active part of the EMCAL visible in which no or only a few corresponding charged hits can be found. This becomes more obvious in the ratio of the veto and the EMCAL hit map, which is also shown in Figure 7.13. Blue

<sup>10</sup>The intrinsic efficiency of the PC3 was assumed to be 100%.

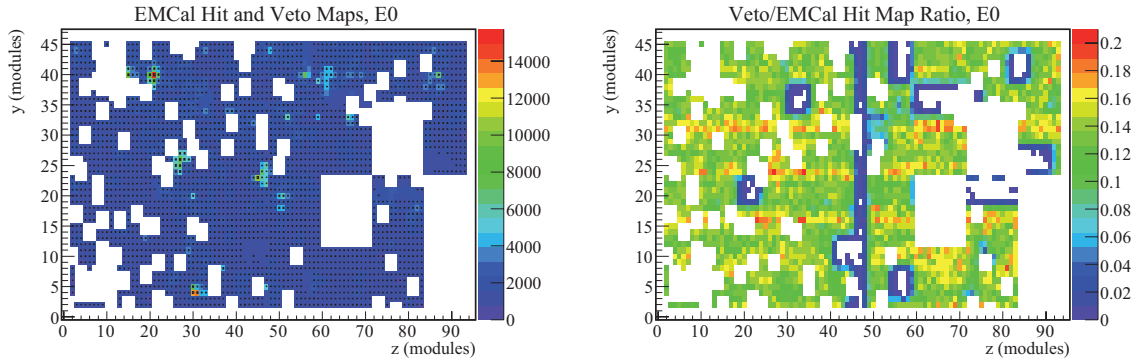


**Figure 7.13:** EMCal hit map (colored boxes) and veto map (open boxes) for the PbGl sector E0 (left figure). The size of the open boxes determine the number of EMCal hits that have a corresponding charged hit projection within a radius of 4 cm. White areas are bad modules which are excluded from the analysis. The figure on the right shows the ratio of the veto and the EMCal hit map. Blue areas indicate areas in the PC3 coverage which show only little activity and can therefore be regarded as inactive. The blue region in the middle of the EMCal sector is caused by a gap in the PC3 due to its mechanical structure.

areas in the ratio indicate areas in the EMCal which have significantly less corresponding charged hits in the PC3. There is a blue region along the  $y$ -direction at  $z = 46 \pm 1$  modules which can be found for all EMCal sectors. This region can be ascribed to a gap in the PC3 coverage which is due to the mechanical structure of the pad chamber. A cut on the ratio was introduced which defined active and inactive regions in the PC3. The threshold was chosen in such a way that the physical gap in the PC3 coverage in the middle of each EMCal sector was removed by the cut, i.e. was defined as inactive. A constant fraction of 0.09 was found to be suitable for all sectors. Figure 7.14 shows the area of the PC3 which is defined as inactive in the acceptance of the EMCal sector E0 by the cut on the ratio. The ratio of the EMCal area in which the PC3 is defined as inactive and the full active EMCal acceptance gives the PC3 efficiency. The efficiency is determined for each EMCal sector separately. Also a very small run dependence of the PC3 efficiency was found. In order to account for this, the data sets were divided into two segments (one covering the first and the other one covering the second half of Run III) and the efficiency was estimated for both segments separately. The average of both segments was then calculated by weighting with the number of events in the corresponding segment. The average PC3 efficiency for the PbGl and the PbSc was then calculated by weighting with the number of active towers in the corresponding sectors. Table 7.7 shows the estimated efficiencies of the PC3 in the acceptance of the PbGl and PbSc, respectively.

The PC3 efficiency was also estimated following a different approach. Instead of dividing the veto and the EMCal hit map the distribution of hits per tower in the EMCal that

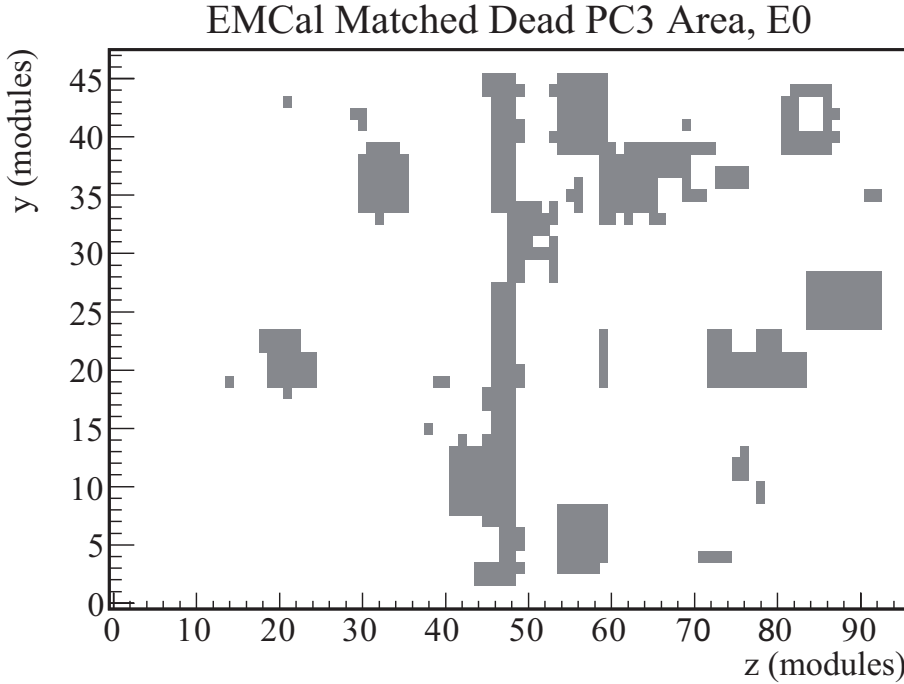


**Figure 7.14:** Dead map of the PC3 matched to the acceptance of the PbGl sector E0. The inactive area is defined by a cut of 0.09 on the ratio of the veto and the EMCal hit map shown in Figure 7.13.

have a corresponding hit in the PC3 (i.e. within a radius of 4 cm) was studied for each sector separately. A threshold was chosen to cut out towers which showed significantly less entries than the average in the same sector. The efficiencies derived in this method for the PbGl and PbSc were found to be similar to the values given in Table 7.7 with an uncertainty of  $\pm 5\%$ . It must be emphasized that both methods only represent an estimation of the PC3 efficiency. However, within the errors the derived values are believed to be reasonable.

The fraction of charged particles  $X_{ch}$  in the spectrum of photon-like clusters (with PID cuts) was calculated for the minimum bias and the ERT filtered event sample separately.

	PC3 efficiency $\epsilon_{PC3}$
PbGl	$79\% \pm 5\%$
PbSc	$92\% \pm 5\%$

**Table 7.7:** Estimation of the PC3 efficiency in the acceptance of the PbGl and PbSc, respectively. The intrinsic efficiency of the PC3 was assumed to be 100%. The errors were estimated by following two different approaches to determine the efficiency (see text for more details).

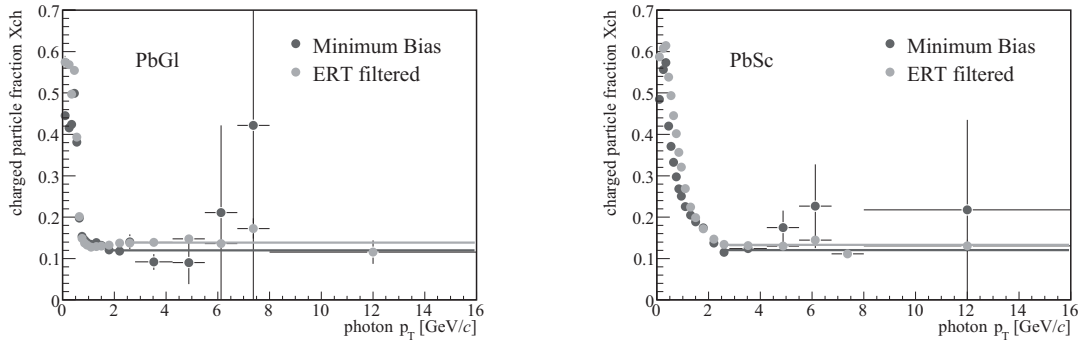


**Figure 7.15:** Fraction of charged particles  $X_{ch}$  in the photon-like cluster spectrum (PID3) derived for the two data samples and for the PbGl and PbSc, respectively. Because of the small statistics the fraction is extrapolated to larger  $p_T$  by a constant fit.

$X_{ch}$  is shown in Figure 7.15 as a function of the photon  $p_T$  for the two data sets and for the PbGl and PbSc, respectively. The large contribution of charged particles at low transverse momenta is due to charged hadrons, which were not removed by the shower shape cut. Charged hadrons deposit only a small fraction of their energy in the EMCal since both subsystems have only a depth of about one nuclear absorption length (see Table 5.1). Also the different response to hadrons in the PbGl and PbSc is obvious, i.e. the PbSc as a scintillator is more susceptible to hadrons (see Section 5.4). The fraction  $X_{ch}$  levels off at a constant value above  $p_T \approx 2 \text{ GeV}/c$ . This is expected since for  $p_T > 2 \text{ GeV}/c$  the main contribution to the charged background originates from the conversion of photons ( $\gamma \rightarrow e^+e^-$ ) and therefore is determined by the conversion probability  $p_{\text{conv}}$ . Since the statistical fluctuations become large at high  $p_T$  the data is replaced by a constant fit. The fit region was chosen for each data set and subsystem individually and ranged from  $p_T^{\min} = 1.8 - 2.6 \text{ GeV}/c$  to  $p_T^{\max} = 16 \text{ GeV}/c$ . The charged fraction above  $3 \text{ GeV}/c$  is about 14% in the PbGl and about 13% in the PbSc.

### Photon Conversion

High-energy photons traversing a material with high atomic number have a non-negligible probability  $p_{\text{conv}}$  to convert into  $e^+e^-$  pairs. Since most photons that hit the EMCal originate at the collision vertex they have to pass through all the material between the vertex and the EMCal in the PHENIX detector. Electrons and photons from pair production that takes place in front of the PC3 contribute to the charged particle fraction  $X_{ch}$  and are therefore removed from the data sample. Conversions that take place between the PC3 and the EMCal do not have to be considered. Because of the small distance between PC3 and EMCal any created  $e^+e^-$  pair will form one single cluster in the EMCal which

is identified as a photon cluster with the full energy of the original photon. In order to correct for photons that convert on their way to the EMCAL the conversion probability in the material from the vertex up to the PC3 is calculated.  $p_{\text{conv}}$  can be derived from the high-energy limit of the total  $e^+e^-$  pair-production cross section as given in [Yao06]:

$$p_{\text{conv}} = 1 - \exp\left(-\frac{7}{9} \cdot \sum_i \frac{X_i}{X_0}\right), \quad (7.21)$$

where the material budget of subsystem  $i$  is given in terms of the radiation length ( $X_i/X_0$ ). Table 7.8 lists the material budget of the relevant subsystems which were installed in Run III p + p. The calculated conversion probabilities are given in Table 7.9 for photons that hit the PbGl and PbSc, separately. Since this approach to estimate the conversion probability does not take into account any detector specific effects a conservative uncertainty of  $\pm 0.02$  is applied to the probability. The total material budget is different in the east and west arm of PHENIX, hence the conversion probability is calculated for PbGl, PbSc East and PbSc West separately. The average conversion probability for the PbSc is calculated by weighting with the number of PbSc sectors in the east and west arm.

## Neutral Background

Besides the charged background in the photon-like cluster spectrum also neutral particles remain in the spectrum after the shower shape cut. Neutral particles comprise primarily neutrons and antineutrons. The fraction of neutral particles in the photon-like cluster spectrum, after the subtraction of charged particles, was determined in simulations of Au + Au collisions for different centralities [KB04a]. The efficiency of the EMCAL for

Material	$X/X_0$		
	PbGl	PbSc East	PbSc West
beam pipe, air, DC, MVD	0.013	0.013	0.013
PC1	0.012	0.012	0.012
RICH	0.021	0.021	0.021
PC2	—	—	0.024
TEC/TRD	0.064	0.064	—
Air	0.003	0.003	0.003
Total	0.113	0.113	0.073

**Table 7.8:** The material budget in terms of radiation length  $X_0$  used in the analysis to determine the conversion probability in front of the PC3. The values are taken from [d'E04].

	$p_c$
PbGl	0.084
PbSc East	0.084
PbSc West	0.055
PbSc (mean)	0.065

**Table 7.9:** Estimation of the photon conversion probabilities between the collision vertex and the PC3 using the material budget from Run III p + p determined separately for the PbGl, PbSc East and West. The mean for the PbSc is calculated by weighting with the number of PbSc sectors in each arm.

neutrons and antineutrons is determined via the embedding of simulated particles into real events. These merged events are then analyzed within the same analysis framework as the real data and the influence of the detector as well as the the various analysis cuts on the measured spectrum can be studied. The flux of neutrons and antineutrons into the acceptance of the EMCAL is determined with a GEANT simulation of the PHENIX experiment. Knowing the detector efficiency and the input spectrum the response of the EMCAL to neutrons and antineutrons can be determined. For the input spectrum of neutrons and antineutrons a parameterization of the measured proton and antiproton spectrum in PHENIX is employed. This approach is justified under the assumption that the production of nucleons does not depend on the isospin. More details on the efficiency calculation can be found in [KB04a].

The derived spectrum of neutral particles is compared to the measured photon-like cluster spectrum in the EMCAL, after subtraction of the charged background. This comparison gives the fraction of neutrons and antineutrons to the cluster spectrum. Figure 7.16 shows the contribution of neutrons and antineutrons  $X_{n\bar{n}}$  in peripheral Au + Au collisions<sup>11</sup> after the employment of the shower shape cut in the two EMCAL subsystems. Above  $p_T \approx 2$  GeV/c the neutral contribution becomes negligible. The error bars shown in Figure 7.16 are systematic errors. More details on systematic uncertainties due to the various corrections are given in Section 7.3.4.

### Geometric ERT Efficiency

Events in the Gamma3 data set required an energy deposition in a sum of  $4 \times 4$  towers (i.e. a  $4 \times 4$  trigger tile) in the EMCAL above a certain threshold (see Section 5.5.2 and Table 5.2). All clusters in the EMCAL for such a high- $p_T$  event are recorded and written to disk. In principle, the geometric ERT efficiency  $\epsilon_\gamma^{\text{Gamma3}}$  corrects for photons that are lost

<sup>11</sup>Peripheral Au + Au collisions can be taken as a good approximation for p + p reactions.

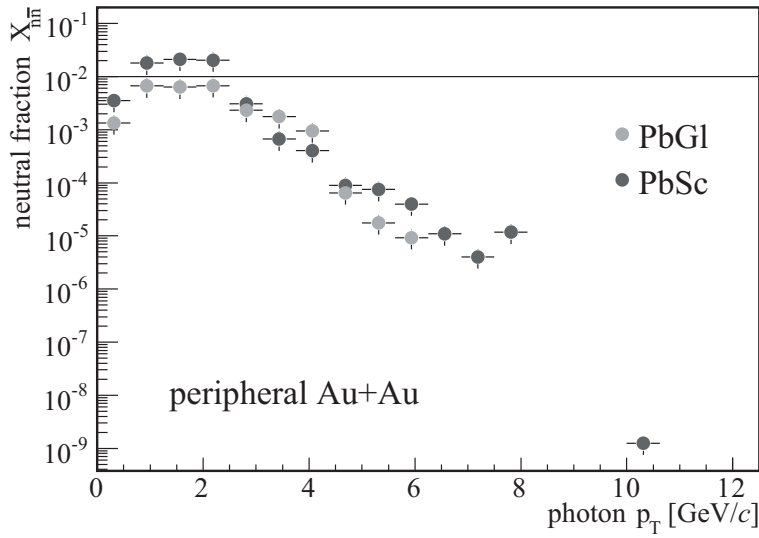


**Figure 7.16:** Fraction of neutrons and antineutrons in the photon-like cluster spectrum, after subtraction of the charged background. The shower shape cut is applied to the EMCAL data and considered in the efficiency calculation of neutrons and antineutrons.

for two reasons: First, single suspicious trigger tiles or even whole FEM's were masked off during data taking or in the offline analysis. EMCAL clusters in such areas might not fire the trigger although they deposit enough energy. And second, events containing only low energy photons are not recorded because the energy deposit does not exceed the threshold and hence do not fire the trigger. Both effects reduce the efficiency of the high- $p_T$  trigger. However, by calculating and applying the ERT efficiency the loss of these photons is corrected. At large  $p_T$ , i.e. well above the trigger threshold, the geometric ERT efficiency is determined solely by the number of inactive trigger tiles in the acceptance of the EMCAL. This so-called *geometric limit* can be calculated as follows:

$$\epsilon_\gamma^{\text{Gamma3}}(\text{geo. limit}) = 1 - \frac{N_{\text{tower}}^{\text{masked}}}{N_{\text{tower}}^{\text{active}}} , \quad (7.22)$$

where  $N_{\text{tower}}^{\text{masked}}$  denotes the number of active EMCAL towers which are located in masked trigger tiles (and hence do not contribute to the trigger) and  $N_{\text{tower}}^{\text{active}}$  is the number of active towers in the EMCAL acceptance. Since all EMCAL towers in masked trigger tiles are removed from the analysis (and are corrected by the geometric acceptance correction described above) the geometric limit of the ERT efficiency is 100% by construction, i.e.  $N_{\text{tower}}^{\text{masked}} = 0$ .

The geometric ERT efficiency for single photons over the entire  $p_T$  range can be determined directly from the data by comparing the photon yields obtained in the minimum

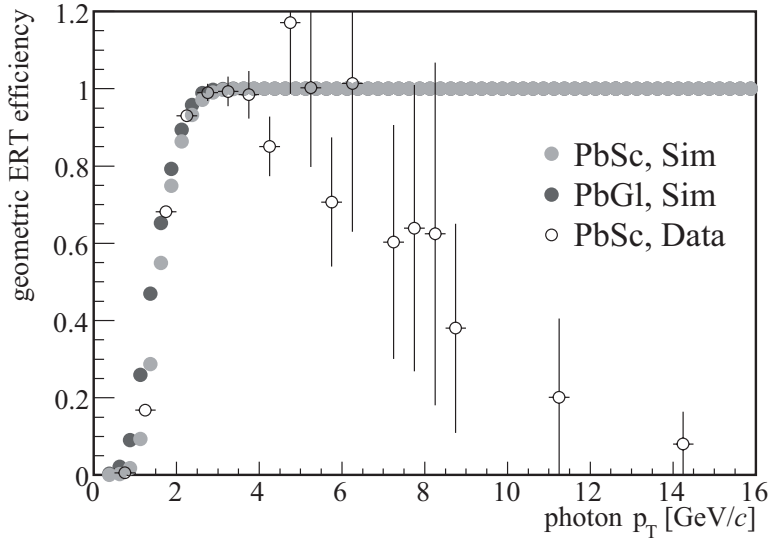


**Figure 7.17:** The geometric ERT efficiency simulated with the fast Monte-Carlo for the PbGl and PbSc. The trigger threshold distribution is determined by a fit to the measured turn-on curve shown here for the PbSc (open circles). The statistics of the minimum bias sample becomes very low above a few  $p_T$  leading to the large statistical errors on the data points in the geometric limit.

bias data sample and the Gamma3 data sample. This so-called *turn-on curve* is shown in Figure 7.17 for the PbSc data (open circles). However, since the statistics of the minimum bias sample drops off rather quickly after the geometric limit has been reached the ERT efficiency is not well defined by the data in the geometric limit (although the data already indicate a geometric limit of 100% between  $p_T = 3 - 4$  GeV/c). Therefore instead of extracting the trigger efficiency directly from the data the turn-on curve is used to determine the effective trigger thresholds of the ERT. Although Table 5.2 implies constant trigger thresholds they are in fact better described by the sum of two Gaussians around the nominal value of the threshold which account for the Gaussian-like ADC-threshold distribution and the asymmetric non-Gaussian tails of the gain-factor distribution. This was studied thoroughly as part of the neutral pion analysis in Run III p + p [Bat05b]. The parameters of the effective trigger threshold distributions in PbGl and PbSc, respectively, are derived by fitting the integrated distribution to the corresponding measured turn-on curve. These trigger thresholds are then used as input in a fast Monte-Carlo simulation to simulate the geometric trigger efficiency with equal statistical accuracy at all  $p_T$ . The result is also shown in Figure 7.17 for the PbGl and PbSc. The comparison of the turn-on curve derived from the PbSc data and the corresponding simulated ERT efficiency shows

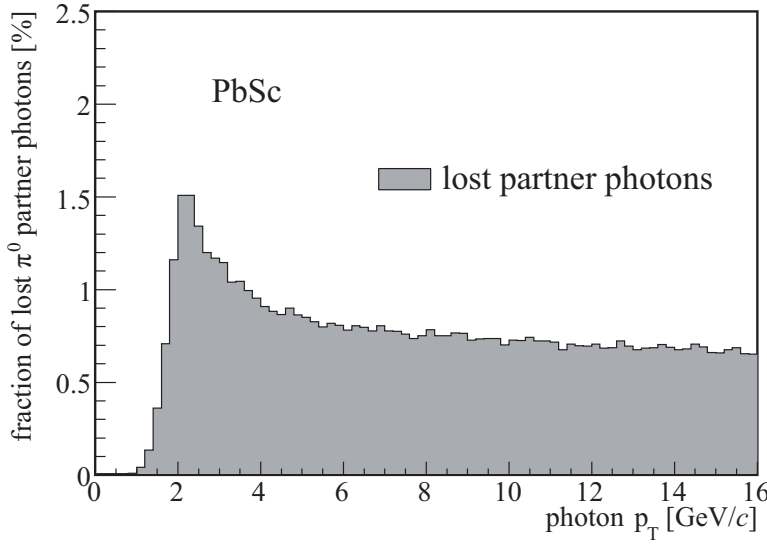


**Figure 7.18:** Fraction of partner photons in  $\pi^0$  decays which are lost due to the FEM requirement even though their energy is sufficient to fire the ERT trigger. Above  $p_T \approx 3$  GeV/ $c$  less than 1% of partner photons are lost. Only the PbSc was simulated because a single FEM of the PbSc covers a larger area than a FEM of the PbGl because of the larger granularity of the PbSc. Therefore the effect is expected to be smaller in the PbGl.

very good agreement in the  $p_T$  range where the trigger turns on. The simulated ERT efficiency is used to correct the Gamma3 data.

In the fast Monte-Carlo only single photons are simulated, i.e. the derived geometric ERT efficiency is valid only for the case that at most one photon per FEM and event fired the trigger (the trigger board for each FEM stores only the information if the ERT trigger fired on this FEM but not in which specific trigger tile and how many times). In order to keep the ERT efficiency under control the so-called *FEM requirement* is introduced in the analysis of the Gamma3 filtered data. This condition accepts a photon in a Gamma3 event only if it lies on a FEM for which the ERT trigger is set and if the photon has the maximum energy on this FEM in this event. Due to this requirement the accepted photon is very likely the photon that fired the ERT trigger. Photons that do not meet these conditions are removed from the sample but are added back by the ERT efficiency correction. The FEM requirement is based on the assumption that only one photon per event fires the ERT trigger on one specific FEM. Because of the low multiplicity in  $p + p$  collisions this assumption is likely to be true for uncorrelated photons since the probability that uncorrelated photons hit the same FEM and fire both the ERT trigger is negligible. However, decay photons e.g. originating from high-energetic  $\pi^0$  decays are correlated

and both could have, in the case of a symmetric decay, a transverse momentum above the trigger threshold. Since the opening angle of the decay photons decreases with increasing  $p_T$  both decay photons might hit the same FEM. In this case the FEM requirement would remove one of the trigger photons (the less energetic one) but the ERT efficiency would *not* correct for this (the removed photon has a  $p_T$  in the geometric limit where the ERT efficiency is 100%). In order to investigate the size of this effect  $\pi^0$  decays were simulated in the fast Monte-Carlo. Only such  $\pi^0$  decays were studied, where at least one decay photon fired the trigger. The two decay photons were subdivided into the *trigger photon*, which is the more energetic photon and fires the trigger and the *partner photon*. It was then studied how many partner photons hit the same FEM and have sufficient energy to fire the Gamma3 trigger. Because of the smeared trigger threshold distribution it is also possible that the less energetic photon is the trigger photon while the more energetic photon does not fire the trigger. This case is also taken into account in the simulation. The result is shown in Figure 7.18. Above  $p_T \approx 3 \text{ GeV}/c$  the loss of partner photons is less than 1%. This was deemed to be negligible. The loss of partner photons was not simulated for the PbGl since the finer granularity of the PbGl towers leads to a smaller area covered by one single FEM. Thus the effect will be even smaller than in the PbSc.

### 7.3.3 Fully Corrected Inclusive Photon Spectrum

The corrected yield of inclusive photon production  $\frac{\Delta\tilde{N}_{\text{cluster}}}{\Delta p_T \Delta y}$  is calculated taking into account all corrections described in the previous section. The Lorentz invariant form of the yield is achieved by multiplication with a factor:

$$\frac{1}{2\pi p_T N_{\text{evt}}} \cdot \frac{d^2 N_\gamma^{\text{incl}}}{dp_T dy} = \frac{1}{2\pi p_T N_{\text{evt}}} \cdot \frac{\Delta\tilde{N}_{\text{cluster}}}{\Delta p_T \Delta y}, \quad (7.23)$$

where  $\frac{d^2 N_\gamma^{\text{incl}}}{dp_T dy}$  gives the fully corrected number of photons in the rapidity range  $\Delta y$  at mid-rapidity and in the transverse momentum interval  $[p_T - \Delta p_T/2, p_T + \Delta p_T/2]$ . The spectrum is derived from the minimum bias and the ERT filtered data sample independently. The final spectrum is a combination of the two with the transition chosen to be at  $p_T = 3 \text{ GeV}/c$ , i.e. the minimum bias spectrum is used for  $p_T < 3 \text{ GeV}/c$  and the Gamma3 spectrum is used for  $p_T > 3 \text{ GeV}/c$ .<sup>12</sup> In order to normalize both samples to the same number of minimum bias events the ERT spectrum needs to be scaled down by the rejection factor  $f_{\text{reject}}^{\text{gamma3}}$  derived in Section 7.2.4. A couple of additional corrections

---

<sup>12</sup>Note that the Gamma3 spectrum is only used in the geometric limit of the ERT trigger. In this  $p_T$  range the application of the ERT trigger efficiency is not crucial. However, the ERT spectrum below  $p_T < 3 \text{ GeV}/c$  (where the trigger efficiency quickly declines) was used for comparison reasons to assure consistency of the minimum bias and the Gamma3 data sample.

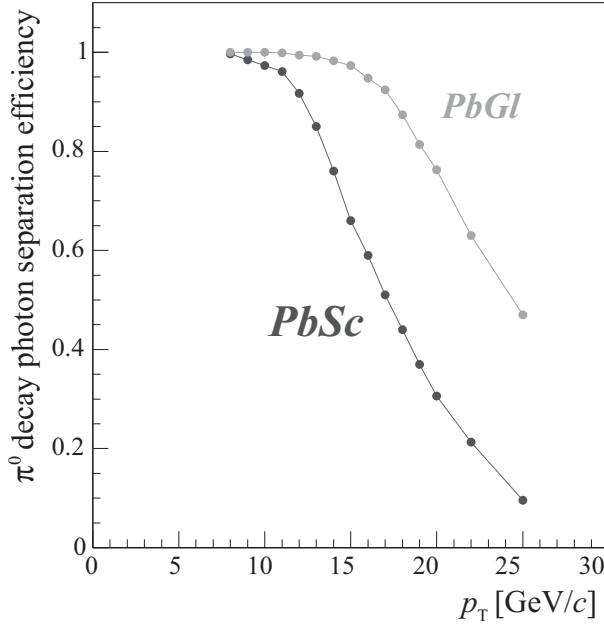


**Figure 7.19:** Probability that the EMCAL clustering routine can separate the two decay photons of a  $\pi^0$  decay as a function of  $\pi^0 p_T$ . The EMCAL clustering starts having problems at a  $p_T$  of  $\sim 10$  GeV/c and  $\sim 15$  GeV/c for the PbSc and PbGl, respectively. The plot is taken from [Bat05b].

are required to calculate the fully corrected Lorentz invariant cross section of inclusive photon production which is described in the following.

### Shower Merging Correction

As mentioned in the discussion of the reconstruction efficiency the measured inclusive photon spectrum is distorted by the so-called *cluster* (or *shower*) *merging effect*. The opening angle between the two decay photons of a  $\pi^0$  decay decreases with increasing transverse momentum of the neutral pion. At large transverse momenta the  $\pi^0$  decay photons cannot be separated efficiently by the EMCAL clustering routine resulting in so-called *merged clusters*. Figure 7.19 shows the probability that the two  $\pi^0$  decay photons can be separated by the clustering routine as a function of the  $\pi^0 p_T$ . The probability was determined in a fast Monte-Carlo simulation which takes into account the shape of the measured neutral pion spectrum, the geometry of the EMCAL and a parameterization of the electromagnetic shower profile obtained from test beam data (see [Bat05b]). Moreover, an energy asymmetry cut of 0.8 was applied in the simulation. The figure illustrates that shower merging in the PbSc (PbGl) becomes significant above a transverse momentum of  $p_T > 10$  GeV/c (15 GeV/c). In the PbGl the effect is less severe because of the finer granularity.

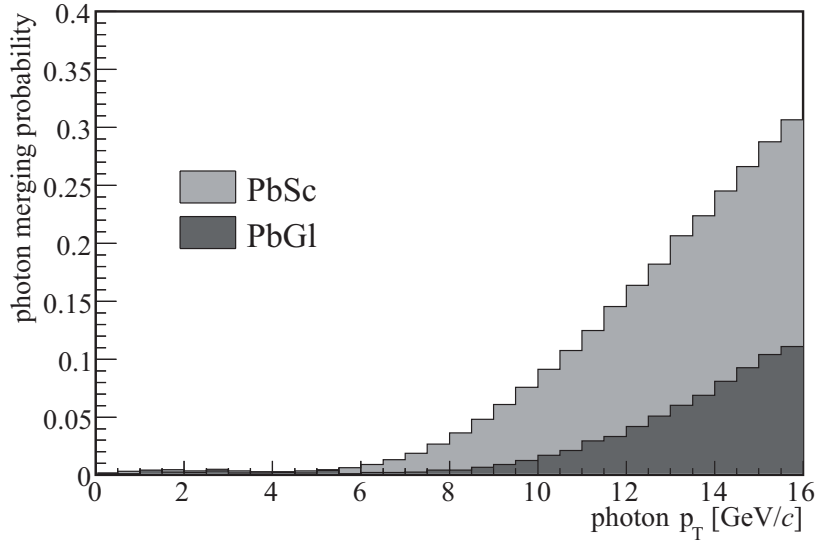


**Figure 7.20:** Probability for a  $\pi^0$  decay photon to merge with its partner photon as a function of the photon  $p_T$ . The effect becomes significant for  $p_T \gtrsim 8$  GeV/ $c$  in the PbSc. In the PbGl shower merging is less severe in the considered  $p_T$  range because of the finer granularity.

Because of the large lateral extension of merged clusters for  $\pi^0$   $p_T$  below 20 GeV/ $c$  (compared to single electromagnetic showers at the same  $p_T$ ), all merged photons are efficiently removed by the shower shape cut in the analysis. Hence, all merged photons are missing in the photon-like cluster spectrum. In order to quantify the bias of the inclusive photon spectrum due to  $\pi^0$  shower merging in conjunction with the shower shape cut the probability for a  $\pi^0$  decay photon to merge with its partner photon  $p_\gamma^{\text{merging}}$  is required as a function of the photon  $p_T$ .  $p_\gamma^{\text{merging}}$  was determined with the same fast Monte-Carlo code as was used to derive the separation efficiency shown in Figure 7.19. The result is shown in Figure 7.20 for the PbGl and PbSc. As one can see in the figure the loss of decay photons due to shower merging in conjunction with the shower shape cut becomes significant for photon  $p_T \gtrsim 8$  GeV/ $c$  ( $p_T \gtrsim 12$  GeV/ $c$ ) in the PbSc (PbGl).

It should be noted that  $\eta$  decay photons also tend to overlap with increasing transverse momentum. The  $\eta$  meson decays into two photons with a branching ratio of approximately 40%. However, the opening angle of a two-photon meson decay increases with the invariant mass of the meson. Since the  $\eta$  meson is almost four times heavier than the neutral pion shower merging of  $\eta$  decay photons can be neglected completely for  $p_T < 16$  GeV/ $c$ .

The cluster merging effect is taken into account at two different points in the photon analysis:

1. In the simulation of the reconstruction efficiency for single photons,
2. in the simulation of background photons from  $\pi^0$  decays.

The simulation of the reconstruction efficiency depends on the shape of the true inclusive photon spectrum  $f(p_T)_{\text{true}}$  (see Equation 7.13).  $f(p_T)_{\text{true}}$  is determined iteratively from the measured inclusive photon spectrum  $f(p_T)_{\text{measured}}$  in which merged clusters from  $\pi^0$  decays are missing. Therefore the shape of the inclusive photon spectrum used in the simulation of the reconstruction efficiency is biased due to  $\pi^0$  shower merging. In order to correct this bias, the merging probability  $p_\gamma^{\text{merging}}$ , the simulated  $\gamma/\pi^0$  ratio for  $\pi^0$  decay photons (see Section 7.5) and the measured  $\pi^0$  spectrum  $\pi^0_{\text{meas}}$ , taken from [Bat05a], are used to calculate the number of  $\pi^0$  decay photons  $\Delta\gamma^{\text{merging}}$  which are lost due to shower merging and the shower shape cut as a function of photon  $p_T$ :

$$\Delta\gamma^{\text{merging}} = \left[ (\gamma^{\pi^0}/\pi^0)_{\text{sim}} - (\gamma^{\pi^0}/\pi^0)_{\text{sim}}^{\text{w/o}} \right] \cdot \pi^0_{\text{meas}}. \quad (7.24)$$

As will be discussed in more detail in Section 7.5  $(\gamma^{\pi^0}/\pi^0)_{\text{sim}}$  is simulated in a fast Monte-Carlo simulation using the measured  $\pi^0$  spectrum as input.  $(\gamma^{\pi^0}/\pi^0)_{\text{sim}}^{\text{w/o}}$  is the same simulation, however, with all merged photons removed according to the calculated merging probability  $p_\gamma^{\text{merging}}$ .  $\Delta\gamma^{\text{merging}}$  is calculated as a function of photon  $p_T$  and is added to the measured photon spectrum ( $f(p_T)_{\text{measured}}$  in Equation 7.13). The shape of this corrected spectrum is used as input to the simulation which thus yields the unbiased reconstruction efficiency for single photons.

Note that the shower merging corrected inclusive photon spectrum is not used to extract the direct-photon signal. Instead  $(\gamma^{\pi^0}/\pi^0)_{\text{sim}}^{\text{w/o}}$ , which is utilized in the correction of the reconstruction efficiency, is also used in the double ratio  $R_\gamma$  (see Equation 7.1) or more precisely in the simulated background cocktail from hadronic decays. Section 7.5 describes the details of the background simulation and how the effect of shower merging is taken into account.

### Minimum Bias Trigger Efficiency

The Lorentz invariant cross section is related to the Lorentz invariant yield (Equation 7.23) via the total inelastic cross section in p + p collisions  $\sigma_{\text{pp}}^{\text{inel}}$ :

$$E \frac{d^3\sigma}{dp^3} = \frac{1}{2\pi p_T N_{\text{evt}}} \cdot \frac{d^2N_\gamma^{\text{incl}}}{dp_T dy} \cdot \sigma_{\text{pp}}^{\text{inel}}. \quad (7.25)$$

Because of the low multiplicity in p + p collisions the minimum bias trigger condition (at least one PMT in each BBC must fire in a minimum bias event) is not satisfied in each

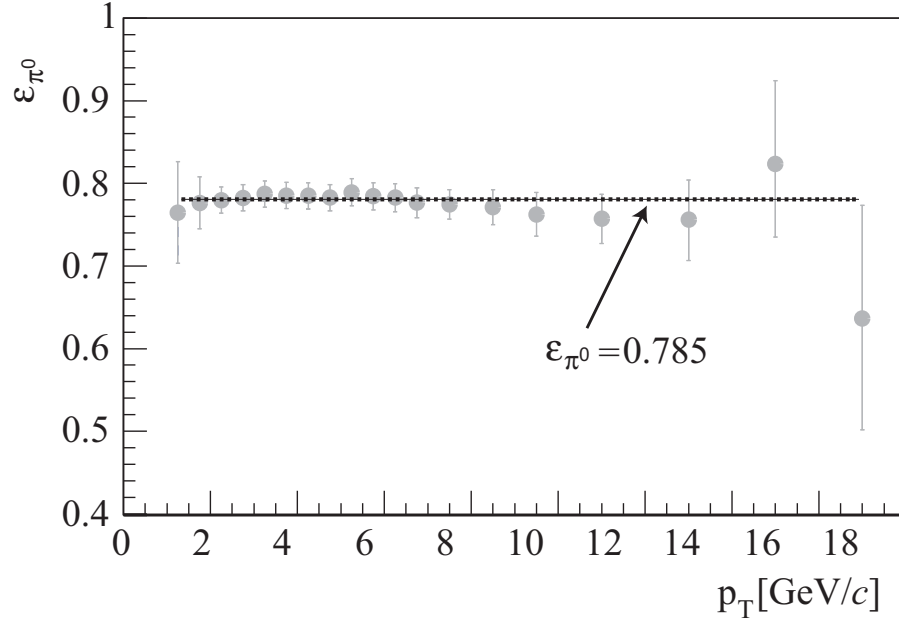


**Figure 7.21:** Ratio of measured neutral pions in the ERT\_4×4b data sample with and without minimum bias requirement. The fraction is independent of the transverse momentum of the  $\pi^0$  and therefore can be described by a constant fit of  $\epsilon_{\pi^0} = 0.785$ .

inelastic collision. Due to this limited efficiency of the minimum bias trigger  $\epsilon_{\text{trig}}^{\text{MB}}$  in  $p + p$  events the measured number of events  $N_{\text{evt}}$  does not correspond to the actual number of inelastic  $p + p$  collisions  $N_{\text{inel}}$  that occurred in the experiment:

$$N_{\text{evt}} = \epsilon_{\text{trig}}^{\text{MB}} \cdot N_{\text{inel}}. \quad (7.26)$$

This can also be expressed in terms of the total inelastic cross section: the minimum bias trigger efficiency limits the fraction of the total inelastic cross section that is seen by the BBC's in  $p + p$  collisions. The actually measured BBC cross section is given by:

$$\sigma_{\text{BBC}} = \epsilon_{\text{trig}}^{\text{MB}} \cdot \sigma_{pp}^{\text{inel}}. \quad (7.27)$$

The BBC cross section in Run III  $p + p$  was extrapolated from  $p + p$  data recorded in Run II to be  $\sigma_{\text{BBC}} = (23.0 \pm 2.2) \text{ mb}$  [Baz05]. An extrapolation of world  $p + p$  data to  $\sqrt{s} = 200 \text{ GeV}$  results in a total inelastic cross section of  $\sigma_{pp}^{\text{inel}} = 42.2 \text{ mb}$  and hence a trigger efficiency of  $\epsilon_{\text{trig}}^{\text{MB}} \approx 55\%$ , i.e. the minimum bias trigger records only half of all inelastic  $p + p$  collisions.

At the same time the limited minimum bias trigger efficiency effects the number of measured photons by the EMCAL  $N_{\gamma}^{\text{incl}}$ . However, although  $\epsilon_{\text{trig}}^{\text{MB}}$  is only about 50% the fraction of photons which hit the EMCAL ( $\epsilon_{\gamma}$ ) is 79.0%. This is due to the fact that events

that do not trigger the BBC's are likely to emit less photons at mid-rapidity. The fraction of photons which hit the EMCAL from events that satisfy the minimum bias trigger is assumed to be equal to the fraction of neutral pions which hit the EMCAL under the same conditions, i.e.  $\epsilon_\gamma = \epsilon_{\pi^0}$ .  $\epsilon_{\pi^0}$  was determined as part of the neutral pion analysis [Bat05b] using EMCAL data recorded with the ERT\_4×4b trigger (see Section 5.5.2) in coincidence with the minimum bias trigger as well as without minimum bias condition. The comparison of the measured  $\pi^0$  yields obtained with these two data sets is used to extract  $\epsilon_{\pi^0}$ . Figure 7.21 shows the ratio of the two  $\pi^0$  yields (ERT in coincidence with minimum bias/ERT only) summed over all eight EMCAL sectors and reflects how many  $\pi^0$ 's that hit the EMCAL are from events that also satisfy the minimum bias trigger. The ratio is independent of  $p_T$  and can therefore be approximated by a constant fit of  $\epsilon_{\pi^0} = 0.785$ .

The ERT\_4×4b data sample was recorded without vertex information, i.e. no vertex cut can be applied, so that the  $z$ -vertex of ERT\_4×4b events is only limited by the central magnet nose cones which effectively allows collision vertices of  $|z_{\text{vertex}}| < 40$  cm. Since in the minimum bias and Gamma3 data sample a vertex cut of  $|z_{\text{vertex}}| < 30$  cm is applied (see Section 7.2.4)  $\epsilon_{\pi^0}$  obtained from ERT\_4×4b data must be corrected to account for this. An analysis of BBC hit multiplicities as a function of the collision vertex described in [Baz05] yielded the value stated above ( $\epsilon_{\pi^0} = 0.79 \pm 0.02$ ).

Both aspects of the limited minimum bias trigger efficiency bias the measurement and therefore must be taken into account in the calculation of the Lorentz invariant cross section of inclusive photon production. The unbiased form of Equation 7.25 is given by:

$$E \frac{d^3\sigma_\gamma^{\text{incl}}}{d\vec{p}^3} = \frac{1}{2\pi p_T N_{\text{evt}}} \cdot \frac{\epsilon_{\text{trig}}^{\text{MB}}}{\epsilon_\gamma} \frac{d^2N_\gamma^{\text{incl}}}{dp_T dy} \cdot \sigma_{\text{pp}}^{\text{inel}} \quad (7.28)$$

$$= \frac{1}{2\pi p_T N_{\text{evt}}} \cdot \frac{1}{\epsilon_\gamma} \frac{d^2N_\gamma^{\text{incl}}}{dp_T dy} \cdot \sigma_{\text{BBC}}. \quad (7.29)$$

### Bin-Shift Correction

The  $p_T$  distribution of inclusive photons is a steeply falling spectrum. The yield is calculated in  $p_T$  bins of a certain finite size. Simply placing the data points in the middle of each bin would not be correct, since the center of a bin does not represent the center-of-gravity of the steeply falling distribution within the bin. Instead the data points can be shifted in the vertical direction by calculating the true value of the distribution at the bin center<sup>13</sup>. Since the true distribution is not known the shift must be calculated iteratively. The true distribution  $f(p_T)^{\text{true}}$  is approximated by the parameterization given in

<sup>13</sup> Alternatively the data points can be shifted horizontally, in the  $p_T$ -direction, to the true center-of-gravity within the bin. However, for the comparison of spectra it is advantageous to have the data points in the middle of each bin.

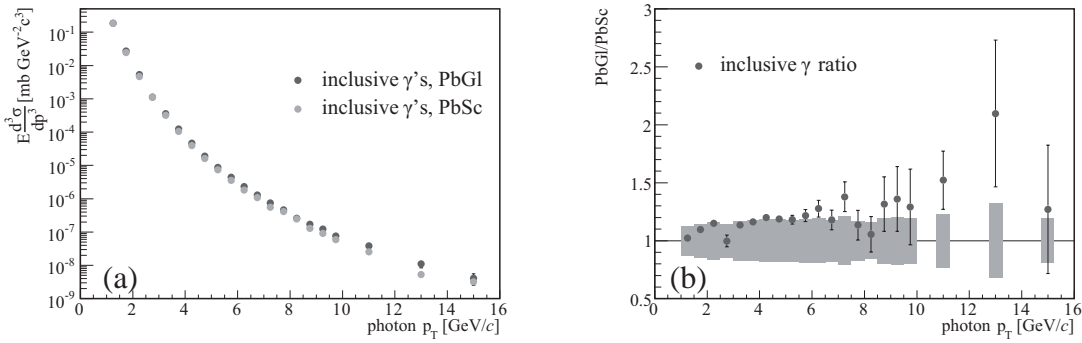


**Figure 7.22:** (a) The cross section of inclusive photon production in  $p + p$  collisions at  $\sqrt{s} = 200$  GeV in PbGl and PbSc. (b) The ratio of the spectra shows that the PbGl spectrum is 15-20% higher than the spectrum in the PbSc. This discrepancy is covered by the systematic uncertainty assigned to the energy scale (grey boxes). No shower merging correction is applied leading to a larger discrepancy between the spectra in the two EMCAL subsystems with increasing transverse momentum.

Equation 7.19. In the next step the ratio of the average yield of  $f(p_T)_{\text{true}}$  in a given  $p_T$  bin  $[p_T^c - \Delta/2, p_T^c + \Delta/2]$  and the value of  $f(p_T)_{\text{true}}$  at the center of the bin  $p_T^c$  is calculated:

$$r = \frac{1/\Delta \cdot \int_{p_T^c - \Delta/2}^{p_T^c + \Delta/2} f(p_T)_{\text{true}} dp_T}{f(p_T^c)_{\text{true}}} . \quad (7.30)$$

The ratio  $r$  represents the yield correction and is applied to the measured yield in the given bin:

$$dN/dp_T|_{\text{shifted}} = \frac{1}{r} \cdot dN/dp_T . \quad (7.31)$$

If  $f(p_T)_{\text{true}}$  would be the true distribution the correction shown in Equation 7.31 would shift the data points to the true yield in the middle of each  $p_T$  bin. However, in the first iteration the parameterization is only an approximation and the first correction shifts the data points closer to the true distribution. The process must be repeated with a new fit to the shifted spectrum. After a couple of iterations the correction  $r$  becomes negligible. The total correction is of the order of a few percent and increases with increasing bin width and steeper falling spectra.

### Inclusive Photon Cross Section

Figure 7.22(a) shows the cross section of inclusive photon production in  $p + p$  collisions at  $\sqrt{s} = 200$  GeV at mid-rapidity. Tables listing the inclusive photon cross section in the PbGl and PbSc can be found in Appendix E.1. Note that all corrections are applied except

for shower merging which is only used to derive the unbiased reconstruction efficiency and is instead implemented in the simulation of the background  $\gamma/\pi^0$  ratio (see Section 7.5.2). Therefore the effect of shower merging leads to the increasing deviation of the inclusive photon spectra in PbGl and PbSc with increasing  $p_T$ . The PbGl spectrum is some 15-20% higher than the spectrum in the PbSc which is illustrated on a linear scale by plotting the ratio of the two spectra (Figure 7.22(b)). As will be discussed later only the uncertainty due to the energy scale is considered to be uncorrelated between PbGl and PbSc. Since only uncorrelated uncertainties can account for the difference observed between the two EMCAL subsystems only the energy scale uncertainty is shown as grey boxes in the PbGl/PbSc ratio. The discrepancy is covered by the systematic uncertainty assigned to the spectra. A detailed description of the systematic uncertainties of the inclusive photon analysis is given in the next section.

### 7.3.4 Systematic Uncertainties of the Inclusive Photon Spectrum

The corrections discussed in Section 7.3.2 which are necessary to derive the inclusive photon spectrum from the raw cluster yield are all afflicted with uncertainties which have to be propagated to the final corrected spectrum. The dominant sources of systematic uncertainties are listed in Table 7.10 for the PbGl (PbSc). The relative uncertainty on the inclusive photon yield is given for three different  $p_T$  bins. There are two types of systematic uncertainties (referred to as type A and B in the following) in the analysis of direct photons<sup>14</sup>. Even though all errors are correlated in  $p_T$ , i.e. they all move in the same direction within the uncertainty, for type A errors the magnitude of the shift can change point-by-point while for type B errors all data points are moved by the same factor. Type B errors thus represent a normalization (or scaling) error and therefore are not shown for each data point separately. In fact, in the direct-photon analysis presented in this thesis only the uncertainty of the BBC cross section  $\sigma_{\text{BBC}}$  is considered as a normalization error and therefore is displayed separately at the bottom of Table 7.10. All other systematic uncertainties are considered to be of type A and are added in quadrature. In the following all systematic uncertainties listed in Table 7.10 are described in more detail.

**Reconstruction Efficiency:** The result of the efficiency calculation is dominated by the energy resolution of the detector. The uncertainty of the reconstruction efficiency is therefore determined by the uncertainty of the energy smearing applied in the fast Monte-Carlo (see Equation 7.8). As described before the energy resolution of the detector is estimated by adjusting the simulated  $\pi^0$  peak width to the measured width. It was

---

<sup>14</sup>In fact this is also true for the neutral pion analysis.

Systematic Error of the Inclusive Photon Spectrum in PbGl (PbSc)				
	$p_T$ indep.	5-5.5 GeV/c	9.5-10 GeV/c	14-16 GeV/c
efficiency		3.7% (3.5%)	3.5% (3.1%)	3.6% (3.4%)
global energy scale		10.7% (10.8%)	10.6% (10.6%)	10.6% (10.8%)
acceptance	2.5% (2.5%)			
photon conversion	2.0% (2.0%)			
charged background	1.0% (1.0%)			
neutral background	1.0% (1.0%)			
$\epsilon_\gamma$	2.5% (2.5%)			
quadratic sum		12.2% (12.3%)	12.1% (11.9%)	12.1% (12.2%)
$\sigma_{BBC}$	9.7% (9.7%)			

**Table 7.10:** Systematic uncertainties of the inclusive photon yield in the PbGl (PbSc) in three different  $p_T$  bins. The analysis demonstrated that there is only a minor  $p_T$ -dependence. The uncertainty on the measured BBC cross section  $\sigma_{BBC}$  is considered to be a normalization error while the remaining errors cause the data points to move in the same direction, but not necessarily all by the same factor. The normalization error is not included in the quadratic sum.

shown in the neutral pion analysis of Run II Au + Au that an additional smearing of 2% is required to observe a clear disagreement between the measured and the simulated peak width of neutral pions. Hence the influence of the energy smearing uncertainty on the photon yield was studied by changing the constant term  $C_2$  in Equation 7.8 by additional 2%. The additionally smeared spectrum from the simulation was then compared to the simulated yield obtained with the default energy resolution<sup>15</sup>. The relative error on the yield due to the uncertainty of the energy smearing in the fast Monte-Carlo is shown in Figure 7.23 for the PbGl and PbSc. The uncertainty indicates only a small  $p_T$ -dependence above  $p_T = 4$  GeV/c. The dotted line represents a polynomial adapted to the simulated data points. The systematic error is < 4% for all transverse momenta.

**Global Energy Scale:** The energy scale of the EMCAL is determined using the measured position of the  $\pi^0$  peak. The uncertainty of the energy scale arises from the fact that the actual alignment of the EMCAL is not perfectly known. The size of this uncertainty was estimated as part of the Run II neutral pion analyses by comparing the energy calibration obtained from different sources:  $\pi^0$  peak position, MIP peak position of charged hadrons and  $E/p$  ratios of electrons [Baz03c, Rey03b]. These studies resulted in an uncertainty of

<sup>15</sup>The photon spectrum is simulated in the fast Monte-Carlo by generating single photons with a flat  $p_T$  distribution which is subsequently weighted by the measured spectrum. The energy and position of photons in the acceptance of the detector is then smeared according to the parameters given in the fast Monte-Carlo.

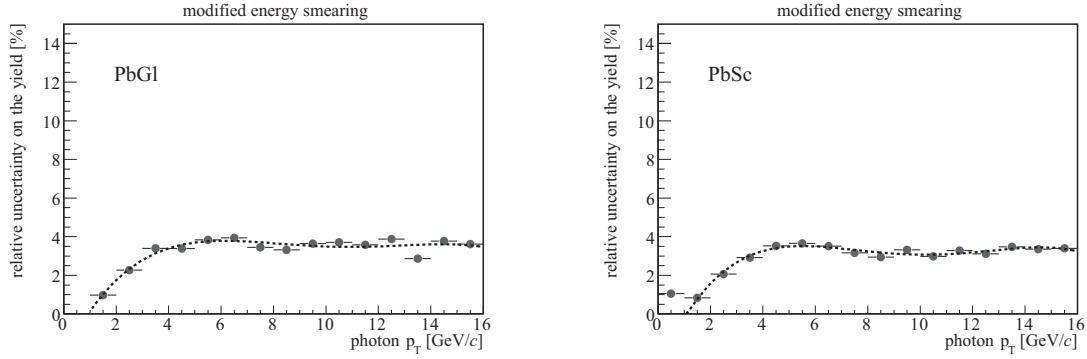


**Figure 7.23:** Relative error of the inclusive photon yield due to the uncertainty of the energy resolution in both subsystems of the EMCAL. The error is estimated by changing the constant term of the energy smearing in the fast Monte-Carlo. The dotted line represents a polynomial fitted to the simulated data points.

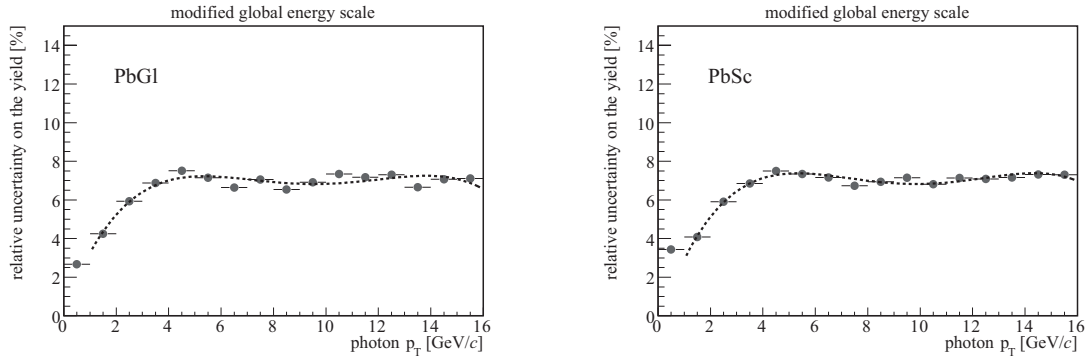


**Figure 7.24:** Relative error of the inclusive photon yield due to the uncertainty of the energy scale in PbGl and PbSc. The error is estimated by changing the global energy scale in the fast Monte-Carlo by 1.2%. The dotted line represents a polynomial fitted to the simulated data points.

1% on the energy calibration. The  $\pi^0$  peak position and thus the energy scale is affected by non-vertex  $\pi^0$  decays (see Section 7.2.5). An uncertainty of 0.7% was assigned to the corresponding correction applied in the efficiency calculation [Bat05a].

Both uncertainties are added in quadrature resulting in an overall error on the energy scale of 1.2%. This uncertainty was propagated to the yield by changing the energy scale in the fast Monte-Carlo by 1.2%. The simulated photon yield based on the changed energy scale was compared to the yield obtained with the default energy scale. The comparison is illustrated in Figure 7.24 for the PbGl and PbSc. Above  $p_T = 4$  GeV/c the uncertainty is a constant of approximately 7%. The dotted lines indicate a polynomial fitted to the simulated data points. However, the comparison of the inclusive photon

spectra in PbGl and PbSc (see Figure 7.22) indicates a possible underestimation of the systematic uncertainty. Therefore the systematic uncertainty due to the global energy scale was increased by 8% on the photon yield added in quadrature<sup>16</sup> which covered the remaining discrepancy observed in the comparison of the inclusive photon spectra.

**Geometric Acceptance:** The geometric acceptance is in principle a well known quantity. However, the parameterization used in the fast Monte-Carlo to describe the difference between the position of the tower with the maximum energy within the cluster and the impact position of the photon (maximum tower parameterization, see Section 7.3.2) introduces an uncertainty on the acceptance correction. In the  $\pi^0$  analysis this uncertainty was estimated with the help of a full PISA simulation, which does not depend on such a parameterization. Comparisons with the result of the fast Monte-Carlo yielded an uncertainty of 3.5% on the yield. The acceptance of neutral pions depends on the kinematics of two decay photons. For single photons the uncertainty on the acceptance is therefore assumed to be smaller. Therefore an uncertainty of 2.5% on the yield was assigned to the acceptance correction of the inclusive photon spectrum. Tests in which the corresponding parameters of the maximum tower parameterization in the fast Monte-Carlo were changed confirmed this uncertainty.

**Photon Conversion:** As was stated in Section 7.3.2 the absolute uncertainty on the conversion probability was estimated to be  $\pm 0.02$  for both PbGl and PbSc. Because of the small conversion probability compared to unity this translates to an relative error on the photon yield of approximately 2%.

**Charged Background:** The uncertainty on the charged correction is determined by the uncertainty of the PC3 efficiency (see Table 7.7). The uncertainty due to the combinatorial background in the  $X_{\text{ch}}$  analysis can be neglected. An uncertainty of  $\Delta \epsilon_{\text{PC3}} = \pm 5\%$  was assigned to the PC3 efficiency by comparing  $\epsilon_{\text{PC3}}$  obtained with the two methods described in Section 7.3.2. Translating the uncertainty  $\Delta \epsilon_{\text{PC3}}$  to the photon yield results in an relative uncertainty of approximately 1%.

**Neutral Background:** The correction of neutrons and antineutrons is based on simulations (see Section 7.3.2). Since the correction is very small above  $p_T = 3 \text{ GeV}/c$  the uncertainty has only a very minor effect. However, comparison of the simulation results employed in this analysis to simulations used in [Aki05] imply an uncertainty on the

---

<sup>16</sup>The possible misalignment of the EMCAL found in [Per05] justifies this additional systematic uncertainty in Run III (see Section 7.2.5).

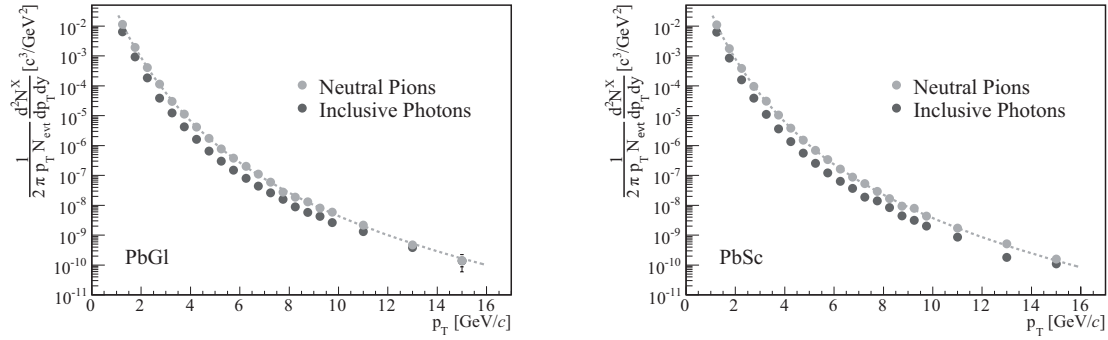


**Figure 7.25:** The Lorentz invariant yield of neutral pions and inclusive photons measured with the PbGl and PbSc in Run III  $p + p$ . The data points of the  $\pi^0$  spectrum are taken from [Bat05a]. The dotted lines represent fits to the  $\pi^0$  spectrum. The parameterization of the neutral pion spectrum is also given by Equation 7.19.

yield due to the neutral background correction of the order of 1%.

**BBC Cross Section and Trigger Bias:** The uncertainty on the BBC cross section  $\sigma_{BBC}$  in Run III was determined to be 9.7% [Baz05], while the fraction of photons in minimum bias events that hit the EMCAL  $\varepsilon_\gamma$  is known with an accuracy of 2.5% [Baz05]. Since both corrections enter the cross section calculation as scaling factors the relative uncertainty can be directly translated to the yield uncertainty. Note that the same uncertainties are employed in the neutral pion analysis of Run III  $p + p$ .

## 7.4 The Measured $\gamma/\pi^0$ Ratio

The analysis of direct photons presented in this thesis is based on the cocktail method, in which the direct-photon signal is determined as a fraction of the inclusive photon spectrum (see Equation 7.2). The determination of inclusive photons from the raw cluster spectrum measured with the PHENIX EMCAL was described in detail in Section 7.3. The fraction of direct photons in the yield of inclusive photons (also called the photon excess), however, is not derived from the inclusive photon spectrum directly. Instead the yield of inclusive photons is calculated per neutral pion in the same  $p_T$  bin. This has the advantage that many systematic uncertainties which have the same origin in the photon and neutral pion analysis cancel in the  $\gamma/\pi^0$  ratio (this will be described in more detail in Section 7.4.1).

In order to calculate the inclusive photon production per  $\pi^0$  the measured inclusive  $\pi^0$  spectrum must be known. The spectrum of neutral pions in Run III  $p + p$  was determined in an independent analysis using the same data set [Bat05b, Bat05a]. Neutral pions are

measured via their decay into two photons with a branching ratio of 98.8%. Neutral pions are reconstructed from the data via the determination of the invariant mass of measured photon pairs. The photon analysis presented in this thesis and the neutral pion analysis are related in many ways: they utilize the same energy calibration of the EMCal, employ the same fast Monte-Carlo code for the calculation of the geometric acceptance and reconstruction efficiency, apply the same PID cuts and exclude the same bad towers from the analysis. This ensures that many of the systematics of the analyses are similar and cancel to some extent in the ratio of the spectra. Figure 7.25 shows the Lorentz invariant yield of neutral pions and inclusive photons as measured with the PHENIX EMCal in Run III  $p + p$ . The data points of the  $\pi^0$  spectrum are taken from [Bat05a] and are listed in Appendix E.2. Only statistical uncertainties are shown (visible only at the highest transverse momentum in PbGl). Systematic uncertainties will be discussed in Section 7.4.1. Unlike the distribution of inclusive photons the  $\pi^0$  spectrum shown in Figure 7.25 is corrected for shower merging. The dotted lines in Figure 7.25 represent a fit to the measured neutral pion spectrum. Analogous to the inclusive photon spectrum the shape of the  $p_T$  distribution is well described by a combination of a Hagedorn function at low  $p_T$  and a power law at high  $p_T$  (see Equation 7.19). When calculating the measured  $\gamma/\pi^0$  ratio the inclusive photon spectrum is divided by the parameterization rather than the data points. By doing this the statistical uncertainty of the measured neutral pion spectrum is propagated to the systematic uncertainty of the fit (see Section 7.4.1). The measured  $\gamma/\pi^0$  ratios for the PbGl and PbSc are shown in Figure 7.26. Only statistical uncertainties (i.e. the statistical uncertainty of the measured inclusive photon spectrum) are shown. If only decay photons would contribute to the inclusive photon spectrum the  $\gamma/\pi^0$  ratio would level off at a constant (see Section 7.5) determined by the power of the power law that describes the spectrum of the decaying particle at large transverse momenta. Figure 7.26 indicates a rise of the spectrum towards high  $p_T$  implying an excess of photons due to direct photons.

### 7.4.1 Systematic Uncertainties of the Measured $\gamma/\pi^0$ Ratio

The total systematic uncertainty of the measured  $\gamma/\pi^0$  ratio includes besides the systematic errors of the inclusive photon spectrum discussed in Section 7.3.4 also the systematic errors of the neutral pion analysis. Table 7.11 lists all dominant sources that contribute to the total systematic uncertainty of the measured  $\gamma/\pi^0$  ratio. The uncertainty due to the  $\pi^0$  peak extraction and the  $\pi^0$  shower merging correction are directly adopted from the  $\pi^0$  analysis [Bat05a]. The uncertainties due to the charged and neutral background are unique to the photon measurement and are therefore identical to the uncertainties specified in Table 7.10. The strength of using  $\gamma/\pi^0$  ratios is the fact that some systematic uncertainties of the analyses cancel in the ratio. This is particularly true for the global energy scale. However, in the ratio of the photon and  $\pi^0$  spectra the linearity of the

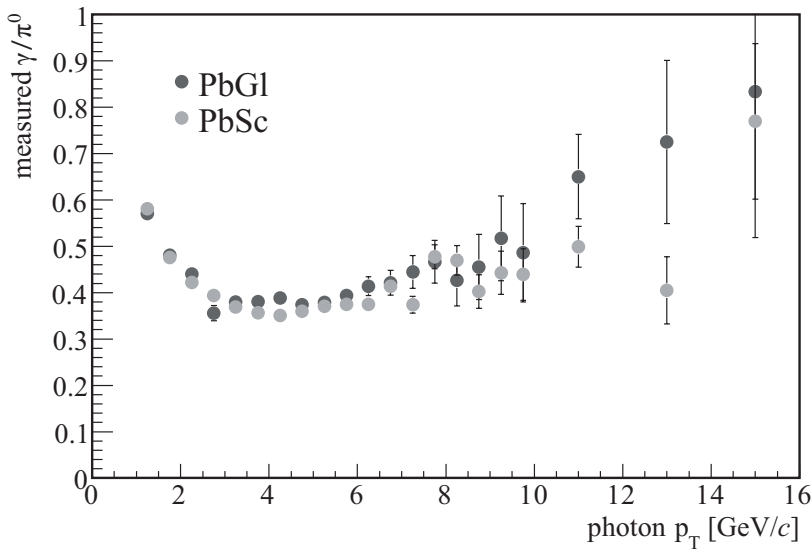


**Figure 7.26:** The measured  $\gamma/\pi^0$  ratio in the PbGl and PbSc. For the  $\pi^0$  spectrum the parameterization is used rather than the data points. The error bars represent the statistical uncertainties of the measured inclusive photon spectrum.

energy scale becomes important. The estimation of the various systematic uncertainties of the measured  $\gamma/\pi^0$  ratio is discussed in the following. Table 7.11 summarizes the estimated uncertainties for the PbGl and PbSc in three different  $p_T$  bins. All systematic errors of the  $\gamma/\pi^0$  ratio are considered to be of type A (see Section 7.10).

**$\pi^0$  peak extraction and shower merging:** Both uncertainties are adopted from the Run III  $p + p$  neutral pion analysis. While the uncertainty of the  $\pi^0$  yield due to the  $\pi^0$  extraction method shows only a small  $p_T$ -dependence but is significant for all  $p_T$ , the uncertainty due to the shower merging correction becomes significant only at the largest  $p_T$  bin, which is due to the negligible shower merging correction at smaller  $p_T$ . More details can be found in [Bat05b, Bat05a].

**$\pi^0$  Parameterization:** Instead of the  $\pi^0$  data points a parameterization of the form given in Equation 7.19 is used in the calculation of the measured  $\gamma/\pi^0$  ratio. The parameters of the functional form are determined by fitting Equation 7.19 to the measured data points of the neutral pion spectrum taking the statistical uncertainties into account as weights. Since the statistical point-by-point fluctuations are smoothed out by using a fit to the data points the statistical uncertainty of the neutral pion spectrum must be propagated to the systematic uncertainty of the parameterization.

Systematic Errors of the Measured $\gamma/\pi^0$ Ratio in PbGl (PbSc)				
	$p_T$ indep.	5-5.5 GeV/c	9.5-10 GeV/c	14-16 GeV/c
peak extraction		2.2% (2.2%)	2.1% (2.1%)	2.1% (2.1%)
$\pi^0$ merging		0.0% (0.0%)	0.0% (0.0%)	2.1% (5.9%)
$\pi^0$ fit		1.8% (1.2%)	6.2% (3.3%)	11.0% (5.9%)
efficiency	1.9% (1.1%)			
global energy scale		0.2% (0.2%)	0.2% (0.1%)	0.6% (0.5%)
non-linearity	7.0% (7.0%)			
acceptance	0.5% (0.5%)			
photon conversion	2.0% (2.0%)			
charged background	1.0% (1.0%)			
neutral background	1.0% (1.0%)			
quadratic sum		8.2% (7.9%)	10.1% (8.5%)	13.7% (11.4%)

**Table 7.11:** Systematic uncertainties of the measured  $\gamma/\pi^0$  ratio in the PbGl (PbSc) in three different  $p_T$  bins. All errors are considered to be of type A. Some errors like the  $\pi^0$  peak extraction or the charged background are unique to the neutral pion respectively photon analysis and are therefore identical to the uncertainty of the corresponding spectrum. Other errors like the global energy scale which have the same origin in the  $\pi^0$  and photon analysis cancel to some extent.

The error propagation was done according to the procedure described in [Bat05c] for the PbGl and PbSc spectrum separately. When fitting a parameterization to a spectrum of measured data points, where the statistical errors are used as weight, the errors of the fitted parameters reflect the statistical uncertainties of the measured spectrum. However, assuming a parameterization implies the knowledge of the functional form of the measured spectrum. Hence the uncertainties of the parameters are expected to become smaller than the actual uncertainties of the data points. A slightly modified parameterization compared to Equation 7.19 with six free parameters was used. In order to estimate the uncertainty of the parameterization in a certain  $p_T$  bin each parameter was changed according to its error given by the default fit in the positive and negative  $y$ -direction. Only one parameter was changed and fixed at a time and the fit was repeated with the other five parameters as the free parameters of the fit. This procedure results in twelve additional fits. The deviation of these fits to the default one is illustrated in Figure 7.27 for the PbGl and PbSc. The black solid lines are the twelve fits with changed parameters divided by the default fit. The grey histogram denotes the envelope of the ratios which indicates the propagated statistical error from the data points to the parameterization. The statistical errors of the data points allow point-by-point fluctuations, i.e. they can be considered as

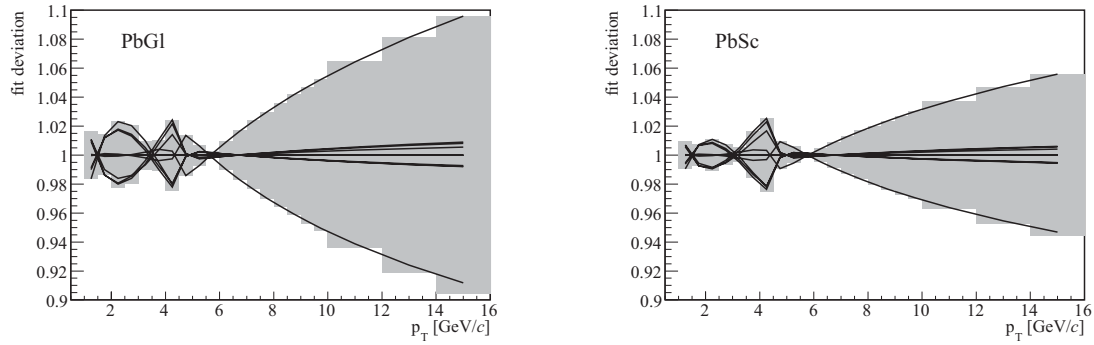


**Figure 7.27:** Error propagation of the  $p_T$ -uncorrelated statistical uncertainty of the measured neutral pion spectrum to a systematic  $p_T$ -correlated uncertainty of the  $\pi^0$  parameterization (grey histogram) for the PbGl and PbSc. The black solid lines represent the ratio of the twelve fits to the  $\pi^0$  spectrum with one changed and fixed parameter and the default fit. The grey histogram is the envelope of the twelve ratios.

$p_T$ -uncorrelated. However, due to the assumption of a functional form that describes the spectrum the statistical errors are propagated into a  $p_T$ -correlated systematic uncertainty, i.e. all points move in the same direction but not necessarily by the same amount (type A).

The result of the error propagation shown in Figure 7.27 was checked with a slightly different approach. Rather than changing the fit parameters the data points of the  $\pi^0$  spectrum were shifted randomly by their statistical errors in the positive or negative  $y$ -direction. The changed data spectrum was then fitted with the parameterization given in Equation 7.19 and the deviation to the default parameterization in each  $p_T$  bin of the  $\pi^0$  spectrum was calculated. This procedure was repeated 500 times which resulted in a Gaussian distribution of deviations from the default parameterization in each  $p_T$  bin. The propagated uncertainty was extracted by calculating the sigma of each distribution. The result is shown in Figure 7.28 for the PbGl and PbSc (data point variation (sigma)). In addition the maximum uncertainty given by the distributions in each  $p_T$  bin (data point variation (max)) along with the uncertainty derived by changing the fit parameters (fit variations) and the statistical error of the data points are shown. It is obvious from the figure that both methods yield a similar result for the propagated error when considering  $1\sigma$  errors. Moreover, as expected the knowledge of the functional form of the spectrum strongly reduces the statistical uncertainty in the propagation to the parameterization. However, it should be noted that this estimation does not include any systematic uncertainty due to the choice of the functional form. For the measured  $\gamma/\pi^0$  ratio the uncertainties obtained with the fit parameter variation method are applied.

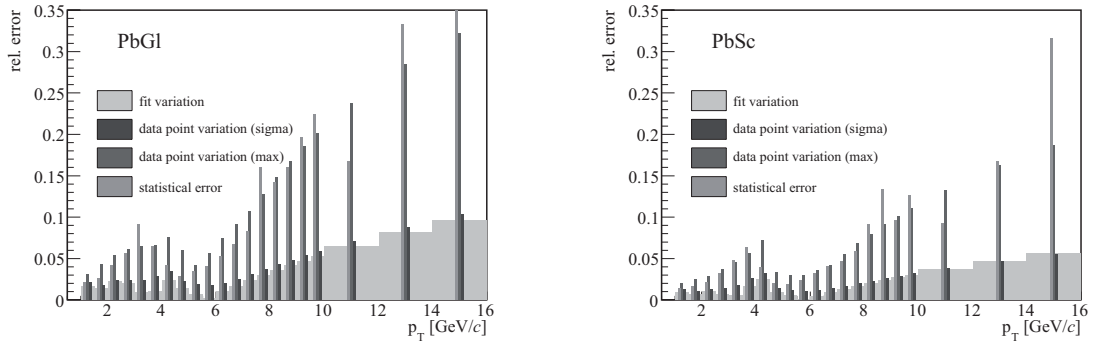


**Figure 7.28:** The relative systematic error of the fit to the  $\pi^0$  spectrum in the PbGl and PbSc obtained with two different methods. The uncertainties obtained by changing the fit parameters agree with the uncertainties obtained by changing the data points when considering  $1\sigma$  errors. Also shown is the uncertainty obtained by changing the data points and considering the maximum possible error. Comparison to the statistical errors of the data points shows how the uncertainty is reduced when propagated to the parameterization when changing the fit parameters or considering  $1\sigma$  errors in the data point variation method.

**Reconstruction Efficiency:** The efficiency calculations in the  $\pi^0$  and the photon analysis are similar to some extent. However, the detection of neutral pions depends on the reconstruction of the invariant mass of two photons inside a certain mass window. The limited energy resolution of the EMCAL can result in a shift of the invariant mass of a  $\pi^0$  decay photon pair out of the accepted mass window. Such photon pairs are lost which affects the reconstruction efficiency. The uncertainty on the  $\gamma/\pi^0$  ratio due to the uncertainty of the limited energy resolution of the EMCAL was studied in a similar way as for single photons.<sup>17</sup> An additional constant energy smearing of 2% was introduced in the fast Monte-Carlo and the additionally smeared  $\gamma/\pi^0$  ratio was compared to the  $\gamma/\pi^0$  ratio obtained with the default smearing. The result for the PbGl and PbSc is shown in Figure 7.29. The uncertainty due to the energy smearing uncertainty cancels partially in the  $\gamma/\pi^0$  ratio. It is constant above  $p_T = 2 \text{ GeV}/c$  being approximately 2% in the PbGl and 1% in the PbSc. The black solid line represents a constant fit to the simulated data points for  $p_T > 2 \text{ GeV}/c$ .

**Global Energy Scale:** The uncertainty of the global energy scale is 1.2% as stated in the discussion on the systematic uncertainties of the inclusive photon measurement. The effect of this uncertainty on the  $\gamma/\pi^0$  ratio was estimated in the same way. The energy scale

<sup>17</sup>The spectrum of neutral pions is simulated with a flat  $p_T$  distribution and subsequently weighted by the measured  $\pi^0$  spectrum. The decay photons in the acceptance of the detector are smeared according to the parameters in the fast Monte-Carlo. Pairs of smeared photons are counted as neutral pions if their invariant mass is reconstructed within the same mass window as used in the analysis of the data.

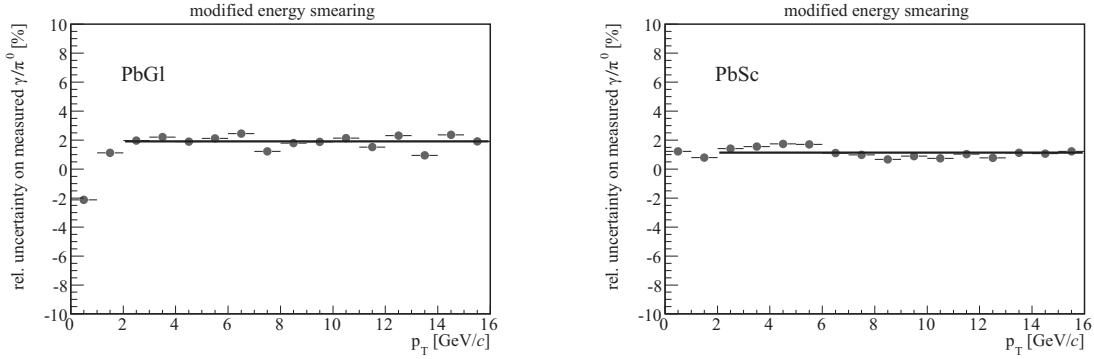


**Figure 7.29:** Effect of the energy smearing uncertainty on the  $\gamma/\pi^0$  ratio in the PbGl and PbSc.

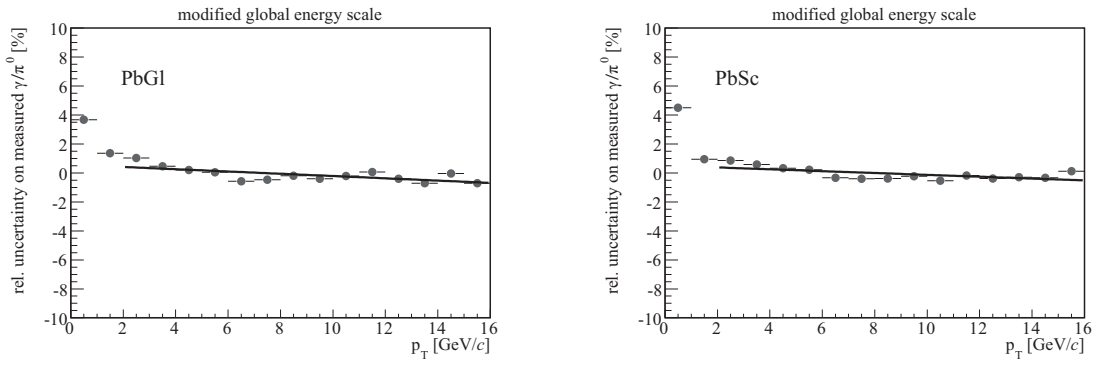


**Figure 7.30:** Uncertainty of the measured  $\gamma/\pi^0$  ratio due to the global energy scale uncertainty for the PbGl and PbSc. The uncertainty almost cancels completely in the ratio. The black solid line is a polynomial of first order fitted to the simulated data points. The uncertainty is  $\lesssim 0.5\%$  for all  $p_T$ .

was changed by 1.2% in the fast Monte-Carlo and the smeared  $\gamma/\pi^0$  ratio was compared to the smeared  $\gamma/\pi^0$  ratio with the default energy scale. The result is shown in Figure 7.30 for the PbGl and PbSc. The uncertainty due to the global energy scale cancels almost completely in the  $\gamma/\pi^0$  ratio. This is expected since the uncertainty is independent of  $p_T$  and identical in the photon and  $\pi^0$  analysis. The solid black line is a polynomial of first order fitted to the simulated data points. The uncertainty is  $\lesssim 0.5\%$  for the entire  $p_T$  range.

**Energy Non-Linearity:** As discussed in Section 5.2 the EMCAL suffers from non-linearity effects on the energy scale which are taken into account in the DST production and in the energy calibration using the  $\pi^0$  mass peak (Section 7.2.5). The systematic uncertainty of the inclusive photon yield introduced by the non-linearity of the scale is covered by the global energy scale error. This is illustrated in Figure 7.31(a). It shows schematically the influence of a possible non-linearity on the measured energy compared

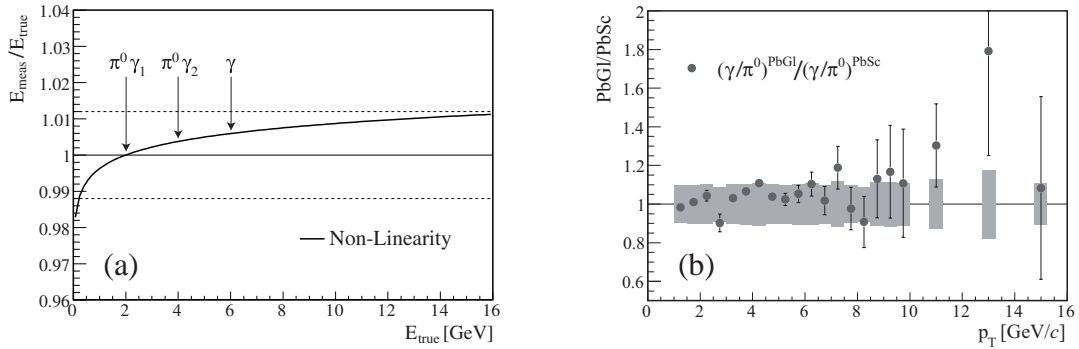


**Figure 7.31:** (a) Schematic illustration of the non-linearity of the energy scale in the EMCAL (solid line). The functional form is based on light attenuation in the detector material and normalized at  $E = 2$  GeV. The dotted lines indicate the uncertainty of the global energy scale. The non-linearity is therefore covered by the uncertainty of the global scale in the measurement of single photons. The arrows indicate the different non-linearities which are experienced by the photons of the  $\gamma/\pi^0$  ratio at a certain  $p_T$ . See text for explanation. (b) Estimation of the uncertainty of the measured  $\gamma/\pi^0$  ratio due to the energy non-linearity using the measured double  $\gamma/\pi^0$  ratio PbGl/PbSc.

to the true energy as a function of the true photon energy. The dotted line represents the uncertainty of the global energy scale of  $\pm 1.2\%$ . The functional form of the non-linearity (solid line) is motivated by light attenuation in the material which depends on the shower depth. The energy scale is best known around  $E \approx 2$  GeV/c hence the estimated non-linearity is normalized at this transverse momentum.

A neutral pion with a certain  $p_T$  is reconstructed from two decay photons which both have transverse momenta that differ from the  $\pi^0 p_T$ . Therefore, in a certain  $p_T$  bin of the measured  $\gamma/\pi^0$  ratio the corresponding photons are subject to different non-linearities. This is indicated in Figure 7.31(a) for a  $\gamma/\pi^0$  ratio at  $p_T = 6$  GeV/c. The inclusive photon ( $\gamma$ ) experiences a different non-linearity than the two decay photons ( $\gamma_1$  and  $\gamma_2$ ). Hence, although the global scale uncertainty almost cancels completely in the ratio this is not expected for the linearity of the energy scale. This was confirmed by fast Monte-Carlo simulations in which the energy scale was shifted according to a non-linearity similar to the function illustrated in Figure 7.31(a). However, rather than using an *ad-hoc* parameterization to describe the non-linearity of the energy scale<sup>18</sup> the measured  $\gamma/\pi^0$  ratios in the PbGl and PbSc were used to estimate the uncertainty of the  $\gamma/\pi^0$  ratio due to the linearity. The assumption is that the difference between PbGl and PbSc arises only

<sup>18</sup>The non-linearity depends on the material and the detection mechanism of the EMCAL. Both are different for the PbGl and PbSc. Moreover, not only attenuation but also leakage affects the linearity of the detectors. All of this is difficult to be taken correctly into account in a simple parameterization.

from the non-linearity of the two detector subsystems because all other uncertainties either cancel in the ratio or are correlated between PbGl and PbSc. Correlated errors only allow a shift in the same direction and therefore cannot explain any differences between two measurements. The PbGl/PbSc ratio of the  $\gamma/\pi^0$  ratios is shown in Figure 7.31(b). An uncertainty of 7% was assigned to the  $\gamma/\pi^0$  ratios in each EMCal subsystem due to the non-linearity. This results in an error on the PbGl/PbSc ratio indicated by the grey boxes in Figure 7.31(b) which covers the observed difference between PbGl and PbSc.

**Geometric Acceptance and Photon Conversion:** Both uncertainties are expected to cancel to some extent in the  $\gamma/\pi^0$  ratio. For the acceptance correction an uncertainty of 0.5% independent of  $p_T$  was assigned to the ratio. Since the neutral pion decays into two photons the uncertainty due to the photon conversion correction is assumed to cancel only once. The uncertainty assigned to the  $\gamma/\pi^0$  ratio is therefore identical to the uncertainty estimated for single photons (2%, see Section 7.3.4).

**Charged and Neutral Background:** The correction of charged and neutral clusters is unique to the photon analysis and therefore the uncertainty of 1% can be directly adopted for the  $\gamma/\pi^0$  ratio (see Section 7.3.4).

**BBC Cross Section and  $\varepsilon_\gamma$ :** The uncertainties of  $\sigma_{\text{BBC}}$  and  $\varepsilon_\gamma$  cancel completely in the  $\gamma/\pi^0$  ratio since the corresponding corrections are scaling factors of the corresponding yield independent of  $p_T$ .

## 7.5 The Simulated $\gamma/\pi^0$ Ratio

The spectrum of measured photons per  $\pi^0$  derived in the previous section contains direct photons and background photons from hadronic decays. In order to extract the signal of direct photons the background must be subtracted. The background cocktail is determined with the help of a fast Monte-Carlo simulation<sup>19</sup>. The simulation requires a parameterization of the measured neutral pion spectrum as input. As was mentioned in the previous section a functional form given by Equation 7.19 was chosen. Within the fast Monte-Carlo neutral pions are generated with a  $p_T$ , rapidity and  $z$ -vertex distribution equal to the distributions employed for single photons. However, the rapidity range for neutral pions is extended to  $\Delta y = \pm 1.0$  around mid-rapidity since  $\pi^0$ 's with  $|\eta| > 0.45$  can also emit photons in the rapidity range  $|\eta| < 0.45$ . Each neutral pion then decays according to the possible branching ratios (see Table 7.12) and the spectrum of decay photons that

---

<sup>19</sup>The same code which was used to simulate the efficiencies and the geometric acceptance.

hit the active area of the EMCal is recorded weighted according to the  $p_T$  distribution of the measured neutral pion spectrum. The acceptance correction derived in Section 7.3.2 is applied to determine the yield of decay photons in the rapidity interval  $|y| < 0.45$ . The background of decay photons is then given as a function of transverse momentum per  $\pi^0$ , the simulated  $\gamma/\pi^0$  ratio. This has the advantage that no absolute normalization is necessary, i.e. only the shape of the  $\pi^0$   $p_T$  distribution must be known.

$\pi^0$  decays account for a large portion of the background but nevertheless are not the only source. Other contributions to the *background cocktail* which are considered in the simulation come from  $\eta$ ,  $\omega$  and  $\eta'$  decays. In principle the corresponding hadronic  $p_T$  distribution must be known in order to simulate their contribution to the cocktail. However, since the hadronic spectra of  $\eta$ ,  $\omega$  and  $\eta'$  are not measured with sufficient accuracy in  $p + p$  reactions at  $\sqrt{s} = 200$  GeV their contribution was estimated from the measured neutral pion spectrum using the so-called  $m_T$ -scaling method. Details of the background simulation are given in the following section.

### 7.5.1 Background Cocktail

The hadrons considered in the simulation of the decay background are listed in Table 7.12. The dominant decay branches that have a photon in the final state are shown with the respective branching ratio [Yao06]. Decay branches with a  $\pi^0$  in the final state which subsequently decay after a very short life time into two photons are not considered since they are already included in the measured neutral pion spectrum.

The shape of the  $p_T$ -distribution for the  $\eta$ ,  $\omega$  and  $\eta'$  is determined via  $m_T$ -scaling. The underlying idea depends on the phenomenological observation that the shape of a hadronic spectrum when expressed as a function of the transverse momentum  $m_T$  does not depend on the hadronic species  $h$ . In other words the  $m_T$ -distributions of different hadrons differ only by a constant factor [Bou76]:

$$E \frac{d\sigma_h}{d\vec{p}^3} = C_h \cdot f(m_T), \quad (7.32)$$

where  $f(m_T)$  is the production cross section of a hadron as a function of  $m_T$  and  $C_h$  is a constant scaling factor. The  $\eta$  and  $\omega$  spectra were measured by PHENIX and the scaling factor relative to the  $\pi^0$  measurement was determined to be  $C_\eta/C_{\pi^0} = 0.48 \pm 0.03$  [Adl06a] and  $C_\omega/C_{\pi^0} = 1.0 \pm 0.5$  [Rya06], respectively. The  $\eta'$  production ratio with respect to the  $\pi^0$  measurement was not measured by PHENIX but is taken from [Adl05a]. In the background simulation the spectrum of decay photons from  $\eta$ ,  $\omega$  and  $\eta'$  decays are weighted according to  $m_T$ -scaling using the shape of the measured neutral pion spectrum and the hadron production ratios  $C_h/C_{\pi^0}$  given in Table 7.12. The result of the simulation, i.e. the  $\gamma/\pi^0$  ratios for the different hadron species, is shown in Figure 7.32 as determined

hadron $h$	$C_h/C_{\pi^0}$	decay branch	branching ratio
$\pi^0$	1.0	$\pi^0 \rightarrow \gamma\gamma$	98.8%
		$\pi^0 \rightarrow e^+e^-\gamma$	1.2%
$\eta$	$0.48 \pm 0.03$	$\eta \rightarrow \gamma\gamma$	39.42%
		$\eta \rightarrow \pi^+\pi^-\gamma$	4.68%
		$\eta \rightarrow e^+e^-\gamma$	0.6%
		$\eta \rightarrow \mu^+\mu^-\gamma$	0.03%
$\omega$	$1.0 \pm 0.5$	$\omega \rightarrow \pi^0\gamma$	8.9%
		$\omega \rightarrow \pi^0\pi^0\gamma$	0.007%
$\eta'$	$0.25 \pm 0.13$	$\eta' \rightarrow \rho^0\gamma$	29.5%
		$\eta' \rightarrow \omega\gamma$	3.03%
		$\eta' \rightarrow \gamma\gamma$	2.12%

**Table 7.12:** List of hadrons considered in the simulation of the decay background. The production ratios  $C_h/C_{\pi^0}$  are employed in the  $m_T$ -scaling. The branching ratios of the dominant decay branches are taken from [Yao06].

from the  $\pi^0$  spectrum in the PbGl. As stated before the main contribution comes from  $\pi^0$  decays (81%). The contributions of the remaining hadrons are 15% ( $\eta$ ), 3% ( $\omega$ ) and 0.5% ( $\eta'$ ).

### 7.5.2 Effect of Shower Merging

As discussed in Section 7.3.3 a fraction of the  $\pi^0$  decay photons is removed from the measured inclusive photon spectrum by the shower shape cut due to shower merging. This biased spectrum is denoted as  $\gamma_{w/o}^{incl}$  in the following. When calculating the signal of direct photons using  $\gamma_{w/o}^{incl}$  via  $\gamma_{biased}^{direct} = \gamma_{w/o}^{incl} - \gamma^{decay}$  (see Equation 7.2) it becomes immediately clear that the extracted direct-photon signal  $\gamma_{biased}^{direct}$  is also biased if the effect of shower merging is not taken into account in the calculation of the background  $\gamma^{decay}$ . The direct-photon spectrum would be distorted at large transverse momenta. Therefore, the shower merging probability of  $\pi^0$  decay photons,  $p_\gamma^{merging}$ , introduced in Section 7.3.3, is applied in the background simulation to remove the same fraction of  $\pi^0$  decay photons as is removed in the real data by shower merging in conjunction with the shower shape cut. The resulting spectrum of decay photons is denoted as  $\gamma_{w/o}^{decay}$ . However,  $\gamma_{w/o}^{decay}$  is not determined directly in the simulation. Instead the number of decay photons per  $\pi^0$  is

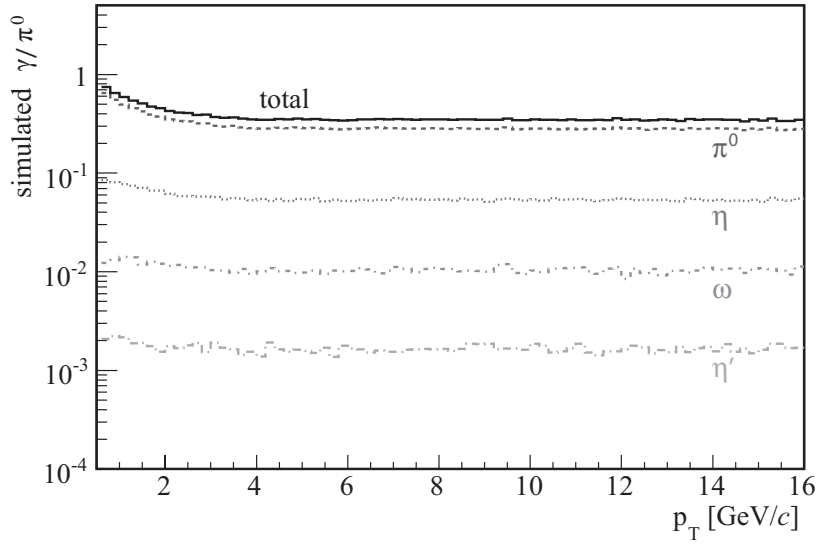


**Figure 7.32:** Simulated  $\gamma/\pi^0$  ratio for the various contributions from  $\pi^0$ ,  $\eta$ ,  $\omega$  and  $\eta'$  decays. The sum of all hadronic decays is shown by the solid line (total). The shape of the hadronic spectra is based on the measured  $\pi^0$  spectrum in the PbGl.

calculated, i.e. in case of  $\pi^0$  decay photons the ratio  $(\gamma^{\pi^0}/\pi^0)_{\text{sim}}^{\text{w/o}}$  is simulated, which is also used in the calculation of the unbiased reconstruction efficiency (see Section 7.3.3). According to Equation 7.2 the unbiased direct-photon spectrum can be calculated as follows:

$$\gamma^{\text{direct}} = \gamma_{\text{w/o}}^{\text{incl}} - \gamma_{\text{w/o}}^{\text{decay}} = \left(1 - \frac{1}{R_{\gamma}^{\text{w/o}}}\right) \cdot \gamma_{\text{w/o}}^{\text{incl}}. \quad (7.33)$$

The background cocktail comprises photons from  $\pi^0$ ,  $\eta$ ,  $\omega$  and  $\eta'$  decays. Only  $\pi^0$  decay photons are subject to shower merging in the analyzed  $p_T$  region due to the higher mass of the other mesons. Therefore only  $(\gamma^{\pi^0}/\pi^0)_{\text{sim}}^{\text{w/o}}$  needs to be calculated. Contributions to  $\gamma/\pi^0$  from other hadronic decays are calculated as described above.

In the simulation the spectrum of  $\pi^0$  decay photons consists of two components:

1. Both  $\pi^0$  decay photons hit active towers of the EMCal.
2. Only one  $\pi^0$  decay photon hits an active tower of the EMCal.

Only photons of the first component can suffer from shower merging and hence photons are only removed from this sample according to the shower merging probability of  $\pi^0$

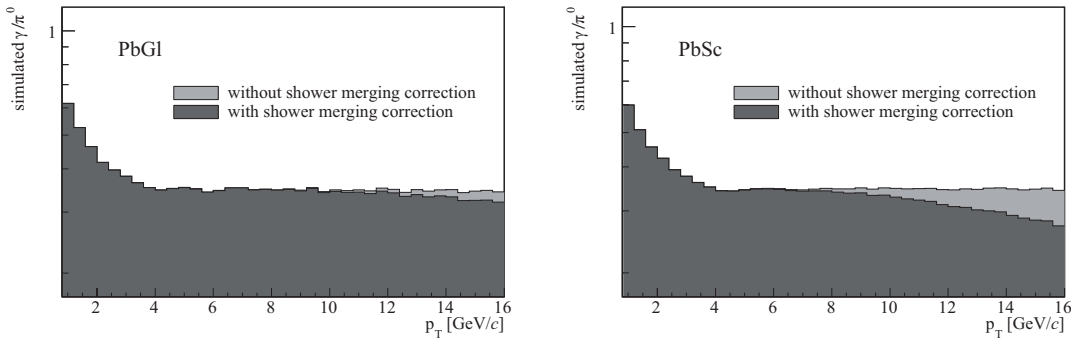


**Figure 7.33:** Illustration of the shower merging effect on the simulated  $\gamma/\pi^0$  ratio in the PbGl and PbSc. Merged clusters are removed on a statistical basis from the spectrum of  $\pi^0$  decay photons. The loss of photons due to shower merging is more pronounced in the PbSc because of the coarser granularity compared to the PbGl.

decay photons<sup>20</sup>.  $(\gamma^{\pi^0}/\pi^0)_{\text{sim}}^{\text{w/o}}$  is then given as the sum of both components after the removal of merged clusters from the first component.

The simulated  $\gamma/\pi^0$  ratio (including decays of all considered hadrons) before and after the removal of merged clusters is shown in Figure 7.33 for the PbGl and PbSc. The loss of photons in the PbSc due to shower merging ranges from 4.1% at  $p_T = 9 - 10 \text{ GeV}/c$  to 19.7% at  $p_T = 15 - 16 \text{ GeV}/c$ , while in the PbGl the loss ranges from 0.6% to 6.4% in the same  $p_T$  range. As noted before the PbGl is less affected by shower merging because of its finer granularity. Table 7.13 gives the photon loss in different  $p_T$  bins in the PbGl and PbSc derived from the fast Monte-Carlo simulation. The simulated  $\gamma/\pi^0$

<sup>20</sup>The merging probability is determined in a similar way. Only photon pairs are considered if both hit active towers of the EMCAL.

$p_T$ [GeV/c]	photon loss [%]	
	PbGl	PbSc
7-8	0.2	1.3
9-10	0.6	4.1
11-12	1.8	8.5
13-14	3.8	13.9
15-16	6.4	19.7

**Table 7.13:** Photon loss due to shower merging in different  $p_T$  bins in the two EMCAL subsystems. The effect is less significant in the PbGl because of its finer granularity.

Systematic Errors of the Simulated $\gamma/\pi^0$ Ratio in PbGl (PbSc)				
	$p_T$ indep.	5-5.5 GeV/c	9.5-10 GeV/c	14-16 GeV/c
$\gamma$ shower merging		0.1% (0.3%)	0.6% (2.5%)	2.9% (8.2%)
hadron/ $\pi^0$		2.7% (2.7%)	2.8% (2.8%)	3.1% (3.1%)
quadratic sum		2.7% (2.7%)	2.9% (3.8%)	4.2% (8.8%)

**Table 7.14:** Systematic uncertainties of the simulated  $\gamma/\pi^0$  ratio in three different  $p_T$  bins in the PbGl (PbSc). The uncertainties are considered to be of type A. The uncertainty due to shower merging becomes significant only at high transverse momentum where the correction becomes relevant. Since the correction is larger in the PbSc the uncertainty is also larger in the PbSc. The uncertainty due to the error of the hadron/ $\pi^0$  ratios ( $C_h/C_{\pi^0}$ ) is identical for the PbGl and PbSc since the shape of the simulated  $\gamma/\pi^0$  ratio is very similar in PbGl and PbSc.

ratio after the removal of merged clusters from  $\pi^0$  decays is used to calculate the double ratio  $R_\gamma^{w/o}$  which is then used to calculate the unbiased direct-photon signal according to Equation 7.33.

### 7.5.3 Systematic Uncertainties of the Simulated $\gamma/\pi^0$ Ratio

The uncertainty of the simulated background cocktail is dominated by two sources: the correction of shower merging and the hadron/ $\pi^0$  ratios applied in the  $m_T$ -scaling. Both sources result in a  $p_T$ -correlated uncertainty of the simulated  $\gamma/\pi^0$  ratio of type A. Table 7.14 shows the uncertainties of the simulated  $\gamma/\pi^0$  ratio for three different  $p_T$  bins for the PbGl (PbSc).

**Shower Merging:** The probability of shower merging in the EMCal is simulated with the help of a fast Monte-Carlo (see Section 7.3.3). The uncertainty of the corresponding correction is determined by three factors [Bat05b]:

1. shower profile parameterization
2. global energy scale
3. energy non-linearity

The corresponding parameters were changed in the Monte-Carlo according to the assigned errors, i.e. the energy scale was shifted by  $\pm 1.2\%$ . To estimate the error due to the energy non-linearity the energy scale was multiplied by a parameterization similar to

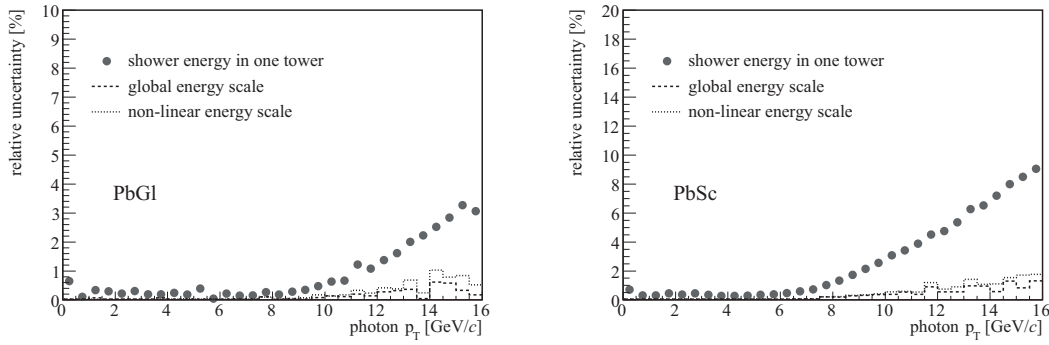


**Figure 7.34:** Uncertainties of the shower merging probability due to the uncertainty of the shower parameterization, global energy scale and energy scale non-linearity in the PbGl and PbSc.

the function illustrated in Figure 7.31(a)<sup>21</sup>. The uncertainty due to the parameterization of the shower shape was estimated in a very conservative way: the shower merging correction was calculated for the extreme case that each shower deposits all its energy in one single tower. For each modified simulation the shower merging probability  $p_\gamma^{\text{merging}}$  was calculated. The deviation from the default probability is shown in Figure 7.34 for the PbGl and PbSc. The uncertainty due to the energy scale is small compared to the shower parameterization and is therefore neglected. The uncertainty due to the shower shape parameterization becomes significant for  $p_T \gtrsim 12$  GeV/c ( $p_T \gtrsim 8$  GeV/c) in the PbGl (PbSc). Note the different scales in Figure 7.34 for PbGl and PbSc. The uncertainty of  $p_\gamma^{\text{merging}}$  translates to the uncertainty of the simulated  $\gamma/\pi^0$  ratio shown in Table 7.14 for three different  $p_T$  bins.

**Hadron/ $\pi^0$  Ratios:** The hadron/ $\pi^0$  ratios ( $C_h/C_{\pi^0}$ ) used in the  $m_T$ -scaling are listed in Table 7.12. The stated uncertainties of the ratios are propagated to the simulated  $\gamma/\pi^0$  ratio by shifting all parameters by the error in the positive and negative direction. The resulting  $\gamma/\pi^0$  ratios are shown in Figure 7.35(a) together with the ratio using the default hadron/ $\pi^0$  ratios. The deviation depends only on the absolute uncertainty of the hadron/ $\pi^0$  ratio but not on the sign. The relative deviation of the shifted simulated  $\gamma/\pi^0$  ratios from the default ratio is shown in Figure 7.35(b). The error above  $p_T = 3$  GeV/c is approximately 3% with only a slight  $p_T$  dependence. The uncertainty does not depend on the EMCAL subsystem since the shape of the simulated  $\gamma/\pi^0$  ratio is very similar in PbGl and PbSc (see the  $\gamma/\pi^0$  ratios without shower merging in Figure 7.33) and so the error is determined only by the uncertainties of the hadron/ $\pi^0$  ratios.

<sup>21</sup>For the estimation of the error of the shower merging correction due to the energy non-linearity it was decided that the usage of an *ad-hoc* parameterization to describe the non-linearity is sufficient.

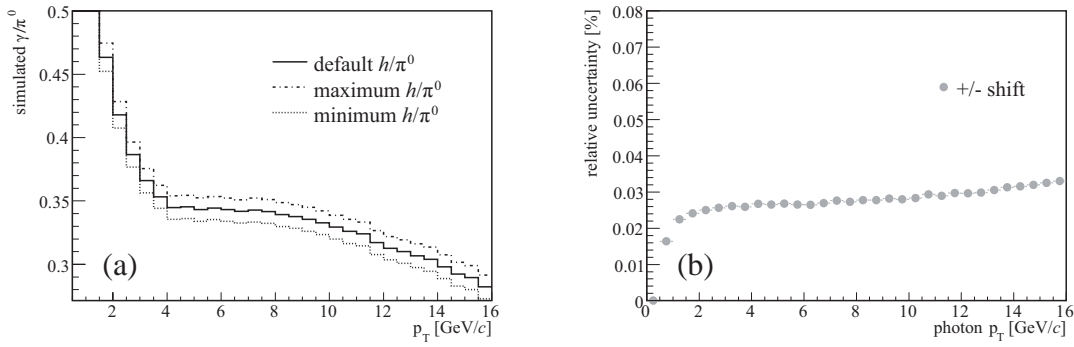


**Figure 7.35:** Systematic error of the simulated  $\gamma/\pi^0$  ratio due to the uncertainty of the hadron/ $\pi^0$  ratios required in the  $m_T$ -scaling. (a) Simulated  $\gamma/\pi^0$  ratio with the hadron/ $\pi^0$  ratios shifted in the positive and negative direction. The deviation is symmetric around the default  $\gamma/\pi^0$  ratio. (b) The relative uncertainty of the simulated  $\gamma/\pi^0$  ratio derived from the simulations shown in (a).

## 7.6 Derivation of the Direct-Photon Signal

The direct-photon signal is derived as a fraction of the inclusive photon yield (see Equation 7.2)<sup>22</sup>. The fraction is determined by the ratio of the measured and the simulated  $\gamma/\pi^0$  ratio, the double ratio  $R_\gamma$ . The double ratio is also referred to as the *direct-photon excess*, since for  $R_\gamma > 1$  the fraction given by  $\left(1 - \frac{1}{R_\gamma}\right)$  is  $> 0$  and a positive direct-photon signal can be extracted, i.e. the measured inclusive photon spectrum does not consist of decay photons alone. Equation 7.2 requires that the measured neutral pion yield and the parameterization used in the simulation cancel each other in the double ratio. This should be true by construction. However, because the shape of the parameterization is not perfectly constrained by the measured spectrum a small systematic uncertainty is introduced. This uncertainty is covered by the error on the  $\pi^0$  parameterization.

### 7.6.1 Calculation of the Photon Excess

The photon excess  $R_\gamma$  (see Equation 7.1) was calculated for the PbGl and PbSc separately. The measured  $\gamma/\pi^0$  ratio was divided by the simulated ratio after the merging correction. Figure 7.36 shows the  $\gamma/\pi^0$  ratios and the calculated photon excess for both EMCal subsystems. For the data statistical (error bars) and total systematic errors (grey boxes) are shown (except the normalization error). The error boxes of the photon excess also include the systematic uncertainty of the simulated background (all errors are added in quadra-

<sup>22</sup>In fact Equation 7.33 is used in order to account for shower merging. However, this is not explicitly mentioned in the following anymore.

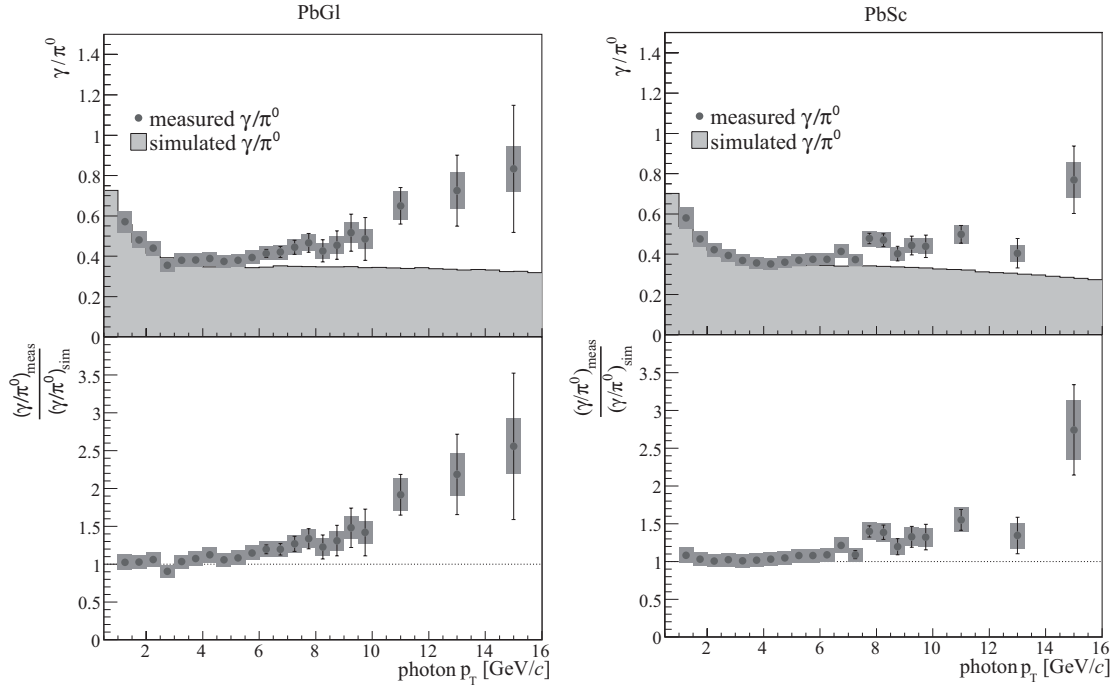


**Figure 7.36:** Measured and simulated  $\gamma/\pi^0$  ratios and the photon excess derived in the PbGl and PbSc. Statistical errors are given as error bars. The grey boxes around the data points represent the total systematic errors (except the normalization error).

ture). For both subsystems the comparison of the measured and the simulated  $\gamma/\pi^0$  ratios indicates a clear excess of photons in the data above the expected background at large transverse momenta. In the double ratio this is demonstrated by values above 1 (dotted line in lower panels of Figure 7.36). However, a significant direct-photon signal can only be extracted for double ratios where the statistical error does not allow values below 1. For the systematic uncertainty the situation is more complicated. This is discussed in Section 7.6.3.

## 7.6.2 Signal-To-Background Ratio

The challenge in the measurement of direct photons in p + p collisions employing the cocktail method is based on the small signal in the large background of decay photons, i.e. the small signal-to-background ratio  $S/B$ . It is solely determined by the double ratio  $R_\gamma$ :

$$\begin{aligned} S/B &= \frac{\gamma^{\text{direct}}}{\gamma^{\text{decay}}} \\ &= R_\gamma - 1 , \end{aligned} \tag{7.34}$$

$p_T$ [GeV/c]	$R_\gamma - 1$ [%]	
	PbGl	PbSc
3.0 – 3.5	3	1
5.0 – 5.5	8	8
7.0 – 7.5	27	9
9.0 – 9.5	48	33
11.0 – 13.0	119	34
13.0 – 15.0	156	174

**Table 7.15:** Signal-to-background ratios,  $S/B = R_\gamma - 1$ , in the measurement of direct photons in several  $p_T$  bins in the two subsystems of the EMCal.

where the relations  $\gamma^{\text{direct}} = \gamma^{\text{incl}} - \gamma^{\text{decay}}$  and  $R_\gamma = \gamma^{\text{incl}}/\gamma^{\text{decay}}$  were used. Hence the  $S/B$  ratio is simply given by the excess of the double ratio above 1. Table 7.15 shows the signal-to-background ratio in several  $p_T$  bins for the PbGl and PbSc. Below  $p_T = 7.0$  GeV/c the direct-photon signal is very weak and hence difficult to detect, especially in the PbSc. The  $S/B$  ratio directly influences the error calculation by enhancing some of the systematic uncertainties when propagated to the direct-photon spectrum, diluting any possible conclusions at low  $p_T$ . This will be discussed in more detail in the following section.

### 7.6.3 Direct-Photon Error Propagation

The statistical and systematic uncertainties of the inclusive photon spectrum and the measured and simulated  $\gamma/\pi^0$  ratios (see Section 7.3.4, 7.4.1 and 7.5.3) must be propagated to the direct-photon signal. Gaussian error propagation is not sufficient in this case because within the fluctuations of  $R_\gamma$  the term  $(1 - \frac{1}{R_\gamma})$  does not show sufficient linear behavior near  $R_\gamma = 1$ . Instead the error of  $\gamma^{\text{direct}}$  is calculated by changing  $R_\gamma$  and  $\gamma^{\text{incl}}$  in Equation 7.2 by the corresponding errors  $\Delta R_\gamma$  and  $\Delta\gamma^{\text{incl}}$ :

$$\Delta\gamma_{\pm}^{\text{direct}} = \pm \left[ \left( 1 - \frac{1}{R_\gamma \pm \Delta R_\gamma} \right) \cdot (\gamma^{\text{incl}} \pm \Delta\gamma^{\text{incl}}) - \gamma^{\text{direct}} \right]. \quad (7.35)$$

Because of the term  $(1 - 1/R_\gamma)$  the uncertainty becomes asymmetric for some of the errors involved in the analysis. It can be shown that this approach propagates the relative statistical uncertainty of the photon excess above unity ( $R_\gamma - 1$ ) directly to the direct-photon signal:

$$\frac{\Delta\gamma^{\text{direct}}}{\gamma^{\text{direct}}} = \frac{\Delta R_\gamma}{R_\gamma - 1}. \quad (7.36)$$

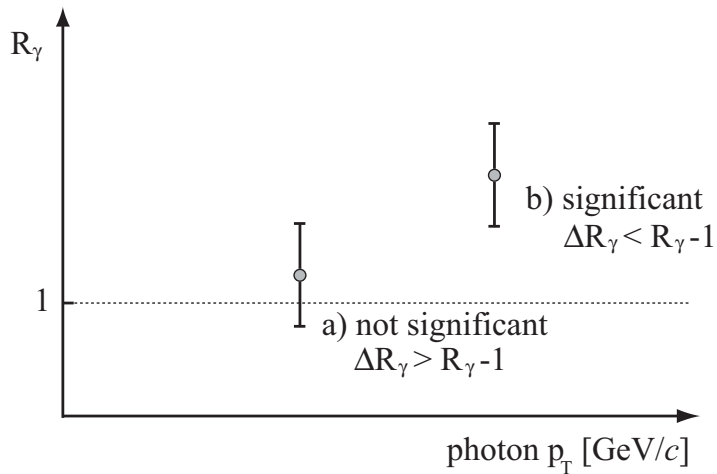


**Figure 7.37:** Schematic illustration of the significance given by the photon excess  $R_\gamma$ . a) The relative uncertainty of  $R_\gamma - 1$  is  $> 100\%$ . Therefore, only an upper limit for the derived direct-photon cross section can be calculated. b) The relative uncertainty of  $R_\gamma - 1$  is  $< 100\%$  which allows the calculation of a significant direct-photon signal. See text for more details.

$\Delta\gamma^{\text{direct}}/\gamma^{\text{direct}}$  is the relative uncertainty or *significance* of the corresponding direct-photon signal. Figure 7.37 illustrates schematically the significance given by the photon excess. For  $\Delta R_\gamma > R_\gamma - 1$  (case a) in Figure 7.37) the uncertainty of the corresponding direct-photon signal allows a negative cross section, i.e. only an upper limit of the cross section can be quoted. For  $\Delta R_\gamma < R_\gamma - 1$  (case b) in Figure 7.37) the extracted direct-photon signal is significantly above zero with the same relative uncertainty as  $R_\gamma - 1$ . Equation 7.36 holds not only for the statistical uncertainty but also for all systematic uncertainties of the inclusive photon spectrum that do not cancel partially or completely in the  $\gamma/\pi^0$  ratio (e.g. charged and neutral correction). However, many of the systematic uncertainties either do cancel at least partially in the  $\gamma/\pi^0$  ratio (e.g. global energy scale) or affect only the double ratio  $R_\gamma$  (e.g. energy scale non-linearity, hadron/ $\pi^0$  ratio). In these cases the propagated uncertainties do not follow the relation given by Equation 7.36.

There are three extreme cases for the uncertainties that arise in this analysis. Their behavior expressed in terms of the signal-to-background ratio  $R_\gamma - 1$ , when propagated to the direct-photon signal, is described in the following:

1. Uncertainty of the inclusive photon spectrum  $\gamma^{\text{incl}}$  with no corresponding error in the measured  $\pi^0$  spectrum, i.e. it does not cancel in the  $\gamma/\pi^0$  ratio. In this case

$\Delta R_\gamma = R_\gamma \cdot (\Delta\gamma^{\text{incl}}/\gamma^{\text{incl}}) \neq 0$  and  $\Delta\gamma^{\text{incl}} \neq 0$ . For the relative uncertainty of the direct-photon spectrum follows:

$$\frac{\Delta\gamma_+^{\text{direct}}}{\gamma^{\text{direct}}} = \frac{\Delta\gamma_-^{\text{direct}}}{\gamma^{\text{direct}}} = \frac{\Delta\gamma^{\text{incl}}}{\gamma^{\text{incl}}} \cdot \frac{R_\gamma}{R_\gamma - 1}. \quad (7.37)$$

This is equivalent to

$$\Delta\gamma_+^{\text{direct}} = \Delta\gamma_-^{\text{direct}} = \Delta\gamma^{\text{incl}}. \quad (7.38)$$

Thus the uncertainty of the direct-photon signal is symmetric and increased by the signal-to-background ratio  $R_\gamma - 1$  in such a way that the absolute error of the direct-photon signal is the same as the absolute error of the inclusive photon spectrum. It can be shown using Equation 7.38 and the relation  $\Delta R_\gamma = R_\gamma \cdot (\Delta\gamma^{\text{incl}}/\gamma^{\text{incl}})$  that Equation 7.36 is valid for this type of uncertainty (statistical error, charged and neutral correction).

2. Uncertainty of the inclusive photon spectrum  $\gamma^{\text{incl}}$  that cancels in the  $\gamma/\pi^0$  ratio, i.e.  $\Delta R_\gamma \approx 0$  and  $\Delta\gamma^{\text{incl}} \neq 0$ . According to Equation 7.35 the error is calculated as follows:

$$\Delta\gamma_\pm^{\text{direct}} = \pm \left[ \left( 1 - \frac{1}{R_\gamma} \right) \cdot (\gamma^{\text{incl}} \pm \Delta\gamma^{\text{incl}}) - \gamma^{\text{incl}} \right]. \quad (7.39)$$

This results in a symmetric relative error of  $\gamma^{\text{direct}}$  given by:

$$\frac{\Delta\gamma_\pm^{\text{direct}}}{\gamma^{\text{direct}}} = \frac{\Delta\gamma^{\text{incl}}}{\gamma^{\text{incl}}}. \quad (7.40)$$

Thus the relative error of the direct-photon signal is identical to the relative error of the measured inclusive photon spectrum and does not depend on the signal-to-background ratio.

3. Uncertainty affects only the double ratio  $R_\gamma$ , i.e. it arises from the neutral pion analysis or the simulated  $\gamma/\pi^0$  ratio. If the error of the quantity  $x$  is given by  $\Delta x$  it can be written:  $\Delta R_\gamma = R_\gamma \cdot \Delta x/x \neq 0$ ,  $\Delta\gamma^{\text{incl}} = 0$  and Equation 7.35 becomes:

$$\Delta\gamma_\pm^{\text{direct}} = \pm \left[ \left( 1 - \frac{1}{R_\gamma \pm \Delta R_\gamma} \right) \cdot \gamma^{\text{incl}} - \gamma^{\text{direct}} \right]. \quad (7.41)$$

The uncertainty is asymmetric and is given by:

$$\frac{\Delta\gamma_\pm^{\text{direct}}}{\gamma^{\text{direct}}} = \frac{\Delta x/x}{1 \pm \Delta x/x} \cdot \frac{1}{R_\gamma - 1} \quad (7.42)$$

This uncertainty is increased by a small signal-to-background ratio and hence worsens the significance of the direct-photon signal. The energy non-linearity belongs to this type of uncertainty and is the dominant contributor to the systematic uncertainty of the direct-photon signal.

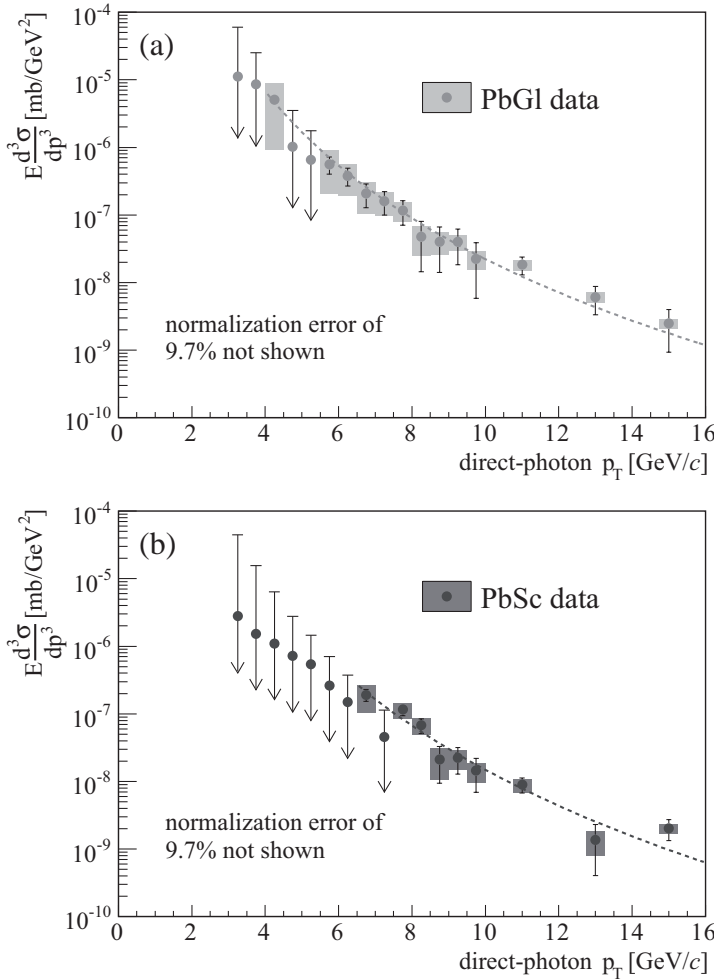


**Figure 7.38:** Cross section of direct-photon production in  $p + p$  collisions at  $\sqrt{s} = 200$  GeV measured in the PbGl (a) and PbSc (b). Error bars represent statistical errors and grey boxes represent the total systematic error (except for the normalization error).

Note that these three categories are extreme cases and not all uncertainties belong to just one of them but are a mixture of 1. and 2. because the systematic error cancels only partially in the  $\gamma/\pi^0$  ratio.

#### 7.6.4 Direct-Photon Cross Section

From the excess of direct photons indicated in the double ratio shown in Figure 7.36 the direct-photon signal is calculated according to Equation 7.2 as a fraction of the measured inclusive photon cross section (see Section 7.3.3). The cross section of direct-photon production in  $p + p$  collisions at  $\sqrt{s} = 200$  GeV is tabulated in Appendix E.3 and shown in

Propagated Systematic Errors of the Direct-Photon Spectrum in PbGl				
	$p_T$ indep.	5-5.5 GeV/c	9.5-10 GeV/c	14-16 GeV/c
peak extraction		27.0%/25.8%	5.1%/4.9%	1.3%/1.3%
$\pi^0$ merging		—/—	—/—	1.4%/1.3%
$\pi^0$ fit		22.7%/21.9%	15.9%/14.0%	7.9%/6.3%
efficiency		26.6%/27.4%	8.0%/8.1%	4.8%/4.8%
global energy scale		12.4%/12.8%	11.1%/11.2%	11.0%/11.0%
non-linearity		92.1%/80.1%	18.0%/15.7%	4.8%/4.2%
acceptance		8.5%/8.7%	3.7%/3.7%	2.8%/2.8%
$\gamma$ conversion		26.5%/26.5%	6.8%/6.8%	3.3%/3.3%
charged background		13.2%/13.2%	3.4%/3.4%	1.6%/1.6%
neutral background		13.2%/13.2%	3.4%/3.4%	1.6%/1.6%
$\varepsilon_\gamma$	2.5%/2.5%			
$\gamma$ shower merging		1.6%/1.6%	1.4%/1.4%	1.9%/1.8%
hadron/ $\pi^0$		33.4%/31.6%	6.9%/6.5%	2.0%/1.9%
quadratic sum		113.3%/103.0%	30.4%/28.1%	16.4%/15.6%
min. bias trigger eff.	9.7%/9.7%			

**Table 7.16:** Systematic uncertainties of the direct-photon spectrum in PbGl in three different  $p_T$  bins. The quoted values give the  $-/+$  (i.e. low/high) error of the asymmetric uncertainty. The quadratic sum corresponds to the grey error boxes in Figure 7.38. The normalization error due to the BBC cross section is not included in the quadratic sum. The main contribution to the total systematic uncertainty comes from the energy scale non-linearity, which is amplified by the small signal-to-background ratio.

Figure 7.38 as measured with the (a) PbGl and (b) PbSc for transverse momenta above  $p_T = 3$  GeV/c. In the  $p_T$  range below 3 GeV/c the direct-photon signal is very small and hence difficult to measure. This is reflected in the systematic errors which become extremely large at low  $p_T$ . The data points for  $p_T < 3$  GeV/c are therefore not shown to draw the attention to the more significant  $p_T$  range. For  $p_T > 3$  GeV/c the double ratio exceeds unity in each  $p_T$  bin for the PbGl and PbSc and therefore a direct-photon cross section can be calculated in all  $p_T$  bins (indicated by the full circles in Figure 7.38). Statistical errors are represented by error bars. The total systematic uncertainty displayed as grey boxes is the quadratic sum of the individual contributions (energy scale,  $\pi^0$  parameterization, merging etc.). The normalization error is not shown in the figures. If the lower total relative systematic error exceeds 100%, i.e. the result is consistent with no signal, the error is indicated by an arrow pointing downwards with a 90% confidence level upper limit on the cross section. It is determined by  $\sigma_{\text{up}}^{90\%} = 1.28 \cdot \Delta\gamma_+^{\text{direct}}$ , where  $\Delta\gamma_+^{\text{direct}}$  is the

Propagated Systematic Errors of the Direct-Photon Spectrum in PbSc				
	$p_T$ indep.	5-5.5 GeV/ $c$	9.5-10 GeV/ $c$	14-16 GeV/ $c$
peak extraction		27.9%/26.8%	6.6%/6.3%	1.2%/1.2%
$\pi^0$ merging		—/—	—/—	3.6%/3.2%
$\pi^0$ fit		15.0%/14.7%	10.7%/10.0%	3.6%/3.2%
efficiency		17.1%/17.8%	6.4%/6.6%	4.0%/4.1%
global energy scale		12.8%/13.3%	10.9%/11.0%	11.1%/11.1%
non-linearity		95.4%/83.0%	23.3%/20.3%	4.3%/3.8%
acceptance		8.7%/9.0%	4.0%/4.1%	2.8%/2.8%
$\gamma$ conversion		27.4%/27.4%	8.2%/8.2%	3.1%/3.1%
charged background		13.7%/13.7%	4.1%/4.1%	1.6%/1.6%
neutral background		13.7%/13.7%	4.1%/4.1%	1.6%/1.6%
$\varepsilon_\gamma$	2.5%/2.5%			
$\gamma$ shower merging		4.1%/4.1%	8.1%/7.7%	5.1%/4.4%
hadron/ $\pi^0$		34.6%/32.8%	8.9%/8.4%	1.8%/1.7%
quadratic sum		114.0%/103.0%	33.6%/31.1%	15.6%/15.1%
min. bias trigger eff.	9.7%/9.7%			

**Table 7.17:** Same as Table 7.16 but for the PbSc.

quadratic sum of the statistical error and the upper total systematic error (without normalization error). For the PbGl only upper limits on the direct-photon production cross section can be quoted up to  $p_T = 5.5$  GeV/ $c$  (except in the bin  $p_T = 4.0 - 4.5$  GeV/ $c$ ). For the PbSc the situation is even worse: only upper limits are quoted up to  $p_T = 7.5$  GeV/ $c$  (except in the bin  $p_T = 6.5 - 7.0$  GeV/ $c$ ).

The  $p_T$ -distribution of direct photons is well described by a power law in the displayed  $p_T$  range of significant data points as indicated by the dotted lines in Figure 7.38. The contributions of the individual systematic uncertainties propagated to the direct-photon signal according to Equation 7.35 are listed in Table 7.16 and 7.17 for the PbGl and PbSc, respectively. The main contribution to the systematic uncertainty at low and intermediate transverse momenta comes from the uncertainty of the energy scale non-linearity which is amplified by the small signal-to-background ratio in the respective  $p_T$  range. Figure 7.39 shows the relative deviation of the data points in PbGl and PbSc from the power law fit to the PbGl spectrum (dotted line in Figure 7.38(a)). While the PbGl points in Figure 7.39 illustrate the quality of the fit, the PbSc points indicate the discrepancy of the spectra measured in the two EMCal subsystems. Error bars and grey boxes represent statistical errors and systematic errors due to the energy scale, respectively. All other systematic uncertainties are considered to be correlated between PbGl and PbSc and hence cannot

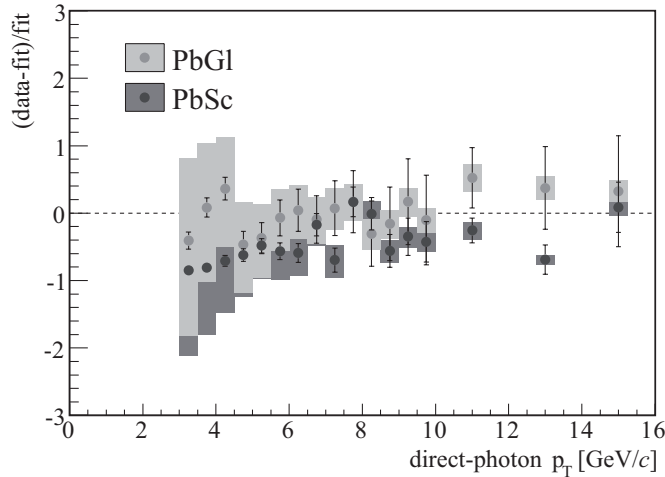


**Figure 7.39:** Comparison of the measured direct-photon spectra in PbGl and PbSc. The PbGl is fitted with a power law and the relative deviation of the data points (PbGl and PbSc) to the fit is calculated. Error bars represent statistical errors and grey boxes the systematic uncertainty due to the energy scale. The spectra agree within the assigned uncorrelated errors.

explain the observed deviation of the data points. The direct-photon spectra as measured with the PbGl and PbSc agree within the assigned errors. It is apparent that the direct-photon spectra deviate some 40-60% above  $p_T = 5 \text{ GeV}/c$ . This discrepancy is larger than observed for the measured inclusive photon and neutral pion  $p_T$ -distributions. However, it can be shown that the ratio of the direct-photon signals is given by:

$$\frac{\gamma_{\text{PbGl}}^{\text{direct}}}{\gamma_{\text{PbSc}}^{\text{direct}}} = \frac{R_{\gamma}^{\text{PbGl}} - 1}{R_{\gamma}^{\text{PbSc}} - 1} \cdot \frac{\gamma_{\text{PbGl}}^{\text{decay}}}{\gamma_{\text{PbSc}}^{\text{decay}}} . \quad (7.43)$$

Equation 7.43 illustrates that the deviation of the direct-photon spectra is determined by the deviation of the decay photon spectra in PbGl and PbSc, which is determined by the deviation of the measured neutral pion spectra, amplified by the ratio of the signal-to-background ratios. Since the  $S/B$  ratio is smaller in the PbSc the difference in the decay photon spectra is enhanced.

## 7.7 Combination of PbGl and PbSc Direct-Photon Spectra

One advantageous feature of the PHENIX EMCAL is the employment of two different subsystems which rely on different detection principles (see Section 5.2). The independent

analysis of the PbGl and PbSc data provides a valuable internal cross check. In the previous sections comparisons of the inclusive and direct-photon spectra as measured with the PbGl and PbSc were compared to each other and found to be consistent within the assigned uncertainties. Thus in order to have one single final result that utilizes the full statistics accumulated by the EMCAL the individual spectra are combined. However, since the error calculation results in partially asymmetric systematic errors (see Section 7.6.3) instead of combining the direct-photon spectra directly the measured  $\gamma/\pi^0$  ratio and the measured inclusive photon spectra measured with the PbGl and PbSc are combined. The expected background in the combined EMCAL subsystems is calculated in a fast Monte-Carlo utilizing a parameterization of the combined EMCAL neutral pion spectrum. The  $\pi^0$   $p_T$  distributions as measured with the PbGl and PbSc were combined as part of the neutral pion analysis described in [Bat05a]. The combined direct-photon  $p_T$ -distribution is then determined according to Equation 7.2.

### 7.7.1 Combination Method

For the combination the same approach was chosen as for the combination of the neutral pion spectra [Bat05a]. The combined  $\gamma/\pi^0$  ratio and inclusive photon spectrum are point-by-point weighted averages of the PbGl and PbSc  $p_T$ -distributions:

$$\bar{X}_{\text{EMCAl}}(p_T) = \frac{w_{\text{PbGl}}(p_T) \cdot X_{\text{PbGl}}(p_T) + w_{\text{PbSc}}(p_T) \cdot X_{\text{PbSc}}(p_T)}{w_{\text{PbGl}}(p_T) + w_{\text{PbSc}}(p_T)}, \quad (7.44)$$

where  $X_i$  is either the  $\gamma/\pi^0$  ratio or the inclusive photon yield at a certain  $p_T$  and  $w_i$  is the corresponding weight for the PbGl and PbSc data points at this  $p_T$ . This procedure is also described in [Yao06]. As was noted before only errors which are uncorrelated between the EMCAL subsystems can shift data points in the PbGl and PbSc in opposite directions. Hence in Equation 7.44 the data points of PbGl and PbSc are weighted only by the uncorrelated uncertainties. Since the data sets accumulated by the PbGl and PbSc are completely independent the statistical errors are obviously uncorrelated. For the systematic uncertainties the situation is not as simple. For most of the systematic errors the degree of correlation is not known. Therefore as a conservative estimation it was decided to treat all systematic uncertainties as correlated except the uncertainty due to the energy scale. The energy scale is believed to account for the difference observed in particle spectra measured with the PbGl and PbSc, e.g.  $\pi^0$  and inclusive photon production. Moreover, the non-linearity of the energy scale depends on the detection principle which is very different in both subsystems and therefore justifies the assumption that the corresponding uncertainties are uncorrelated. Thus in the combination of the measured  $\gamma/\pi^0$  ratios the statistical errors and the systematic errors due to the energy scale non-linearity are used

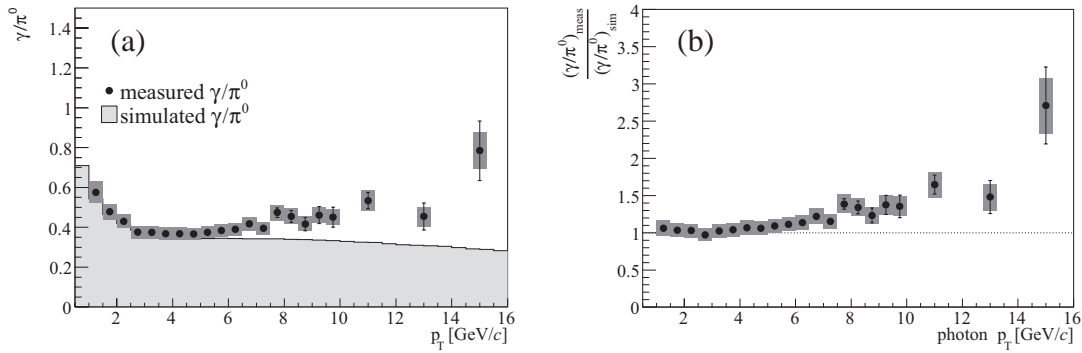


**Figure 7.40:** Combined results of (a) the measured  $\gamma/\pi^0$  ratio compared to the expectation from hadronic decays and (b) the derived photon excess. Error bars are statistical, grey boxes are systematic errors. The normalization error is not included.

as weight (the global scale uncertainty almost cancels completely in the ratio and therefore can be neglected). In the combination of the inclusive photon spectra the statistical errors and systematic errors due to the global energy scale error are used as weight (for the inclusive photon spectra the non-linearity is included in the global energy scale error). The weights  $w_i$  are calculated as follows:

$$w_i(p_T) = \frac{1}{\delta X_i(p_T)^2}, \quad \delta X_i(p_T)^2 = \sum_j \delta X_i^j(p_T)^2, \quad (7.45)$$

where  $i = \text{PbGl, PbSc}$  and  $\delta X_i(p_T)$  is the quadratic sum of the uncorrelated errors  $X_i^j(p_T)$  at a certain  $p_T$  ( $j$  denotes the various error sources). In this method correlated errors are combined in the same way as the data points, i.e. the weighted mean of the PbGl and PbSc errors is calculated according to Equation 7.44 by substituting the yield or ratio  $X_i$  by the correlated error at this  $p_T$ . Uncorrelated errors are reduced in the combination process:

$$\begin{aligned} \delta \bar{X}_{\text{EMCal}}^j(p_T)^2 &= \frac{1}{2} \left[ \frac{w_{\text{PbGl}}}{w_{\text{PbGl}} + w_{\text{PbSc}}} \cdot \delta X_{\text{PbGl}}^j(p_T)^2 \right. \\ &\quad \left. + \frac{w_{\text{PbSc}}}{w_{\text{PbGl}} + w_{\text{PbSc}}} \cdot \delta X_{\text{PbSc}}^j(p_T)^2 \right]. \end{aligned} \quad (7.46)$$

However, since the energy scale uncertainty, especially the non-linearity, is not fully understood it was decided not to reduce the corresponding errors in the combination process. Instead the combined uncertainty of the uncorrelated systematic uncertainties is also calculated according to Equation 7.44 in order to provide a conservative error estimation. Thus only the statistical error is reduced.

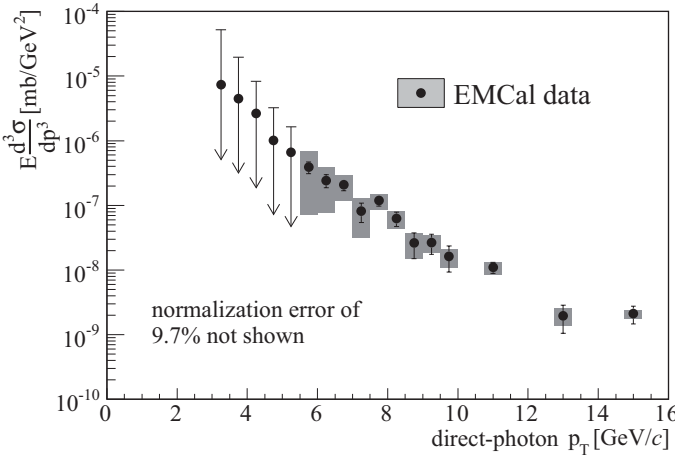


**Figure 7.41:** Final result of the combined direct-photon cross section in p + p at  $\sqrt{s} = 200$  GeV. Error bars and grey boxes represent statistical and systematic errors as in Figure 7.40.

## 7.7.2 Combined Results

Following the rules described in the previous section the data points and errors of the measured  $\gamma/\pi^0$  ratio and inclusive photon spectrum in PbGl and PbSc were combined. Tables of the combined inclusive photon and neutral pion spectrum are listed in Appendix E.1 and E.2. Figure 7.40(a) shows the combined result of the measured  $\gamma/\pi^0$  ratio compared to the expectation from hadronic decays. The double ratio of the combined result is shown in Figure 7.40(b). The large excess of photons above the simulated background is translated into the direct-photon signal according to Equation 7.2 as a fraction of the combined inclusive photon spectrum. The final combined cross section of direct-photon production is tabulated in Appendix E.3 and shown in Figure 7.41. This result represents the most precise measurement of direct photons in elementary p + p collisions at  $\sqrt{s} = 200$  GeV to date. Error bars in Figure 7.41 indicate statistical errors while the grey error boxes represent the total systematic errors except the normalization error of 9.7% which is not shown. As was noted above the combined systematic uncertainty is a weighted mean (according to Equation 7.44) of the uncertainties assigned to the PbGl and PbSc results. The combined result of the uncertainties of the inclusive photon spectra (see Table 7.10), of the measured  $\gamma/\pi^0$  ratios (see Table 7.11) and of the simulated  $\gamma/\pi^0$  ratios (see Table 7.14) are summarized in Table 7.18 and 7.19 for three different  $p_T$  bins. The propagation of the combined systematic errors according to Equation 7.35 yields the systematic errors of the combined direct-photon signal listed in Table 7.20. Naturally, as in the case of the individual EMCAL subsystems, the main contribution to the systematic error at low and intermediate  $p_T$  comes from the energy non-linearity uncertainty. The

<b>Combined Systematic Errors of the Inclusive Photon Spectrum</b>				
	$p_T$ indep.	5-5.5 GeV/ $c$	9.5-10 GeV/ $c$	14-16 GeV/ $c$
efficiency		3.6%	3.2%	3.5%
global energy scale		10.9%	10.7%	10.9%
acceptance	2.5%			
photon conversion	2.0%			
charged background	1.0%			
neutral background	1.0%			
$\epsilon_\gamma$	2.5%			
quadratic sum		12.3%	12.0%	12.2%
$\epsilon_{\text{trig}}^{\text{BBC}}$	9.7%			

**Table 7.18:** Combined systematic errors of the inclusive photon spectrum in three different  $p_T$  bins. The errors are weighted means of the corresponding uncertainties assigned to the PbGl and PbSc analysis.

<b>Combined Systematic Errors of the Measured and Simulated <math>\gamma/\pi^0</math> Ratios</b>				
	$p_T$ indep.	5-5.5 GeV/ $c$	9.5-10 GeV/ $c$	14-16 GeV/ $c$
peak extraction		2.2%	2.1%	2.0%
$\pi^0$ merging		0.0%	0.0%	4.8%
$\pi^0$ fit		1.5%	4.1%	7.1%
efficiency	1.5%			
global energy scale		0.2%	0.1%	0.5%
non-linearity	7.0%			
acceptance	0.5%			
photon conversion	2.0%			
charged background	1.0%			
neutral background	1.0%			
quadratic sum		8.0%	8.9%	11.6%
$\gamma$ shower merging		0.3%	2.2%	6.8%
hadron/ $\pi^0$		2.7%	2.8%	3.1%
quadratic sum		2.7%	3.6%	7.5%

**Table 7.19:** Combined systematic errors of the measured and simulated  $\gamma/\pi^0$  ratios in three different  $p_T$  bins. The uncertainties are weighted means of the corresponding uncertainties assigned to the PbGl and PbSc analysis.

Systematic Errors of the Combined Direct-Photon Spectrum				
	$p_T$ indep.	5-5.5 GeV/c	9.5-10 GeV/c	14-16 GeV/c
peak extraction		24.2%/23.2%	6.0%/5.7%	1.2%/1.2%
$\pi^0$ merging		0.0%/0.0%	0.0%/0.0%	3.0%/2.7%
$\pi^0$ fit		16.5%/16.0%	12.1%/11.1%	4.5%/3.9%
efficiency		19.5%/20.2%	6.8%/7.0%	4.2%/4.3%
global energy scale		12.5%/12.9%	11.0%/11.1%	11.1%/11.2%
non-linearity		82.8%/71.9%	21.3%/18.5%	4.4%/3.8%
acceptance		7.9%/8.1%	3.9%/3.9%	2.8%/2.8%
$\gamma$ conversion		24.0%/24.0%	7.6%/7.6%	3.2%/3.2%
charged background		12.0%/12.0%	3.8%/3.8%	1.6%/1.6%
neutral background		12.0%/12.0%	3.8%/3.8%	1.6%/1.6%
$\epsilon_\gamma$	2.5%/2.5%			
$\gamma$ shower merging		3.4%/3.4%	6.3%/6.0%	4.3%/3.7%
hadron/ $\pi^0$		30.0%/28.4%	8.1%/7.7%	1.9%/1.7%
quadratic sum		100.4%/91.1%	31.9%/29.6%	15.6%/15.1%
min. bias trigger eff.	9.7%/9.7%			

**Table 7.20:** Systematic errors ( $-/+$ ) of the combined direct-photon spectrum propagated from the combined errors of the  $\gamma/\pi^0$  ratios and the inclusive photon spectra.

quadratic sum of the systematic errors listed in Table 7.20 except for the normalization error allows the extraction of a significant direct-photon signal for  $p_T > 5.5$  GeV/c. For  $3$  GeV/c  $< p_T < 5.5$  GeV/c the photon excess is above unity but the extracted direct-photon cross section is compatible with no signal because of the large systematic uncertainty.

## 7.8 Comparisons with the Final Direct-Photon Spectrum

PHENIX has measured the production of mid-rapidity direct photons in p + p at  $\sqrt{s} = 200$  GeV in the second year of physics running (see Section 6.3). However, the result suffered from the small statistics accumulated in the p + p Run. Significant direct-photon signals could only be extracted in three  $p_T$  bins. Figure 7.42 shows a comparison of the significant Run II data points with the spectrum measured in Run III (also at mid-rapidity and the same energy) and presented in this thesis in the corresponding  $p_T$  range of the

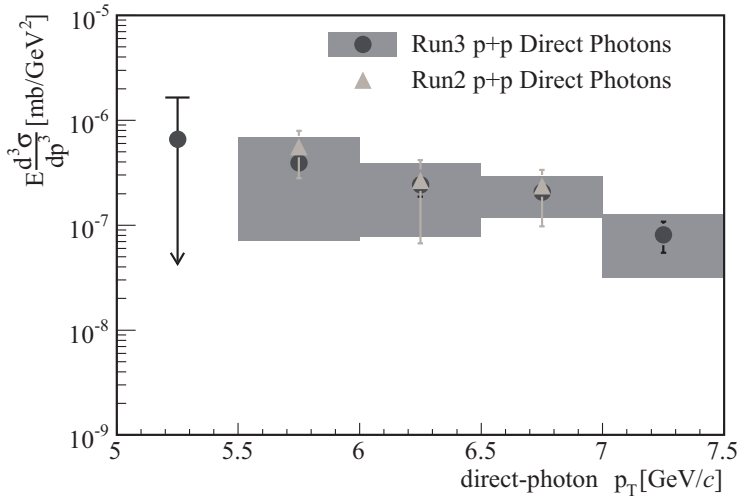


**Figure 7.42:** Comparison of the data points obtained in the direct-photon analysis of Run II and Run III  $p + p$  in the  $p_T$  range covered by the Run II measurement. Only the significant data points and the statistical errors of the Run II spectrum are shown.

Run II measurement. The data points of the two measurements are in excellent agreement although the statistical errors of the Run II measurement are very large. Systematic uncertainties are only shown for the Run III data points.

The measured Run III  $p + p$  direct-photon cross section can be utilized to test theoretical predictions over a wider  $p_T$  range compared to the Run II result. Figure 7.43(a) shows the final data points obtained with the EMCAL in comparison to NLO pQCD calculations for three choices of theory scales ( $\mu = p_T/2$ ,  $\mu = p_T$  and  $\mu = 2p_T$ ). The calculations (performed by W. Vogelsang) include prompt and fragmentation photons and uses the CTEQ6M parton distribution functions [Pum02] and the BFGII parton to photon fragmentation functions [Bou98].<sup>23</sup> Figure 7.43(b) shows the fractional difference between data points and the theoretical prediction for  $\mu = p_T$ . The upper and lower dashed curves in the figure show the uncertainty introduced by the different choices of theory scales in the calculation. The data are well described by the prediction over the entire  $p_T$  range, even though the systematic uncertainties of the measurement are large, especially below  $p_T = 5.5 \text{ GeV}/c$  where only upper limits of the cross section could be extracted.

The good agreement between data and NLO pQCD calculation for direct-photon production in  $p + p$  at  $\sqrt{s} = 200 \text{ GeV}$  demonstrated in Figure 7.43 is an important result for

<sup>23</sup>In fact, the same calculations were used to illustrate the contribution of fragmentation photons to the inclusive direct-photon spectrum in Figure 6.3 of Section 6.1.2.

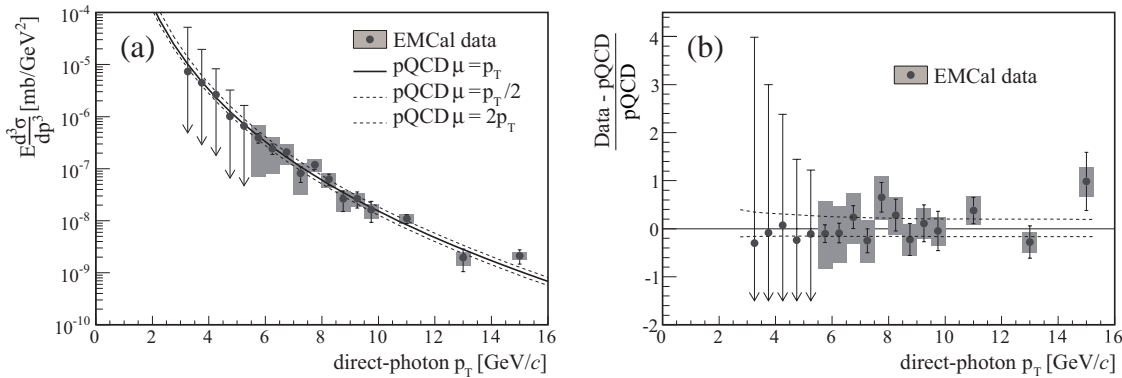


**Figure 7.43:** Comparison of the final direct-photon cross section with pQCD predictions at next-to-leading order for three different choices of theory scales. (a) shows the cross section, while (b) shows the deviation of the measurement from the calculation with  $\mu = p_T$ . The upper and lower dashed curves illustrate the theoretical uncertainty due to the choice of the theory scales. The shown uncertainties are as in Figure 7.41.

the interpretation of Au + Au direct-photon data at the same energy. It justifies the use of the NLO pQCD calculation as  $p + p$  reference in the calculation of the nuclear modification factor shown in Figure 6.4 and thus puts the drawn conclusions on a firm experimental basis. Moreover, the successful theoretical description of direct-photon production at RHIC is an important step towards the ultimate extraction of the gluon distribution inside longitudinally polarized protons.

The PHENIX direct-photon cross section measurement in  $p + p$  over four orders of magnitude presented in this thesis marks the most precise measurement of inclusive direct-photon production at  $\sqrt{s} = 200$  GeV to date. It complements the existing set of world direct-photon data which covers energies below 63 GeV and above 546 GeV (see Figure 6.6). As discussed in Section 6.3 the necessity of  $k_T$  enhancement in the theoretical predictions is still an open question. The measurement presented in this thesis provides a first indication that direct-photon production at energies between fixed-target energies and collider energies above 500 GeV do not support the need for a significant intrinsic transverse momentum of the initial state partons in the calculations.

## **Part II**

# **Double Helicity Asymmetry**



# 8. The Proton Structure

The structure of the proton has been intensively studied for many years in experiments in which high-energy leptons are scattered off of a proton target. Leptons are highly suitable since they are, to current knowledge, point-like particles without inner structure. The interaction between a charged lepton and a proton can be precisely calculated by the theory of QED. Since the coupling constant of QED is substantially smaller than 1 ( $\alpha \approx 1/137$ ) higher order corrections play only a minor role. Electrons as well as muons are employed in the scatterings experiments. Although the cross sections are identical for electron and muon scattering, the latter have the advantage that they can be created with higher energies. Complementary information is gained by neutrino scattering which is governed by the weak interaction. However, the following discussion will focus on the scattering of charged leptons.

## 8.1 Elastic and Inelastic Scattering

The scattering of relativistic electrons off of a spinless, point-like target with charge  $Z \cdot e$  taking into account the electron spin of  $1/2$  is referred to as *Mott scattering* with the differential cross section given by [Pov99, Per00] ( $\hbar = c = 1$ ):

$$\left( \frac{d\sigma}{d\Omega} \right)_{\text{Mott}} = \frac{4Z^2\alpha^2 E'^2}{Q^4} \frac{E'}{E} \cdot \left( 1 - \beta^2 \sin^2 \frac{\theta}{2} \right), \quad (8.1)$$

where  $Q^2$  is the four-momentum transfer,  $\beta = v/c$ ,  $E$  is the initial energy of the electron and  $E'$  is the energy of the scattered electron at a scattering angle of  $\theta$ . The spin dependence of the scattering is given by the factor  $(1 - \beta^2 \sin^2 \frac{\theta}{2})$ . The term  $\frac{4Z^2\alpha^2 E'^2}{Q^4}$  is the relativistic *Rutherford* cross section, while the term  $E'/E$  accounts for the recoil of the proton target.

In the elastic scattering the particles in the initial and final state are identical and the kinematics of the scattering process is well-defined, i.e. for a given incident energy  $E$  the energy of the scattered particle  $E'$  is defined by the scattering angle  $\theta$ .

In case of inelastic scattering some fraction of the incident energy is used to excite the target particle, which subsequently decays into two or more particles. The kinematics is not well-defined but depends on the excitation energy.

### 8.1.1 Form Factors

Elastic Mott scattering (Equation 8.1) assumes a point-like target. It was observed in elastic electron-proton scattering experiments that the measured cross section is systematically smaller than the corresponding Mott cross section. The deviation depends on the momentum transfer  $Q^2$  from the electron to the proton, which in elastic reactions is given by the kinematics of the scattering. Only for  $Q^2 \rightarrow 0$  the measured cross section is identical to the Mott cross section. Since  $Q^2$  is related to the wavelength of the virtual photon which is exchanged in the scattering process, it determines the spatial resolution at which the target nucleon is probed. For increasing  $Q^2$  the wavelength of the virtual photon decreases which results in a larger spatial resolution. Therefore the observed  $Q^2$  dependent deviation of the electron-proton elastic scattering cross section indicates that protons are not point-like but have a finite spatial expansion. The scattering of electrons with  $Q^2 > 0$  probes only a fraction of the proton charge and therefore the measured cross section is smaller than given by Equation 8.1.

The charge distribution within the proton can be expressed in terms of an *electric form factor*  $G_E(Q^2)$  which depends on the momentum transfer in the reaction. For small values of  $Q^2$   $G_E$  is proportional to the Fourier transform of the charge distribution. Mott scattering takes only into account the charge of the target. However, the magnetic moment of the proton, which was first measured by Stern, Frisch and Estermann in 1933, interacts with the current of the electron and thus also influences the scattering cross section. Analogous to the charge distribution the "magnetic distribution" of the proton can be expressed in terms of a *magnetic form factor*  $G_M(Q^2)$ .

The differential cross section of elastic electron-proton scattering is given by the *Rosenbluth formula* [Pov99, Ros50]:

$$\left( \frac{d\sigma}{d\Omega} \right) = \left( \frac{d\sigma}{d\Omega} \right)_{\text{Mott}} \cdot \left[ \frac{G_E^2(Q^2) + \tau G_M^2(Q^2)}{1 + \tau} + 2\tau G_M^2(Q^2) \tan^2 \frac{\theta}{2} \right], \quad (8.2)$$

where  $\tau = \frac{Q^2}{4M^2c^2}$  with proton mass  $M$ .

The electric and magnetic form factors can be determined by measuring the differential elastic cross section for different momentum transfers. Such measurements were essentially carried out during the 1960's and 1970's. For  $Q^2 \rightarrow 0$   $G_E$  approaches unity while  $G_M$  vanishes and Equation 8.2 reduces to the Mott cross section.

### 8.1.2 Structure Functions

In the scattering of high-energy electrons off of protons also inelastic scattering is observed. In inelastic reactions some fraction of the transferred energy is used to excite the

proton. Therefore the measured energy of the scattered electron is less than expected for a given scattering angle according to elastic scattering kinematics, i.e. the momentum transfer cannot be deduced from the scattering angle and the initial electron energy. Similar to the form factors which describe the "elastic structure" of the proton so-called *structure functions* are introduced to describe the "inelastic structure" of the proton. The double differential cross section for inelastic electron-proton scattering is given by [Pov99]:

$$\left( \frac{d^2\sigma}{d\Omega dE'} \right)_{\text{inel}} = \left( \frac{d\sigma}{d\Omega} \right)_{\text{Mott}} \frac{E}{E'} \left[ W_2(Q^2, v) + 2W_1(Q^2, v) \tan^2 \frac{\theta}{2} \right], \quad (8.3)$$

where  $v = P \cdot Q / M$  with  $P$  being the initial four-momentum of the proton and  $W_1$  and  $W_2$  are the proton structure functions. In the laboratory system with the proton at rest  $v$  is given by  $v = E - E'$ , i.e.  $v$  represents the energy which is transferred from the electron to the proton (recoil energy). Unlike the elastic form factors, the structure functions depend on two parameters, e.g. the momentum transfer and the recoil energy. Similar to Equation 8.2 the second term in Equation 8.3 contains the magnetic interaction.

Instead of the dimensional quantities  $W_1$  and  $W_2$  the structure functions of the proton are commonly expressed by the dimensionless structure functions  $F_1$  and  $F_2$ :

$$\begin{aligned} F_1(x, Q^2) &= Mc^2 W_1(Q^2, v) \\ F_2(x, Q^2) &= v W_2(Q^2, v), \end{aligned} \quad (8.4)$$

where the dimensionless variable  $x = Q^2 / 2P \cdot Q$  (Bjorken- $x$ ) is introduced.

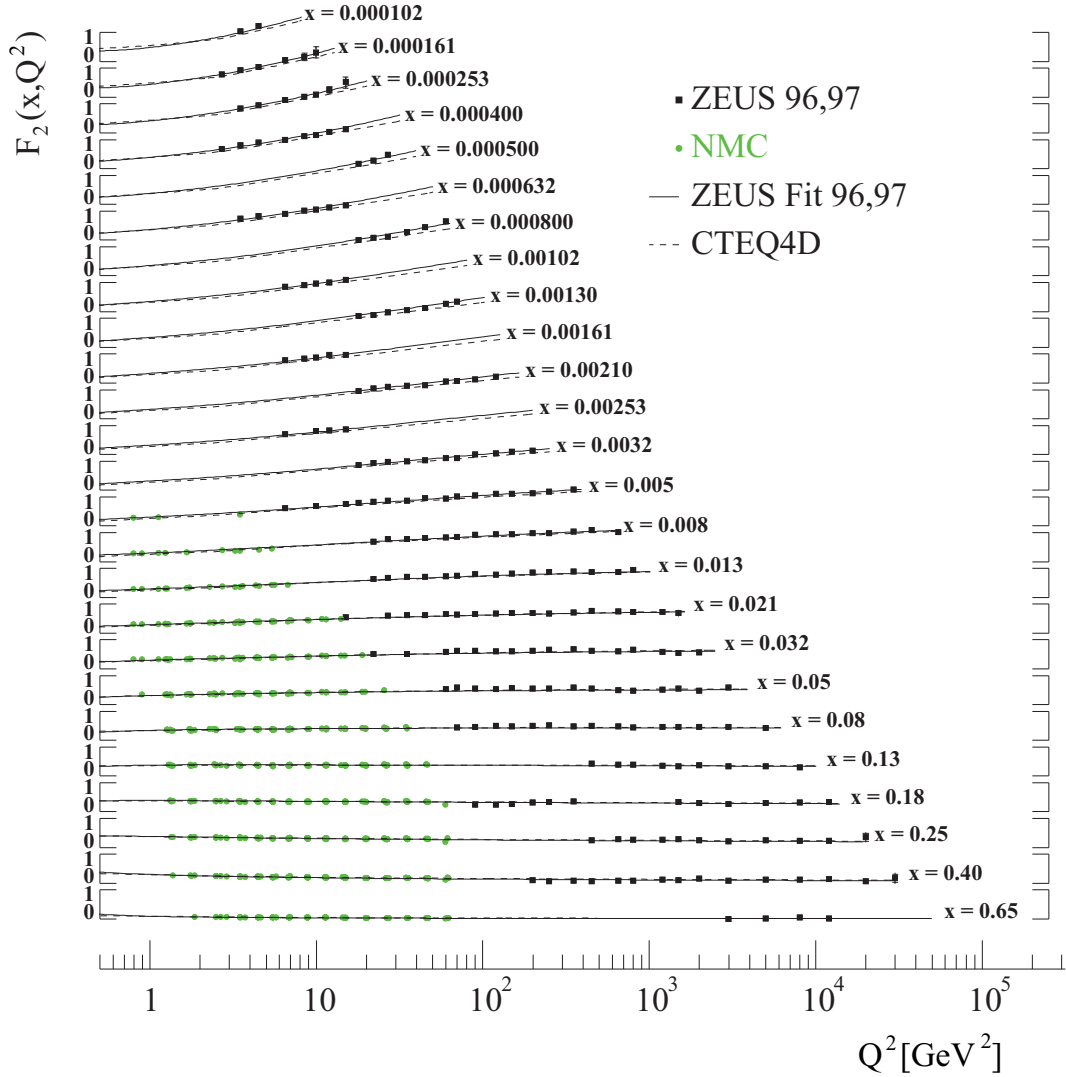
It was shown in the 1960's in deep-inelastic (i.e. large  $Q^2$ ) electron-proton scattering (DIS) experiments at the Stanford Linear Accelerator Center (SLAC) that the proton structure functions they measured have only little dependence on the momentum transfer [Blo69, Bre69]. It was predicted by Bjorken already in 1969 that the scattering off of approximately free point-like subcomponents in the proton would result in structure functions which do not depend on  $Q^2$  for a given  $x$  [Bjo69]. This behavior is referred to as *Bjorken scaling*. It implies that the inelastic electron-proton scattering at large  $Q^2$  can be regarded as the elastic scattering of electrons off of point-like constituents within the proton. The SLAC result was the first experimental observation of *hard* subcomponents within the proton and a strong evidence for the, by then, hypothetical parton model.

Figure 8.1 shows results of the proton structure function  $F_2(x, Q^2)$  measured in DIS of electrons (ZEUS<sup>1</sup>) and muons (NMC<sup>2</sup>) off of protons over a wide kinematic range in  $x$  and  $Q^2$ . One can see that for  $x \gtrsim 0.02$  the measured  $F_2$  is nearly flat as a function of  $Q^2$  which indicates that the probed point-like partons within the proton are approximately

---

<sup>1</sup>ZEUS experiment at the HERA collider at DESY.

<sup>2</sup>New Muon Collaboration at the CERN SPS.



**Figure 8.1:** The proton structure function  $F_2$  measured by the ZEUS (HERA) and NMC (CERN) collaboration in electron-proton and muon-proton DIS, respectively. The solid and dashed lines represent different QCD fits. The plot is taken from [Wod99].

free. However, at small values of  $x$  a deviation from Bjorken scaling is observed. This behavior does not arise from a substructure of the quark but is due to the continuous interactions in the nucleon, e.g. gluon exchange and quark-pair production ( $g \rightarrow q + \bar{q}$ ).

As will be discussed in Section 8.1.3 gluons dominate at small values of  $x$  and therefore this *scaling violation* can be utilized to extract the gluon distribution in the proton.

For partons with spin 1/2 Callan and Gross predicted that in the kinematic range in which Bjorken scaling holds (Bjorken scaling limit) the two structure functions  $F_1$  and  $F_2$  obey the following relation [Cal69]:

$$2xF_1(x) = F_2(x). \quad (8.5)$$

It was shown in the late 1970's in experiments at SLAC that the ratio of  $2xF_1$  and  $F_1$  is equal to unity within errors (for large  $x$ ) and therefore provided a strong indication for the assumption that the point-like quarks within the proton carry spin 1/2 [Bod79].

### 8.1.3 Parton Distribution Functions

The observation of the scaling behavior of the structure function  $F_2$  subsequently led to the acceptance of the parton model in which the proton consists of quarks, antiquarks and gluons. In DIS experiments the incident lepton is scattered elastically off of a collection of partons and hence the partonic distribution within the proton is probed. The momentum of the proton is composed of the momentum distributions of its constituents. For large proton momentum, i.e. when the transverse momenta of the constituents can be neglected, the Bjorken- $x$  can be viewed as the fraction of the proton's momentum carried by the parton<sup>3</sup>. The parton distribution function (PDF), denoted  $q_f(x)$  ( $\bar{q}_f(x)$ ) for quarks (antiquarks) and  $g(x)$  for gluons, then reflects the probability<sup>4</sup> of finding a quark (antiquark) of flavor  $f$  or gluon with momentum fraction  $x$ , respectively. Hence the proton structure functions in the Bjorken limit,  $F_1(x)$  and  $F_2(x)$ , represent a measure of the probability of scattering off of a quark within the proton with momentum fraction  $x$ . In the simple parton model the scaling structure functions can be expressed in terms of the PDF's of the different quark flavors<sup>5</sup>:

$$\begin{aligned} F_1(x) &= \frac{1}{2} \sum_f e_f^2 \cdot [q_f(x) + \bar{q}_f(x)] \\ F_2(x) &= x \cdot \sum_f e_f^2 \cdot [q_f(x) + \bar{q}_f(x)], \end{aligned} \quad (8.6)$$

---

<sup>3</sup>This interpretation of  $x$  was already used in Equation 2.5 in Section 2.2.1.

<sup>4</sup>In fact, PDF's represent number densities rather than probabilities, i.e.  $q_f(x)dx$  gives the number of quarks (of flavor  $f$ ) between  $x$  and  $x+dx$ . However, in the following also the term probability is used, keeping in mind that PDF's are not normalized to 1.

<sup>5</sup>The virtual photon in DIS couples only to the electric charge and gluons are electrically neutral.

where  $e_f$  is the electric charge of the quark of flavor  $f$ . The sum runs over all quark and antiquark flavors. It was found in DIS experiments that

$$\int_0^1 x \cdot \sum_f [q_f(x) + \bar{q}_f(x)] dx \approx 0.5, \quad (8.7)$$

i.e. only half of the proton's momentum is carried by the electrically charged quarks and antiquarks. The remaining fraction therefore is carried by the exchange particles of QCD, the gluons.

Parton distribution functions cannot be predicted by pQCD because of the non-perturbative structure of bound partons. In principle PDF's can be calculated using other theoretical techniques such as lattice QCD (see e.g. [Org06]). However, pQCD also offers a different approach: if the parton distribution is known at some scale  $Q_0^2$  pQCD predicts its evolution in  $Q^2$  using the so-called DGLAP<sup>6</sup> evolution equations [Dok77, Gri72, Alt77]. The parameters of the input distributions are determined from the measured structure functions. DIS experiments (collider as well as fixed-target experiments) that have contributed significantly to the understanding of the unpolarized proton structure were (or still are) carried out at DESY, CERN, SLAC and Fermilab. The procedure for the extraction of PDF's from  $F_2$  data is roughly as follows. An analytic shape for the parton distributions is assumed at some input scale  $Q^2 = Q_0^2$ . Although the choice of  $Q_0^2$  is arbitrary the corresponding  $\alpha_s(Q_0^2)$  must be small enough to make perturbative calculations applicable. The input distribution at fixed  $x$  is then evolved to different values of  $Q^2$  and predictions of the structure function are calculated. The predictions are then fitted to the  $F_2$  data (QCD fits, which are e.g. shown in Figure 8.1) and the fit parameters constrain the analytic shape of the input PDF's at the input scale.

Over the years a wealth of DIS data has been accumulated by the different experiments, each covering a certain range in  $x$  and  $Q^2$ . Global analyses of this world data have been conducted by different groups in order to develop parton distribution functions which best describe the existing data in a broad kinematic range. Sets of PDF's which are based on recent data are developed by the MRS [Mar94], CTEQ [Lai95] and GRV [Glu95] groups. A general overview of the analysis methods applied by these groups in order to derive their global QCD fits is given in [CS98]. A recent set of PDF's at the input scale  $Q^2 = 4 \text{ GeV}^2$  extracted by the CTEQ group is depicted in Figure 8.2. As one can see in the figure gluons are dominant at small  $x$ . Their large number explains how the gluons can account for half of the proton's momentum. While the valence quarks are likely to carry large momentum fractions, the probability to find one single valence quark which carries all of the proton's momentum is very small. The sea quarks are only significant at small  $x$ . A comprehensive review on structure functions and PDF's can be found in [CS98].

---

<sup>6</sup>The name acknowledges contributions from Dokshitzer, Gribov, Lipatov, Altarelli and Parisi.

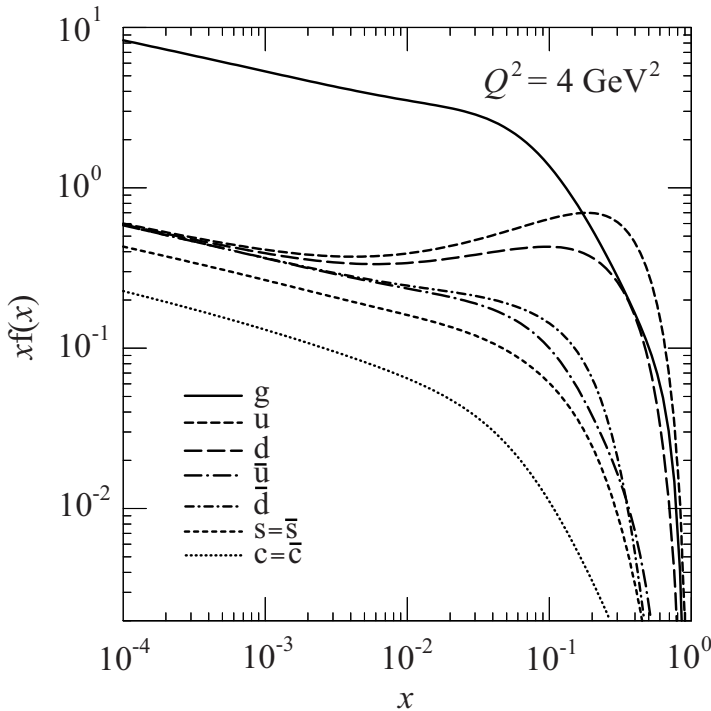


**Figure 8.2:** Overview of CTEQ6M parton distribution functions at the input scale  $Q^2 = 4 \text{ GeV}^2$  [Pum02].

While the distributions of the valence and sea quarks are directly probed in DIS experiments and complementary information is obtained via the scattering of muons (electrons) and neutrinos off of the nucleon, these measurements are not directly sensitive to the gluon PDF. However, as was noted in Section 8.1.2 the scaling violation of the structure function is related to the gluon momentum distribution. The quarks within the proton continuously radiate and absorb gluons, which carry a small fraction of the proton's momentum. Gluons also create quark-antiquark pairs, which subsequently decay again into gluons. When probing the proton with small  $Q^2$  the resolution is also small and the complex system consisting of quarks, antiquarks and gluons cannot be resolved. With increasing  $Q^2$ , however, the lepton sees more details of the complex system, i.e. that the proton's momentum is shared by a larger number of partons. Therefore, at low  $x$ , the structure function  $F_2$  increases with increasing  $Q^2$ , i.e. the probability to find a parton with small  $x$  increases because the resolution increases at which the proton substructure is probed (see Figure 8.1).<sup>7</sup> This mechanism leads to the observed scaling violation of  $F_2$  at small values of  $x$  ( $x \lesssim 0.02$ ) and allows an indirect determination of the gluon distribution function.

<sup>7</sup>At large values of  $x$  the effect is opposite, i.e.  $F_2$  decreases with increasing  $Q^2$ .

## 8.2 Spin Structure of the Proton

In the discussion of the spin structure of the proton it must be distinguished between the longitudinal (the spin of the proton is parallel to the proton's momentum) and the transverse spin structure (the spin is perpendicular to the proton's momentum). Because Lorentz boosts and spatial rotations do not commute it is not possible to deduce the transverse from the longitudinal distributions or vice versa. This fact complicates the understanding of the spin structure on the one hand. On the other hand the difference between the longitudinal and the transverse distributions provides information on the relativistic character of quark motion in the proton.

The following discussion is confined to the longitudinal spin structure (also referred to as helicity structure). For more information related to the transverse spin structure please refer to [Aid06, Bas05] and references therein.

### 8.2.1 The Proton Spin Puzzle

In the late 1920's and the early 1930's it was discovered in short succession that the proton is a fermion of spin 1/2 and carries an anomalous magnetic moment. The latter observation marks the first indication that the proton cannot be point-like and initiated the interest in the proton spin structure. In the naive quark-parton model one might expect that the spin 1/2 of the proton is simply given by the sum of the three spin 1/2 valence quarks, two oriented parallel and one antiparallel to the proton spin. However, deep-inelastic scattering experiments of longitudinally polarized muons off of a longitudinally polarized proton target (polarized DIS or pDIS) carried out by the EMC<sup>8</sup> experiment at CERN discovered that the valence and sea quarks account for only approximately 12% of the proton spin [Ash88, Ash89]. This surprising result, which is often referred to as the proton spin puzzle, has inspired vast experimental as well as theoretical activities to understand the spin structure of the proton. More recent experiments covering a broad kinematic range have confirmed the result and today the fraction of the proton spin carried by quarks and antiquarks is believed to be between about 15% and 35% [Bas05].

The longitudinal spin sum rule, which is valid at infinite momentum of the proton, relates the contributions of the partons to the spin of the proton (see e.g. [Glu01]):

$$\frac{1}{2}\Delta\Sigma + \Delta G + L_{q,g} = \frac{1}{2}, \quad (8.8)$$

where  $\frac{1}{2}\Delta\Sigma$  denotes the total quark spin,  $\Delta G$  the contribution of the gluon polarization and  $L_{q+g}$  the orbital angular momentum (OAM) of quarks and gluons. Today even after

---

<sup>8</sup>European Muon Collaboration

more than 15 years of intensive experimental and theoretical work succeeding the EMC result the spin structure of the proton is still far from being understood. While a lot of progress has been made in the investigation of the quark spin contribution mainly due to pDIS experiments, the contribution of the gluon is still not well constrained today, since pDIS experiments are not directly sensitive to the gluon. However, other experimental methods such as particle production in polarized  $p + p$  collisions at RHIC have started to provide direct access to the polarized gluon distribution and first results are on their way (see Section 8.3). Even more problematic is the investigation of the OAM contribution of the partons. Only first ideas to access the OAM have been proposed, which involve the measurement of *generalized* PDF's which are in principle accessible in exclusive reactions (see e.g. [Die03].)

### 8.2.2 Polarized Parton Distribution Functions

Unpolarized parton distributions (see Section 8.1.3) describe the momentum distribution of the parton within the nucleon regardless of the spin of the parton. The polarized parton distributions for quarks, denoted  $\Delta q_f$ , are defined as follows<sup>9</sup>:

$$\Delta q_f(x) = q_f^+(x) - q_f^-(x), \quad (8.9)$$

where  $q_f^{+(-)}(x)$  is the momentum distribution of a quark having the same (+) or opposite (-) helicity compared to the proton (see Equation 9.2 for a definition of the helicity). If all quark spins were oriented in the same direction  $\Delta q_f(x)$  would be given by the unpolarized distribution function,  $\pm q_f(x)$ , with the sign representing the helicity of the quarks with respect to the proton. The gluon polarization is defined in a similar way:

$$\Delta g(x) = g^+(x) - g^-(x). \quad (8.10)$$

The polarized parton distributions reflect the probability<sup>10</sup> of finding the helicity of the parton at a certain momentum fraction  $x$  to be the same as that of the nucleon (a negative probability means opposite spin orientation).  $\Delta\Sigma$  and  $\Delta G$  in Equation 8.8 are derived as the integrals of the corresponding polarized PDF's over the momentum fraction  $x$ :

$$\begin{aligned} \Delta\Sigma &= \int_0^1 \sum_f [\Delta q_f(x) + \Delta \bar{q}_f(x)] dx \\ \Delta G &= \int_0^1 \Delta g(x) dx. \end{aligned} \quad (8.11)$$

---

<sup>9</sup> $\Delta \bar{q}_f(x)$  for antiquarks is defined completely analogous.

<sup>10</sup>As in the unpolarized case polarized PDF's are strictly speaking number densities.

If the proton spin is carried only by quarks and antiquarks  $\Delta\Sigma$  is exactly 1.

Polarized parton distributions, also referred to as helicity distributions in case of the longitudinal spin structure, can be extracted from the polarized structure function  $g_1(x)$  which in the simple parton model is described in a similar way as  $F_1(x)$  in terms of the polarized PDF's (see Equation 8.6):

$$g_1(x) = \frac{1}{2} \sum_f e_f^2 \cdot [\Delta q_f(x) + \Delta \bar{q}_f(x)] . \quad (8.12)$$

$g_1(x)$  is measured in deep-inelastic scattering experiments with leptons polarized parallel or antiparallel to the spin of the target proton. Due to the conservation of angular momentum the spin of the quark needs to be antiparallel to the spin of the exchanged virtual photon. Hence the scattering cross section is different for leptons polarized parallel and antiparallel to the proton spin, respectively, if the polarized quark (antiquark) distribution is not zero. The measured polarized structure functions show a similar Bjorken scaling as the unpolarized structure functions.

The fixed-target DIS experiments HERMES<sup>11</sup> at DESY and COMPASS<sup>12</sup> at CERN are devoted to the thorough investigation of the proton spin structure. The HERMES experiment measures i.a. inclusive and semi-inclusive reactions in collisions of longitudinally polarized electrons or positrons with a nucleon target [Zih05, Sei07]. The target can be polarized either longitudinally or transversely. The latter allows to study the transverse spin structure of the proton. The inclusive measurement provides a significant contribution to the polarized structure function  $g_1(x)$ . The contribution from the different quark flavors, including the sea, is determined from semi-inclusive reactions, in which a hadron is identified in coincidence with the scattered lepton. The COMPASS experiment at the CERN SPS also measures inclusive and semi-inclusive reactions using a longitudinally polarized muon beam on a longitudinally polarized target. Besides the measurement of the quark contribution to the proton spin COMPASS is especially interested in the gluon polarization. The photon-gluon fusion (PGF) process, in which the virtual photon fuses with a gluon radiating a quark-antiquark pair, provides a more direct way to the gluon distribution than the scaling violation of  $g_1(x)$  at low  $x$ . COMPASS was especially designed to be able to tag such PGF events by identifying open charm production [Abb07, Mie05].

Analogous to the extraction of unpolarized PDF's global QCD fits to the existing pDIS data have been performed in order to extract sets of polarized parton distribution functions which best describe the world data. Figure 8.3 shows polarized distribution functions extracted by the Asymmetry Analysis Collaboration (AAC) [Got00, Hir04] for the  $u$  and  $d$  valence quarks and antiquarks  $\bar{q}$  (solid line). The shaded area indicates the uncertainty. As one can see from the figure the valence quark distributions are best constrained by

---

<sup>11</sup>HERA MEasurement of Spin

<sup>12</sup>COmmon Muon and Proton Apparatus for Structure and Spectroscopy

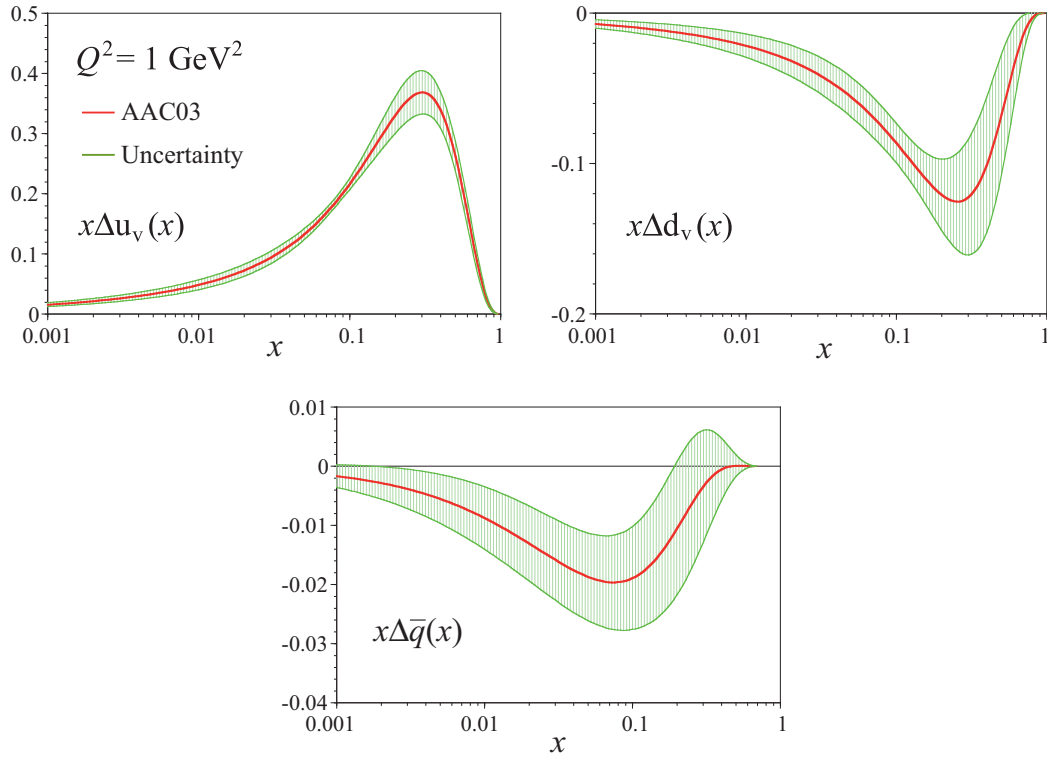


**Figure 8.3:** Polarized parton distribution functions and their uncertainties for the  $u$  and  $d$  valence quarks determined in a global analysis by the AAC [Hir04].

pDIS data, while the antiquark distribution still has a large relative uncertainty, which even allows a positive contribution at large values of  $x$ .

The gluon polarization, determined via scaling violation and photon-gluon fusion is currently the least constrained by pDIS measurements. Figure 8.4 shows the best QCD fit of  $\Delta g$  extracted by the AAC. Because of the large uncertainty in the extraction of  $\Delta g$  from pDIS data not only the magnitude of the gluon polarization is largely unknown, even the sign cannot be fixed by present data.

### 8.3 Measurement of $\Delta G$ at RHIC

A major emphasis of the PHENIX spin physics program at RHIC is the investigation of the gluon polarization  $\Delta G$  in collisions of ultra-relativistic polarized  $p + p$  collisions. RHIC allows the measurement of  $\Delta g(x)$  over a large range of gluon momentum fraction and with large momentum transfer  $Q^2$  [Bun00]. The latter ensures the applicability of

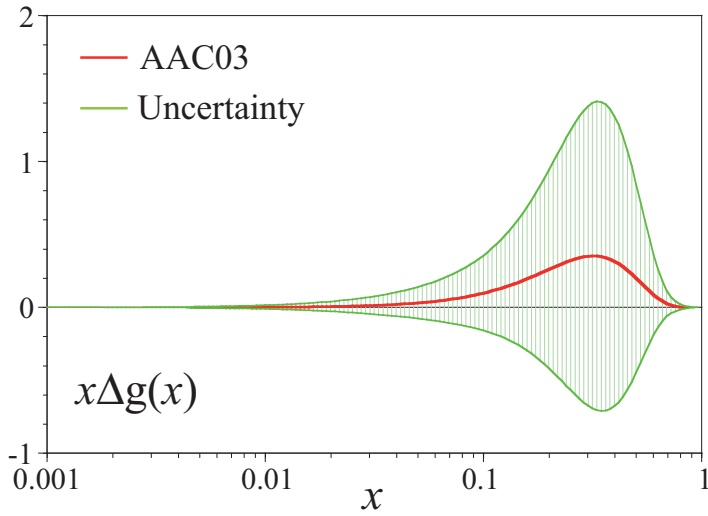


**Figure 8.4:** Polarized gluon distribution function and its uncertainty determined in a global analysis by the AAC [Hir04].

pQCD to describe the scattering process. Several channels are suited to directly access the polarized gluon distribution in polarized p + p collisions:

- prompt photon production:  $p + p \rightarrow \gamma + X$
- jet production:  $p + p \rightarrow \text{jet} + X$
- heavy-flavor production: e.g.  $p + p \rightarrow c\bar{c} + X$

As one can see in Figure 8.5 all these channels involve an initial state gluon in the production process at leading order in pQCD. The cleanest channel is provided by prompt-photon production, since it does not require the non-perturbative fragmentation process (the fragmentation function in Equation 2.5 simply reduces to a  $\delta$ -function). As was described in Chapter 6 in addition to quark-gluon Compton scattering (see Figure 8.5(a)) also annihilation,  $q + \bar{q} \rightarrow g + \gamma$ , contributes to prompt photon production at leading order. However, the annihilation process is suppressed in p + p collisions, due to the smaller  $\bar{q}$  density compared to  $g$ . This fact makes the approximate calculation of the corresponding cross section relatively simple. The calculation of *polarized* cross sections at large momentum transfer is done in a completely similar manner as described in Section 2.2.1 utilizing

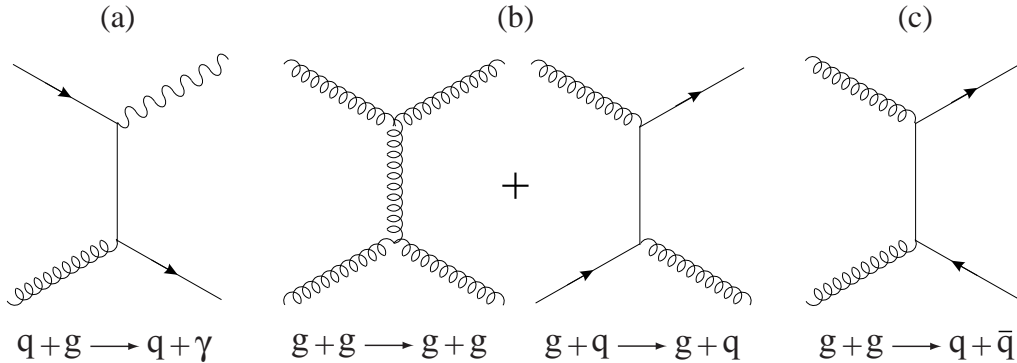


**Figure 8.5:** Selected Feynman diagrams of the parton processes involving a gluon in the initial state at leading order in  $p + p$  collisions: (a) quark-gluon Compton scattering for prompt-photon production, (b) gluon-gluon and gluon-quark scattering for jet production, and (c) gluon-gluon fusion for the production of heavy quark pairs.

the factorization theorem in pQCD<sup>13</sup>. However, the polarized cross section is usually not measured in spin experiments. Instead the spin asymmetry of the process given by

$$A_{LL} = \frac{d\Delta\sigma}{d\sigma} \quad (8.13)$$

is determined, where  $d\Delta\sigma$  is the polarized cross section and  $d\sigma$  is the unpolarized cross section of the channel which is investigated. The subscript of  $A_{LL}$  indicates that the colliding protons are both longitudinally polarized (and hence the helicity distributions are studied). The asymmetry in Equation 8.13 is usually referred to as double helicity asymmetry of the corresponding process.

All of prompt-photon production can be calculated at leading order (neglecting the contribution from annihilation) as a function of photon  $p_T$  via [Bun00]:

$$\begin{aligned} A_{\text{LL}}^{\gamma}(p_T) &\approx \frac{\sum_q \Delta q(x_T) \otimes \Delta g(x_T) \otimes d\Delta\sigma^{\text{hard}}(q+g \rightarrow q+\gamma)}{\sum_q q(x_T) \otimes g(x_T) \otimes d\sigma^{\text{hard}}(q+g \rightarrow q+\gamma)} \\ &\approx \frac{\Delta g(x_T)}{g(x_T)} \cdot \frac{g_1(x_T)}{F_1(x_T)} \cdot a_{\text{LL}}^{\text{hard}}(q+g \rightarrow q+\gamma), \end{aligned} \quad (8.14)$$

where the average probed momentum fraction  $x_T$  in each  $p_T$  bin can be approximated by:  $x_T \approx 2p_T/\sqrt{s}$ . Since the partonic spin asymmetry  $a_{\text{LL}}^{\text{hard}}$  at large momentum transfer can be calculated in pQCD and  $\frac{g_1(x_T)}{F_1(x_T)}$  has been measured in DIS experiments  $\frac{\Delta g(x_T)}{g(x_T)}$  can be extracted from the measured double helicity asymmetry. However, since quark-gluon

<sup>13</sup>The unpolarized PDF's and the unpolarized partonic cross section are exchanged by the polarized counterparts in the calculation of the polarized cross section.

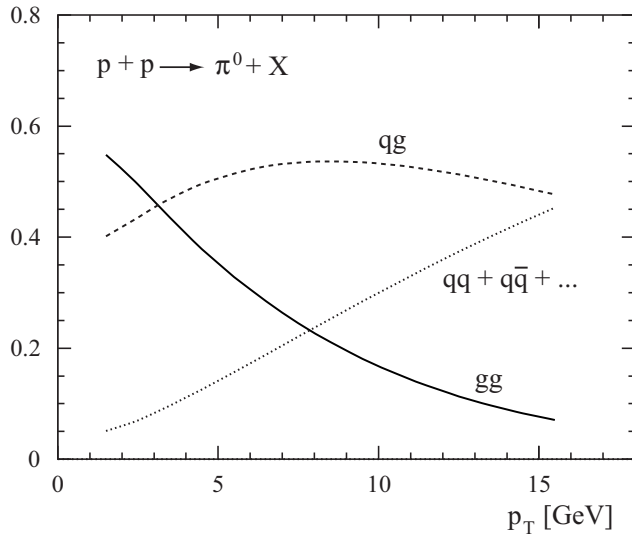


**Figure 8.6:** Relative contribution of partonic processes to the production of neutral pions in  $p + p$  collisions at  $\sqrt{s} = 200$  GeV at mid-rapidity.

Compton scattering is not the only process contributing to prompt-photon production the extraction of the polarized gluon distribution is not as simple as implied by Equation 8.14. Also, the measurement of prompt photons in  $p + p$  collisions is a demanding challenge and requires careful analysis of the data (as demonstrated in Chapters 6 and 7).

An alternative channel which is somewhat easier to access experimentally is the production of jets (Figure 8.5(b)), especially the production of neutral pions ( $\pi^0$ ) which has a comparatively large cross section. The fractional contribution of partonic processes to the production of  $\pi^0$ 's in  $p + p$  collisions at  $\sqrt{s} = 200$  GeV at mid-rapidity as a function of  $p_T$  is illustrated in Figure 8.6 (calculations performed by W. Vogelsang). Below  $p_T \approx 5$  GeV/c approximately 85% of produced  $\pi^0$ 's come from processes involving a gluon in the initial state. Therefore the measurement of the double helicity spin asymmetry in  $\pi^0$  production in this kinematic range is highly sensitive to the gluon. However, the extraction of the polarized gluon density requires the knowledge of the non-perturbative fragmentation function describing the fragmentation of the scattered parton to the neutral pion, which poses an additional uncertainty on the measurement. The  $\pi^0$  channel is the first which is being investigated in PHENIX in order to constrain the gluon polarization in longitudinally polarized protons. These analyses set the stage for further measurements of the double helicity spin asymmetry, ultimately utilizing the prompt-photon channel.

The production of heavy flavor in p + p collisions (see Figure 8.5c)) as a tool to measure  $\Delta g$  is not discussed here. However, a concise description of how to access the polarized gluon distribution via the production of heavy flavor in p + p collisions is given in [Bun00] and references therein.



# 9. Double Helicity Asymmetry in $\pi^0$ Production

As discussed in Section 8 the double helicity asymmetry in the production of neutral pions in longitudinally polarized ultra-relativistic  $p + p$  collisions (in the following referred to as  $\pi^0 A_{\text{LL}}$  or  $A_{\text{LL}}^{\pi^0}$ ) can be related to the polarized gluon distribution  $\Delta g(x)$  inside the polarized proton. Therefore, the measurement of  $A_{\text{LL}}^{\pi^0}$  can give valuable insight to the proton spin puzzle (see Section 8.2.1). The analysis presented in this work is the first attempt to measure the double helicity asymmetry of  $\pi^0$  production in a high-energy collider. Both the integrated luminosity as well as the average polarization of the proton beams were sufficient in the third physics Run of PHENIX to expect a significant result for  $A_{\text{LL}}^{\pi^0}$ .

The analysis is based on the same set of nanoDST's as were analyzed for the direct-photon measurement described in Chapter 7. In the following the various analysis steps involved in the determination of  $A_{\text{LL}}$  in  $\pi^0$  production in polarized  $p + p$  collisions are described.

## 9.1 Analysis Method

The double helicity asymmetry in  $\pi^0$  production is defined as given in Equation 8.13. In terms of the production cross sections for the different helicity combinations of the colliding protons  $A_{\text{LL}}^{\pi^0}$  can be written as:

$$A_{\text{LL}}^{\pi^0} = \frac{\sigma_{\text{like}} - \sigma_{\text{unlike}}}{\sigma_{\text{like}} + \sigma_{\text{unlike}}} , \quad (9.1)$$

where  $\sigma_{\text{like}}$  and  $\sigma_{\text{unlike}}$  denote the cross section of inclusive  $\pi^0$  production when the two protons have the same helicity (like) and opposite helicity (unlike), respectively. The helicity  $h$  of a particle can either be  $+$  or  $-$  and is defined by the orientation of its spin vector  $\vec{s}$  with respect to its momentum vector  $\vec{p}$ :<sup>1</sup>

$$h = \frac{\vec{s} \cdot \vec{p}}{|\vec{s}| |\vec{p}|} . \quad (9.2)$$

Section 3.1 describes how protons are polarized at RHIC. The stable polarization direction in the collider is vertical, i.e. transverse to the beam direction. In order to obtain

---

<sup>1</sup>For the definition of  $A_{\text{LL}}^{\pi^0}$  in Equation 9.1 the helicity is considered in the laboratory frame.

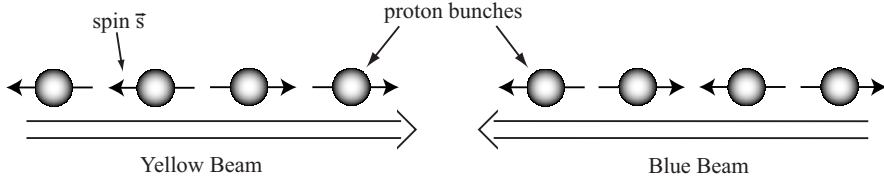


**Figure 9.1:** Illustration of the polarization direction pattern at the interaction point of PHENIX. The pattern is chosen in such a way at RHIC that all four helicity combinations occur alternating during one fill.

longitudinally polarized proton bunches at the interaction point the polarization direction of the proton bunches is rotated from transverse to longitudinal by spin rotators prior to collision and back to transverse after the collision. The polarization pattern in each ring at RHIC is chosen in such a way that all four possible combinations of polarization directions, i.e. helicity combinations, in the collisions of the bunches occur during the same fill. This is illustrated in Figure 9.1. For the calculation of  $A_{LL}$  using Equation 9.1 it is not distinguished between the helicity combinations “++” and “--” and “+-” and “-+”, respectively. The first two represent collisions of protons with equal helicity and the corresponding reaction cross sections are summarized in “ $\sigma_{\text{like}}$ ”, while the latter two represent collisions of protons with opposite helicity and the corresponding cross sections are summarized in “ $\sigma_{\text{unlike}}$ ”.

As discussed in Section 3.1.1 there are a number of depolarizing resonances that reduce the initial polarization during acceleration. Although RHIC utilizes so-called Siberian Snakes (see Section 3.1.2) to avoid depolarizing resonances and sustain initial polarization from the proton source, it is unfeasible to achieve a polarization of 100% in the proton bunches<sup>2</sup>. Therefore the colliding bunches can not be considered as ensembles of protons with all spins aligned in the same direction. To account for this the actual polarization of the proton beams must enter the calculation of  $A_{LL}$ .

The cross section of particle production can be expressed in terms of experimental yield ( $N$ ) and integrated luminosity ( $L$ ):

$$\sigma \propto \frac{N}{L} . \quad (9.3)$$

Since it can be assumed that detector acceptance and detection efficiency are identical for all bunch crossings, i.e. independent of beam polarization, Equation 9.1 can be written using Equation 9.3 as:

$$A_{LL} = \frac{1}{|P_B||P_Y|} \frac{N_{++} - RN_{+-}}{N_{++} + RN_{+-}}, \quad R = \frac{L_{++}}{L_{+-}}, \quad (9.4)$$

<sup>2</sup>In fact, the design polarization at RHIC is 70% (see Section 3.1).

where  $N_{++}$  and  $N_{+-}$  denote the number of neutral pions measured in bunch crossings with both proton bunches having the same helicity (++) and opposite helicity (+−), respectively.  $R$  is referred to as relative luminosity and indicates any difference in the number of collisions with like and unlike helicities measured in one fill. In Equation 9.4 the average polarization of the blue ( $P_B$ ) and the yellow ( $P_Y$ ) beam account for the limited polarizations of the proton beams. For the analysis it was assumed that the polarization did not change during one fill. The beam polarizations were measured for the blue and yellow beam using polarimeters installed in each ring (see Section 3.1.4).

For the calculation of  $A_{\text{LL}}^{\pi^0}$  the number of neutral pions needs to be determined for like and unlike helicity combinations separately. The double helicity asymmetry was calculated in four different  $p_T$  bins: 1–2 GeV/ $c$ , 2–3 GeV/ $c$ , 3–4 GeV/ $c$  and 4–5 GeV/ $c$ .<sup>3</sup>

## 9.2 Data Selection

The information stored in the nanoDST’s which are required for the analyses presented in this work are described in Section 7.2.1. For the double helicity asymmetry analysis only events that satisfy the ERT\_4×4c trigger in coincidence with the minimum bias trigger, referred to as Gamma3 data sample in the direct-photon analysis, are analyzed. As was described in Section 7.2.2 this data set is enriched with high-energy photons.

### Analyzed Runs

As was discussed in Section 7.2.3 the individual runs recorded during Run III  $p + p$  were subject to certain quality tests prior to the actual analysis. In addition to the requirements necessary for the direct-photon analysis the measurement of the relative luminosity  $R$ , required for each run in the  $A_{\text{LL}}^{\pi^0}$  analysis, posed another constraint on the run selection. The determination of  $R$  is based on hits recorded with the BBC and ZDC (this is described in more detail in Section 9.3). However, for a few runs the corresponding data was not available. These runs were excluded from the  $A_{\text{LL}}^{\pi^0}$  analysis. Eventually a total of 158 runs in 47 fills were analyzed for the double helicity asymmetry. The list of “good” runs in the Gamma3 data sample is given in Appendix B.2.

### Event Selection

In the  $A_{\text{LL}}^{\pi^0}$  analysis only events are accepted that satisfy the condition  $\Delta z_{\text{vertex}} = \pm 30$  cm, where  $\Delta z_{\text{vertex}}$  is the deviation of the measured  $z$ -vertex position from the nominal vertex.

---

<sup>3</sup>A finer segmentation in transverse momentum is not reasonable because of the large statistical errors that arise.

Unlike in the direct-photon analysis, only the vertex position as measured by the BBC is utilized. After the vertex cut a total of  $N_{\text{evt}}^{\text{gamma}3} = 43.5$  million Gamma3 filtered events remained for the analysis. As was described in Section 7.2.4 the Gamma3 trigger had a mean rejection factor of  $f_{\text{reject}}^{\text{gamma}3} \approx 109$  in Run III p + p. However, the normalization required in the determination of the cross section to account for the ERT rejection factor is not necessary in the calculation of  $A_{\text{LL}}^{\pi^0}$  since it cancels in Equation 9.4.

### 9.3 Relative Luminosity

For the determination of the double helicity asymmetry  $A_{\text{LL}}$  the relative luminosity  $R$  defined in Equation 9.4 must be known. The integrated luminosity  $L$  in p + p collisions is defined as:

$$L = \frac{1}{\sigma_{\text{pp}}^{\text{inel}}} \int dN , \quad (9.5)$$

where  $\int dN$  is the number of inelastic collisions (events) integrated over a certain time period and  $\sigma_{\text{pp}}^{\text{inel}}$  is the total inelastic p + p cross section. Hence the integrated luminosity analyzed for  $A_{\text{LL}}^{\pi^0}$  is:  $L = N_{\text{evt}}^{\text{gamma}3} \times f_{\text{reject}}^{\text{gamma}3} \times \epsilon_{\text{trig}}^{\text{MB}} \approx 0.21 \text{ pb}^{-1}$ , where the rejection factor of the Gamma3 trigger and the trigger bias of the minimum bias trigger is taken into account.

For the asymmetry analysis of  $A_{\text{LL}}^{\pi^0}$  the ratio of the integrated luminosity in bunch crossings with like helicities ( $L_{++}$ ) to unlike helicities ( $L_{+-}$ ) must be known. The corresponding analysis for the Run III p + p data is described in detail in [Tan03].  $R$  was determined for each run by counting BBCLL1 live<sup>4</sup> triggers with a  $z$ -vertex cut of  $\pm 30$  cm, i.e. minimum bias trigger counts, for each bunch crossing.  $R$  is then calculated for each fill by summing BBCLL1 triggers for all bunch crossings with like and unlike helicities and dividing the sums.

A detector needs to satisfy several requirements in order to serve as a luminosity detector: (i) sensitive to the same collisions in which the investigated processes occur, (ii) small background from beam-gas events etc., (iii) high statistics and (iv) small spin asymmetry in the detector. For the detection of neutral pions all this is accomplished by the BBC of PHENIX or more precisely by the BBCLL1 trigger, because  $\pi^0$ 's are measured in coincidence with this trigger and therefore have the same  $z$ -vertex acceptance. It was shown that a possible spin asymmetry of the BBC is close to zero [Tan03].

In order to have an estimate of the uncertainty of the relative luminosity measurement, information provided by a second detector was utilized. The ZDC also meets the requirements stated above except that the  $z$ -vertex resolution is considerably worse than in the

---

<sup>4</sup>In PHENIX a trigger count is called a *live* trigger if the DAQ is not busy on arrival of the trigger and hence the event could be further processed by the data acquisition system.

BBC. Trigger counts from both detectors were compared to each other and from this an uncertainty of  $\partial R = 2.5 \times 10^{-4}$  was estimated. The uncertainty of  $A_{\text{LL}}^{\pi^0}$  introduced by the uncertainty of the relative luminosity is given by:

$$\partial A_{\text{LL}} \approx \frac{1}{2|P_B||P_Y|} \partial R , \quad (9.6)$$

where the approximations  $N_{++} \equiv N_{+-}$  and  $R \equiv 1$  were used. With the average beam polarizations achieved in Run III (see Section 9.4) the estimated  $\partial R$  translates into  $\partial A_{\text{LL}} \approx 1.2 \times 10^{-3}$ .

## 9.4 Polarization Measurement

The absolute beam polarizations at RHIC are measured with proton-carbon polarimeters installed in each of the two rings (see Section 3.1.4). For the Run III p + p data set the pC polarimeters were calibrated using a polarized proton-jet target. In the measurement of  $A_{\text{LL}}$  the accuracy of the polarization measurement plays a decisive role. From Equation 9.4 it can be derived (for simplicity  $P_B = P_Y = P_{\text{beam}}$ ):

$$\frac{\partial A_{\text{LL}}}{A_{\text{LL}}} = 2 \cdot \frac{\partial P_{\text{beam}}}{P_{\text{beam}}} . \quad (9.7)$$

Thus the relative uncertainty of the double helicity asymmetry due to the polarization is twice as large as the relative uncertainty of the polarization measurement. However, since the measured asymmetry scales with the polarization, the uncertainty of the polarization does not change the statistical significance (relative uncertainty) of a non-zero  $A_{\text{LL}}$  result.

The average beam polarization was determined for each fill of Run III p + p. Figure 9.2 shows the distribution of polarizations in the blue and yellow ring as a function of the fill number. The beam polarization averaged over the complete Run III, weighted by the number of triggered events was 30% in the yellow ring and 35% in the blue ring. The product of both beam polarizations poses a scale uncertainty of 28%<sup>5</sup> on the  $A_{\text{LL}}^{\pi^0}$  result [Adl06b].

## 9.5 Energy Scale Correction

The analysis of the  $\pi^0$  double helicity asymmetry was carried out prior to the direct-photon analysis described in Chapter 7. Although both analyses are based on the same

---

<sup>5</sup>The scale uncertainty includes statistical and systematic uncertainties of the polarization measurement.

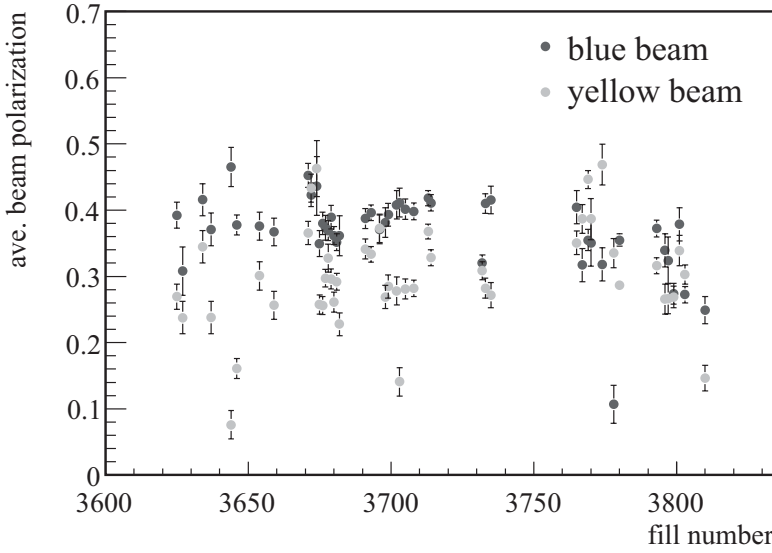


**Figure 9.2:** Absolute polarization of the beam in the blue and yellow ring measured in each fill. The weighted average over all fills is 35% in the blue ring and 30% in the yellow ring.

nanoDST's, i.e. the energy calibration is identical in both cases, the correction of the energy scale non-linearity differs slightly for the two analyses. For the direct-photon analysis the parameters of the correction were determined for each of the eight EMCAL sectors individually. For the  $A_{LL}^{\pi^0}$  analysis the non-linearity correction was available sector-wise only for the PbGl. For the PbSc the correction was determined as a mean of all six sectors. While for the correction of the PbGl data the chosen functional form of the non-linearity was the same in the  $A_{LL}^{\pi^0}$  and direct-photon analysis (see Equation 7.10) the form of the correction applied to the PbSc data slightly differed in the  $A_{LL}^{\pi^0}$  analysis. It was given by an exponential [Baz03a]:

$$\frac{E_{\text{corr}}}{E} = 1 + e^{c_0 \cdot E + c_1}, \quad (9.8)$$

where  $E$  is the measured energy given in the nanoDST's and  $c_0$  and  $c_1$  are free parameters of the correction.

The difference in the corrections applied in the two analyses is negligible compared to the statistical errors obtained in the  $A_{LL}^{\pi^0}$  analysis and the systematic uncertainties assigned to the non-linearity in the direct-photon analysis.

## 9.6 Geometric Acceptance

In the analysis of the double helicity asymmetry the correction for the limited geometric acceptance of the EMCal is not required. However, dead and bad towers in the PbGl and PbSc must be identified and removed from the data analysis, since they would affect the reconstruction of neutral pions. The method for the identification of erroneous towers was described in Section 7.2.6. In fact, the list of bad towers (bad tower map) applied in the direct-photon analysis was originally determined for the  $A_{\text{LL}}^{\pi^0}$  analysis presented in this work and then adopted in the direct-photon measurement.

The bad tower maps for each EMCal sector for the Run III  $p + p$  data set are shown in Appendix C. A cluster in the EMCal is removed from the data set if the tower with maximum energy within the cluster coincides with a tower marked as bad (including first order neighbors) in the bad tower map.

## 9.7 Photon-Like Cluster Sample

The data sample obtained with the EMCal contains not only photons but also hits from charged and neutral hadrons as well as electrons. This was already discussed in Section 7.3 for the measurement of the inclusive photon spectrum. Neutral pions are identified in the EMCal data via an invariant mass analysis of photon pairs. Details of this method are discussed in Section 9.8. In order to reduce the background from hadronic sources particle identification cuts are applied to the data sample prior to the  $\pi^0$  reconstruction. Similar to the direct-photon analysis presented in this work and the cross-section measurement of neutral pion production [Bat05b, Bat05a] the shape of the shower in the EMCal is primarily utilized to remove hadronic showers from the cluster sample analyzed for  $A_{\text{LL}}^{\pi^0}$ . In the PbGl a cut on the dispersion of the shower is applied, while in the PbSc the deviation of the shower shape from parameterizations is used to remove non-electromagnetic clusters (see Section 7.3.1). Also a minimum cluster energy is required to reduce electronic noise. In the  $A_{\text{LL}}^{\pi^0}$  analysis the energy threshold was set to 0.2 GeV (0.1 GeV) for the PbGl (PbSc). The photon sample after the application of the PID cuts is referred to in the following as photon-like cluster sample.

In the direct-photon analysis a restriction on the photons in the Gamma3 data sample that pass the PID criteria is introduced and referred to as *FEM requirement* (see Section 7.3.2). In the  $A_{\text{LL}}^{\pi^0}$  analysis this condition is checked for pairs of photon-like clusters. Here the FEM requirement ensures that only photon pairs are accepted in which the more energetic photon most likely triggered the ERT.

## 9.8 Reconstruction of Neutral Pions

Neutral pions are reconstructed in the analysis by the calculation of the invariant mass  $m_{\text{inv}}$  of photon pairs (neutral pions decay into two photons with a branching ratio of 98.8%) as a function of the pair  $p_T$  and subsequent comparison to the expected mass for  $\pi^0$ 's.  $m_{\text{inv}}$  is given by the absolute value of the sum of the four-momenta of the decay photons. Assuming the two measured photon-like clusters originate from a  $\pi^0$  decay the invariant mass of the pair can be calculated from the measured energy of the two decay photons,  $E_1$  and  $E_2$ , and the opening angle  $\theta$  of the decay:<sup>6</sup>

$$m_{\text{inv}} = \sqrt{2E_1E_2 \cdot (1 - \cos \theta)} . \quad (9.9)$$

The measured sample of photon-like clusters does not only contain decay photons from  $\pi^0$  decays. There are also contributions from  $\eta$  decays, direct photons and electrons. Also neutral and charged hadrons which pass the PID cuts contaminate the photon-like cluster spectrum. Because of these background sources events in  $p + p$  collisions usually contain more than two photon candidates. Since it is not known which photon-like cluster in the data sample originates from a  $\pi^0$  decay all possible photon-pair combinations per event have to be considered in the invariant mass analysis. Pairing photon-like clusters which are uncorrelated yields a random invariant mass. Uncorrelated photon-pairs constitute the combinatorial background (already introduced in Section 7.3.2 for the charged correction of the inclusive photon spectrum). The number of possible pair combinations  $N_{\text{pair}}$  (correlated and uncorrelated) in a single event is determined solely by the multiplicity  $N$ , i.e. the number of photon-like clusters in the event:  $N_{\text{pair}} = \frac{N}{2} \cdot (N - 1)$ .

Figure 9.3 shows the invariant mass distributions derived from the full data set (sum of PbGl and PbSc) in each of the four  $p_T$  bins used in the  $A_{\text{LL}}^{\pi^0}$  analysis. As was stated in Section 7.2.5 the rest mass of the  $\pi^0$  is approximately  $135 \text{ MeV}/c^2$ . In all four  $p_T$  bins in Figure 9.3 a large peak is visible around the nominal  $\pi^0$  mass. Note that the smaller peak visible at higher mass values (around  $\sim 550 \text{ MeV}/c^2$ ) in Figure 9.3 especially above  $p_T = 2 \text{ GeV}/c$  indicates correlated photon pairs originating from  $\eta$  decays. The  $\eta$  decays into two photons with a branching ratio of about 40% (see Section 7.5.1). The combinatorial background decreases with increasing transverse momentum since the multiplicity also decreases towards higher  $p_T$ . In the cross section measurement of  $\pi^0$  production the combinatorial background must be subtracted from the  $\pi^0$  peak in order to determine the corrected number of neutral pions in a given  $p_T$  bin. However, in the asymmetry measurement presented in this thesis the background contribution to  $A_{\text{LL}}^{\pi^0}$  is calculated differently. This is described in more detail in Section 9.9.

---

<sup>6</sup>This is true for all pairs of massless particles.

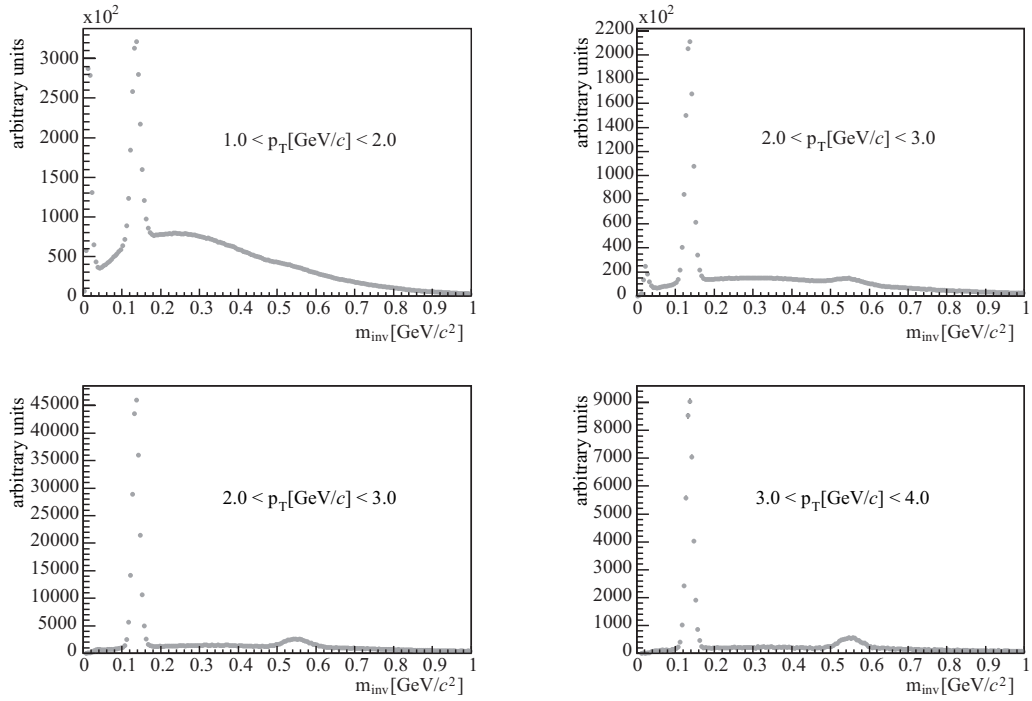


**Figure 9.3:** Invariant mass histograms of photon pairs measured with the PHENIX EMCal in four different  $p_T$  bins used in the  $A_{LL}^{\pi^0}$  analysis. The large peak around  $140 \text{ MeV}/c^2$  indicates reconstructed neutral pions. The combinatorial background is largest for small  $p_T$  and decreases as the multiplicity decreases with increasing  $p_T$ . The peak around  $m_{\text{inv}} = 550 \text{ MeV}/c^2$  clearly visible for  $p_T > 2 \text{ GeV}/c$  originates from the two-photon eta decay.

The background from uncorrelated pairs can be reduced in the analysis by introducing a cut on the energy asymmetry  $\alpha$  of the photon-like cluster pairs (see Equation 7.9). This is illustrated schematically in Figure 9.4. The distribution of the energy asymmetry of  $\pi^0$  decays is flat. However, this is not true for uncorrelated photon pairs. The  $p_T$  distribution of inclusive photons is steeply falling. Therefore, a highly energetic photon is more likely paired with other low-energy photons within the same event (hadrons in the photon-like cluster sample also have small energies). This results in a large energy asymmetry. By setting a maximum asymmetry of  $\alpha_{\text{max}} = 0.7$  as indicated in Figure 9.4 the signal-to-background ratio is improved significantly. Since it can be assumed that the energy asymmetry is independent of the helicity combination in the  $p + p$  collision the loss of correlated photon pairs does not need to be corrected in the calculation of  $A_{LL}^{\pi^0}$ .

The analysis of the  $\pi^0$  double helicity asymmetry was carried out for the data accumulated separately with the two subsystems of the PHENIX EMCal (PbGl and PbSc) and using the full statistics of the complete EMCal. The calorimeter consists of eight sec-

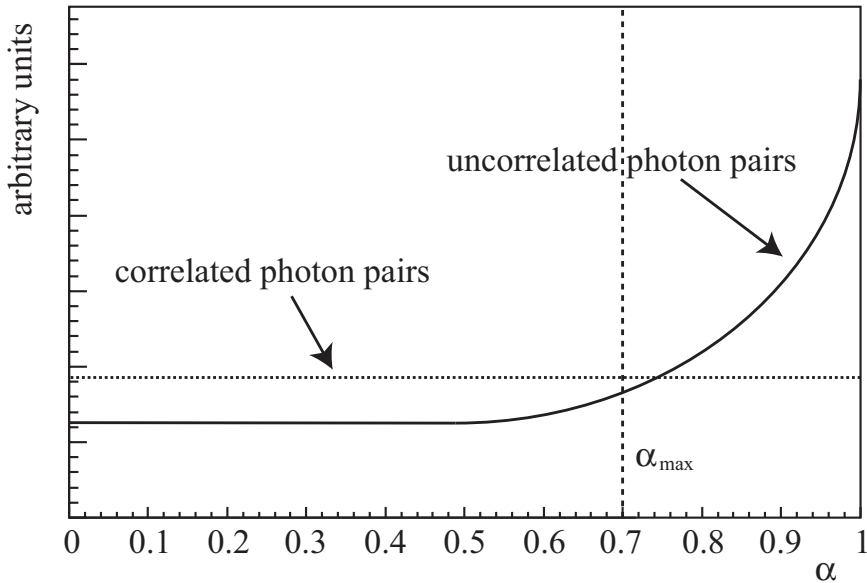


**Figure 9.4:** Schematic illustration of the energy asymmetry of correlated and uncorrelated photon pairs. The threshold  $\alpha_{\max}$  improves the signal-to-background ratio significantly.

tors, four in each arm of the central spectrometer (see Figure 7.1 for illustration). The  $\pi^0$  decay photons are not required to hit the same sector for the invariant mass analysis. Certain sector combinations are chosen to generate invariant mass distributions for the PbGl, PbSc and EMCAL. This is illustrated in Figure 9.5. For the PbGl only two sectors have to be considered (E0, E1). Both  $\pi^0$  decay photons must hit one of the two PbGl sectors resulting in three possible sector combinations. The PbSc consists of six sectors, two in the east (E2, E3) and four in the west arm (W0, W1, W2, W3). In the considered  $p_T$  range the opening angle  $\theta$  of a  $\pi^0$  decay is limited in such a way<sup>7</sup> that the two decay photons of a neutral pion decay do not hit the two outermost sectors of the same arm. For the same reason sectors from the east and west do not need to be combined. Hence in the analysis of the PbSc data twelve sector combinations are considered. In order to utilize the full statistics recorded by the EMCAL all sector combinations of the PbGl and PbSc are accepted, adding three sector combinations in the east arm that join PbGl and PbSc sectors (ignoring the combination of the outermost sectors (E0, E3)).

The invariant mass distributions shown in Figure 9.3 were derived from the full statistics accumulated with the EMCAL and are independent of the beam polarization, i.e. events from all bunch crossings were combined. However, for the  $A_{LL}^{\pi^0}$  analysis the invariant mass histograms have to be generated for each helicity combination separately. In fact, invari-

<sup>7</sup>The opening angle  $\theta$  of a  $\pi^0$  decay decreases with increasing transverse momentum.

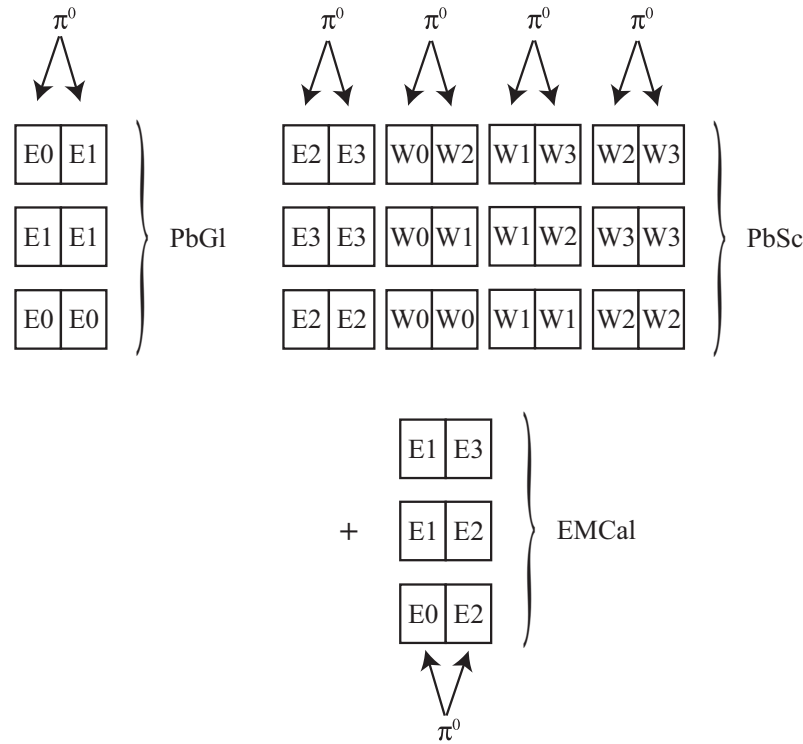


**Figure 9.5:** Illustration of the sector combinations applied in the invariant mass analysis of photon pairs to derive  $\pi^0$  yields in the PbGl, PbSc and the combined EMCAL.

ant mass histograms were generated for each of the 120 bunch crossings<sup>8</sup>. The yields derived from the invariant mass distributions were then added for the two helicity combinations (like and unlike helicity of the two colliding protons) required in the calculation of  $A_{\text{LL}}^{\pi^0}$ .

### 9.8.1 Yield Corrections

Unlike in the cross-section measurement where a number of corrections have to be applied to the raw  $\pi^0$  yield (e.g. reconstruction efficiency, geometric acceptance, ERT efficiency, photon conversion, shower merging) for the calculation of  $A_{\text{LL}}^{\pi^0}$  these yield corrections are not required. The corresponding corrections cancel in the yield ratio of Equation 9.4, provided that the correction does not depend on the helicity combination of the p + p collision, which is assumed in the analysis presented in this work.

A convenient feature of the invariant mass analysis is the fact that contributions to the photon-like cluster sample from charged and neutral hadrons as well as electrons do

<sup>8</sup>Note that not all bunch crossings contain a p + p collision (see Section 9.8.2).

not have to be corrected explicitly. These background particles are paired in the analysis with other hits of the same event forming uncorrelated pairs and are thus part of the combinatorial background. The correction of the combinatorial background in the  $A_{\text{LL}}^{\pi^0}$  analysis is described in more detail in Section 9.9.1.

### 9.8.2 Bunch Crossing Numbering

As described in Chapter 3 the beam in each of the two rings of the RHIC collider is divided into 120 bunches. The bunches are numbered from 0 to 119 and each has either a positive or negative sign in polarization prepared at the source transverse to the beam. At PHENIX, bunch  $i$  of the blue beam collides with bunch  $(i + 80) \% 120^9$  of the yellow beam. In the analysis the number  $i$  was used to tag the corresponding bunch crossing (bunch crossing ID). Not all bunches in the two rings are necessarily filled with protons. In the  $p + p$  Run of year III the RHIC collider was operated in a 55-bunch mode, i.e. 55 bunches in each beam were filled with protons. Bunch crossings with odd numbering were empty. Because of the abort gaps all bunch crossings from 30-39 and from 110-119 were empty<sup>10</sup>. This results in  $p + p$  collisions occurring in 50 bunch crossings.

For the analysis of the double helicity asymmetry it is vital that the bunch crossing ID's are correctly assigned, in order to be able to determine the  $\pi^0$  yields for the different helicity combinations. It was found [Tan03] that because of an error in the GL1 trigger system the bunch crossing ID was shifted by a constant for a few runs. This was corrected run-by-run during the generation of the invariant mass distributions. Figure 9.6 shows the number of events per bunch crossing for a single run with correctly assigned bunch crossing ID's. The total number of events in all bunch crossings for this run is  $N^{\text{evt}} = 476105$ . Bunch 20 in both beams was used for beam steering feedback and was unstable because of this. Hence bunch crossings 20 and 60 were excluded from the analysis.

## 9.9 $A_{\text{LL}}$ Calculation

For the calculation of the  $\pi^0$  double helicity asymmetry  $\pi^0$  yields have to be extracted from the invariant mass histograms in the four  $p_T$  bins and for the different helicity combinations. As was noted in Section 9.8 the combinatorial background under the  $\pi^0$  peak is not subtracted prior to the  $\pi^0$  yield extraction. Instead the  $\pi^0$  signal  $N^{\pi^0+\text{bg}}$  consisting of  $\pi^0$  yield and combinatorial background under the  $\pi^0$  peak is determined. With these yields the double helicity asymmetry  $A_{\text{LL}}^{\pi^0+\text{bg}}$  is calculated according to Equation 9.4.  $A_{\text{LL}}^{\pi^0+\text{bg}}$  is referred to as signal  $A_{\text{LL}}$ .

---

<sup>9</sup>Here % is the modulo operator.

<sup>10</sup>In Run III  $p + p$  the abort gap was chosen to comprise ten empty bunches in each ring.

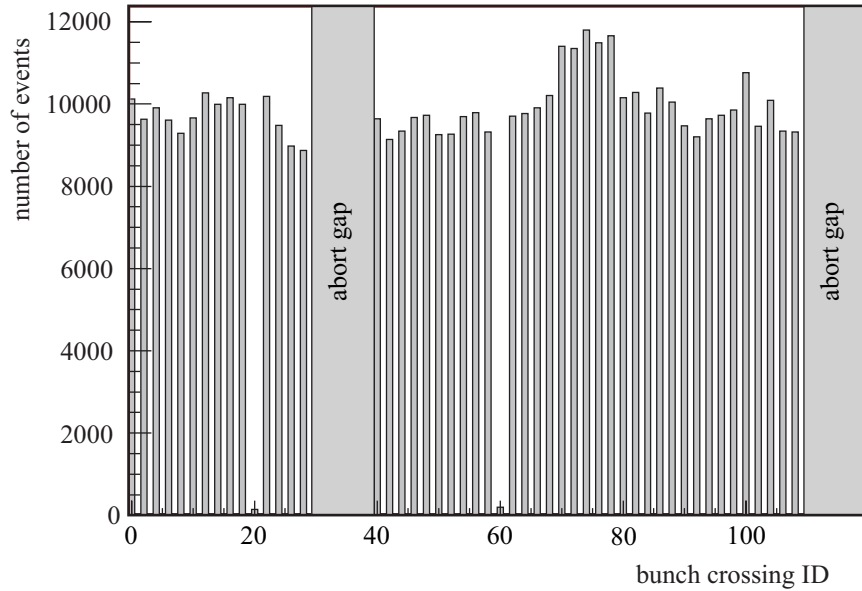


**Figure 9.6:** Number of recorded events per bunch crossing for a single run. Bunch crossings with odd ID's are empty. Also the empty bunch crossings due to the abort gaps in the blue and the yellow ring are marked.

The nominal mass of the neutral pion is  $m_{\pi^0} \approx 135 \text{ MeV}/c^2$  as noted before. However, due to the steeply falling  $p_T$  spectrum and the finite energy resolution of the detector the measured  $\pi^0$  mass is shifted to higher values<sup>11</sup> and is distributed Gaussian-like around the measured value. The  $\pi^0$  signal was determined by integrating over a certain range in invariant mass. The position of the  $\pi^0$  mass peak (given by the mean of the Gaussian distribution) is almost constant in the considered  $p_T$  range at a value of  $m_{\pi^0}^{\text{meas}} \approx 137 \text{ MeV}/c^2$ . The resolution of the EMCAL during data taking was such that the  $1\sigma$ -width of the  $\pi^0$  peak varied from  $12 \text{ MeV}/c^2$  in the lowest  $p_T$  bin to  $9.5 \text{ MeV}/c^2$  in the highest  $p_T$  bin. In order to cover the relevant region of the  $\pi^0$  mass peak the integration range was chosen to cover  $\pm 25 \text{ MeV}/c^2$  around  $m_{\pi^0}^{\text{meas}}$ . Because of the finite bin size chosen in the analysis the effective integration range was:

$$m_{\text{inv}} \in [110 \text{ MeV}/c^2, 165 \text{ MeV}/c^2]. \quad (9.10)$$

This range is illustrated in Figure 9.7. In order to have a measure of the contribution of the background to  $A_{\text{LL}}^{\pi^0+\text{bg}}$ , the double helicity asymmetry was also calculated for the

<sup>11</sup>More decay photons are shifted to higher energies than vice versa.

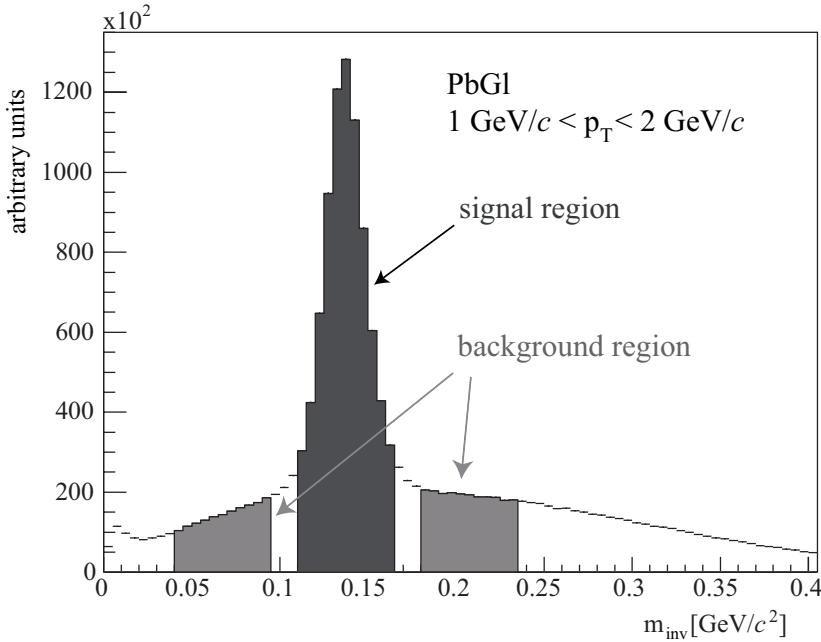


**Figure 9.7:** Illustration of the integration ranges applied in the analysis of the double helicity asymmetry to derive yields in the signal and background region.

combinatorial background. For this reason two regions adjacent to the  $\pi^0$  mass peak were defined with a width of  $55 \text{ MeV}/c^2$  each:

$$\begin{aligned} m_{\text{inv}} &\in [40 \text{ MeV}/c^2, 95 \text{ MeV}/c^2], \\ m_{\text{inv}} &\in [180 \text{ MeV}/c^2, 235 \text{ MeV}/c^2]. \end{aligned} \quad (9.11)$$

The background signal  $N^{\text{bg}}$  is the sum of signals obtained in both mass ranges and contains only pairs of photon candidates in the combinatorial background. The double helicity asymmetry calculated from  $N^{\text{bg}}$  is referred to as background  $A_{\text{LL}}$  or  $A_{\text{LL}}^{\text{bg}}$ .

The background corrected double helicity asymmetry of the pure  $\pi^0$  signal is then calculated by weighting the signal  $A_{\text{LL}}$  with  $\frac{1}{1-r}$  and subtracting the background  $A_{\text{LL}}$  weighted with  $\frac{r}{1-r}$ :

$$A_{\text{LL}}^{\pi^0} = \frac{A_{\text{LL}}^{\pi^0+\text{bg}} - r \cdot A_{\text{LL}}^{\text{bg}}}{1 - r}, \quad (9.12)$$

where the contribution of the combinatorial background in the signal region is given by  $r$ , i.e.  $r$  is the ratio of the combinatorial background to the uncorrected yield in the  $\pi^0$  mass peak region. Thus the combinatorial background must be determined in the peak region in order to derive  $A_{\text{LL}}^{\pi^0}$ .

A summary of the statistics obtained in the analysis of the full Gamma3 data set is given in Table 9.1.  $N^{\pi^0+\text{bg}}$  and  $N^{\text{bg}}$  represent the result of the integration in the respective

invariant mass range for a given  $p_{\text{T}}$  bin. Since the geometric acceptance of the PbSc is larger more pairs are counted in the PbSc than in the PbGl. The numbers given for the EMCal are larger than the simple sum of the PbGl and PbSc numbers. This is because the combined EMCal subsystems provide more sector combinations than the sum of the individual subsystems.

### 9.9.1 Background Estimation

For the calculation of the background corrected double helicity asymmetry (see Equation 9.12) the fraction  $r$  of the combinatorial background under the  $\pi^0$  peak must be known. The shape of the combinatorial background can be determined using the technique of mixing photon candidates from different events. The same method was applied to remove the background from the charged particle contribution to the inclusive photon spectrum (see Section 7.3.2). In order to determine the combinatorial background in the invariant mass distributions each photon candidate of the current event is paired with photon candidates from older events.<sup>12</sup>

For the event mixing it is important to use only unbiased events, i.e. minimum bias events. However, when analyzing Gamma3 filtered data all events in the data sample have triggered the ERT. Hence in the event mixing a high- $p_{\text{T}}$  photon would be paired with other high- $p_{\text{T}}$  photons from other events. This would bias the result of the mixed event distributions and therefore would not represent the correct shape of the real combinatorial background. This problem is avoided by generating so-called *pseudo minimum bias* events: one photon candidate is excluded from each event used for the event mixing (except the current event). This photon-like cluster must fulfill the conditions also

---

<sup>12</sup>Each event is analyzed one after another. Hence “old events” means events which were analyzed previously to the current event.

$p_{\text{T}}$ [GeV/ $c$ ]	PbGl		PbSc		EMCal	
	$N^{\pi^0+\text{bg}}$	$N^{\text{bg}}$	$N^{\pi^0+\text{bg}}$	$N^{\text{bg}}$	$N^{\pi^0+\text{bg}}$	$N^{\text{bg}}$
1.0 – 2.0	803413	365318	1184614	841979	2132896	1329199
2.0 – 3.0	266467	50260	802318	181400	1089209	238612
3.0 – 4.0	45822	4218	166023	17449	213458	21933
4.0 – 5.0	8814	601	31823	2552	40727	3180

**Table 9.1:** Number of counts obtained in the signal and background region of the invariant mass distributions in the four  $p_{\text{T}}$  bins for the PbGl, PbSc and the combination of the two calorimeter subsystems. The counts are added from all helicity combinations.

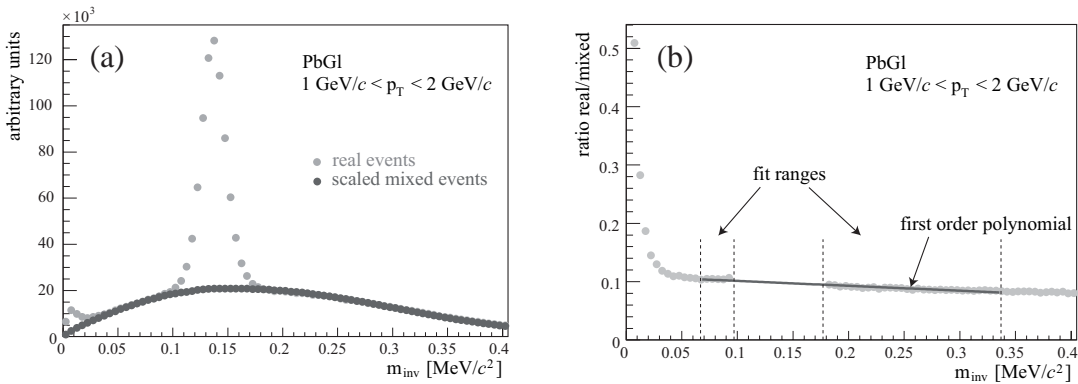


**Figure 9.8:** (a) Invariant mass distribution of photon pairs in real and mixed events (scaled) measured with the PbGl in the lowest  $p_T$  bin. The combinatorial background determined with the mixed event method reproduces the measured background very well. (b) The ratio of the invariant mass distributions in real and mixed events. The scaling factor of the mixed distribution is a first order polynomial fitted to the ratio in regions adjacent to the neutral pion mass peak.

required for the FEM flag and hence is likely the photon that triggered the ERT. Thus in the event mixing the high- $p_T$  photon is very likely not paired with any other trigger photon from older events and the shape of the mixed event combinatorial background is very similar to the unbiased distribution.

Figure 9.8(a) shows the invariant mass distribution obtained in the event mixing and scaled to the real distribution. The scaling factor is a first order polynomial adjusted to the ratio of the real and mixed distribution on both sides of the  $\pi^0$  mass peak (illustrated in Figure 9.8(b)). The background contribution under the  $\pi^0$  peak is given by the ratio of the integrals of the two distributions in the  $\pi^0$  peak region given by the mass range specified

$p_T$ [ $\text{GeV}/c$ ]	PbGl	PbSc	EMCal
	$r$ [%]		
1.0 – 2.0	27.7	40.0	35.4
2.0 – 3.0	10.8	12.4	12.0
3.0 – 4.0	5.2	5.8	5.7
4.0 – 5.0	3.7	4.3	4.3

**Table 9.2:** Contribution of the combinatorial background under the neutral pion mass peak in the PbGl, PbSc and EMCal obtained in the four  $p_T$  bins using an event mixing method.

in 9.10. In Table 9.2 the background contribution  $r$  determined in the four  $p_{\text{T}}$  bins for the PbGl, PbSc and EMCAL is listed. Since the PbSc is more susceptible to hadrons than the PbGl the background under the  $\pi^0$  peak is larger in the PbSc.

The uncertainty of  $r$  was estimated by applying polynomials of different orders to describe the ratio of the real and mixed histograms. Moreover, in a different approach the combinatorial background under the  $\pi^0$  mass peak was determined by fitting a combination of polynomial and Gauss function to the invariant mass distribution of real events, applying different polynomials and fit regions. The comparison of the various results yielded a relative uncertainty of 2% on the background fraction  $r$ .

### 9.9.2 $A_{\text{LL}}$ Error Calculation

In the double helicity analysis presented in this work only the statistical uncertainty of the reconstructed neutral pions or more precisely the statistical uncertainty of the signals obtained in the signal and background regions, i.e.  $N^{\pi^0+\text{bg}}$  and  $N^{\text{bg}}$ , is considered.<sup>13</sup> As was stated in Section 9.3 the accuracy of the relative luminosity measurement implies an uncertainty of  $\partial A_{\text{LL}} \approx 0.1\%$  which is negligible compared to the statistical uncertainty of the  $\pi^0$  measurement.

Both  $A_{\text{LL}}^{\pi^0+\text{bg}}$  and  $A_{\text{LL}}^{\text{bg}}$  are calculated using Equation 9.4. Gaussian error propagation yields:

$$\Delta A_{\text{LL}} = \frac{1}{|P_{\text{B}}||P_{\text{Y}}|} \frac{2RN_{++}N_{+-}}{(N_{++} + N_{+-})^2} \sqrt{\left(\frac{\Delta N_{++}}{N_{++}}\right)^2 + \left(\frac{\Delta N_{+-}}{N_{+-}}\right)^2}. \quad (9.13)$$

Because the deviation of the relative luminosity from unity is small (i.e.  $R \approx 1$ ) and the asymmetry  $\alpha = \frac{N_{++}-N_{+-}}{N_{++}+N_{+-}}$  almost vanishes Equation 9.13 can be simplified to:

$$\Delta A_{\text{LL}} = \frac{1}{|P_{\text{B}}||P_{\text{Y}}|} \frac{1}{\sqrt{N_{++} + N_{+-}}}, \quad (9.14)$$

where  $\Delta N_{++} = \sqrt{N_{++}}$  and  $\Delta N_{+-} = \sqrt{N_{+-}}$ , assuming that the measured numbers  $N_{++}$  and  $N_{+-}$  follow Poisson distributions. If the combinatorial background is subtracted prior to the asymmetry calculation  $\Delta r$  must be considered in the error calculation of  $A_{\text{LL}}$ :

$$\Delta A_{\text{LL}} = \frac{1}{|P_{\text{B}}||P_{\text{Y}}|} \sqrt{\frac{1}{\tilde{N}_{++} + \tilde{N}_{+-}} + \frac{1}{2} \left(\frac{\Delta r}{1-r}\right)^2}, \quad (9.15)$$

where  $\tilde{N}_{++}$  and  $\tilde{N}_{+-}$  represent the uncorrected yields under the  $\pi^0$  mass peak for the respective helicity combination. Especially in the two lowest  $p_{\text{T}}$  bins the error  $\Delta r/r = 0.02$  cannot be neglected compared to the statistics given by  $N^{\pi^0+\text{bg}}$  in Table 9.1.

---

<sup>13</sup>The uncertainty due to the polarization measurement enters the result as a normalization error.

However, since the background is not subtracted prior to the asymmetry calculation the uncertainty of  $A_{\text{LL}}^{\pi^0+\text{bg}}$  and  $A_{\text{LL}}^{\text{bg}}$  is calculated according to Equation 9.14. Taking  $\Delta A_{\text{LL}}^{\pi^0+\text{bg}}$  and  $\Delta A_{\text{LL}}^{\text{bg}}$  into account the statistical uncertainty of  $A_{\text{LL}}^{\pi^0}$  is given by:

$$\Delta A_{\text{LL}}^{\pi^0} = \frac{\sqrt{\left(\Delta A_{\text{LL}}^{\pi^0+\text{bg}}\right)^2 - \left(r \cdot \Delta A_{\text{LL}}^{\text{bg}}\right)^2}}{1-r}. \quad (9.16)$$

The uncertainty of  $A_{\text{LL}}^{\pi^0}$  due to  $r$  can be calculated as follows:

$$\Delta A_{\text{LL}}^{\pi^0} = \left|A_{\text{LL}}^{\pi^0+\text{bg}} - A_{\text{LL}}^{\text{bg}}\right| \cdot \frac{\Delta r}{(1-r)^2}. \quad (9.17)$$

Since the asymmetries ( $A_{\text{LL}}^{\pi^0+\text{bg}}$  and  $A_{\text{LL}}^{\text{bg}}$ ) are small the uncertainty of  $A_{\text{LL}}^{\pi^0}$  introduced by  $\Delta r = 0.02$  can be neglected compared to the statistical uncertainty of  $A_{\text{LL}}^{\pi^0}$ .

The calculation of  $A_{\text{LL}}^{\pi^0}$  requires large statistics in order to yield small uncertainties. Because of the relatively small statistics accumulated in Run III p + p the obtained statistical error bars are large. This makes the analysis of systematic uncertainties unnecessary since they are expected to be considerably smaller than the statistical uncertainties.

### 9.9.3 Signal and Background $A_{\text{LL}}$

The absolute beam polarizations established during the data taking period of Run III p + p varied from fill to fill. Therefore the double helicity asymmetry of the signal and the background were calculated for each of the 47 fills separately using Equation 9.4. Figure 9.9 shows the signal  $A_{\text{LL}}$  obtained with the PbGl in each  $p_{\text{T}}$  bin as a function of the fill number. The analyzed fills ranged from 3625 to 3810.<sup>14</sup> The statistical fluctuations increase with increasing  $p_{\text{T}}$  (note the different scales for different  $p_{\text{T}}$  bins) since the statistics of the reconstructed neutral pions decline rather quickly. The average signal  $A_{\text{LL}}$  is determined as a constant fit to the distribution of  $A_{\text{LL}}^{\pi^0+\text{bg}}$  per fill (shown by the grey line). The background  $A_{\text{LL}}$  obtained for each fill and  $p_{\text{T}}$  bin with the PbGl is shown in Figure 9.10. The average  $A_{\text{LL}}^{\text{bg}}$  is also given by a constant fit to the data.

All values of  $A_{\text{LL}}^{\pi^0+\text{bg}}$  and  $A_{\text{LL}}^{\text{bg}}$  obtained for each fill and  $p_{\text{T}}$  bin measured with the PbGl, PbSc and the combined EMCAL subsystems are listed in Appendix F.1. For the calculation of the double helicity asymmetry it was required that at least one  $\pi^0$  or background pair was counted for either helicity combination, i.e.  $N_{++} \geq 1$  and  $N_{+-} \geq 1$ . For a few

<sup>14</sup>At RHIC fills are numbered consecutively. If a stable storage of the two beams in the RHIC collider cannot be established the two beams are dumped and a new fill is initiated. Therefore the specified range comprises more fills than were actually analyzed.

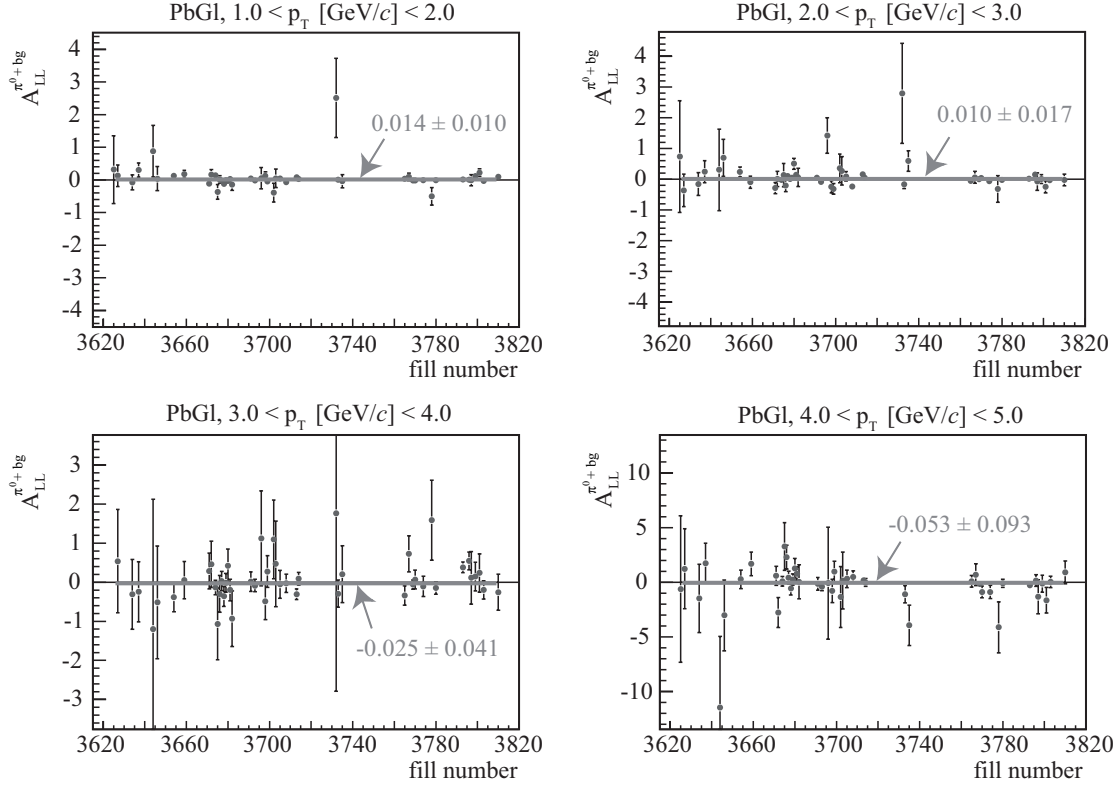


**Figure 9.9:** Signal  $A_{LL}$  as measured with the PbGl in four  $p_T$  bins determined for each fill separately. The error bars represent the statistical error of the measured signal (i.e.  $N\pi^0+bg$ ). The average  $A_{LL}^{\pi^0+bg}$  over the full data set is determined by a constant fit (grey line).

fills the accumulated statistics were too small to meet this condition, especially in the highest  $p_T$  bin, so that no asymmetry could be calculated (hence no  $A_{LL}$  is given for the corresponding fill and  $p_T$  bin in Appendix F.1).

The extracted average values of  $A_{LL}^{\pi^0+bg}$  and  $A_{LL}^{bg}$  measured with the PbGl, PbSc and the combined EMCAL subsystems are summarized in Table 9.3 and depicted in Figure 9.11.

#### 9.9.4 Final Corrected $A_{LL}$

The results of  $A_{LL}^{\pi^0+bg}$  and  $A_{LL}^{bg}$  determined in the four  $p_T$  bins and with the different EMCAL subsystems shown in Figure 9.11 are utilized to derive the final background corrected double helicity asymmetry  $A_{LL}^{\pi^0}$  according to Equation 9.12. The background contribution  $r$  is listed in Table 9.2. The uncertainty  $\Delta A_{LL}^{\pi^0}$  is calculated according to Equation 9.16.

The final result of the  $\pi^0$  double helicity asymmetry obtained with the PbGl, PbSc and EMCAL is listed in Table 9.4 and shown in Figure 9.12. The error bars represent

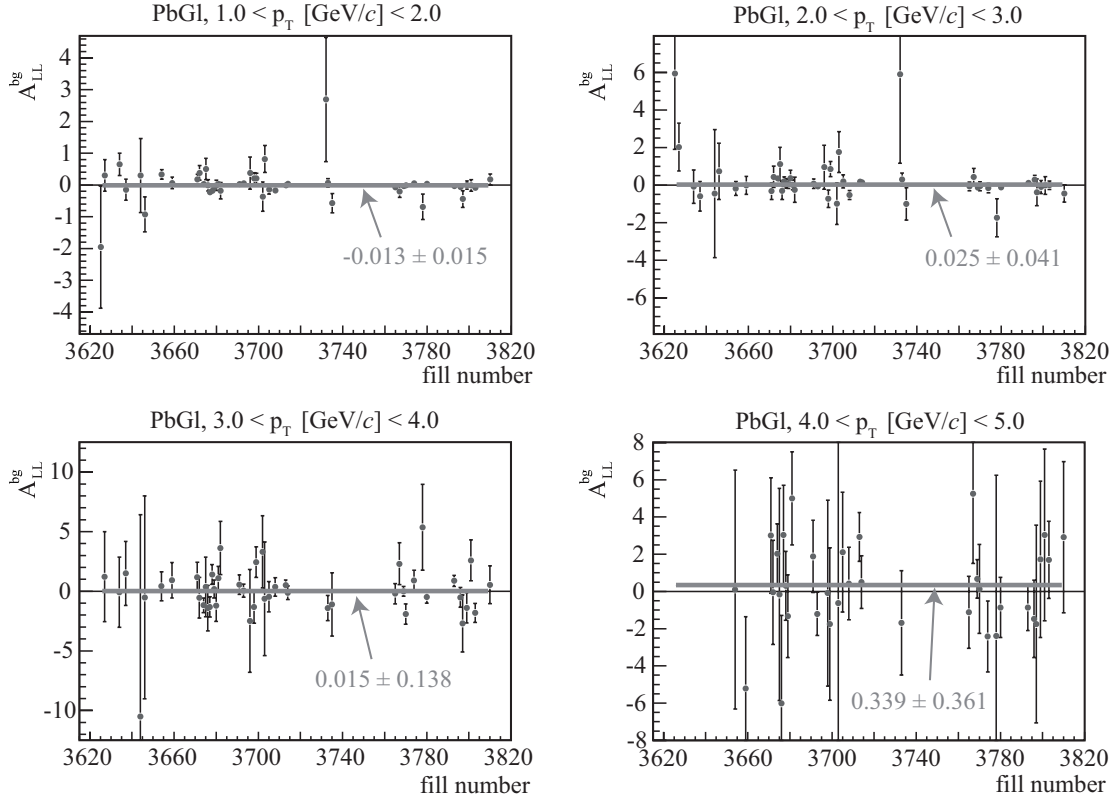


**Figure 9.10:** Background  $A_{LL}$  as measured with the PbGl in four  $p_T$  bins determined for each fill separately. The error bars represent the statistical error of the measured signal (i.e.  $N^{bg}$ ). The average  $A_{LL}^{bg}$  over the full data set is determined by a constant fit (grey line).

statistical  $1\sigma$  errors, i.e. the true value lies in the interval  $[A_{LL}^{\pi^0} - \Delta A_{LL}^{\pi^0}, A_{LL}^{\pi^0} + \Delta A_{LL}^{\pi^0}]$  with a probability of 68%. An important cross check of the measurement is the comparison of

$p_T$ [GeV/c]	$A_{LL}^{\pi^0+bg}$ [%]			$A_{LL}^{bg}$ [%]		
	PbGl	PbSc	EMCal	PbGl	PbSc	EMCal
1.0 – 2.0	$1.4 \pm 1.0$	$-0.9 \pm 0.9$	$0.1 \pm 0.6$	$-1.3 \pm 1.5$	$1.6 \pm 1.1$	$0.4 \pm 0.8$
2.0 – 3.0	$1.0 \pm 1.7$	$-2.1 \pm 1.0$	$-1.3 \pm 0.9$	$2.5 \pm 4.1$	$-2.9 \pm 2.2$	$-1.7 \pm 1.9$
3.0 – 4.0	$-2.5 \pm 4.1$	$-0.5 \pm 2.2$	$-0.8 \pm 1.9$	$1.5 \pm 13.8$	$2.8 \pm 6.8$	$2.4 \pm 6.1$
4.0 – 5.0	$-5.3 \pm 9.3$	$-4.6 \pm 4.9$	$-4.6 \pm 4.3$	$33.9 \pm 36.1$	$9.3 \pm 17.7$	$14.1 \pm 15.8$

**Table 9.3:** Averaged  $A_{LL}^{\pi^0+bg}$  and  $A_{LL}^{bg}$  obtained in different  $p_T$  bins with the PbGl, PbSc and combined EMCal subsystems.

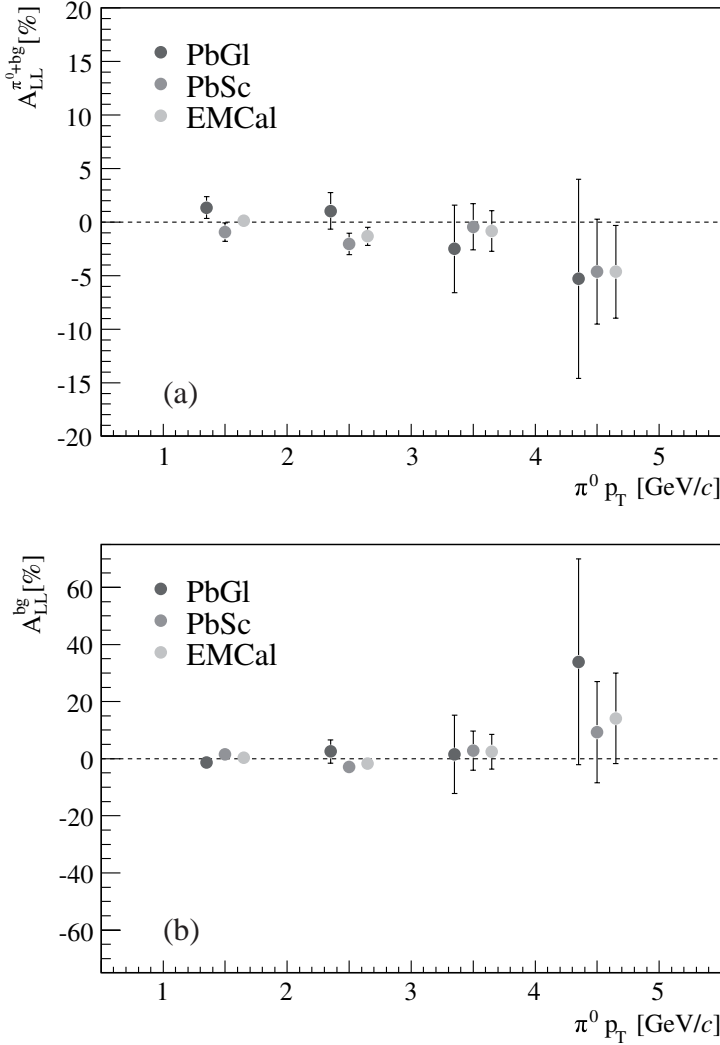


**Figure 9.11:** (a) Double helicity asymmetry ( $A_{\text{LL}}^{\pi^0+\text{bg}}$ ) calculated in the  $\pi^0$  peak region from data obtained with the PbGl, PbSc and the combined EMCAL subsystems. (b) Double helicity asymmetry ( $A_{\text{LL}}^{\text{bg}}$ ) calculated in the background regions adjacent to the  $\pi^0$  mass peak. Please note the different scale in the y-direction compared to (a). In (a) as well as in (b) the data points in each  $p_T$  bin are shifted for better illustration.

the results obtained with the PbGl and PbSc. The  $\chi^2$  of the PbGl and PbSc data points in each  $p_T$  bin is calculated using [Yao06]:

$$\chi^2 = \frac{(A_{\text{LL}}^{\text{PbGl}} - \bar{A}_{\text{LL}})^2}{\sigma_{\text{PbGl}}^2} + \frac{(A_{\text{LL}}^{\text{PbSc}} - \bar{A}_{\text{LL}})^2}{\sigma_{\text{PbSc}}^2}, \quad (9.18)$$

where  $\bar{A}_{\text{LL}}$  is the weighted mean of the PbGl ( $A_{\text{LL}}^{\text{PbGl}}$ ) and PbSc ( $A_{\text{LL}}^{\text{PbSc}}$ ) data points and  $\sigma_{\text{PbGl}}$  and  $\sigma_{\text{PbSc}}$  are the corresponding statistical errors. If the deviation between  $A_{\text{LL}}^{\text{PbGl}}$

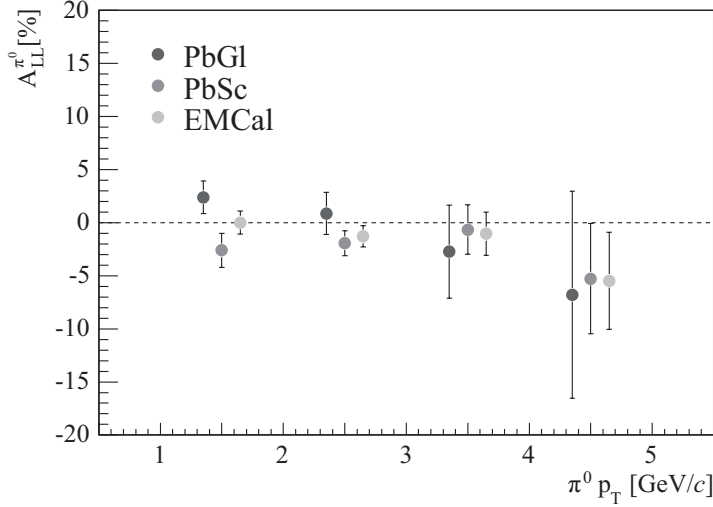


**Figure 9.12:** Corrected double helicity asymmetry in  $\pi^0$  production obtained with the PbGl, PbSc and combined EMCAL subsystems. The data points within the  $p_T$  bins are shifted for better illustration.

and  $A_{LL}^{\text{PbSc}}$  is exactly  $\sqrt{\sigma_{\text{PbGl}}^2 + \sigma_{\text{PbSc}}^2}$  then  $\chi^2 = 1$ . By looking at the  $\chi^2$  distribution for one degree of freedom one can derive the level of confidence that these two measurements agree. In 68% of a large number of measurements a  $\chi^2$  less than unity will be obtained. In this case it is said that the two data points agree within  $1\sigma$ . In 95% of all measurements a  $\chi^2$  less than 4 is obtained and the data points are said to agree within  $2\sigma$ .

Apart from the lowest  $p_T$  bin the corrected double helicity asymmetries obtained with the PbGl and PbSc agree within approximately  $1\sigma$ . For  $p_T = 1 - 2 \text{ GeV}/c$  the data points agree within slightly more than  $2\sigma$ . This illustrates the good agreement of the data points obtained with the PbGl and the PbSc.

$p_T [\text{GeV}/c]$	$A_{LL}^{\pi^0} [\%]$		
	PbGl	PbSc	EMCAL
1.0 – 2.0	$2.4 \pm 1.5$	$-2.6 \pm 1.6$	$0.0 \pm 1.1$
2.0 – 3.0	$0.9 \pm 2.0$	$-1.9 \pm 1.2$	$-1.3 \pm 1.0$
3.0 – 4.0	$-2.7 \pm 4.4$	$-0.7 \pm 2.3$	$-1.0 \pm 2.0$
4.0 – 5.0	$-6.8 \pm 9.8$	$-5.3 \pm 5.2$	$-5.5 \pm 4.6$

**Table 9.4:** Corrected double helicity asymmetry in  $\pi^0$  production in different  $p_T$  bins obtained with the PbGl, PbSc and combined EMCAL subsystems.

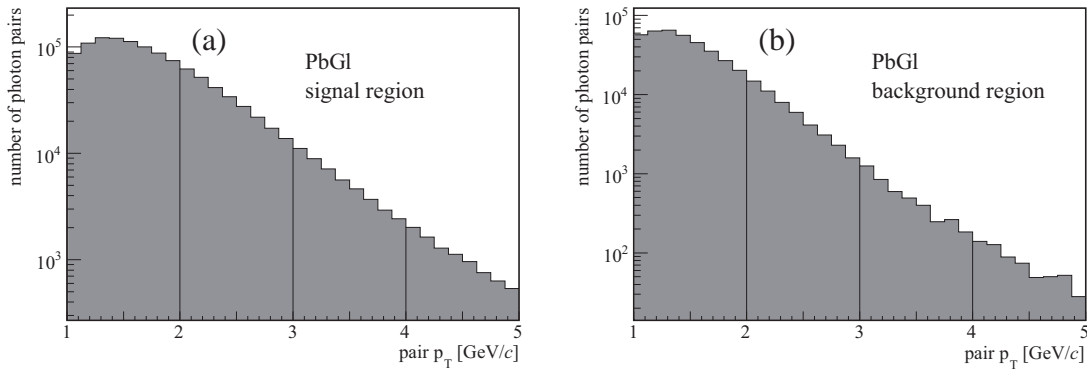


**Figure 9.13:** Distributions of photon pairs in the (a) signal region and (b) background region as a function of the transverse momentum of the pair.

For the subsequent discussion and comparison to theoretical models only the result utilizing the full EMCAL statistics is considered.

### 9.9.5 Average Transverse Momentum

In Figures 9.11 and 9.12 the data points are placed at the center of each bin or are shifted by  $\Delta p_T = \pm 0.15$  GeV/c around the bin center. However, this is not correct since the underlying  $p_T$ -distributions of correlated or uncorrelated photon pairs are not uniform. This is illustrated in Figure 9.13 by the  $p_T$  distributions of photon pairs measured with the PbGl in the signal (a) and background (b) region. Based on the discussion of particle spectra in Section 2.2.1 the distributions can be approximated by an exponential at low  $p_T$  and a power law at high  $p_T$  ( $p_T \gtrsim 2 - 3$  GeV/c). The dip at low  $p_T$  is due to the limited acceptance of the detector for photon pairs in this  $p_T$  region. In the  $A_{\text{LL}}$  analysis presented in this work it was chosen to shift the final  $A_{\text{LL}}^{\pi^0}$  data points in the  $p_T$  bins according to the underlying neutral pion  $p_T$  distribution. Two approaches were followed to determine the average  $\pi^0 p_T$  in each  $p_T$  bin:

First, the  $p_T$  distribution of correlated photon pairs in the invariant mass range of the neutral pion, i.e. the background corrected  $\pi^0$  spectrum, was determined. The combinatorial background was identified using the mixed event technique described in Section 9.9.1. The background was subtracted from the invariant mass distribution and the number of remaining photon pairs in the  $\pi^0$  mass range was counted as a function of pair  $p_T$ . This neutral pion  $p_T$  distribution is shown in Figure 9.14 for the PbGl. The average  $p_T$  in each  $p_T$  bin is given by the weighted mean in the bin.

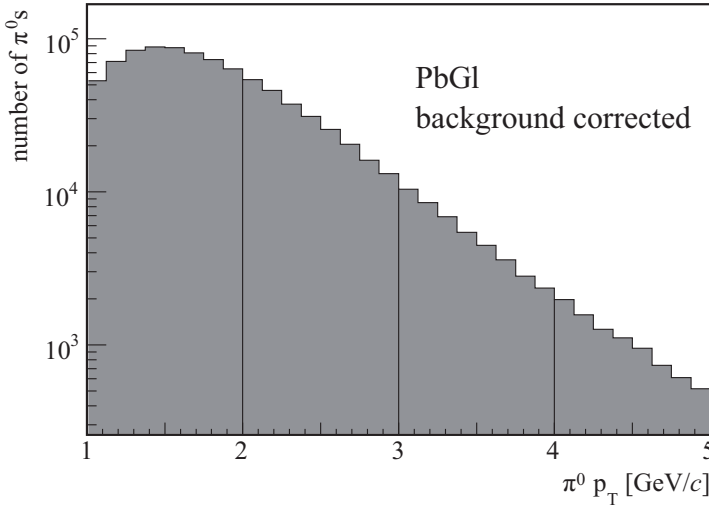


**Figure 9.14:** Background corrected  $p_T$  distribution of photon pairs in the neutral pion mass range.

In a second approach, the average  $p_T$  was determined in the  $p_T$  distributions of photon pairs in the signal region  $\langle p_T \rangle^{\pi^0 + \text{bg}}$  and background region  $\langle p_T \rangle^{\text{bg}}$  shown in Figure 9.13(a) and 9.13(b), respectively. The corrected average transverse momentum  $\langle p_T \rangle^{\pi^0}$  of the  $\pi^0$  spectrum is then given analogous to Equation 9.12 by:

$$\langle p_T \rangle^{\pi^0} = \frac{\langle p_T \rangle^{\pi^0 + \text{bg}} - r \cdot \langle p_T \rangle^{\text{bg}}}{1 - r}, \quad (9.19)$$

where  $r$  is the contribution of the combinatorial background to the  $\pi^0$  mass peak listed in Table 9.2.

The average  $p_T$  obtained in each bin for the PbGl, PbSc and combined EMCAL agree perfectly in both methods. Table 9.5 lists the values of  $\langle p_T \rangle^{\pi^0}$  which are used in the representation of the final  $A_{\text{LL}}^{\pi^0}$  result.

$p_T$ [GeV/c]	$\langle p_T \rangle^{\pi^0}$ [GeV/c]		
	PbGl	PbSc	EMCal
1.0 – 2.0	1.51	1.63	1.57
2.0 – 3.0	2.37	2.40	2.39
3.0 – 4.0	3.37	3.37	3.37
4.0 – 5.0	4.38	4.38	4.38

**Table 9.5:** Average transverse momentum  $\langle p_T \rangle^{\pi^0}$  in each  $p_T$  bin of the underlying  $\pi^0$   $p_T$  distributions measured with the PbGl, PbSc and combined EMCAL system.

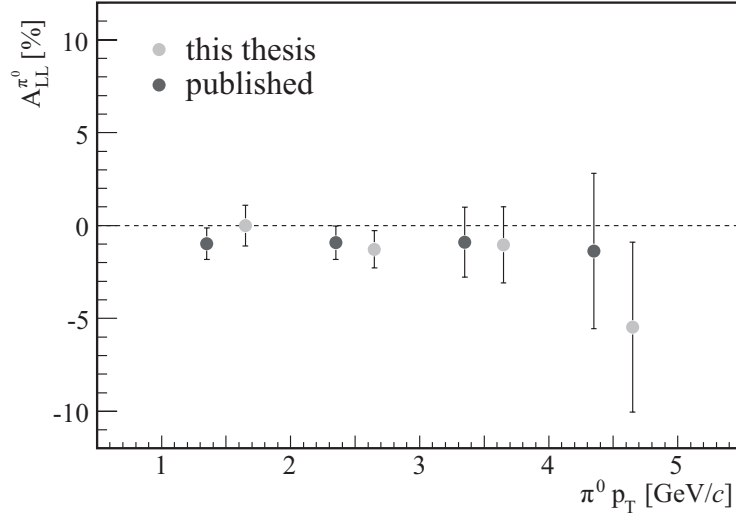


**Figure 9.15:** Comparison of  $A_{LL}^{\pi^0}$  obtained with the EMCAL in the analysis described in this thesis and in an independent analysis. The result of the latter analysis is published in [Adl06b]. The data points are shifted in  $p_T$  direction for better illustration.

## 9.10 Cross Checks

In addition to the analysis described in this thesis the double helicity asymmetry in  $\pi^0$  production was determined in an independent analysis, which is based on the same Run III  $p + p$  data set [Baz04]. In this analysis additional PID cuts were applied. These included a cut on the time-of-flight measured by the EMCAL and a charge veto cut, which utilized information provided by the PC3. The cuts were optimized to minimize the background under the  $\pi^0$  mass peak. A comparison of the corrected  $A_{LL}^{\pi^0}$  obtained with the combined EMCAL system in these two analyses is shown in Figure 9.15. All data points agree within  $1\sigma$  illustrating the good agreement between the two analyses.

### Single Spin Asymmetry $A_L$ :

In addition to the double helicity asymmetry the single spin asymmetry  $A_L$  in  $\pi^0$  production was calculated. It is defined as follows:

$$A_L = -\frac{\sigma_+ - \sigma_-}{\sigma_+ + \sigma_-}, \quad (9.20)$$

where  $\sigma_+$  and  $\sigma_-$  denote the cross section of inclusive  $\pi^0$  production in  $p + p$  collisions in which one of the colliding protons has positive or negative helicity, while the helicity of the other proton is undefined. Since parity conservation is assumed to hold for the production mechanisms of inclusive  $\pi^0$  production in  $p + p$  collisions the difference between

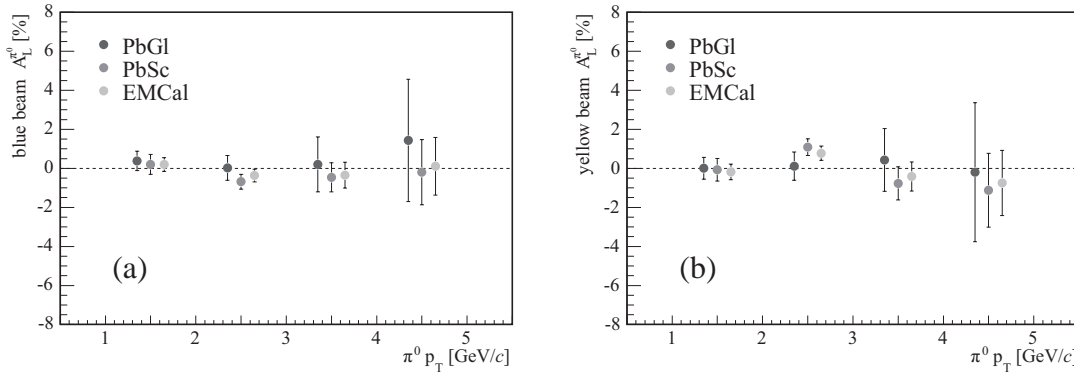


**Figure 9.16:** Single spin asymmetry in  $\pi^0$  production in Run III  $p + p$  with (a) the polarized blue and (b) the polarized yellow beam measured with the PbGl, PbSc and the combined EMCal system.

$\sigma_+$  and  $\sigma_-$  is expected to vanish. Therefore, any deviation of  $A_L$  from zero would indicate problems with the data or analysis technique. For the measurement of the single spin asymmetry only one beam is required to be polarized. Thus  $A_L$  is calculated for the blue and the yellow beam separately. The analysis method is the same as for the double helicity analysis.  $A_L$  is calculated for each fill in the  $\pi^0$  and background mass range. The average values in each  $p_T$  bin are determined by a constant fit to the  $A_L$ -per-fill distribution. The background corrected single spin asymmetry is then calculated similar to Equation 9.12. The result obtained with the polarized blue as well as with the polarized yellow beam for the PbGl, PbSc and combined EMCal system is shown in Figure 9.16 and listed in Table 9.6. The consistency of the measured  $A_L$  with the expectation, i.e.  $A_L = 0$ , can

$p_T$ [GeV/c]	blue beam $A_L^{\pi^0}$ [%]			yellow beam $A_L^{\pi^0}$ [%]		
	PbGl	PbSc	EMCal	PbGl	PbSc	EMCal
1.0 – 2.0	$0.4 \pm 0.5$	$0.2 \pm 0.5$	$0.2 \pm 0.4$	$0.0 \pm 0.6$	$-0.1 \pm 0.6$	$-0.2 \pm 0.4$
2.0 – 3.0	$0.0 \pm 0.6$	$-0.7 \pm 0.4$	$-0.4 \pm 0.3$	$0.1 \pm 0.7$	$1.1 \pm 0.4$	$0.8 \pm 0.4$
3.0 – 4.0	$0.2 \pm 1.4$	$-0.5 \pm 0.7$	$-0.3 \pm 0.7$	$0.4 \pm 1.6$	$-0.8 \pm 0.8$	$-0.4 \pm 0.7$
4.0 – 5.0	$1.4 \pm 3.1$	$-0.2 \pm 1.7$	$0.1 \pm 1.5$	$-0.2 \pm 3.6$	$-1.1 \pm 1.9$	$-0.7 \pm 1.7$

**Table 9.6:** Single spin asymmetry in  $\pi^0$  production in Run III  $p + p$  with the polarized blue and yellow beam measured with the PbGl, PbSc and the combined EMCal system.

be evaluated by calculating the  $\chi^2$ . For the comparison of data to theory  $\chi^2$  is calculated via [Yao06]:

$$\chi^2 = \sum_{i=1}^n \frac{(x_i - \mu_i)^2}{\sigma_i^2}, \quad (9.21)$$

where  $x_i$  is one of the  $n$  measured Gaussian distributed data points with standard deviation  $\sigma_i$  and  $\mu_i$  is the theory expectation. The data points can be regarded as consistent with zero if  $\chi^2$  does not significantly exceed  $n$  (here  $n = 4$ ). The maximum  $\chi^2$  is obtained for  $A_L$  in the yellow beam measured with the PbSc ( $\chi^2 \approx 7.5$ ). All other calculated  $\chi^2$  are considerably smaller. Hence, the measured single spin asymmetry is consistent with zero indicating that both data and analysis method are correct.

### Parity Violating Double Helicity Asymmetry

The parity violating (PV) double helicity asymmetry is given by:

$$A_{LL}^{++ \text{ vs. } --} = \frac{\sigma_{++} - \sigma_{--}}{\sigma_{++} + \sigma_{--}} \quad (9.22)$$

$$A_{LL}^{+- \text{ vs. } -+} = \frac{\sigma_{+-} - \sigma_{-+}}{\sigma_{+-} + \sigma_{-+}}, \quad (9.23)$$

where  $\sigma$  denotes the  $\pi^0$  production cross section in  $p + p$  collisions where either both protons have positive (++) or negative (--) helicity or both protons have opposite helicity with the two possible combinations +- and -+. Assuming parity conservation holds for the production mechanisms of inclusive  $\pi^0$  production in  $p + p$  collisions the difference in the corresponding cross sections should be zero, i.e.  $\sigma_{++} = \sigma_{--}$  and  $\sigma_{+-} = \sigma_{-+}$ . Thus the corresponding double helicity asymmetries  $A_{LL}^{++ \text{ vs. } --}$  and  $A_{LL}^{+- \text{ vs. } -+}$  should vanish. The measurement of the parity violating double helicity asymmetries is completely analogous to the calculation of  $A_{LL}^{\pi^0}$  and  $A_L$ . The results of  $A_{LL}^{++ \text{ vs. } --}$  and  $A_{LL}^{+- \text{ vs. } -+}$  for the PbGl, PbSc and combined EMCal system are shown in Figure 9.17 and listed in Table 9.7.

$p_T$ [GeV/c]	PV (++ vs. --) $A_{LL}^{\pi^0}$ [%]			PV (+- vs. -+) $A_{LL}^{\pi^0}$ [%]		
	PbGl	PbSc	EMCal	PbGl	PbSc	EMCal
1.0 – 2.0	$-1.4 \pm 2.2$	$0.1 \pm 2.3$	$0.0 \pm 1.5$	$-1.2 \pm 2.2$	$-0.8 \pm 2.2$	$-1.0 \pm 1.5$
2.0 – 3.0	$0.0 \pm 2.8$	$-0.6 \pm 1.7$	$-0.6 \pm 1.4$	$0.7 \pm 2.8$	$4.9 \pm 1.7$	$3.2 \pm 1.4$
3.0 – 4.0	$-3.0 \pm 6.2$	$2.9 \pm 3.3$	$1.5 \pm 2.9$	$0.7 \pm 6.2$	$0.0 \pm 3.3$	$0.5 \pm 2.9$
4.0 – 5.0	$-7.0 \pm 13.9$	$2.6 \pm 7.4$	$0.6 \pm 6.5$	$-2.5 \pm 13.7$	$-1.9 \pm 7.3$	$-1.3 \pm 6.4$

**Table 9.7:** ++ vs. -- and +- vs. -+ parity violating double helicity asymmetry in  $\pi^0$  production in Run III  $p + p$  measured with the PbGl, PbSc and combined EMCal system.

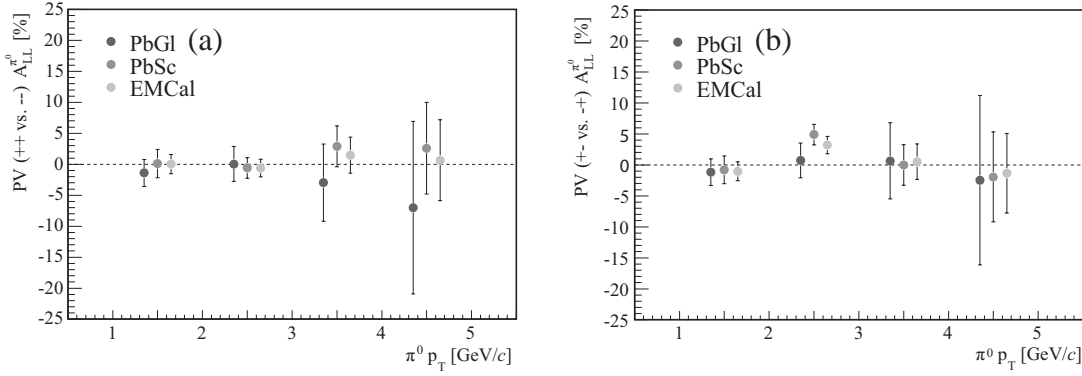


**Figure 9.17:** Parity violating double helicity asymmetry in  $\pi^0$  production in Run III p + p measured with the PbGl, PbSc and combined EMCAL system: (a)  $++$  vs.  $--$  and (b)  $-+$  vs.  $-+$ .

The calculation of  $\chi^2$  with respect to the expectation (i.e.  $A_{LL}^{++ \text{ vs. } --} = A_{LL}^{+- \text{ vs. } -+} = 0$ ) according to Equation 9.21 yields only for  $A_{LL}^{+- \text{ vs. } -+}$  measured with the PbSc a considerably larger value than  $n = 4$  ( $\chi^2 \approx 8.5$ ). This value is dominated by the PbSc data point in the bin  $p_T = 2 - 3 \text{ GeV}/c$ . However, since all other data points are much more consistent with zero this deviation is considered to be a statistical fluctuation. Therefore, the parity violating double helicity asymmetry reveals no systematic deviation from zero.

## 9.11 Comparison to Model Calculations

The analysis of the double helicity asymmetry in  $\pi^0$  production presented in this thesis covers a moderate  $p_T$  range ( $p_T = 1 - 5 \text{ GeV}/c$ ) at mid-rapidity. As was noted in Section 8.3 the momentum fraction of the gluon probed in the scattering can be estimated from the transverse momentum of the neutral pion:  $x \approx 2p_T/\sqrt{s}$ . A more exact definition of the probed momentum fractions of the colliding partons in jet production is given in [Jag04b]. According to this the polarized gluons are probed at  $x \lesssim 0.1$  in the kinematic range of the measurement presented here. Thus the  $\pi^0$  production is dominated by gluon-gluon and quark-gluon processes and hence the double helicity asymmetry is highly sensitive to the gluon distribution inside the proton.

The statistical uncertainties of the measured double helicity asymmetry in Run III p + p are large. Therefore the data points are compared to next-to-leading order (NLO) pQCD calculations rather than extracting an estimate of the gluon polarization.  $A_{LL}^{\pi^0}$  at

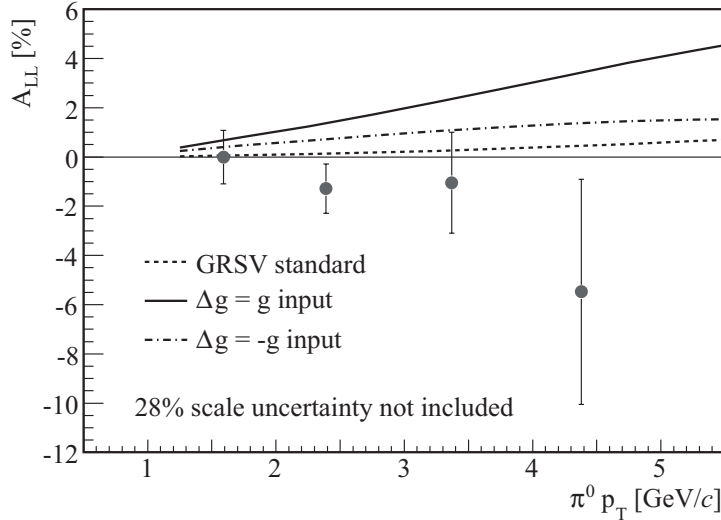


**Figure 9.18:** Comparison of the measured double helicity asymmetry of  $\pi^0$  production with three NLO pQCD calculations assuming different polarized gluon distributions. “GRSV standard” utilizes a  $\Delta g$  that best fits world DIS data, while the other two assume a  $\Delta g$  of  $g(x)$  and  $-g(x)$ , respectively, at the input scale of  $Q^2 = 0.4 \text{ GeV}^2$ . The calculations are taken from [Jag04a].

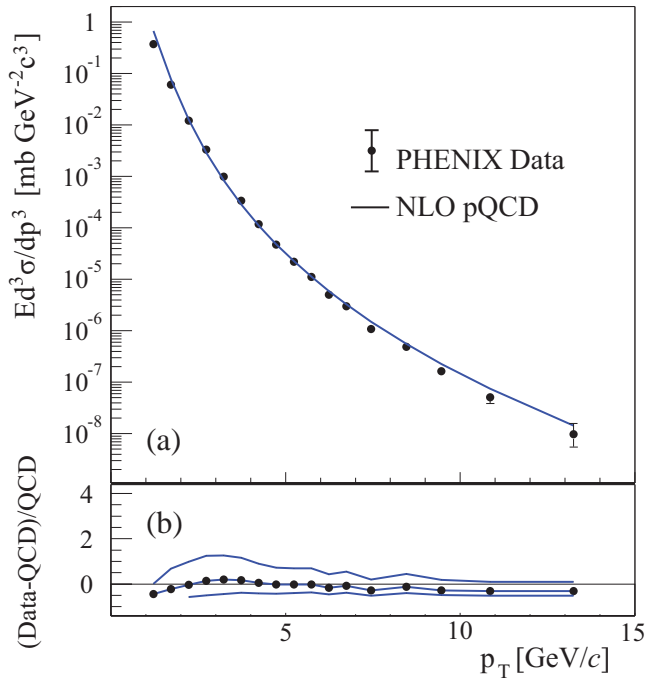
mid-rapidity in  $p + p$  collisions at  $\sqrt{s} = 200 \text{ GeV}$  has been calculated utilizing different assumptions of  $\Delta g$  extracted from deep-inelastic scattering experiments [Jag04a].

Figure 9.18 shows in addition to the  $A_{LL}^{\pi^0}$  data points three NLO pQCD calculations of  $A_{LL}$  in  $\pi^0$  production, using different assumptions for  $\Delta g$ , which were extracted in the global analysis of DIS data presented in [Glu01]. “GRSV standard” utilizes the best global fit to world DIS data. The other two calculations represent extreme cases where the input gluon distribution is assumed to be equal to the unpolarized gluon distribution  $g(x)$  and  $-g(x)$ , respectively, at the input scale  $Q^2 = 0.4 \text{ GeV}^2$ . The gluon distributions are evolved to the scale  $Q^2 = (p_T^{\pi^0})^2$ .

Although the statistical accuracy of the measured double helicity asymmetry in  $\pi^0$  production is limited the comparison already indicates a possible trend of  $\Delta g$  measured in polarized  $p + p$  collisions. The measurement favors a small gluon polarization. The calculation of  $\chi^2$  including only statistical uncertainties<sup>15</sup> yields  $\chi^2 \approx 4.1$  for “GRSV standard” and  $\chi^2 \approx 14.8$  for  $\Delta g = g$ . This is related to the probability that another measurement would yield a  $\chi^2$  at least as large as obtained in this measurement. For “GRSV standard” this probability is about 35% – 40% and for  $\Delta g = g$  about 0.5% – 1.0%.

It must be noted that in the lowest  $p_T$  bin ( $p_T = 1 – 2 \text{ GeV}/c$ ) the contribution from soft physics to  $\pi^0$  production might be significant. Figure 9.19 shows the spin averaged,

<sup>15</sup>The uncertainty due to the polarization measurement is not included.



**Figure 9.19:** (a) Neutral pion cross section measured by the PHENIX collaboration in  $p + p$  collisions at  $\sqrt{s} = 200$  GeV. The solid line represents a NLO pQCD calculation. (b) Relative deviation between data points and pQCD calculations for three different scales:  $\mu = p_T/2$ ,  $p_T$  and  $2p_T$  [Adl03b].

i.e. unpolarized,  $\pi^0$  cross section at mid-rapidity measured by PHENIX in  $p + p$  collisions at  $\sqrt{s} = 200$  GeV [Adl03b]. The data is compared to a NLO pQCD calculation. As one can see from the figure the agreement between data and theory is very impressive for this measurement. However, as the bottom panel shows (Figure 9.19(b)) the theoretical prediction depends to some extent on the QCD scales chosen in the calculation, especially at low  $p_T$ . This theoretical uncertainty must be taken into account and allows for a possible significant contribution of soft processes at least in the lowest  $p_T$  bin of the  $A_{LL}^{\pi^0}$  measurement. Since the soft spectrum decreases exponentially the contribution to  $p_T > 2$  GeV/c is likely to be negligible.

The standard GRSV fit at the scale  $Q^2 = 1$  GeV $^2$  results in a contribution to the proton spin of  $\int_0^1 \Delta g(x) dx \approx 0.4$ . A large polarization of the gluon as was suggested following the EMC result therefore seems to be ruled out by the analysis presented in this thesis. Subsequent measurements of the double helicity asymmetry with larger statistical accuracy extending to higher transverse momenta, especially when utilizing the prompt-

photon channel, will shed further light on the composition of the proton spin and will allow better constraints on  $\Delta G$ .



# Summary

This work consists of two parts: first the measurement of the cross section of direct-photon production in unpolarized  $p + p$  collisions at a center-of-mass energy of  $\sqrt{s} = 200$  GeV is described. And second the measurement of the double helicity spin asymmetry in the production of neutral pions in longitudinally polarized  $p + p$  collisions at the same center-of-mass energy is presented. The data were collected with the PHENIX experiment at RHIC/BNL. Unpolarized measurements in polarized  $p + p$  collisions at RHIC are obtained by averaging over the different  $p + p$  polarization combinations.

Direct photons produced in ultra-relativistic nucleon-nucleon collisions provide a unique tool to study several aspects of QCD, the quantum field theory describing the strong interaction. The underlying mechanisms in the production of direct photons (as well as other particles) with large transverse momenta ( $p_T$ ) are characterized by large momentum transfers and can be described with perturbative QCD (pQCD). At leading order (LO) in pQCD direct-photon production is dominated by quark-gluon Compton scattering and quark-antiquark annihilation. In these reactions the photon is directly emitted in the hard scattering of the partons. In addition, photons are emitted as part of the parton-jet fragmentation. So-called fragmentation functions (FF's) which describe this process cannot be predicted using techniques of pQCD but have to be extracted from experimental data. While the production of hadrons always depends on FF's the dependence on parton-to-photon FF's is greatly reduced in direct-photon production. Therefore, the measurement of direct photons tests pQCD calculations more directly than the measurement of hadrons since the predictions are less affected by fragmentation.

The measurement of direct photons in  $p + p$  collisions is crucial for the interpretation of direct-photon data from ultra-relativistic heavy-ion collisions ( $A + A$ ). In the absence of nuclear effects particle production from hard scatterings in  $A + A$  can be extrapolated from the measurement in  $p + p$  by scaling with the number of binary nucleon-nucleon collisions in the  $A + A$  reaction (binary scaling). It was observed in central Au + Au collisions at  $\sqrt{s_{NN}} = 200$  GeV at RHIC that the production of hadrons is suppressed compared to the expectation from scaled  $p + p$  reactions while the production of direct photons follows binary scaling. Since photons are not subject to the strong interaction the hadron suppression cannot be explained by modifications of the initial state parton distributions

(otherwise the same suppression should be observed in direct-photon production) but can be attributed to the energy loss of scattered partons in a medium of high color-charge density, an effect usually referred to as jet-quenching. These results provided a strong indication for the creation of the so-called quark-gluon plasma (QGP) in central Au + Au collisions at RHIC, a phase in which quarks and gluons represent the relevant thermodynamic degrees of freedom. The conclusion that direct photons in Au + Au are not suppressed, however, was based on the comparison to a binary scaled pQCD prediction and not to a measured p + p reference.

For the calculation of inelastic cross sections in QCD the initial non-perturbative momentum distributions of the partons are required. These parton distribution functions (PDF's) are measured in deep-inelastic lepton-nucleon scattering (DIS) experiments. However, since the gluon is electrically neutral DIS experiments are not directly sensitive to the momentum distribution of the gluon inside the proton. Therefore, the gluon PDF is only weakly constrained by DIS, especially for gluon momentum fractions of  $x \gtrsim 0.1$ . However, in p + p collisions the gluon contributes at LO via quark-gluon Compton scattering to the production of direct photons with large transverse momenta. Thus precise measurements of the direct-photon spectrum in ultra-relativistic p + p collisions provides direct access to the gluon distribution inside the proton.

Moreover, the gluon distribution inside the proton possibly plays a significant role in the so-called spin puzzle. It was discovered already in the late 1980's in polarized DIS (pDIS) experiments that the spin of the proton is not simply the sum of spins of the three valence quarks. In fact, it was found that the contribution of quarks and antiquarks likely accounts for less than 35% of the proton spin. Thus the remaining fraction is expected to be shared among the spin of the gluons and the orbital angular momenta (OAM) of the partons inside the proton. While there are only first ideas how to access the OAM of partons experimentally, the polarized gluon distribution  $\Delta g$  can be directly probed in ultra-relativistic collisions of longitudinally polarized protons at RHIC. The cleanest channel which involves the gluon in the initial state is the production of direct photons, since it is only partially affected by fragmentation. Another promising channel is the production of neutral pions, which involves e.g. gluon-gluon and quark-gluon scattering at leading order. However, the theoretical predictions are affected by the parton-jet fragmentation.

The main focus of the analysis work presented in this thesis is the measurement of direct photons in p + p collisions. The measurement is very challenging due to the large background of decay photons, which is dominated by  $\pi^0$  decays. In PHENIX photons are detected with the electromagnetic calorimeter (EMCal). The analyses presented in this work were carried out separately for the two EMCal subsystems, the lead-glass Cherenkov calorimeter and the lead-scintillator sandwich calorimeter. Comparison of the two results provides an excellent internal cross check. The extraction of the direct-photon signal

from the inclusive photon spectrum (direct photons + decay photons) requires thorough analysis of contributions from charged and neutral hadrons. Moreover, photon conversion and detector specific effects such as the limited energy resolution need to be taken into account carefully. The contribution of background photons from  $\pi^0$ ,  $\eta$ ,  $\omega$  and  $\eta'$  decays was calculated using the measured  $\pi^0$  spectrum determined with the same data set. For the first time in PHENIX the inclusive photon spectrum has been measured up to transverse momenta at which decay photons from the same  $\pi^0$  decay overlap in such a way that they cannot be resolved any more. This so-called shower merging results in a significant distortion of the uncorrected direct-photon spectrum at high  $p_T$ . A method is presented in this work that corrects this effect and allows the extraction of the unbiased direct-photon signal over the entire  $p_T$  range covered in the analysis.

A careful analysis of systematic uncertainties allowed the extraction of a significant direct-photon signal in the range  $5.5 \text{ GeV}/c < p_T < 16.0 \text{ GeV}/c$ , the largest  $p_T$  range ever covered by a direct-photon measurement in  $p + p$  collisions at  $\sqrt{s} = 200 \text{ GeV}$ . The data are well described by NLO pQCD predictions and complement existing direct-photon data in nucleon-nucleon collisions at significantly larger and smaller  $\sqrt{s}$ . This result puts the conclusions derived from the earlier Au + Au measurement on a firm experimental ground and represents the first step towards the extraction of the gluon distribution from direct-photon data.

In the second part of this work the double helicity asymmetry ( $A_{\text{LL}}$ ) in  $\pi^0$  production in polarized  $p + p$  collisions was measured. This spin asymmetry is defined by the difference in the production cross sections of  $\pi^0$ 's in collisions of protons with like helicity and unlike helicity.  $A_{\text{LL}}$  is directly related to  $\Delta g$  in the proton and therefore allows to study the contribution of the gluon polarization to the proton spin. The analysis was carried out using the  $\pi^0$  channel rather than direct-photon production since a significant  $A_{\text{LL}}$  result requires large statistics. For transverse momenta below  $5 \text{ GeV}/c$  where the statistical accuracy of particle production is large the direct-photon measurement suffers from the large background of decay photons (dominated by  $\pi^0$  decays) which is reflected in the large systematic uncertainties. By contrast the signal of neutral pions is not diluted significantly by any background at low  $p_T$  and therefore can be measured with large statistical and systematic accuracy. For this analysis basically the same data set as for the direct-photon analysis was evaluated. Neutral pions are reconstructed via their two decay photons. The  $\pi^0$  yield was carefully measured for the two proton helicity combinations. The yields, the measured polarizations of the proton beams and the measured relative luminosities, which account for differences in the number of  $p + p$  collisions with like and unlike helicities, were used to calculate the double helicity asymmetry in  $\pi^0$  production for  $1 \text{ GeV}/c < p_T < 5 \text{ GeV}/c$ . The statistical accuracy of the  $A_{\text{LL}}$  result is limited. However, comparisons to model calculations which utilize different assumptions of the

polarized gluon distribution indicate that a large contribution of the gluon polarization to the proton spin is not likely.

The  $A_{LL}$  measurement presented in this work demonstrates the first measurement of this kind in collisions of polarized protons at ultra-relativistic energies. It allows the first, even though limited, direct access to the polarized gluon distribution in the proton.

# Zusammenfassung

Diese Arbeit umfasst zwei Teile: Im ersten wird die Messung des Wirkungsquerschnitts der Produktion direkter Photonen in unpolarisierten p + p-Kollisionen bei einer Schwerpunktsenergie von  $\sqrt{s} = 200 \text{ GeV}$  beschrieben. Im zweiten wird die Messung der doppelt-longitudinalen Spin-Asymmetrie in der Produktion neutraler Pionen in longitudinal polarisierten p + p-Kollisionen bei der gleichen Schwerpunktsenergie vorgestellt. Die Daten wurden am PHENIX-Experiment des RHIC/BNL aufgenommen. Unpolarisierte Messungen in polarisierten p + p-Kollisionen erhält man am RHIC durch Mittelung über die verschiedenen Polarisationskombinationen der p + p-Stöße.

Direkte Photonen, die in ultrarelativistischen Nukleon-Nukleon-Kollisionen erzeugt werden, stellen eine einzigartige Sonde dar, um verschiedene Aspekte der QCD, der Quantenfeldtheorie der starken Wechselwirkung, zu untersuchen. Die zugrunde liegenden Mechanismen in der Produktion direkter Photonen (wie auch anderer Teilchen) mit hohen Transversalimpulsen ( $p_T$ ) sind durch große Impulsüberträge gekennzeichnet und können mit Hilfe der störungstheoretischen QCD (pQCD) beschrieben werden. In führender Ordnung wird die Produktion direkter Photonen durch Quark-Gluon-Compton-Streuung und Quark-Antiquark-Vernichtung dominiert. In diesen Reaktionen wird das Photon direkt in der harten Streuung der Partonen emittiert. Zusätzlich können Photonen in der Parton-Jet-Fragmentation erzeugt werden. Die so genannten Fragmentations-Funktionen, die diesen Prozess beschreiben, können nicht mit Hilfe der pQCD vorhergesagt werden, sondern müssen aus experimentellen Daten bestimmt werden. Während die Produktion von Hadronen immer von der Fragmentation abhängt, ist diese Abhängigkeit in der Produktion direkter Photonen stark unterdrückt. Die Vorhersagen der pQCD werden somit durch die Messung direkter Photonen eindeutiger überprüft als durch die Messung von Hadronen, da die Vorhersagen weniger durch Fragmentation beeinflusst werden.

Die Messung direkter Photonen in p + p-Kollisionen ist von entscheidender Bedeutung für die Interpretation der Daten direkter Photonen aus ultrarelativistischen Schwerionenkollisionen (A + A). Vorausgesetzt es gibt keine Kern-Effekte, so kann die Teilchenproduktion aus harter Streuung in A + A aus der Messung in p + p durch Skalierung mit der Anzahl der binären Nukleon-Nukleon-Kollisionen in A + A extrapoliert werden (binäre Skalierung). In zentralen Au + Au-Kollisionen bei  $\sqrt{s_{NN}} = 200 \text{ GeV}$  am RHIC ist

beobachtet worden, dass die Produktion von Hadronen unterdrückt ist im Vergleich zur Erwartung aus skalierten  $p + p$ -Reaktionen, während die Produktion direkter Photonen der binären Skalierung folgt. Da Photonen nicht der starken Wechselwirkung unterliegen, kann die Unterdrückung der Hadronen nicht durch Modifikationen des Anfangszustandes erklärt werden (andernfalls müßte die gleiche Unterdrückung in der Produktion direkter Photonen beobachtet werden), sondern kann auf den Energieverlust der gestreuten Partonen in einem Medium mit hoher Farbladungsdichte zurückgeführt werden; ein Effekt, der häufig als *Jet-Quenching* bezeichnet wird. Diese Ergebnisse lieferten einen starken Hinweis für die Erzeugung des so genannten Quark-Gluon-Plasmas (QGP) in zentralen  $Au + Au$ -Kollisionen am RHIC, einem Materiezustand, in dem die Quarks und Gluonen die relevanten, thermodynamischen Freiheitsgrade darstellen. Allerdings basierte die Schlussfolgerung, dass direkte Photonen in  $Au + Au$  nicht unterdrückt sind, auf dem Vergleich mit einer skalierten pQCD-Vorhersage und nicht auf dem Vergleich mit einer gemessenen  $p + p$ -Referenz.

Für die Berechnung inelastischer Wirkungsquerschnitte in der QCD werden die nichtstörungstheoretischen Impulsverteilungen der Partonen im Anfangszustand benötigt. Diese Partonverteilungsfunktionen werden in tiefinelastischen Lepton-Nukleon Streuexperimenten gemessen. Da das Gluon jedoch elektrisch neutral ist, kann die Gluonverteilung im Proton nicht direkt in diesen Messungen bestimmt werden. Daher ist die Gluonverteilung durch tiefinelastische Streuexperimente nur schwach bestimmt, insbesondere für Impulsbruchteile von  $x \gtrsim 0.1$ . In  $p + p$ -Kollisionen trägt das Gluon allerdings in führender Ordnung durch Quark-Gluon-Compton-Streuung zur Produktion direkter Photonen mit hohen Transversalimpulsen bei. Somit ermöglichen genaue Messungen des Spektrums direkter Photonen in ultrarelativistischen  $p + p$ -Kollisionen einen direkten Zugang zur Gluonverteilung im Proton.

Darüber hinaus spielt die Verteilung der Gluonen im Proton möglicherweise eine wichtige Rolle im so genannten Spin-Rätsel. In den späten 80er Jahren des letzten Jahrhunderts ist in polarisierten tiefinelastischen Streuexperimenten entdeckt worden, dass sich der Spin des Protons nicht einfach aus der Summe der Spins der drei Valenzquarks ergibt. Vielmehr ist herausgefunden worden, dass der Beitrag von Quarks und Antiquarks zum Spin des Protons wahrscheinlich weniger als 35% ausmacht. Es wird somit erwartet, dass sich der übrige Anteil auf den Spin der Gluonen und die Bahndrehimpulse der Partonen im Proton verteilt. Während bisher nur erste Vorschläge existieren, wie man experimentell Zugriff auf die Bahndrehimpulse erhält, so kann die polarisierte Gluonverteilung  $\Delta g$  direkt in ultrarelativistischen Kollisionen von longitudinal polarisierten Protonen am RHIC untersucht werden. Der sauberste Kanal mit einem Gluon im Anfangszustand ist die Produktion direkter Photonen, da diese nur zum Teil durch Fragmentation beeinflusst wird. Ein weiterer, vielversprechender Kanal ist die Produktion neutraler Pionen, der z.B.

Gluon-Gluon- und Quark-Gluon-Streuung in führender Ordnung zugrunde liegen. Allerdings werden die theoretischen Vorhersagen durch die Parton-Jet-Fragmentation beeinträchtigt.

Der Schwerpunkt dieser Arbeit liegt in der Analyse direkter Photonen in p + p-Kollisionen. Die Messung ist sehr anspruchsvoll aufgrund des großen Untergrundes durch Zerfallsphotonen, die hauptsächlich aus  $\pi^0$ -Zerfällen stammen. Im PHENIX Experiment werden Photonen mit dem elektromagnetischen Kalorimeter (EMCal) nachgewiesen. Die in dieser Arbeit vorgestellten Analysen wurden separat für die beiden verschiedenen Detektoren des EMCal durchgeführt, einem Bleiglas-Cherenkov-Kalorimeter und einem Bleiszintillator-Sandwich-Kalorimeter. Ein Vergleich der beiden Ergebnisse ermöglicht eine hervorragende interne Überprüfung der Messungen. Die Extraktion des Signals direkter Photonen aus dem Spektrum inklusiver Photonen (Zerfallsphotonen + direkte Photonen) erfordert eine gründliche Analyse der Beiträge von geladenen und neutralen Hadronen. Außerdem müssen die Konversion von Photonen und spezifische Eigenschaften des Detektors wie die begrenzte Energieauflösung sorgfältig berücksichtigt werden. Der Beitrag der Zerfallsphotonen aus  $\pi^0$ -,  $\eta$ -,  $\omega$ - und  $\eta'$ -Zerfällen wurde berechnet unter Verwendung des gemessenen  $\pi^0$ -Spektrums, das aus dem gleichen Datensatz bestimmt wurde. Zum ersten Mal in PHENIX ist das inklusive Photonenspektrum bis zu einem Transversalimpuls gemessen worden, bei dem Zerfallsphotonen aus dem gleichen  $\pi^0$ -Zerfall so überlappen, dass sie nicht mehr aufgelöst werden können. Dieses so genannte *Shower-Merging* führt zu einer signifikanten Verzerrung des unkorrigierten Spektrums direkter Photonen bei hohem  $p_T$ . Es wird eine Methode in dieser Arbeit vorgestellt, die diesen Effekt korrigiert und so eine Extraktion des unverfälschten Signals direkter Photonen für den ganzen  $p_T$ -Bereich, der in der Analyse abgedeckt wird, ermöglicht.

Eine sorgfältige Analyse der systematischen Fehler erlaubte die Extraktion eines signifikanten Signals direkter Photonen in dem Bereich  $5.5 \text{ GeV}/c < p_T < 16.0 \text{ GeV}/c$ , dem größten  $p_T$ -Bereich, der jemals durch eine Messung direkter Photonen in p + p-Kollisionen bei  $\sqrt{s} = 200 \text{ GeV}$  abgedeckt wurde. Die Daten werden sehr gut durch NLO pQCD Vorhersagen beschrieben und ergänzen die bereits existierenden Daten direkter Photonen in Nukleon-Nukleon-Kollisionen bei deutlich höheren und niedrigeren Schwerpunktsenergien. Dieses Ergebnis stellt die aus der früheren Au + Au-Messung abgeleiteten Schlussfolgerungen auf ein sicheres experimentelles Fundament und stellt den ersten Schritt in Richtung der Extraktion der Gluonverteilung aus Daten direkter Photonen dar.

Im zweiten Teil dieser Arbeit wurde die doppelt-longitudinale Spin-Asymmetrie ( $A_{LL}$ ) in der  $\pi^0$ -Produktion in polarisierten p + p-Kollisionen gemessen. Diese Spin-Asymmetrie wird definiert durch die Differenz der Wirkungsquerschnitte der  $\pi^0$ -Produktion in Kollisionen von Protonen mit gleicher und entgegengesetzter Helizität.  $A_{LL}$  hat einen direkten Bezug zu  $\Delta g$  im Proton und erlaubt somit den Beitrag der Gluonpolari-

sation zum Spin des Protons zu untersuchen. In der Analyse wurde der  $\pi^0$ -Kanal verwendet und nicht die Produktion direkter Photonen, da ein signifikantes  $A_{LL}$ -Ergebnis eine große Statistik erfordert. Für transversale Impulse unterhalb von  $5 \text{ GeV}/c$ , wo die statistische Genauigkeit der Teilchenproduktion sehr groß ist, leidet die Messung direkter Photonen unter dem großen Untergrund an Zerfallsphotonen (dominiert von  $\pi^0$ -Zerfällen), was sich in den großen systematischen Fehlern widerspiegelt. Im Gegensatz dazu wird das Signal neutraler Pionen nicht signifikant durch Untergrund bei niedrigem  $p_T$  geschwächt und kann daher mit großer statistischer und systematischer Genauigkeit gemessen werden. Für diese Analyse wurde im Wesentlichen der gleiche Datensatz wie für die direkten Photonen ausgewertet. Neutrale Pionen werden aus ihren zwei Zerfallsphotonen rekonstruiert. Die  $\pi^0$ -Ausbeute wurde sorgfältig für die beiden Helizitätskombinationen gemessen. Die Ausbeuten, die gemessenen Polarisationen der Protonenstrahlen und die gemessene relative Luminosität, die Unterschiede in der Anzahl der  $p + p$ -Kollisionen mit gleicher und entgegengesetzter Helizität berücksichtigt, wurden verwendet, um die doppelt-longitudinale Spin-Asymmetrie in der  $\pi^0$ -Produktion für  $1 \text{ GeV}/c < p_T < 5 \text{ GeV}/c$  zu berechnen. Die statistische Genauigkeit des  $A_{LL}$ -Ergebnisses ist begrenzt. Dennoch weisen Vergleiche mit Modellrechnungen, die verschiedene Annahmen der polarisierten Gluonverteilung verwenden, darauf hin, dass ein großer Beitrag der Gluonpolarisation zum Protonspin nicht sehr wahrscheinlich ist.

Die in dieser Arbeit präsentierte  $A_{LL}$ -Messung stellt die erste Messung dieser Art in Kollisionen von polarisierten Protonen bei ultrarelativistischen Energien dar. Sie erlaubt zum ersten Mal, wenn auch begrenzt, den direkten Zugang zur polarisierten Gluonverteilung im Proton.

# A. Variables of Ultra-Relativistic Kinematics

Particle production in ultra-relativistic collisions of nucleons or nuclei are usually described using kinematic variables which have simple transformation characteristics when changing the reference frame. In high-energy physics particles are usually described by their four-momenta<sup>1</sup>:

$$P = (p_0, p_1, p_2, p_3) = (E, \vec{p}), \quad (\text{A.1})$$

where  $p_0 = E$  is the energy and  $(p_1, p_2, p_3) = \vec{p} = (p_x, p_y, p_z)$  is the usual three-momentum vector of the particle. The square of the four-momentum is defined by:

$$P^2 = p_0^2 - p_1^2 - p_2^2 - p_3^2 = E^2 - \vec{p}^2. \quad (\text{A.2})$$

$P^2$  is a Lorentz invariant quantity, which is identified with the square of the *invariant mass*  $m_{\text{inv}}$  of the particle. For a free particle  $m_{\text{inv}}$  is identical to its rest mass  $m_0$ . Then Equation A.2 becomes the known relativistic energy-momentum relation:

$$E^2 = m_0^2 + \vec{p}^2. \quad (\text{A.3})$$

In accelerator experiments the beam axis is usually chosen to be the  $z$ -axis of the coordinate system. Then the components of the three-momentum transverse and longitudinal to the beam axis can be written as:

$$p_T = |\vec{p}| \cdot \sin \vartheta = \sqrt{p_x^2 + p_y^2}, \quad (\text{A.4})$$

$$p_L = |\vec{p}| \cdot \cos \vartheta = p_z, \quad (\text{A.5})$$

where  $\vartheta$  is the angle between  $\vec{p}$  and the  $z$ -axis.

Instead of the transverse momentum  $p_T$  sometimes the so-called transverse mass  $m_T$  is used:

$$m_T = \sqrt{p_T^2 + m_0^2}. \quad (\text{A.6})$$

Unlike  $p_T$  the longitudinal momentum is not invariant under Lorentz transformations. Therefore the so-called *rapidity*  $y$  is introduced, which is defined as:

$$y = \frac{1}{2} \ln \left( \frac{E + p_L}{E - p_L} \right). \quad (\text{A.7})$$

---

<sup>1</sup>For convenience all kinematic variables described here are given in natural units ( $\hbar \equiv c \equiv 1$ ).

Although this dimensionless quantity is also not invariant under Lorentz transformations, it is only changed by an additive constant when going to a reference frame that moves at the velocity  $\beta$  with respect to the original reference frame along the  $z$ -axis:

$$y' = y + \text{atanh}(\beta). \quad (\text{A.8})$$

Equation A.8 implies that the shape of a distribution is independent of the reference frame when it is expressed in terms of the rapidity.

For the calculation of the rapidity the energy and the longitudinal momentum of the particle have to be measured. This is not always possible. In this case the so-called *pseudo-rapidity*  $\eta$  is used instead:

$$\eta = \frac{1}{2} \ln \left( \frac{|\vec{p}| + p_L}{|\vec{p}| - p_L} \right) = -\ln \left[ \tan \left( \frac{\vartheta}{2} \right) \right]. \quad (\text{A.9})$$

The pseudo-rapidity depends only on the angle  $\vartheta$  introduced earlier and is therefore easier to measure. In the limit  $E \approx |\vec{p}| \gg m_0$  the rapidity can be approximated by the pseudo-rapidity.

For calculations in ultra-relativistic reactions such as  $1 + 2 \rightarrow 3 + 4$  (also referred to as  $2 \rightarrow 2$  processes) usually the Lorentz invariant *Mandelstam variables*  $s$ ,  $t$  and  $u$  are used. They are defined as follows in terms of the four-momenta  $P_{1\dots 4}$ :

$$s = (P_1 + P_2)^2 = (P_3 + P_4)^2, \quad (\text{A.10})$$

$$t = (P_1 - P_3)^2 = (P_2 - P_4)^2, \quad (\text{A.11})$$

$$u = (P_1 - P_4)^2 = (P_2 - P_3)^2. \quad (\text{A.12})$$

$s$ ,  $t$  and  $u$  are connected via the relation:

$$s + t + u = m_1^2 + m_2^2 + m_3^2 + m_4^2 = \text{const.}, \quad (\text{A.13})$$

where  $m_{1\dots 2}$  are the invariant masses of particles 1...4. While  $\sqrt{s}$  represents the available energy in the reaction in the center-of-mass frame,  $t$  represents the momentum transfer in the reaction, i.e.  $t = Q^2$ .

## B. List of Analyzed Runs

### B.1 Direct-Photon Analysis

#### B.1.1 List of Analyzed Minimum Bias Runs

88115	88125	88127	88131	88243	88258	88260	88350	88351	88396
88460	88462	88466	88471	88475	88578	88580	88582	88584	88586
88825	88827	88829	88845	88846	88869	88873	88875	88877	88879
88943	88944	88946	88962	88964	88993	88995	88997	88999	89001
89003	89080	89092	89096	89098	89100	89103	89117	89119	89121
89128	89130	89135	89211	89297	89299	89303	89316	89318	89321
89323	89325	89345	89451	89453	89463	89520	89527	89529	89541
89618	89624	89626	89629	89634	89642	89644	89646	89648	89683
89685	89693	89695	89697	89707	89709	89711	89713	89715	90202
90209	90211	90213	90215	90217	90219	90226	90228	90302	90303
90306	90402	91085	91314	91316	91318	91321	91375	91443	91447
91449	91451	91452	91455	91457	91460	91462	91464	91472	91474
91476	91478	91596	91599	91601	91679	91681	91716	91718	91720
91726	91729	91731	91840	91842	91844	91846	91848	91851	91853
91855	91977	91979	91983	91985	91987	92002	92018	92030	92034
92047	92192	92194	92228	92230	92232	92234	92238	92242	92244
92432	92434	92436	92438	92440	92444	92446			

**Table B.1:** List of runs containing minimum bias events analyzed for the direct-photon analysis.

**B.1.2 List of Analyzed Gamma3 Filtered Runs**

88115	88125	88127	88131	88243	88258	88260	88350	88351	88396
88460	88462	88466	88471	88475	88578	88580	88582	88584	88586
88825	88827	88829	88845	88846	88869	88873	88875	88877	88879
88943	88944	88946	88962	88964	88993	88995	88997	88999	89001
89003	89080	89092	89096	89098	89100	89103	89117	89119	89121
89128	89130	89135	89211	89297	89299	89303	89316	89318	89321
89323	89325	89345	89451	89453	89463	89520	89527	89529	89541
89618	89624	89626	89629	89634	89642	89644	89646	89648	89683
89685	89693	89695	89697	89707	89709	89711	89713	89715	90202
90209	90211	90213	90215	90217	90219	90226	90228	90302	90303
90306	90402	90701	90703	90707	90709	91085	91314	91316	91318
91321	91375	91443	91447	91449	91451	91452	91455	91457	91460
91462	91464	91472	91474	91476	91478	91596	91601	91679	91681
91716	91718	91720	91726	91729	91731	91840	91842	91844	91846
91848	91851	91853	91855	91977	91979	91983	91985	91987	92002
92018	92030	92034	92047	92192	92194	92228	92230	92232	92234
92238	92242	92244	92432	92434	92436	92438	92440	92444	92446

**Table B.2:** List of runs containing Gamma3 filtered events analyzed for the direct-photon analysis.

## B.2 Double Helicity Asymmetry Analysis

88115	88125	88127	88131	88243	88258	88260	88351	88396	88460
88462	88466	88471	88475	88578	88580	88582	88584	88586	88825
88829	88846	88869	88873	88877	88879	88944	88946	88962	88964
88993	88995	88999	89001	89003	89005	89080	89092	89096	89098
89100	89103	89117	89119	89121	89128	89130	89135	89211	89297
89299	89303	89316	89318	89321	89323	89325	89345	89451	89453
89463	89520	89527	89529	89541	89618	89624	89626	89629	89634
89642	89644	89646	89648	89683	89685	89693	89695	89697	89707
89709	89711	89713	89715	90202	90209	90211	90213	90215	90217
90219	90226	90302	90303	90306	91314	91316	91318	91321	91375
91443	91447	91449	91452	91455	91457	91460	91462	91464	91472
91474	91476	91478	91596	91599	91601	91679	91681	91716	91718
91720	91726	91731	91840	91842	91844	91846	91848	91851	91853
91855	91977	91979	91983	91985	91987	92002	92018	92030	92034
92036	92038	92047	92192	92194	92228	92230	92232	92238	92242
92244	92432	92434	92436	92438	92440	92444	92446		

**Table B.3:** List of runs containing Gamma3 filtered events analyzed for the analysis of the double helicity asymmetry in  $\pi^0$  production.



## C. Bad Tower Maps



**Figure C.1:** Maps of bad towers for all eight sectors of the EMCal. White areas are bad or edge towers. Dark grey towers are first order neighbors. Hits on the remaining towers are accepted in the analysis.



## D. Photon-Like Cluster Spectra

PbGl					PbSc					
$p_T$ [GeV/c $^2$ ]	MinBias		ERT			$p_T$ [GeV/c $^2$ ]	MinBias		ERT	
	PID0	PID3	PID0	PID3	PID0	PID3	PID0	PID3	PID0	PID3
0.25	21043280	2319195	1152901	861071	0.25	58932184	12093245	2953609	640810	
0.75	474571	398245	3138330	2900381	0.75	2107671	1622251	2871290	1544700	
1.25	48112	39924	3114490	2843969	1.25	248488	168497	8851427	5248052	
1.75	8821	7589	1274150	1138486	1.75	39292	29184	5232899	3870977	
2.25	2113	1881	378558	339204	2.25	7721	6603	1430645	1225265	
2.75	548	483	115216	104634	2.75	2065	1865	406155	367404	
3.25	214	197	39589	36388	3.25	674	610	132946	122565	
3.75	76	70	15183	14023	3.75	256	237	50059	46432	
4.25	36	34	6662	6163	4.25	123	113	20779	19344	
4.75	18	16	2992	2748	4.75	41	39	9533	8848	
5.25	13	10	1484	1357	5.25	24	21	4779	4440	
5.75	8	5	807	738	5.75	18	16	2527	2322	
6.25	1	1	449	423	6.25	7	5	1409	1278	
6.75	2	1	281	250	6.75	3	3	886	808	
7.25	1	1	180	158	7.25	4	2	479	436	
7.75	2	1	112	102	7.75	3	3	381	346	
8.25	0	0	67	60	8.25	2	2	248	217	
8.75	0	0	49	42	8.75	2	1	151	123	
9.25	0	0	40	32	9.25	0	0	102	91	
9.75	0	0	26	21	9.75	0	0	77	62	
10.25	0	0	22	17	10.25	0	0	53	45	
10.75	1	0	18	13	10.75	0	0	39	33	
11.25	0	0	12	10	11.25	1	1	40	30	
11.75	0	0	12	11	11.75	0	0	33	20	
12.25	0	0	4	2	12.25	0	0	16	12	
12.75	0	0	14	11	12.75	0	0	18	8	
13.25	0	0	3	1	13.25	0	0	9	6	
13.75	0	0	5	3	13.75	0	0	10	5	
14.25	0	0	6	5	14.25	1	1	16	11	
14.75	0	0	2	2	14.75	0	0	9	6	
15.25	0	0	2	0	15.25	0	0	5	4	
15.75	0	0	1	0	15.75	0	0	3	0	

**Table D.1:** The number of raw photon-like clusters in PbGl and PbSc for the two different data samples with (PID3) and w/o (PID0) PID cuts.



## E. Data Tables - Direct Photons

### E.1 Cross Section of Inclusive Photon Production in p + p Collisions

Inclusive Photon Cross Section in PbGl					
$p_T$ [GeV/c]	$E \frac{d^3\sigma}{d\vec{p}^3}$ [mb · $c^3$ / GeV $^2$ ]	stat. error [mb · $c^3$ / GeV $^2$ ]	sys. error A [mb · $c^3$ / GeV $^2$ ]	sys. error B [mb · $c^3$ / GeV $^2$ ]	total error [mb · $c^3$ / GeV $^2$ ]
1.25	1.873E-01	1.198E-03	1.821E-02	1.817E-02	2.575E-02
1.75	2.684E-02	3.262E-04	2.792E-03	2.604E-03	3.832E-03
2.25	5.328E-03	1.247E-04	5.871E-04	5.168E-04	7.921E-04
2.75	1.124E-03	5.133E-05	1.292E-04	1.090E-04	1.767E-04
3.25	3.624E-04	2.391E-06	4.288E-05	3.515E-05	5.550E-05
3.75	1.231E-04	1.150E-06	1.482E-05	1.194E-05	1.906E-05
4.25	4.715E-05	6.293E-07	5.729E-06	4.573E-06	7.357E-06
4.75	1.916E-05	3.736E-07	2.336E-06	1.859E-06	3.009E-06
5.25	8.716E-06	2.392E-07	1.062E-06	8.454E-07	1.378E-06
5.75	4.353E-06	1.612E-07	5.290E-07	4.222E-07	6.958E-07
6.25	2.334E-06	1.138E-07	2.826E-07	2.264E-07	3.796E-07
6.75	1.278E-06	8.097E-08	1.542E-07	1.239E-07	2.138E-07
7.25	7.576E-07	6.035E-08	9.120E-08	7.349E-08	1.318E-07
7.75	4.646E-07	4.604E-08	5.583E-08	4.506E-08	8.525E-08
8.25	2.567E-07	3.316E-08	3.084E-08	2.490E-08	5.168E-08
8.75	1.706E-07	2.633E-08	2.051E-08	1.655E-08	3.725E-08
9.25	1.238E-07	2.188E-08	1.490E-08	1.200E-08	2.907E-08
9.75	7.618E-08	1.663E-08	9.193E-09	7.389E-09	2.038E-08
11.00	3.851E-08	5.393E-09	4.673E-09	3.736E-09	8.054E-09
13.00	1.118E-08	2.711E-09	1.355E-09	1.084E-09	3.219E-09
15.00	4.055E-09	1.533E-09	4.895E-10	3.933E-10	1.656E-09

**Table E.1:** Cross section of inclusive photon production in the PbGl.

Inclusive Photon Cross Section in PbSc					
$p_T$ [GeV/c]	$E \frac{d^3\sigma}{dp^3}$ [mb · $c^3$ /GeV $^2$ ]	stat. error [mb · $c^3$ /GeV $^2$ ]	sys. error A [mb · $c^3$ /GeV $^2$ ]	sys. error B [mb · $c^3$ /GeV $^2$ ]	total error [mb · $c^3$ /GeV $^2$ ]
1.25	1.832E-01	5.979E-04	1.777E-02	1.777E-02	2.513E-02
1.75	2.451E-02	1.531E-04	2.526E-03	2.377E-03	3.472E-03
2.25	4.633E-03	5.791E-05	5.047E-04	4.494E-04	6.783E-04
2.75	1.126E-03	2.619E-05	1.282E-04	1.092E-04	1.705E-04
3.25	3.195E-04	1.150E-06	3.756E-05	3.099E-05	4.871E-05
3.75	1.059E-04	5.437E-07	1.272E-05	1.027E-05	1.636E-05
4.25	3.930E-05	2.954E-07	4.781E-06	3.812E-06	6.122E-06
4.75	1.614E-05	1.753E-07	1.976E-06	1.566E-06	2.528E-06
5.25	7.377E-06	1.119E-07	9.040E-07	7.156E-07	1.158E-06
5.75	3.577E-06	7.466E-08	4.374E-07	3.470E-07	5.633E-07
6.25	1.828E-06	5.129E-08	2.226E-07	1.773E-07	2.892E-07
6.75	1.083E-06	3.818E-08	1.312E-07	1.051E-07	1.724E-07
7.25	5.493E-07	2.634E-08	6.618E-08	5.329E-08	8.895E-08
7.75	4.097E-07	2.204E-08	4.911E-08	3.974E-08	6.691E-08
8.25	2.433E-07	1.653E-08	2.905E-08	2.360E-08	4.092E-08
8.75	1.296E-07	1.169E-08	1.544E-08	1.258E-08	2.309E-08
9.25	9.102E-08	9.543E-09	1.082E-08	8.829E-09	1.691E-08
9.75	5.900E-08	7.494E-09	7.013E-09	5.723E-09	1.175E-08
11.00	2.530E-08	2.236E-09	3.022E-09	2.454E-09	4.489E-09
13.00	5.329E-09	9.572E-10	6.457E-10	5.170E-10	1.265E-09
15.00	3.190E-09	6.960E-10	3.896E-10	3.094E-10	8.555E-10

**Table E.2:** Cross section of inclusive photon production in the PbSc.

<b>Combined Result of Inclusive Photon Cross Section</b>					
$p_T$ [GeV/c]	$E \frac{d^3\sigma}{dp^3}$ [mb · $c^3$ /GeV $^2$ ]	stat. error [mb · $c^3$ /GeV $^2$ ]	sys. error A [mb · $c^3$ /GeV $^2$ ]	sys. error B [mb · $c^3$ /GeV $^2$ ]	total error [mb · $c^3$ /GeV $^2$ ]
1.25	1.852E-01	6.644E-04	1.798E-02	1.796E-02	2.543E-02
1.75	2.555E-02	1.741E-04	2.645E-03	2.479E-03	3.629E-03
2.25	4.922E-03	6.490E-05	5.390E-04	4.774E-04	7.230E-04
2.75	1.125E-03	2.815E-05	1.287E-04	1.091E-04	1.711E-04
3.25	3.381E-04	1.271E-06	3.988E-05	3.280E-05	5.165E-05
3.75	1.132E-04	6.046E-07	1.361E-05	1.098E-05	1.750E-05
4.25	4.251E-05	3.268E-07	5.169E-06	4.123E-06	6.620E-06
4.75	1.739E-05	1.945E-07	2.125E-06	1.687E-06	2.720E-06
5.25	7.927E-06	1.242E-07	9.688E-07	7.689E-07	1.243E-06
5.75	3.878E-06	8.214E-08	4.729E-07	3.762E-07	6.099E-07
6.25	2.007E-06	5.603E-08	2.438E-07	1.946E-07	3.169E-07
6.75	1.155E-06	4.087E-08	1.397E-07	1.120E-07	1.837E-07
7.25	6.088E-07	2.770E-08	7.331E-08	5.905E-08	9.812E-08
7.75	4.281E-07	2.275E-08	5.137E-08	4.153E-08	6.986E-08
8.25	2.477E-07	1.650E-08	2.964E-08	2.403E-08	4.157E-08
8.75	1.393E-07	1.157E-08	1.663E-08	1.351E-08	2.435E-08
9.25	9.804E-08	9.333E-09	1.169E-08	9.509E-09	1.773E-08
9.75	6.265E-08	7.175E-09	7.476E-09	6.077E-09	1.201E-08
11.00	2.800E-08	2.228E-09	3.359E-09	2.716E-09	4.861E-09
13.00	6.047E-09	9.234E-10	7.327E-10	5.865E-10	1.317E-09
15.00	3.354E-09	6.473E-10	4.085E-10	3.253E-10	8.316E-10

**Table E.3:** Combined result of inclusive photon production in p + p collisions.

## E.2 Invariant Yield of Neutral Pion Production in p + p Collisions

Invariant Neutral Pion Yield in PbGl					
$p_T$ [GeV/c]	$\frac{1}{2\pi p_T N_{\text{evt}}} \cdot \frac{d^2N\pi^0}{dp_T dy}$ [c <sup>3</sup> /GeV <sup>2</sup> ]	stat. error [c <sup>3</sup> /GeV <sup>2</sup> ]	sys. error A [c <sup>3</sup> /GeV <sup>2</sup> ]	sys. error B [c <sup>3</sup> /GeV <sup>2</sup> ]	total error [c <sup>3</sup> /GeV <sup>2</sup> ]
1.25	7.770E-03	1.681E-04	6.580E-04	7.537E-04	1.015E-03
1.75	1.330E-03	3.531E-05	1.008E-04	1.290E-04	1.675E-04
2.25	2.809E-04	1.163E-05	2.155E-05	2.725E-05	3.663E-05
2.75	7.883E-05	4.463E-06	6.218E-06	7.647E-06	1.082E-05
3.25	2.079E-05	1.909E-06	1.694E-06	2.016E-06	3.253E-06
3.75	7.737E-06	1.245E-07	8.123E-07	7.505E-07	1.113E-06
4.25	2.884E-06	5.690E-08	2.739E-07	2.797E-07	3.956E-07
4.75	1.211E-06	3.056E-08	1.102E-07	1.175E-07	1.639E-07
5.25	5.395E-07	1.853E-08	5.015E-08	5.233E-08	7.481E-08
5.75	2.617E-07	1.063E-08	2.503E-08	2.539E-08	3.720E-08
6.25	1.384E-07	7.302E-09	1.360E-08	1.343E-08	2.046E-08
6.75	7.591E-08	5.114E-09	7.647E-09	7.364E-09	1.178E-08
7.25	4.112E-08	3.437E-09	4.239E-09	3.988E-09	6.760E-09
7.75	1.909E-08	3.058E-09	2.011E-09	1.852E-09	4.101E-09
8.25	1.307E-08	1.859E-09	1.406E-09	1.268E-09	2.653E-09
8.75	9.009E-09	1.446E-09	9.874E-10	8.739E-10	1.957E-09
9.25	5.594E-09	1.099E-09	6.243E-10	5.426E-10	1.376E-09
9.75	4.074E-09	9.123E-10	4.626E-10	3.952E-10	1.097E-09
11.00	1.492E-09	2.491E-10	1.763E-10	1.447E-10	3.378E-10
13.00	3.263E-10	1.088E-10	4.101E-11	3.165E-11	1.205E-10
15.00	9.759E-11	5.635E-11	1.318E-11	9.466E-12	5.864E-11

**Table E.4:** Invariant yield of neutral pions in the PbGl.

Invariant Neutral Pion Yield in PbSc					
$p_T$ [GeV/c]	$\frac{1}{2\pi p_T N_{\text{ev}}^{\text{ref}}} \cdot \frac{d^2 N^{\pi^0}}{dp_T dy}$ [ $c^3/\text{GeV}^2$ ]	stat. error [ $c^3/\text{GeV}^2$ ]	sys. error A [ $c^3/\text{GeV}^2$ ]	sys. error B [ $c^3/\text{GeV}^2$ ]	total error [ $c^3/\text{GeV}^2$ ]
1.25	7.490E-03	1.034E-04	6.209E-04	7.266E-04	9.613E-04
1.75	1.210E-03	1.975E-05	8.933E-05	1.174E-04	1.488E-04
2.25	2.640E-04	5.532E-06	1.973E-05	2.561E-05	3.280E-05
2.75	6.621E-05	2.132E-06	5.095E-06	6.423E-06	8.471E-06
3.25	2.119E-05	1.005E-06	1.688E-06	2.056E-06	2.844E-06
3.75	7.225E-06	8.512E-08	7.481E-07	7.009E-07	1.029E-06
4.25	2.628E-06	3.459E-08	2.454E-07	2.549E-07	3.555E-07
4.75	1.053E-06	1.649E-08	9.410E-08	1.022E-07	1.399E-07
5.25	4.739E-07	9.204E-09	4.327E-08	4.596E-08	6.379E-08
5.75	2.329E-07	5.523E-09	2.191E-08	2.260E-08	3.196E-08
6.25	1.125E-07	3.677E-09	1.088E-08	1.091E-08	1.584E-08
6.75	6.022E-08	2.434E-09	5.975E-09	5.841E-09	8.703E-09
7.25	3.650E-08	1.695E-09	3.709E-09	3.540E-09	5.400E-09
7.75	2.014E-08	1.183E-09	2.093E-09	1.954E-09	3.098E-09
8.25	1.147E-08	1.055E-09	1.217E-09	1.112E-09	1.957E-09
8.75	6.538E-09	8.751E-10	7.075E-10	6.342E-10	1.292E-09
9.25	5.476E-09	5.300E-10	6.037E-10	5.312E-10	9.631E-10
9.75	3.006E-09	3.800E-10	3.373E-10	2.916E-10	5.858E-10
11.00	1.187E-09	1.104E-10	1.487E-10	1.152E-10	2.181E-10
13.00	3.547E-10	5.922E-11	5.182E-11	3.440E-11	8.588E-11
15.00	1.103E-10	3.490E-11	1.903E-11	1.070E-11	4.117E-11

**Table E.5:** Invariant yield of neutral pions in the PbSc.

Combined Result of Neutral Pion Yield					
$p_T$ [GeV/c]	$\frac{1}{2\pi p_T N_{\text{evt}}} \cdot \frac{d^2N_{\pi^0}}{dp_T dy}$ [ $c^3/\text{GeV}^2$ ]	stat. error [ $c^3/\text{GeV}^2$ ]	sys. error A [ $c^3/\text{GeV}^2$ ]	sys. error B [ $c^3/\text{GeV}^2$ ]	total error [ $c^3/\text{GeV}^2$ ]
1.25	7.617E-03	9.662E-05	5.195E-04	7.389E-04	9.084E-04
1.75	1.258E-03	1.919E-05	7.995E-05	1.221E-04	1.472E-04
2.25	2.704E-04	5.925E-06	1.751E-05	2.623E-05	3.209E-05
2.75	7.011E-05	2.156E-06	4.689E-06	6.801E-06	8.537E-06
3.25	2.106E-05	9.680E-07	1.453E-06	2.043E-06	2.687E-06
3.75	7.457E-06	7.409E-08	6.272E-07	7.233E-07	9.602E-07
4.25	2.738E-06	3.224E-08	2.150E-07	2.656E-07	3.432E-07
4.75	1.116E-06	1.637E-08	8.558E-08	1.083E-07	1.390E-07
5.25	4.995E-07	9.631E-09	3.910E-08	4.845E-08	6.300E-08
5.75	2.442E-07	5.600E-09	1.961E-08	2.369E-08	3.125E-08
6.25	1.212E-07	3.671E-09	9.980E-09	1.176E-08	1.585E-08
6.75	6.506E-08	2.466E-09	5.475E-09	6.310E-09	8.711E-09
7.25	3.803E-08	1.708E-09	3.257E-09	3.689E-09	5.209E-09
7.75	1.987E-08	1.317E-09	1.730E-09	1.927E-09	2.905E-09
8.25	1.196E-08	9.553E-10	1.061E-09	1.160E-09	1.839E-09
8.75	7.244E-09	7.565E-10	6.565E-10	7.026E-10	1.224E-09
9.25	5.507E-09	5.123E-10	5.030E-10	5.342E-10	8.949E-10
9.75	3.203E-09	3.685E-10	2.980E-10	3.107E-10	5.667E-10
11.00	1.262E-09	1.103E-10	1.232E-10	1.224E-10	2.057E-10
13.00	3.466E-10	5.421E-11	3.616E-11	3.362E-11	7.332E-11
15.00	1.065E-10	3.000E-11	1.155E-11	1.033E-11	3.376E-11

**Table E.6:** Combined result of the invariant neutral pion yield.

### E.3 Direct-Photon Production Cross Section in p + p Collisions

Direct-Photon Cross Section in PbGl						
$p_T$ [GeV/c]	$E \frac{d^3\sigma}{d\vec{p}^3}$ [mb · $c^3$ /GeV $^2$ ]	stat. error [mb · $c^3$ /GeV $^2$ ]	sys. error A [mb · $c^3$ /GeV $^2$ ]	sys. error B [mb · $c^3$ /GeV $^2$ ]	total error [mb · $c^3$ /GeV $^2$ ]	90% CL up. lim. [mb · $c^3$ /GeV $^2$ ]
3.25	1.119E-05	2.391E-06	2.978E-05 (3.283E-05)	1.085E-06	—	3.825E-05
3.75	8.624E-06	1.150E-06	1.001E-05 (1.100E-05)	8.365E-07	—	1.290E-05
4.25	5.100E-06	6.293E-07	3.815E-06 (4.177E-06)	4.947E-07	3.898E-06 (4.253E-06)	—
4.75	1.020E-06	3.736E-07	1.526E-06 (1.680E-06)	9.899E-08	—	2.011E-06
5.25	6.584E-07	2.392E-07	6.781E-07 (7.458E-07)	6.386E-08	—	9.204E-07
5.75	5.623E-07	1.612E-07	3.277E-07 (3.585E-07)	5.454E-08	3.692E-07 (3.969E-07)	—
6.25	3.811E-07	1.138E-07	1.742E-07 (1.897E-07)	3.696E-08	2.113E-07 (2.243E-07)	—
6.75	2.085E-07	8.097E-08	9.669E-08 (1.053E-07)	2.023E-08	1.277E-07 (1.344E-07)	—
7.25	1.604E-07	6.035E-08	5.727E-08 (6.203E-08)	1.555E-08	8.464E-08 (8.793E-08)	—
7.75	1.169E-07	4.604E-08	3.547E-08 (3.822E-08)	1.134E-08	5.921E-08 (6.090E-08)	—
8.25	4.766E-08	3.316E-08	2.059E-08 (2.243E-08)	4.623E-09	3.930E-08 (4.030E-08)	—
8.75	4.043E-08	2.633E-08	1.372E-08 (1.489E-08)	3.922E-09	2.995E-08 (3.050E-08)	—
9.25	4.015E-08	2.188E-08	9.945E-09 (1.067E-08)	3.894E-09	2.435E-08 (2.466E-08)	—
9.75	2.246E-08	1.663E-08	6.303E-09 (6.829E-09)	2.178E-09	1.791E-08 (1.811E-08)	—
11.00	1.842E-08	5.393E-09	3.291E-09 (3.472E-09)	1.787E-09	6.566E-09 (6.658E-09)	—
13.00	6.065E-09	2.711E-09	1.012E-09 (1.069E-09)	5.883E-10	2.953E-09 (2.973E-09)	—
15.00	2.469E-09	1.533E-09	3.853E-10 (4.058E-10)	2.395E-10	1.598E-09 (1.603E-09)	—

**Table E.7:** Cross Section of direct-photon production as measured with the PbGl. When errors are asymmetric the lower error is given in parentheses.

Direct-Photon Cross Section in PbSc						
$p_T$ [GeV/c]	$E \frac{d^3\sigma}{dp^3}$ [mb · $c^3$ /GeV $^2$ ]	stat. error [mb · $c^3$ /GeV $^2$ ]	sys. error A [mb · $c^3$ /GeV $^2$ ]	sys. error B [mb · $c^3$ /GeV $^2$ ]	total error [mb · $c^3$ /GeV $^2$ ]	90% CL up. lim. [mb · $c^3$ /GeV $^2$ ]
3.25	2.795E-06	1.150E-06	2.561E-05 (2.842E-05)	2.711E-07	—	3.282E-05
3.75	1.527E-06	5.437E-07	8.634E-06 (9.564E-06)	1.482E-07	—	1.107E-05
4.25	1.089E-06	2.954E-07	3.237E-06 (3.581E-06)	1.056E-07	—	4.161E-06
4.75	7.235E-07	1.753E-07	1.243E-06 (1.378E-06)	7.018E-08	—	1.607E-06
5.25	5.393E-07	1.119E-07	5.553E-07 (6.145E-07)	5.231E-08	—	7.251E-07
5.75	2.624E-07	7.466E-08	2.687E-07 (2.974E-07)	2.545E-08	—	3.569E-07
6.25	1.500E-07	5.129E-08	1.368E-07 (1.514E-07)	1.455E-08	—	1.871E-07
6.75	1.907E-07	3.818E-08	7.768E-08 (8.495E-08)	1.849E-08	8.851E-08 (9.495E-08)	—
7.25	4.526E-08	2.634E-08	4.175E-08 (4.611E-08)	4.390E-09	—	6.318E-08
7.75	1.165E-07	2.204E-08	2.908E-08 (3.124E-08)	1.130E-08	3.820E-08 (3.987E-08)	—
8.25	6.777E-08	1.653E-08	1.746E-08 (1.877E-08)	6.573E-09	2.492E-08 (2.586E-08)	—
8.75	2.115E-08	1.169E-08	9.803E-09 (1.071E-08)	2.052E-09	1.540E-08 (1.599E-08)	—
9.25	2.237E-08	9.543E-09	6.773E-09 (7.315E-09)	2.170E-09	1.190E-08 (1.222E-08)	—
9.75	1.438E-08	7.494E-09	4.475E-09 (4.834E-09)	1.395E-09	8.839E-09 (9.026E-09)	—
11.00	8.984E-09	2.236E-09	2.035E-09 (2.162E-09)	8.715E-10	3.147E-09 (3.230E-09)	—
13.00	1.364E-09	9.572E-10	5.080E-10 (5.550E-10)	1.323E-10	1.092E-09 (1.114E-09)	—
15.00	2.026E-09	6.960E-10	3.050E-10 (3.158E-10)	1.966E-10	7.849E-10 (7.892E-10)	—

**Table E.8:** Cross Section of direct-photon production as measured with the PbSc. When errors are asymmetric the lower error is given in parentheses.

Combined Result of Direct-Photon Cross Section						
$p_T$ [GeV/c]	$E \frac{d^3\sigma}{d\vec{p}^3}$ [mb · $c^3$ /GeV $^2$ ]	stat. error [mb · $c^3$ /GeV $^2$ ]	sys. error A [mb · $c^3$ /GeV $^2$ ]	sys. error B [mb · $c^3$ /GeV $^2$ ]	total error [mb · $c^3$ /GeV $^2$ ]	90% CL up. lim. [mb · $c^3$ /GeV $^2$ ]
3.25	7.349E-06	1.270E-06	2.735E-05 (3.025E-05)	7.128E-07	—	3.505E-05
3.75	4.465E-06	6.028E-07	9.212E-06 (1.017E-05)	4.332E-07	—	1.182E-05
4.25	2.634E-06	3.251E-07	3.471E-06 (3.825E-06)	2.555E-07	—	4.463E-06
4.75	1.008E-06	1.929E-07	1.350E-06 (1.491E-06)	9.781E-08	—	1.746E-06
5.25	6.607E-07	1.228E-07	6.019E-07 (6.636E-07)	6.409E-08	—	7.863E-07
5.75	3.904E-07	8.088E-08	2.905E-07 (3.199E-07)	3.787E-08	3.039E-07 (3.322E-07)	—
6.25	2.422E-07	5.494E-08	1.491E-07 (1.638E-07)	2.350E-08	1.606E-07 (1.744E-07)	—
6.75	2.078E-07	4.002E-08	8.423E-08 (9.183E-08)	2.016E-08	9.540E-08 (1.022E-07)	—
7.25	8.140E-08	2.703E-08	4.572E-08 (5.014E-08)	7.896E-09	5.370E-08 (5.751E-08)	—
7.75	1.192E-07	2.225E-08	3.109E-08 (3.338E-08)	1.156E-08	3.995E-08 (4.175E-08)	—
8.25	6.290E-08	1.614E-08	1.829E-08 (1.972E-08)	6.101E-09	2.514E-08 (2.620E-08)	—
8.75	2.634E-08	1.134E-08	1.066E-08 (1.160E-08)	2.555E-09	1.577E-08 (1.642E-08)	—
9.25	2.665E-08	9.184E-09	7.424E-09 (7.984E-09)	2.585E-09	1.209E-08 (1.244E-08)	—
9.75	1.638E-08	7.079E-09	4.843E-09 (5.220E-09)	1.589E-09	8.723E-09 (8.938E-09)	—
11.00	1.102E-08	2.196E-09	2.268E-09 (2.396E-09)	1.069E-09	3.333E-09 (3.421E-09)	—
13.00	1.962E-09	9.124E-10	5.489E-10 (5.926E-10)	1.903E-10	1.082E-09 (1.104E-09)	—
15.00	2.116E-09	6.448E-10	3.190E-10 (3.289E-10)	2.052E-10	7.481E-10 (7.524E-10)	—

**Table E.9:** Combined results of the direct-photon production cross section. When errors are asymmetric the lower error is given in parentheses.



## F. Data Tables - $A_{\text{LL}}$

### F.1 Signal and Background $A_{\text{LL}}$

$A_{\text{LL}}^{\pi^0 + \text{bg}}$ per Fill in the PbGl				
Fill No.	$1.0 < p_{\text{T}} [\text{GeV}/c] < 2.0$	$2.0 < p_{\text{T}} [\text{GeV}/c] < 3.0$	$3.0 < p_{\text{T}} [\text{GeV}/c] < 4.0$	$4.0 < p_{\text{T}} [\text{GeV}/c] < 5.0$
3625	$0.31 \pm 1.04$	$0.74 \pm 1.82$	—	$-0.62 \pm 6.71$
3627	$0.13 \pm 0.33$	$-0.37 \pm 0.53$	$0.54 \pm 1.32$	$1.23 \pm 3.66$
3634	$-0.08 \pm 0.23$	$-0.16 \pm 0.37$	$-0.31 \pm 0.89$	$-1.48 \pm 3.13$
3637	$0.30 \pm 0.22$	$0.24 \pm 0.36$	$-0.24 \pm 0.77$	$1.75 \pm 1.82$
3644	$0.88 \pm 0.79$	$0.30 \pm 1.33$	$-1.20 \pm 3.32$	$-11.47 \pm 6.53$
3646	$0.04 \pm 0.37$	$0.69 \pm 0.60$	$-0.52 \pm 1.44$	$-3.03 \pm 3.24$
3654	$0.12 \pm 0.10$	$0.23 \pm 0.16$	$-0.38 \pm 0.37$	$0.26 \pm 0.85$
3659	$0.18 \pm 0.12$	$-0.10 \pm 0.20$	$0.05 \pm 0.48$	$1.68 \pm 1.09$
3671	$-0.11 \pm 0.11$	$-0.29 \pm 0.18$	$0.29 \pm 0.46$	$0.59 \pm 0.87$
3672	$0.16 \pm 0.15$	$0.01 \pm 0.25$	$0.46 \pm 0.59$	$-2.76 \pm 1.37$
3674	$0.14 \pm 0.05$	$-0.03 \pm 0.08$	$-0.13 \pm 0.18$	$0.09 \pm 0.44$
3675	$-0.37 \pm 0.22$	$0.13 \pm 0.38$	$-1.07 \pm 0.92$	$3.27 \pm 2.18$
3676	$0.01 \pm 0.12$	$-0.21 \pm 0.20$	$-0.30 \pm 0.47$	$2.30 \pm 1.09$
3677	$-0.03 \pm 0.06$	$0.10 \pm 0.11$	$0.03 \pm 0.25$	$0.42 \pm 0.59$
3678	$-0.12 \pm 0.06$	$0.01 \pm 0.11$	$-0.36 \pm 0.26$	$-0.57 \pm 0.60$
3679	$-0.01 \pm 0.06$	$0.05 \pm 0.10$	$-0.01 \pm 0.24$	$0.25 \pm 0.52$
3680	$-0.03 \pm 0.11$	$0.50 \pm 0.18$	$0.42 \pm 0.43$	$1.27 \pm 0.92$
3681	$0.03 \pm 0.07$	$0.14 \pm 0.12$	$-0.20 \pm 0.28$	$0.78 \pm 0.64$
3682	$-0.15 \pm 0.17$	$0.06 \pm 0.30$	$-0.93 \pm 0.71$	$0.04 \pm 1.56$
3691	$0.04 \pm 0.06$	$0.05 \pm 0.11$	$0.02 \pm 0.25$	$-0.15 \pm 0.58$
3693	$-0.02 \pm 0.04$	$-0.10 \pm 0.07$	$-0.08 \pm 0.16$	$-0.41 \pm 0.36$
3696	$0.05 \pm 0.33$	$1.42 \pm 0.58$	$1.13 \pm 1.21$	$-0.08 \pm 5.13$
3698	$0.13 \pm 0.12$	$-0.25 \pm 0.20$	$-0.49 \pm 0.47$	$-0.79 \pm 1.07$
3699	$-0.05 \pm 0.11$	$-0.31 \pm 0.17$	$0.27 \pm 0.41$	$0.96 \pm 0.96$
3702	$-0.39 \pm 0.29$	$0.35 \pm 0.47$	$1.10 \pm 1.00$	$-1.35 \pm 2.80$
3703	$0.05 \pm 0.29$	$0.27 \pm 0.46$	$0.47 \pm 1.10$	$0.16 \pm 2.61$
3705	$0.04 \pm 0.09$	$0.09 \pm 0.15$	$-0.06 \pm 0.36$	$0.32 \pm 0.80$
3708	$-0.07 \pm 0.06$	$-0.24 \pm 0.10$	$-0.03 \pm 0.24$	$0.49 \pm 0.54$
3713	$0.08 \pm 0.04$	$0.15 \pm 0.06$	$-0.31 \pm 0.14$	$0.18 \pm 0.32$
3714	$0.03 \pm 0.04$	$0.05 \pm 0.07$	$0.09 \pm 0.16$	$-0.02 \pm 0.36$
3732	$2.51 \pm 1.21$	$2.79 \pm 1.63$	$1.77 \pm 4.56$	—
3733	$0.01 \pm 0.09$	$-0.16 \pm 0.15$	$-0.29 \pm 0.35$	$-1.09 \pm 0.78$
3735	$-0.04 \pm 0.20$	$0.59 \pm 0.33$	$0.21 \pm 0.73$	$-3.94 \pm 1.86$
3765	$0.04 \pm 0.06$	$-0.06 \pm 0.10$	$-0.34 \pm 0.25$	$0.09 \pm 0.54$
3767	$0.09 \pm 0.12$	$0.06 \pm 0.19$	$0.73 \pm 0.46$	$0.69 \pm 1.00$
3769	$-0.02 \pm 0.03$	$0.00 \pm 0.05$	$-0.06 \pm 0.12$	$-0.16 \pm 0.27$
3770	$-0.02 \pm 0.06$	$0.04 \pm 0.10$	$0.07 \pm 0.24$	$-0.89 \pm 0.54$
3774	$-0.01 \pm 0.06$	$-0.07 \pm 0.11$	$-0.11 \pm 0.26$	$-0.89 \pm 0.60$
3778	$-0.50 \pm 0.27$	$-0.32 \pm 0.43$	$1.59 \pm 1.02$	$-4.13 \pm 2.33$
3780	$-0.01 \pm 0.04$	$-0.03 \pm 0.07$	$-0.15 \pm 0.16$	$-0.09 \pm 0.37$
3793	$0.01 \pm 0.03$	$0.02 \pm 0.06$	$0.38 \pm 0.14$	$-0.29 \pm 0.30$
3796	$0.01 \pm 0.06$	$0.14 \pm 0.10$	$0.54 \pm 0.23$	$0.15 \pm 0.53$
3797	$-0.01 \pm 0.17$	$-0.08 \pm 0.29$	$0.11 \pm 0.67$	$-1.33 \pm 1.57$
3799	$0.11 \pm 0.09$	$0.00 \pm 0.15$	$0.14 \pm 0.37$	$-0.13 \pm 0.78$
3801	$0.22 \pm 0.12$	$-0.25 \pm 0.20$	$0.24 \pm 0.49$	$-1.65 \pm 1.18$
3803	$-0.04 \pm 0.06$	$-0.04 \pm 0.10$	$-0.20 \pm 0.24$	$0.03 \pm 0.53$
3810	$0.09 \pm 0.11$	$-0.03 \pm 0.19$	$-0.25 \pm 0.46$	$0.90 \pm 1.04$

**Table F.1:** Signal  $A_{\text{LL}}$  of  $\pi^0$  production measured with the PbGl for each fill.

Fill No.	$A_{LL}^{bg}$ per Fill in the PbGl			
	$1.0 < p_T [\text{GeV}/c] < 2.0$	$2.0 < p_T [\text{GeV}/c] < 3.0$	$3.0 < p_T [\text{GeV}/c] < 4.0$	$4.0 < p_T [\text{GeV}/c] < 5.0$
3625	-1.95 ± 1.92	5.94 ± 4.04	—	—
3627	0.30 ± 0.50	2.03 ± 1.28	1.23 ± 3.77	—
3634	0.65 ± 0.35	-0.08 ± 0.89	-0.08 ± 2.95	—
3637	-0.15 ± 0.33	-0.59 ± 0.79	1.50 ± 2.69	—
3644	0.29 ± 1.17	-0.45 ± 3.41	-10.51 ± 16.94	—
3646	-0.93 ± 0.55	0.73 ± 1.50	-0.52 ± 8.52	—
3654	0.33 ± 0.15	-0.18 ± 0.37	0.42 ± 1.22	0.10 ± 6.41
3659	0.07 ± 0.18	-0.02 ± 0.48	0.92 ± 1.49	-5.21 ± 3.85
3671	0.17 ± 0.17	-0.32 ± 0.44	1.19 ± 1.25	3.00 ± 3.10
3672	0.38 ± 0.23	0.44 ± 0.57	-0.54 ± 1.70	-0.05 ± 2.80
3674	0.03 ± 0.07	0.35 ± 0.18	-1.17 ± 0.62	2.02 ± 1.61
3675	0.50 ± 0.34	1.13 ± 0.89	0.36 ± 2.51	-0.17 ± 5.70
3676	-0.01 ± 0.18	-0.30 ± 0.47	-1.41 ± 1.91	-6.01 ± 4.72
3677	-0.23 ± 0.10	0.18 ± 0.25	-1.32 ± 0.85	3.04 ± 2.67
3678	-0.18 ± 0.10	0.08 ± 0.25	1.40 ± 0.84	0.30 ± 1.85
3679	-0.08 ± 0.09	0.05 ± 0.23	0.19 ± 0.76	-1.33 ± 2.22
3680	-0.01 ± 0.16	0.37 ± 0.41	-1.21 ± 1.31	—
3681	0.03 ± 0.10	0.02 ± 0.27	1.10 ± 0.99	4.99 ± 2.50
3682	-0.18 ± 0.26	-0.25 ± 0.67	3.63 ± 2.22	—
3691	0.03 ± 0.10	0.08 ± 0.25	0.55 ± 0.81	1.88 ± 1.94
3693	0.06 ± 0.06	-0.08 ± 0.16	0.05 ± 0.55	-1.20 ± 1.16
3696	0.38 ± 0.51	0.95 ± 1.17	-2.49 ± 4.32	—
3698	0.21 ± 0.18	-0.72 ± 0.47	-1.33 ± 1.36	-0.09 ± 5.00
3699	0.21 ± 0.16	0.85 ± 0.40	2.44 ± 1.28	-1.75 ± 4.10
3702	-0.36 ± 0.46	-0.99 ± 1.11	3.31 ± 3.04	—
3703	0.82 ± 0.42	1.76 ± 1.09	-0.63 ± 4.77	-0.63 ± 12.53
3705	-0.14 ± 0.14	0.19 ± 0.35	-0.45 ± 1.27	2.11 ± 3.21
3708	-0.17 ± 0.09	-0.53 ± 0.24	0.36 ± 0.78	0.43 ± 1.95
3713	-0.01 ± 0.05	0.18 ± 0.14	0.51 ± 0.44	2.93 ± 1.31
3714	0.04 ± 0.06	0.15 ± 0.17	-0.12 ± 0.57	0.50 ± 1.41
3732	2.69 ± 1.96	5.90 ± 4.74	—	—
3733	0.07 ± 0.13	0.30 ± 0.35	-1.40 ± 1.05	-1.69 ± 2.80
3735	-0.57 ± 0.31	-1.00 ± 0.86	-1.10 ± 2.65	—
3765	-0.07 ± 0.09	-0.07 ± 0.24	-0.21 ± 0.85	-1.12 ± 1.93
3767	-0.21 ± 0.18	0.44 ± 0.45	2.31 ± 1.76	5.24 ± 3.74
3769	-0.03 ± 0.04	-0.14 ± 0.11	-0.01 ± 0.41	0.67 ± 1.04
3770	-0.01 ± 0.09	-0.06 ± 0.24	-1.91 ± 0.85	0.13 ± 2.39
3774	0.05 ± 0.09	-0.17 ± 0.25	0.90 ± 0.86	-2.42 ± 1.91
3778	-0.69 ± 0.40	-1.75 ± 1.02	5.37 ± 3.61	-2.40 ± 8.64
3780	0.03 ± 0.06	-0.13 ± 0.16	-0.48 ± 0.53	-0.86 ± 1.62
3793	-0.04 ± 0.05	0.13 ± 0.14	0.87 ± 0.46	-0.86 ± 1.25
3796	-0.07 ± 0.09	0.29 ± 0.22	-0.51 ± 0.83	-1.48 ± 2.08
3797	-0.44 ± 0.26	-0.39 ± 0.71	-2.70 ± 2.39	-1.76 ± 5.31
3799	-0.01 ± 0.13	-0.10 ± 0.35	-1.39 ± 1.27	1.72 ± 4.20
3801	-0.01 ± 0.18	-0.02 ± 0.48	2.59 ± 1.72	3.04 ± 4.62
3803	-0.09 ± 0.09	-0.01 ± 0.23	-1.82 ± 0.81	1.70 ± 2.07
3810	0.17 ± 0.17	-0.45 ± 0.46	0.54 ± 1.58	2.91 ± 4.06

**Table F.2:** Background  $A_{LL}$  of  $\pi^0$  production measured with the PbGl for each fill.

Fill No.	$A_{\text{LL}}^{\pi^0 + \text{bg}}$ per Fill in the PbSc			
	$1.0 < p_T [\text{GeV}/c] < 2.0$	$2.0 < p_T [\text{GeV}/c] < 3.0$	$3.0 < p_T [\text{GeV}/c] < 4.0$	$4.0 < p_T [\text{GeV}/c] < 5.0$
3625	$1.07 \pm 0.81$	$0.24 \pm 0.97$	$3.00 \pm 2.38$	$3.53 \pm 3.59$
3627	$-0.15 \pm 0.31$	$-0.10 \pm 0.36$	$1.10 \pm 0.74$	$0.29 \pm 1.68$
3634	$0.44 \pm 0.21$	$0.28 \pm 0.23$	$0.05 \pm 0.49$	$-1.98 \pm 1.22$
3637	$0.56 \pm 0.20$	$0.06 \pm 0.22$	$0.03 \pm 0.47$	$0.40 \pm 1.06$
3644	$1.06 \pm 0.74$	$0.39 \pm 0.83$	$-1.30 \pm 1.75$	$-6.81 \pm 3.84$
3646	$-0.13 \pm 0.32$	$0.25 \pm 0.37$	$-1.21 \pm 0.79$	$3.24 \pm 1.91$
3654	$-0.12 \pm 0.09$	$-0.04 \pm 0.10$	$-0.09 \pm 0.21$	$-0.16 \pm 0.49$
3659	$-0.12 \pm 0.10$	$0.06 \pm 0.12$	$0.19 \pm 0.25$	$0.02 \pm 0.56$
3671	$0.03 \pm 0.09$	$-0.05 \pm 0.11$	$0.01 \pm 0.23$	$0.24 \pm 0.52$
3672	$0.15 \pm 0.13$	$0.20 \pm 0.15$	$-0.79 \pm 0.33$	$0.69 \pm 0.67$
3674	$-0.02 \pm 0.04$	$-0.11 \pm 0.05$	$0.20 \pm 0.10$	$0.24 \pm 0.23$
3675	$-0.09 \pm 0.20$	$0.03 \pm 0.22$	$0.44 \pm 0.46$	$0.51 \pm 1.04$
3676	$-0.11 \pm 0.10$	$-0.05 \pm 0.12$	$0.12 \pm 0.26$	$0.15 \pm 0.58$
3677	$0.09 \pm 0.06$	$-0.00 \pm 0.06$	$-0.27 \pm 0.14$	$-0.19 \pm 0.31$
3678	$-0.02 \pm 0.05$	$0.01 \pm 0.06$	$0.02 \pm 0.14$	$-0.02 \pm 0.31$
3679	$-0.05 \pm 0.05$	$-0.06 \pm 0.06$	$-0.10 \pm 0.13$	$-0.01 \pm 0.30$
3680	$-0.11 \pm 0.09$	$-0.07 \pm 0.10$	$0.05 \pm 0.22$	$-1.09 \pm 0.50$
3681	$0.02 \pm 0.06$	$-0.01 \pm 0.07$	$-0.28 \pm 0.15$	$-0.09 \pm 0.34$
3682	$0.22 \pm 0.15$	$-0.01 \pm 0.18$	$0.41 \pm 0.38$	$-0.88 \pm 0.84$
3691	$-0.14 \pm 0.05$	$-0.01 \pm 0.06$	$0.03 \pm 0.13$	$0.09 \pm 0.31$
3693	$0.00 \pm 0.03$	$-0.04 \pm 0.04$	$-0.02 \pm 0.09$	$-0.01 \pm 0.20$
3696	$0.19 \pm 0.30$	$-0.06 \pm 0.31$	$0.19 \pm 0.81$	$1.73 \pm 1.82$
3698	$0.15 \pm 0.10$	$0.07 \pm 0.12$	$0.15 \pm 0.25$	$0.18 \pm 0.54$
3699	$0.07 \pm 0.09$	$0.04 \pm 0.10$	$-0.17 \pm 0.22$	$0.31 \pm 0.50$
3702	$-0.02 \pm 0.24$	$-0.35 \pm 0.27$	$-0.26 \pm 0.60$	$1.34 \pm 1.44$
3703	$0.57 \pm 0.24$	$0.20 \pm 0.27$	$0.61 \pm 0.59$	$-1.83 \pm 1.32$
3705	$-0.11 \pm 0.08$	$0.09 \pm 0.09$	$-0.18 \pm 0.19$	$-0.41 \pm 0.45$
3708	$-0.01 \pm 0.05$	$-0.03 \pm 0.06$	$0.13 \pm 0.12$	$0.43 \pm 0.28$
3713	$-0.02 \pm 0.03$	$-0.02 \pm 0.03$	$0.01 \pm 0.07$	$-0.23 \pm 0.17$
3714	$0.01 \pm 0.04$	$0.00 \pm 0.04$	$-0.12 \pm 0.09$	$0.15 \pm 0.20$
3732	$-1.57 \pm 0.98$	$-0.15 \pm 1.10$	$0.27 \pm 2.34$	$-0.27 \pm 7.19$
3733	$-0.05 \pm 0.07$	$0.01 \pm 0.09$	$0.30 \pm 0.19$	$0.88 \pm 0.43$
3735	$0.24 \pm 0.18$	$0.06 \pm 0.20$	$-0.21 \pm 0.42$	$0.96 \pm 0.93$
3765	$0.05 \pm 0.05$	$-0.09 \pm 0.06$	$-0.12 \pm 0.13$	$-0.04 \pm 0.29$
3767	$-0.16 \pm 0.10$	$0.04 \pm 0.11$	$0.05 \pm 0.23$	$-0.37 \pm 0.55$
3769	$-0.04 \pm 0.02$	$-0.02 \pm 0.03$	$-0.07 \pm 0.06$	$-0.13 \pm 0.13$
3770	$0.03 \pm 0.05$	$-0.04 \pm 0.06$	$0.32 \pm 0.12$	$-0.06 \pm 0.29$
3774	$0.00 \pm 0.05$	$-0.15 \pm 0.06$	$-0.01 \pm 0.13$	$-0.15 \pm 0.30$
3778	$-0.18 \pm 0.21$	$0.27 \pm 0.24$	$0.04 \pm 0.54$	$0.09 \pm 1.23$
3780	$-0.03 \pm 0.03$	$0.01 \pm 0.04$	$0.09 \pm 0.08$	$0.03 \pm 0.19$
3793	$-0.03 \pm 0.03$	$-0.05 \pm 0.03$	$0.05 \pm 0.07$	$-0.16 \pm 0.16$
3796	$0.05 \pm 0.05$	$0.03 \pm 0.06$	$-0.03 \pm 0.12$	$0.25 \pm 0.28$
3797	$-0.03 \pm 0.15$	$0.19 \pm 0.17$	$-0.15 \pm 0.36$	$-0.88 \pm 0.78$
3799	$0.08 \pm 0.07$	$-0.05 \pm 0.08$	$0.10 \pm 0.19$	$-0.75 \pm 0.41$
3801	$-0.07 \pm 0.10$	$-0.08 \pm 0.11$	$-0.09 \pm 0.24$	$-0.22 \pm 0.52$
3803	$0.07 \pm 0.05$	$0.03 \pm 0.06$	$-0.22 \pm 0.12$	$-0.25 \pm 0.28$
3810	$0.04 \pm 0.09$	$0.03 \pm 0.11$	$0.17 \pm 0.23$	$-0.36 \pm 0.54$

**Table F.3:** Signal  $A_{\text{LL}}$  of  $\pi^0$  production measured with the PbSc for each fill.

$A_{LL}^{bg}$ per Fill in the PbSc				
Fill No.	$1.0 < p_T [\text{GeV}/c] < 2.0$	$2.0 < p_T [\text{GeV}/c] < 3.0$	$3.0 < p_T [\text{GeV}/c] < 4.0$	$4.0 < p_T [\text{GeV}/c] < 5.0$
3625	$1.05 \pm 0.99$	$0.74 \pm 2.67$	—	—
3627	$0.07 \pm 0.39$	$0.59 \pm 0.75$	$-1.44 \pm 2.30$	$-3.42 \pm 6.27$
3634	$0.25 \pm 0.26$	$0.17 \pm 0.53$	$2.50 \pm 1.66$	—
3637	$-0.03 \pm 0.24$	$0.27 \pm 0.46$	$2.65 \pm 1.49$	$-5.88 \pm 4.11$
3644	$1.24 \pm 0.91$	$-0.89 \pm 1.80$	$-14.47 \pm 6.13$	—
3646	$-0.29 \pm 0.39$	$1.08 \pm 0.81$	$0.17 \pm 2.46$	$6.63 \pm 6.39$
3654	$0.09 \pm 0.11$	$0.07 \pm 0.21$	$0.76 \pm 0.69$	$2.37 \pm 1.53$
3659	$0.15 \pm 0.13$	$-0.10 \pm 0.26$	$0.75 \pm 0.80$	$-0.23 \pm 2.03$
3671	$0.10 \pm 0.11$	$0.26 \pm 0.22$	$-0.66 \pm 0.72$	$3.61 \pm 1.96$
3672	$0.06 \pm 0.17$	$-0.20 \pm 0.34$	$0.52 \pm 1.05$	$1.78 \pm 3.24$
3674	$0.02 \pm 0.05$	$0.02 \pm 0.10$	$-0.04 \pm 0.31$	$-0.09 \pm 0.86$
3675	$-0.42 \pm 0.24$	$0.03 \pm 0.47$	$-0.82 \pm 1.40$	$-0.17 \pm 4.03$
3676	$-0.16 \pm 0.13$	$0.18 \pm 0.25$	$-0.39 \pm 0.80$	$1.71 \pm 2.82$
3677	$-0.08 \pm 0.07$	$-0.18 \pm 0.14$	$-0.14 \pm 0.43$	$-0.11 \pm 1.17$
3678	$0.05 \pm 0.07$	$0.08 \pm 0.14$	$0.61 \pm 0.42$	$1.02 \pm 1.04$
3679	$0.02 \pm 0.06$	$-0.19 \pm 0.13$	$-0.35 \pm 0.40$	$-1.03 \pm 1.02$
3680	$-0.14 \pm 0.11$	$-0.17 \pm 0.23$	$-0.08 \pm 0.70$	$0.89 \pm 1.57$
3681	$0.02 \pm 0.07$	$0.02 \pm 0.15$	$0.42 \pm 0.47$	$-0.10 \pm 1.16$
3682	$0.26 \pm 0.19$	$-0.36 \pm 0.38$	$0.73 \pm 1.09$	$2.54 \pm 2.87$
3691	$-0.05 \pm 0.06$	$-0.21 \pm 0.13$	$-0.25 \pm 0.42$	$1.57 \pm 1.19$
3693	$0.05 \pm 0.04$	$-0.17 \pm 0.09$	$-0.49 \pm 0.28$	$-0.02 \pm 0.68$
3696	$-0.72 \pm 0.35$	$0.27 \pm 0.69$	$1.59 \pm 2.08$	—
3698	$-0.15 \pm 0.12$	$-0.10 \pm 0.25$	$-0.21 \pm 0.80$	$1.18 \pm 2.09$
3699	$0.07 \pm 0.11$	$0.36 \pm 0.22$	$0.77 \pm 0.71$	$-1.04 \pm 1.84$
3702	$-0.21 \pm 0.29$	$-0.09 \pm 0.60$	$-1.22 \pm 1.76$	$0.42 \pm 4.53$
3703	$-0.04 \pm 0.29$	$0.66 \pm 0.59$	$-1.80 \pm 1.91$	$3.39 \pm 4.92$
3705	$-0.00 \pm 0.09$	$-0.09 \pm 0.19$	$0.45 \pm 0.58$	$-0.76 \pm 1.42$
3708	$0.09 \pm 0.06$	$0.10 \pm 0.12$	$-0.78 \pm 0.38$	$0.19 \pm 1.06$
3713	$0.03 \pm 0.04$	$-0.01 \pm 0.07$	$0.20 \pm 0.22$	$-0.05 \pm 0.56$
3714	$-0.00 \pm 0.04$	$0.01 \pm 0.09$	$-0.02 \pm 0.28$	$-0.08 \pm 0.72$
3732	$1.26 \pm 1.32$	$0.66 \pm 2.28$	—	—
3733	$0.14 \pm 0.09$	$0.09 \pm 0.19$	$0.73 \pm 0.57$	$0.04 \pm 1.62$
3735	$0.18 \pm 0.22$	$0.75 \pm 0.44$	$1.60 \pm 1.21$	$0.38 \pm 2.63$
3765	$0.06 \pm 0.06$	$0.01 \pm 0.13$	$-0.29 \pm 0.40$	$2.48 \pm 1.13$
3767	$0.02 \pm 0.12$	$-0.48 \pm 0.24$	$0.68 \pm 0.69$	$-3.01 \pm 1.83$
3769	$-0.00 \pm 0.03$	$0.17 \pm 0.06$	$0.17 \pm 0.19$	$-0.34 \pm 0.52$
3770	$-0.07 \pm 0.06$	$-0.16 \pm 0.13$	$-0.02 \pm 0.39$	$-0.58 \pm 0.96$
3774	$0.05 \pm 0.07$	$0.12 \pm 0.13$	$0.11 \pm 0.43$	$-0.01 \pm 1.16$
3778	$0.01 \pm 0.26$	$0.21 \pm 0.54$	$0.56 \pm 1.77$	$-2.29 \pm 4.23$
3780	$0.01 \pm 0.04$	$-0.09 \pm 0.08$	$-0.24 \pm 0.26$	$1.43 \pm 0.70$
3793	$-0.00 \pm 0.03$	$-0.19 \pm 0.07$	$0.27 \pm 0.23$	$-0.27 \pm 0.59$
3796	$0.10 \pm 0.06$	$-0.12 \pm 0.12$	$-0.05 \pm 0.40$	$0.05 \pm 1.09$
3797	$-0.27 \pm 0.18$	$-0.38 \pm 0.37$	$-2.05 \pm 1.14$	$-1.58 \pm 2.29$
3799	$0.12 \pm 0.09$	$0.06 \pm 0.19$	$0.21 \pm 0.59$	$0.50 \pm 1.49$
3801	$-0.08 \pm 0.12$	$0.10 \pm 0.24$	$-0.10 \pm 0.80$	$-1.46 \pm 2.00$
3803	$-0.01 \pm 0.06$	$-0.16 \pm 0.12$	$-0.18 \pm 0.38$	$-0.38 \pm 0.97$
3810	$-0.00 \pm 0.12$	$-0.19 \pm 0.24$	$0.69 \pm 0.76$	$-2.03 \pm 2.01$

**Table F.4:** Background  $A_{LL}$  of  $\pi^0$  production measured with the PbSc for each fill.

Fill No.	$A_{\text{LL}}^{\pi^0 + \text{bg}}$ per Fill in the EMCal			
	$1.0 < p_{\text{T}} [\text{GeV}/c] < 2.0$	$2.0 < p_{\text{T}} [\text{GeV}/c] < 3.0$	$3.0 < p_{\text{T}} [\text{GeV}/c] < 4.0$	$4.0 < p_{\text{T}} [\text{GeV}/c] < 5.0$
3625	$0.74 \pm 0.62$	$0.55 \pm 0.85$	$3.69 \pm 2.25$	$2.59 \pm 3.17$
3627	$-0.10 \pm 0.22$	$-0.19 \pm 0.29$	$0.92 \pm 0.64$	$0.61 \pm 1.51$
3634	$0.27 \pm 0.15$	$0.21 \pm 0.20$	$-0.03 \pm 0.43$	$-1.92 \pm 1.14$
3637	$0.39 \pm 0.14$	$0.08 \pm 0.19$	$-0.06 \pm 0.40$	$0.74 \pm 0.92$
3644	$0.86 \pm 0.53$	$0.33 \pm 0.70$	$-1.36 \pm 1.54$	$-7.56 \pm 3.29$
3646	$0.04 \pm 0.23$	$0.34 \pm 0.31$	$-1.05 \pm 0.69$	$1.61 \pm 1.65$
3654	$-0.03 \pm 0.06$	$0.04 \pm 0.08$	$-0.13 \pm 0.18$	$-0.08 \pm 0.42$
3659	$-0.04 \pm 0.08$	$0.03 \pm 0.10$	$0.16 \pm 0.22$	$0.39 \pm 0.50$
3671	$-0.02 \pm 0.07$	$-0.09 \pm 0.09$	$0.05 \pm 0.20$	$0.34 \pm 0.45$
3672	$0.17 \pm 0.10$	$0.19 \pm 0.13$	$-0.46 \pm 0.29$	$0.08 \pm 0.60$
3674	$0.05 \pm 0.03$	$-0.10 \pm 0.04$	$0.12 \pm 0.09$	$0.22 \pm 0.20$
3675	$-0.14 \pm 0.14$	$0.07 \pm 0.19$	$0.12 \pm 0.41$	$1.02 \pm 0.94$
3676	$-0.02 \pm 0.08$	$-0.11 \pm 0.10$	$0.05 \pm 0.23$	$0.66 \pm 0.51$
3677	$0.05 \pm 0.04$	$0.03 \pm 0.05$	$-0.20 \pm 0.12$	$-0.06 \pm 0.28$
3678	$-0.07 \pm 0.04$	$0.01 \pm 0.05$	$-0.08 \pm 0.12$	$-0.12 \pm 0.27$
3679	$-0.03 \pm 0.04$	$-0.03 \pm 0.05$	$-0.07 \pm 0.11$	$0.05 \pm 0.26$
3680	$-0.09 \pm 0.07$	$0.07 \pm 0.09$	$0.13 \pm 0.20$	$-0.54 \pm 0.44$
3681	$0.01 \pm 0.04$	$0.02 \pm 0.06$	$-0.25 \pm 0.13$	$0.11 \pm 0.30$
3682	$0.09 \pm 0.11$	$0.02 \pm 0.15$	$0.13 \pm 0.33$	$-0.71 \pm 0.74$
3691	$-0.07 \pm 0.04$	$0.00 \pm 0.05$	$0.02 \pm 0.12$	$0.04 \pm 0.27$
3693	$-0.01 \pm 0.02$	$-0.06 \pm 0.03$	$-0.03 \pm 0.08$	$-0.11 \pm 0.17$
3696	$0.15 \pm 0.21$	$0.34 \pm 0.27$	$0.53 \pm 0.67$	$1.53 \pm 1.71$
3698	$0.09 \pm 0.07$	$-0.01 \pm 0.10$	$0.02 \pm 0.22$	$0.00 \pm 0.48$
3699	$0.05 \pm 0.07$	$-0.03 \pm 0.09$	$-0.10 \pm 0.19$	$0.45 \pm 0.44$
3702	$-0.15 \pm 0.18$	$-0.16 \pm 0.23$	$0.07 \pm 0.51$	$0.79 \pm 1.28$
3703	$0.33 \pm 0.18$	$0.16 \pm 0.23$	$0.57 \pm 0.52$	$-1.42 \pm 1.18$
3705	$-0.08 \pm 0.06$	$0.08 \pm 0.08$	$-0.15 \pm 0.17$	$-0.20 \pm 0.39$
3708	$-0.03 \pm 0.04$	$-0.08 \pm 0.05$	$0.09 \pm 0.11$	$0.44 \pm 0.25$
3713	$0.02 \pm 0.02$	$0.02 \pm 0.03$	$-0.06 \pm 0.06$	$-0.14 \pm 0.15$
3714	$0.02 \pm 0.03$	$0.02 \pm 0.03$	$-0.08 \pm 0.08$	$0.11 \pm 0.18$
3732	$0.08 \pm 0.75$	$0.74 \pm 0.90$	$0.58 \pm 2.08$	$3.14 \pm 5.87$
3733	$-0.04 \pm 0.05$	$-0.04 \pm 0.07$	$0.15 \pm 0.16$	$0.46 \pm 0.38$
3735	$0.12 \pm 0.13$	$0.23 \pm 0.17$	$-0.08 \pm 0.36$	$-0.00 \pm 0.83$
3765	$0.03 \pm 0.04$	$-0.08 \pm 0.05$	$-0.17 \pm 0.11$	$-0.02 \pm 0.25$
3767	$-0.07 \pm 0.07$	$0.04 \pm 0.09$	$0.18 \pm 0.21$	$-0.15 \pm 0.48$
3769	$-0.03 \pm 0.02$	$-0.02 \pm 0.02$	$-0.07 \pm 0.05$	$-0.14 \pm 0.12$
3770	$0.01 \pm 0.04$	$-0.03 \pm 0.05$	$0.26 \pm 0.11$	$-0.26 \pm 0.25$
3774	$0.01 \pm 0.04$	$-0.12 \pm 0.05$	$-0.03 \pm 0.12$	$-0.30 \pm 0.26$
3778	$-0.26 \pm 0.16$	$0.14 \pm 0.21$	$0.45 \pm 0.48$	$-0.78 \pm 1.09$
3780	$-0.02 \pm 0.02$	$0.00 \pm 0.03$	$0.03 \pm 0.07$	$0.00 \pm 0.17$
3793	$-0.01 \pm 0.02$	$-0.03 \pm 0.03$	$0.13 \pm 0.06$	$-0.18 \pm 0.14$
3796	$0.04 \pm 0.04$	$0.05 \pm 0.05$	$0.09 \pm 0.11$	$0.24 \pm 0.25$
3797	$0.00 \pm 0.11$	$0.12 \pm 0.14$	$-0.11 \pm 0.31$	$-0.96 \pm 0.70$
3799	$0.10 \pm 0.05$	$-0.02 \pm 0.07$	$0.10 \pm 0.17$	$-0.64 \pm 0.36$
3801	$0.06 \pm 0.07$	$-0.12 \pm 0.10$	$-0.04 \pm 0.22$	$-0.45 \pm 0.48$
3803	$0.03 \pm 0.04$	$0.01 \pm 0.05$	$-0.19 \pm 0.11$	$-0.19 \pm 0.25$
3810	$0.06 \pm 0.07$	$0.01 \pm 0.09$	$0.10 \pm 0.21$	$-0.07 \pm 0.48$

**Table F.5:** Signal  $A_{\text{LL}}$  of  $\pi^0$  production measured with the combined EMCal subsystems for each fill.

Fill No.	$A_{LL}^{bg}$ per Fill in the EMCAL			
	$1.0 < p_T [GeV/c] < 2.0$	$2.0 < p_T [GeV/c] < 3.0$	$3.0 < p_T [GeV/c] < 4.0$	$4.0 < p_T [GeV/c] < 5.0$
3625	0.12 ± 0.84	2.30 ± 2.08	—	—
3627	0.14 ± 0.30	1.01 ± 0.63	-0.73 ± 1.96	2.72 ± 4.96
3634	0.32 ± 0.20	0.12 ± 0.45	1.88 ± 1.45	—
3637	-0.07 ± 0.19	0.09 ± 0.39	2.38 ± 1.30	-7.38 ± 3.51
3644	0.89 ± 0.69	-0.96 ± 1.58	-14.02 ± 5.76	—
3646	-0.35 ± 0.31	0.92 ± 0.71	0.12 ± 2.37	3.63 ± 5.98
3654	0.16 ± 0.08	-0.01 ± 0.18	0.71 ± 0.60	2.59 ± 1.45
3659	0.14 ± 0.10	-0.08 ± 0.22	0.70 ± 0.70	-1.30 ± 1.79
3671	0.11 ± 0.09	0.16 ± 0.20	-0.26 ± 0.62	3.44 ± 1.66
3672	0.18 ± 0.13	-0.09 ± 0.29	0.09 ± 0.88	0.73 ± 2.12
3674	0.03 ± 0.04	0.07 ± 0.09	-0.24 ± 0.28	0.38 ± 0.76
3675	-0.11 ± 0.19	0.24 ± 0.41	-0.53 ± 1.21	-0.17 ± 3.29
3676	-0.09 ± 0.10	0.05 ± 0.22	-0.62 ± 0.73	-0.29 ± 2.42
3677	-0.14 ± 0.05	-0.11 ± 0.12	-0.38 ± 0.38	0.62 ± 1.06
3678	-0.05 ± 0.05	0.08 ± 0.12	0.76 ± 0.37	0.85 ± 0.91
3679	-0.02 ± 0.05	-0.15 ± 0.11	-0.23 ± 0.35	-1.08 ± 0.92
3680	-0.07 ± 0.09	-0.05 ± 0.20	-0.36 ± 0.61	-0.39 ± 1.48
3681	0.01 ± 0.06	0.04 ± 0.13	0.59 ± 0.43	0.70 ± 1.05
3682	0.05 ± 0.15	-0.31 ± 0.33	1.36 ± 0.98	1.21 ± 2.73
3691	-0.02 ± 0.05	-0.14 ± 0.12	-0.08 ± 0.37	1.65 ± 1.01
3693	0.06 ± 0.03	-0.15 ± 0.08	-0.38 ± 0.25	-0.32 ± 0.58
3696	-0.38 ± 0.28	0.40 ± 0.59	0.82 ± 1.87	-0.08 ± 5.26
3698	-0.09 ± 0.10	-0.20 ± 0.22	-0.50 ± 0.69	0.99 ± 1.93
3699	0.09 ± 0.09	0.46 ± 0.19	1.18 ± 0.61	-1.16 ± 1.68
3702	-0.27 ± 0.23	-0.30 ± 0.52	-0.29 ± 1.50	-1.35 ± 4.05
3703	0.27 ± 0.23	0.99 ± 0.51	-1.46 ± 1.76	2.44 ± 4.30
3705	-0.07 ± 0.07	-0.03 ± 0.17	0.32 ± 0.52	-0.47 ± 1.29
3708	-0.00 ± 0.05	-0.03 ± 0.11	-0.54 ± 0.34	0.24 ± 0.93
3713	0.02 ± 0.03	0.04 ± 0.06	0.28 ± 0.20	0.41 ± 0.51
3714	0.02 ± 0.03	0.03 ± 0.08	-0.04 ± 0.25	0.09 ± 0.63
3732	1.62 ± 1.06	1.18 ± 2.02	—	—
3733	0.11 ± 0.07	0.12 ± 0.16	0.25 ± 0.50	-0.39 ± 1.40
3735	0.02 ± 0.17	0.40 ± 0.39	1.14 ± 1.10	1.64 ± 2.44
3765	0.01 ± 0.05	0.01 ± 0.11	-0.29 ± 0.37	1.56 ± 0.98
3767	-0.05 ± 0.09	-0.28 ± 0.21	0.89 ± 0.63	-1.33 ± 1.64
3769	-0.01 ± 0.02	0.10 ± 0.05	0.13 ± 0.17	-0.13 ± 0.46
3770	-0.06 ± 0.05	-0.12 ± 0.11	-0.34 ± 0.35	-0.37 ± 0.89
3774	0.06 ± 0.05	0.04 ± 0.12	0.29 ± 0.38	-0.66 ± 0.99
3778	-0.14 ± 0.21	-0.24 ± 0.47	1.23 ± 1.58	-2.22 ± 3.73
3780	0.02 ± 0.03	-0.10 ± 0.07	-0.31 ± 0.23	1.03 ± 0.64
3793	-0.02 ± 0.03	-0.11 ± 0.06	0.40 ± 0.20	-0.35 ± 0.53
3796	0.07 ± 0.05	-0.01 ± 0.10	-0.18 ± 0.36	-0.25 ± 0.95
3797	-0.36 ± 0.14	-0.44 ± 0.32	-2.20 ± 1.02	-1.61 ± 2.10
3799	0.06 ± 0.07	0.03 ± 0.16	0.01 ± 0.53	0.63 ± 1.40
3801	-0.06 ± 0.10	0.03 ± 0.21	0.45 ± 0.72	-0.27 ± 1.79
3803	-0.04 ± 0.05	-0.16 ± 0.11	-0.52 ± 0.34	0.06 ± 0.87
3810	0.06 ± 0.09	-0.19 ± 0.21	0.58 ± 0.68	-1.15 ± 1.79

**Table F.6:** Background  $A_{LL}$  of  $\pi^0$  production measured with the combined EMCAL subsystems for each fill.

# Bibliography

- [Aba06] V. M. Abazov *et al.* *Phys. Lett.* **B639** (2006) 151.
- [Abb07] P. Abbon *et al.* *The COMPASS Experiment at CERN*. hep-ex/0703049, 2007.
- [Abe94] F. Abe *et al.* *Phys. Rev. Lett.* **73** (1994) 2662.
- [Ack03] K. H. Ackermann *et al.* *Nucl. Instrum. Meth.* **A499** (2003) 624.
- [Ada03] M. Adamczyk *et al.* *Nucl. Instrum. Meth.* **A499** (2003) 437.
- [Ada05] J. Adams *et al.* *Nucl. Phys.* **A757** (2005) 102.
- [Adc02] K. Adcox *et al.* *Phys. Rev. Lett.* **88** (2002) 022301.
- [Adc03a] K. Adcox *et al.* *Nucl. Instrum. Meth.* **A499** (2003) 489.
- [Adc03b] K. Adcox *et al.* *Nucl. Instrum. Meth.* **A499** (2003) 469.
- [Adc05] K. Adcox *et al.* *Nucl. Phys.* **A757** (2005) 184.
- [Adl02] C. Adler *et al.* *Phys. Rev. Lett.* **89** (2002) 202301.
- [Adl03a] C. Adler *et al.* *Nucl. Instrum. Meth.* **A499** (2003) 433.
- [Adl03b] S. S. Adler *et al.* *Phys. Rev. Lett.* **91** (2003) 241803.
- [Adl03c] S. S. Adler *et al.* *Nucl. Instrum. Meth.* **A499** (2003) 560.
- [Adl03d] S. S. Adler *et al.* *Phys. Rev. Lett.* **91** (2003) 072301.
- [Adl05a] S. S. Adler *et al.* *Phys. Rev. Lett.* **94** (2005) 082301.
- [Adl05b] S. S. Adler *et al.* *Phys. Rev. Lett.* **94** (2005) 232301.
- [Adl05c] S. S. Adler *et al.* *Phys. Rev.* **D71** (2005) 071102.
- [Adl06a] S. S. Adler *et al.* *Phys. Rev. Lett.* **96** (2006) 202301.

- [Adl06b] S. S. Adler *et al.* *Phys. Rev.* **D73** (2006) 091102.
- [Aid06] C. A. Aidala. *Measurement of the transverse single-spin asymmetry for mid-rapidity production of neutral pions in polarized  $p + p$  collisions at 200-GeV center-of-mass energy.* hep-ex/0601009, 2006.
- [Aiz03] M. Aizawa *et al.* *Nucl. Instrum. Meth.* **A499** (2003) 508.
- [Aki03] H. Akikawa *et al.* *Nucl. Instrum. Meth.* **A499** (2003) 537.
- [Aki05] Y. Akiba *et al.* *Run3pp Direct Photon Measurement (II).* PHENIX Internal Analysis Note 460, 2005.
- [Alb88] C. Albajar *et al.* *Phys. Lett.* **B209** (1988) 385.
- [Ale03] I. Alekseev *et al.* *Nucl. Instrum. Meth.* **A499** (2003) 392.
- [Ali91] J. Alitti *et al.* *Phys. Lett.* **B263** (1991) 544.
- [All03] M. Allen *et al.* *Nucl. Instrum. Meth.* **A499** (2003) 549.
- [Alt77] G. Altarelli and G. Parisi. *Nucl. Phys.* **B126** (1977) 298.
- [Ana82] E. Anassontzis *et al.* *Zeit. Phys.* **C13** (1982) 277.
- [And79] L. W. Anderson *et al.* *Nucl. Instrum. Meth.* **167** (1979) 363.
- [Apa04] L. Apanasevich *et al.* *Phys. Rev.* **D70** (2004) 092009.
- [Aph03] L. Aphecetche *et al.* *Nucl. Instrum. Meth.* **A499** (2003) 521.
- [Aro03] S. H. Aronson *et al.* *Nucl. Instrum. Meth.* **A499** (2003) 480.
- [Ars05] I. Arsene *et al.* *Nucl. Phys.* **A757** (2005) 1.
- [Ash88] J. Ashman *et al.* *Phys. Lett.* **B206** (1988) 364.
- [Ash89] J. Ashman *et al.* *Nucl. Phys.* **B328** (1989) 1.
- [Aur88] P. Aurenche, R. Baier, M. Fontannaz, *et al.* *Nucl. Phys.* **B297** (1988) 661.
- [Aur06] P. Aurenche, M. Fontannaz, J.-P. Guillet, *et al.* *Phys. Rev.* **D73** (2006) 094007.
- [Awe97] T. Awes *et al.* *Report on Testing of PbGlass Supermodules at BNL, 1997, 1997.* PHENIX Internal Report.
- [Bac03] B. B. Back *et al.* *Nucl. Instrum. Meth.* **A499** (2003) 603.

- [Bac05] B. B. Back *et al.* *Nucl. Phys.* **A757** (2005) 28.
- [Bae90] H. Baer, J. Ohnemus, and J. F. Owens. *Phys. Rev.* **D42** (1990) 61.
- [Bai05] M. Bai *et al.* Prepared for Particle Accelerator Conference (PAC 05), Knoxville, Tennessee, 16-20 May 2005.
- [Bal98] G. Ballocchi *et al.* *Phys. Lett.* **B436** (1998) 222.
- [Bar59] V. Bargmann, L. Michel, and V. L. Telegdi. *Phys. Rev. Lett.* **2** (1959) 435.
- [Bas05] S. D. Bass. *Rev. Mod. Phys.* **77** (2005) 1257.
- [Bat02] S. Bathe. *Impulsfluktuationen und Produktion neutraler Pionen in ultrarelativistischen Schwerionenstößen*. Ph.D. thesis, Institut für Kernphysik, Münster, 2002.
- [Bat05a] S. Bathe, A. Bazilevsky, and H. Büsching. *Neutral Pion Spectra measured with the EMCAL in  $\sqrt{s} = 200 \text{ GeV}$   $p + p$ -Collisions PHENIX-Run3 Final Result*, 2005. PHENIX Internal Analysis Note 471.
- [Bat05b] S. Bathe, A. Bazilevsky, and H. Büsching. *Neutral Pion Spectra measured with the EMCAL in  $\sqrt{s} = 200 \text{ GeV}$   $p + p$ -Collisions PHENIX-Run3 Preliminary Result*, 2005. PHENIX Internal Analysis Note 470.
- [Bat05c] S. Bathe and H. Büsching. *Parameterization of the Final Run3  $\pi^0$  Cross Section in  $p + p$* , 2005. PHENIX Internal Analysis Note 472.
- [Bau03] F. Bauer, F. Kajihara, and K. Okada. *EMCal/RICH trigger performance in Run 3*, 2003. PHENIX Internal Analysis Note 228.
- [Baz99] A. V. Bazilevsky, V. I. Kochetkov, V. K. Semenov, *et al.* *Instrum. Exp. Tech.* **42** (1999) 167.
- [Baz03a] A. Bazilevsky. *Private communications*, 2003.
- [Baz03b] A. Bazilevsky *et al.* *AIP. Conf. Proc.* **675** (2003) 584.
- [Baz03c] S. Bazilevsky, B. Fox, Y. Goto, *et al.* *Updated Absolute Cross Section for Neutral Pion Production in Proton-Proton Collisions at  $\sqrt{s} = 200 \text{ GeV}$  with the PbSc Calorimeter*, 2003. PHENIX Internal Analysis Note 176.
- [Baz04] A. Bazilevsky, A. Deshpande, Y. Fukao, *et al.* *Results on Double Longitudinal Spin Asymmetry ( $A_{LL}$ ) in  $\pi^0$  Production in Polarized Proton-Proton Collisions at  $\sqrt{s} = 200 \text{ GeV}$  from Run-3*. PHENIX Internal Analysis Note 277, 2004.

- [Baz05] A. Bazilevsky. *Relative Measurements of BBC Trigger Efficiency in p+p Run2, 3 and 4.* PHENIX Internal Analysis Note 358, 2005.
- [Bjo69] J. D. Bjorken. *Phys. Rev.* **179** (1969) 1547.
- [Blo69] E. D. Bloom *et al.* *Phys. Rev. Lett.* **23** (1969) 930.
- [Bod79] A. Bodek *et al.* *Phys. Rev.* **D20** (1979) 1471.
- [Bou76] M. Bourquin and J. M. Gaillard. *Nucl. Phys.* **B114** (1976) 334.
- [Bou77] C. Bourrely and J. Soffer. *Nuovo Cim. Lett.* **19** (1977) 569.
- [Bou98] L. Bourhis, M. Fontannaz, and J. P. Guillet. *Eur. Phys. J.* **C2** (1998) 529.
- [Bre69] M. Breidenbach *et al.* *Phys. Rev. Lett.* **23** (1969) 935.
- [Büs06] H. Büsching. *Private communications*, December 2006.
- [Bun00] G. Bunce, N. Saito, J. Soffer, *et al.* *Ann. Rev. Nucl. Part. Sci.* **50** (2000) 525.
- [Büs02] H. Büsching. *Azimuthale Photon-Korrelationen in ultrarelativistischen p+A-, Pb+Pb und Au+Au Reaktionen.* Ph.D. thesis, Institut für Kernphysik, Münster, 2002.
- [Cal69] J. Callan, Curtis G. and D. J. Gross. *Phys. Rev. Lett.* **22** (1969) 156.
- [Col85] J. C. Collins, D. E. Soper, and G. Sterman. *Nucl. Phys.* **B261** (1985) 104.
- [CS98] A. M. Cooper-Sarkar, R. C. E. Devenish, and A. De Roeck. *Int. J. Mod. Phys. A* **13** (1998) 3385.
- [Dav98] G. David *et al.* *IEEE Trans. Nucl. Sci.* **45** (1998) 692.
- [d'E04] D. d'Enterria. *Photon and  $\pi^0$  efficiency losses due to photon conversions in PHENIX central-arms for Run 1-3.* PHENIX Internal Analysis Note 322, 2004.
- [Der78] Y. S. Derbenev *et al.* *Part. Accel.* **8** (1978) 115.
- [Die03] M. Diehl. *Phys. Rept.* **388** (2003) 41.
- [Dok77] Y. L. Dokshitzer. *Sov. Phys. JETP* **46** (1977) 641.
- [Dre02] A. Drees. *Nucl. Phys.* **A698** (2002) 331.

- [Fab03] C. W. Fabjan and F. Gianotti. *Rev. Mod. Phys.* **75** (2003) 1243.
- [Fro60] M. Froissart and R. Stora. *Nucl. Instrum. Meth.* **7** (1960) 297.
- [Glu95] M. Gluck, E. Reya, and A. Vogt. *Z. Phys.* **C67** (1995) 433.
- [Glu01] M. Gluck, E. Reya, M. Stratmann, *et al.* *Phys. Rev.* **D63** (2001) 094005.
- [GM64] M. Gell-Mann. *Phys. Lett.* **8** (1964) 214.
- [Gor93] L. E. Gordon and W. Vogelsang. *Phys. Rev.* **D48** (1993) 3136.
- [Got00] Y. Goto *et al.* *Phys. Rev.* **D62** (2000) 034017.
- [Gri72] V. N. Gribov and L. N. Lipatov. *Sov. J. Nucl. Phys.* **15** (1972) 438.
- [Gyu03] M. Gyulassy, I. Vitev, X.-N. Wang, *et al.* *Jet quenching and radiative energy loss in dense nuclear matter.* nucl-th/0302077, 2003.
- [Har03] M. Harrison, T. Ludlam, and S. Ozaki. *Nucl. Instrum. Meth.* **A499** (2003) 235.
- [Hir04] M. Hirai, S. Kumano, and N. Saito. *Phys. Rev.* **D69** (2004) 054021.
- [Hus95] J. Huston *et al.* *Phys. Rev.* **D51** (1995) 6139.
- [Iar83] E. Iarocci. *Nucl. Instrum. Meth.* **217** (1983) 30.
- [Jag04a] B. Jager, M. Stratmann, S. Kretzer, *et al.* *Phys. Rev. Lett.* **92** (2004) 121803.
- [Jag04b] B. Jager, M. Stratmann, and W. Vogelsang. *Phys. Rev.* **D70** (2004) 034010.
- [Jin04a] O. Jinnouchi *et al.* *Measurement of the analyzing power of proton-carbon elastic-scattering.* nucl-ex/0412053, 2004.
- [Jin04b] O. Jinnouchi *et al.* *Results from the RHIC PC CNI Polarimeter for 2003, 2004.* RHIC/CAD Accelerator Physics Note 171.
- [KB00] C. Klein-Bösing. *Simulation der Detektoreigenschaften des Bleiglaskalorimeters in den Experimenten WA98 und PHENIX.* Diplomarbeit, University of Münster, 2000.
- [KB04a] C. Klein-Bösing. *Production of Neutral Pions and Direct Photons in Ultra-Relativistic Au+Au Collisions.* Ph.D. thesis, Institut für Kernphysik, Münster, 2004.

- [KB04b] C. Klein-Bösing, K. Reygers, and T. Awes. *Direct Photons measured with the PbGl and the PbSc in  $\sqrt{s_{\text{NN}}} = 200 \text{ GeV}$  Au + Au Collisions (Run02)*. PHENIX Internal Analysis Note 353, 2004.
- [Khi89] F. Z. Khiari *et al.* *Phys. Rev.* **D39** (1989) 45.
- [Lai95] H. L. Lai *et al.* *Phys. Rev.* **D51** (1995) 4763.
- [Lee86] S. Y. Lee and S. Tepikian. *Phys. Rev. Lett.* **56** (1986) 1635.
- [Lib78] S. B. Libby and G. Sterman. *Phys. Rev.* **D18** (1978) 3252.
- [Lui97] G. Luijckx *et al.* Prepared for 17th IEEE Particle Accelerator Conference (PAC 97): Accelerator Science, Technology and Applications, Vancouver, British Columbia, Canada, 12-16 May 1997.
- [Man05a] S. R. Mane, Y. M. Shatunov, and K. Yokoya. *J. Phys.* **G31** (2005) R151.
- [Man05b] S. R. Mane, Y. M. Shatunov, and K. Yokoya. *Rept. Prog. Phys.* **68** (2005) 1997.
- [Mar94] A. D. Martin, R. G. Roberts, and W. J. Stirling. *MRS (1994): Parton distributions of the proton*. hep-ph/9409257, 1994.
- [Mie05] A. Mielech. *Nucl. Phys.* **A752** (2005) 191.
- [Mor00] Y. Mori *et al.* *Rev. Sci. Instrum.* **71** (2000) 1237.
- [Org06] K. Orginos, T. Blum, and S. Ohta. *Phys. Rev.* **D73** (2006) 094503.
- [Pap82] C. Papavassiliou, N. Mobed, and M. Svec. *Phys. Rev.* **D26** (1982) 3284.
- [Pei96] T. Peitzmann *et al.* *Nucl. Instrum. Meth.* **A376** (1996) 368.
- [Per00] D. H. Perkins. *Introduction to High Energy Physics*. Cambridge University Press, Cambridge, 2000.
- [Per05] D. Peressounko, T. Moukhanova, A. Kazantsev, *et al.* *Estimate of EMCAL alignment using charged tracks*, 2005. PHENIX Internal Analysis Note 377.
- [Pov99] B. Povh, K. Rith, C. Scholz, *et al.* *Teilchen und Kerne*. Springer-Verlag, Berlin, Heidelberg, New York, 1999.
- [Pti95] V. I. Ptitsin, Y. M. Shatunov, and S. Peggs Prepared for 16th IEEE Particle Accelerator Conference (PAC 95) and International Conference on High-Energy Accelerators (IUPAP), Dallas, Texas, 1-5 May 1995.

- [Pum02] J. Pumplin *et al.* *JHEP* **07** (2002) 012.
- [Rey03a] K. Reygers. *Fast Monte-Carlo Simulation for  $\pi^0$  and Photon Analysis.* PHENIX CVS Repository offline/analysis/PbGl/gampi0v2/acceptance/, 2003.
- [Rey03b] K. Reygers *et al.* *Measurement of Neutral Pions in  $\sqrt{s} = 200$  GeV p + p-Collisions with the PbGl Calorimeter.* PHENIX Internal Analysis Note 175, 2003.
- [Ros50] M. N. Rosenbluth. *Phys. Rev.* **79** (1950) 615.
- [Ros89] T. Roser. *AIP Conf. Proc.* **187** (1989) 1442.
- [Rya06] V. Ryabov. *Nucl. Phys.* **A774** (2006) 735.
- [Sch94] H. Schlagheck. *Konstruktion und Kalibration eines Bleiglaskalorimeters für ultrarelativistische Schwerionenreaktionen.* Diplomarbeit, Institut für Kernphysik, Münster, 1994.
- [Sei07] B. Seitz. *Nucl. Phys. Proc. Suppl.* **164** (2007) 9.
- [Sta05] P. Stankus. *Ann. Rev. Nucl. Part. Sci.* **55** (2005) 517.
- [Tan03] K. Tanida. *Relative Luminosity in Run3 pp.* PHENIX Internal Analysis Note 222, 2003.
- [Tho27] L. H. Thomas. *Phil. Mag.* **3** (1927) 1.
- [Toj02] J. Tojo *et al.* *Phys. Rev. Lett.* **89** (2002) 052302.
- [Tru02] T. L. Trueman. *Energy dependence of CNI analyzing power for proton carbon scattering.* hep-ph/0203013, 2002.
- [Tur04] S. Turbide, R. Rapp, and C. Gale. *Phys. Rev.* **C69** (2004) 014903.
- [Wil82] F. Wilczek. *Ann. Rev. Nucl. Part. Sci.* **32** (1982) 177.
- [Wod99] M. J. Wodarczyk. *Measurement of the F2 structure function of the proton at HERA from 1996 and 1997 ZEUS data,* 1999. UMI-99-56314.
- [Won94] C.-Y. Wong. *Introduction to High-Energy Heavy-Ion Collisions.* World Scientific, Singapore, 1994.
- [Yag05] K. Yagi, T. Hatsuda, and Y. Miike Cambridge, UK: Univ. Pr. (2005) 446 p.
- [Yao06] W. M. Yao *et al.* *J. Phys.* **G33** (2006) 1.

- [Zih05] B. Zihlmann. *The spin structure of the nucleon as seen by HERMES*, 2005.  
DESY-HERMES-05-05.
- [Zwe64] G. Zweig. 1964. CERN Report No. 8419/Th 412 (unpublished).

# Danksagung

Zu guter Letzt möchte ich mich bei all denen bedanken, die mich in meiner Zeit als Doktorand unterstützt und zum Gelingen dieser Arbeit beigetragen haben.

Bei Herrn Prof. Dr. Johannes P. Wessels möchte ich mich dafür bedanken, dass er mir die Möglichkeit gegeben hat, diese Arbeit in seiner Forschungsgruppe anzufertigen. Die sehr guten Arbeitsbedingungen in seiner Gruppe haben vieles erleichtert und mir geholfen, mich auf das Wesentliche meiner Arbeit zu konzentrieren. Außerdem danke ich ihm für die Ermöglichung zahlreicher Aufenthalte am BNL und der Teilnahme an mehreren Konferenzen und Workshops im In- und Ausland.

PD Dr. Klaus Reygers danke ich für die angenehme Zusammenarbeit und Betreuung meiner Arbeit. Ohne die zahlreichen Diskussionen, die entscheidend zur Klärung vieler meiner physikalischen und technischen Fragen beigetragen haben, wäre diese Arbeit in der vorliegenden Form nicht möglich gewesen.

Für die gute Zusammenarbeit bei den Analysen danke ich insbesondere Dr. Stefan Bathe und Dr. Henner Büsching, die mir viele Hilfestellungen gegeben haben. Dr. Kensuke Okada danke ich für die zahlreichen Diskussionen und Anmerkungen zur Analyse direkter Photonen. Bei Dr. Alexander Bazilevsky und Yoshinori Fukao bedanke ich mich für die fruchtbare Zusammenarbeit bei der Analyse der doppelt longitudinalen Spin Asymmetrie.

Für die anregende Mitarbeit zur Veröffentlichung der Resultate der Analyse direkter Photonen danke ich Dr. Y. Akiba, Dr. G. Bunce, Dr. H. Büsching, Dr. K. Okada und Dr. K. Reygers.

Bei Markus Rammler, Baldo Sahlmüller und Alexander Wilk bedanke ich mich für die gute Atmosphäre im Büro und die Möglichkeit, auch mal über nicht-physikalische Dinge diskutieren zu können.

Mein Dank gilt außerdem der gesamten PHENIX Kollaboration, die nun schon seit vielen Jahren gemeinschaftlich durch Fleiß und Einsatzwillen dafür sorgt, dass das PHENIX Experiment erfolgreich Daten liefert.

Für die angenehme Arbeitsatmosphäre bedanke ich mich bei allen aktuellen und ehemaligen Mitgliedern der Arbeitsgruppe: J. Auffenberg, Dr. S. Bathe, B. Bathen, C. Bau-

mann, Dr. D. Bucher, K. Büscher, Dr. H. Büsching, Dr. T. Dietel, Dr. R. Glasow, H. Gottschlag, H. Grimm, J. F. Grosse-Oetringhaus, N. Heine, H. Hünteler, Dr. C. Klein-Bösing, M. Klein-Bösing, A. Kumpmann, R. Lüchtenborg, J.-F. Pietschmann, M. Rammler, B. Sahlmüller, Prof. em. Dr. R. Santo, E. Sicking, W. Verhoeven, U. Westerhoff, A. Wilk und S. Wulff.

C. Baumann, M. Klein-Bösing, Dr. T. Dietel, B. Sahlmüller, A. Wilk und insbesondere Dr. K. Reygers und Dr. C. Klein-Bösing danke ich für die kritische Durchsicht meiner Arbeit.

Zum Schluss möchte ich mich bei meiner Familie bedanken, bei meinen Eltern und meiner Schwester, die mich immer unterstützt und mir Mut zugesprochen haben, bei meinen Schwiegereltern, die sich um viel gekümmert haben, damit ich mich auf meine Arbeit konzentrieren konnte, bei Enrico, der immer für etwas Ablenkung gesorgt hat und vor allem bei meiner Frau Britta: Deine Unterstützung und Dein Zuspruch, insbesondere in den letzten Wochen, haben alles etwas leichter gemacht. Danke!

## **Lebenslauf und Bildungsgang**

<b>Name:</b>	Oliver Zaudtke
<b>geb.:</b>	27.03.1977 in Haselünne
<b>Eltern:</b>	Bodo Zaudtke Sigrid Zaudtke, geb. Weber
<b>Familienstand:</b>	verheiratet
<b>Schulbildung:</b>	Grundschule: 1983–1987 Marienschule Meppen
	Orientierungsstufe: 1987 – 1989 Anne-Frank Schule Meppen
	Gymnasium: 1989 – 1996 Windthorst-Gymnasium Meppen
<b>Hochschulreife:</b>	am 21.05.1996 in Meppen
<b>Studium:</b>	10/1996 – 03/2003 Diplomstudiengang Physik an der Westfälischen Wilhelms-Universität Münster
<b>Prüfungen:</b>	Vordiplom: 02.11.1998 Diplom: 24.03.2003
<b>Auslandsstudium:</b>	09/1999 – 09/2000 Masterstudiengang: Physik und Technik von Kernreaktoren an der Universität Birmingham
<b>Abschluss:</b>	Master of Science: 14.12.2000
<b>Tätigkeiten:</b>	12/2000–03/2003 stud. Hilfskraft, 04/2003–06/2003 wiss. Hilfskraft, seit 07/2003 wiss. Mitarbeiter
<b>Beginn der Dissertation:</b>	01.04.2003 am Institut für Kernphysik bei Prof. Dr. J. P. Wessels



